



**HAL**  
open science

# Probing light-matter interaction in the many-body regime of superconducting quantum circuits

Javier Puertas

► **To cite this version:**

Javier Puertas. Probing light-matter interaction in the many-body regime of superconducting quantum circuits. Mesoscopic Systems and Quantum Hall Effect [cond-mat.mes-hall]. Université Grenoble Alpes, 2018. English. NNT : 2018GREAY021 . tel-01839210v2

**HAL Id: tel-01839210**

**<https://theses.hal.science/tel-01839210v2>**

Submitted on 19 Nov 2018

**HAL** is a multi-disciplinary open access archive for the deposit and dissemination of scientific research documents, whether they are published or not. The documents may come from teaching and research institutions in France or abroad, or from public or private research centers.

L'archive ouverte pluridisciplinaire **HAL**, est destinée au dépôt et à la diffusion de documents scientifiques de niveau recherche, publiés ou non, émanant des établissements d'enseignement et de recherche français ou étrangers, des laboratoires publics ou privés.

## THÈSE

Pour obtenir le grade de

### **DOCTEUR DE LA COMMUNAUTÉ UNIVERSITÉ GRENOBLE ALPES**

Spécialité : NANOPHYSIQUE

Arrêté ministériel : 25 mai 2016

Présentée par

**Javier PUERTAS**

Thèse dirigée par **Olivier BUISSON**, CNRS

et codirigée par **Nicolas ROCH**

préparée au sein de l'Institut Néel

dans l'École Doctorale Physique

**Interaction lumière-matière dans le régime à  
N-corps des circuits quantiques  
supraconducteurs.**

**Probing light-matter interaction in the many-  
body regime of superconducting quantum  
circuits.**

Thèse soutenue publiquement le **29 juin 2018**,  
devant le jury composé de :

**Monsieur Olivier Buisson**

Directeur de Recherche, Institut Néel, Directeur de thèse

**Monsieur Gary Steele**

Associate Professor, Delft University of Technology, Rapporteur

**Monsieur Fabien Portier**

Directeur de Recherche, CEA Saclay, Rapporteur

**Monsieur Denis Basko**

Directeur de Recherche, Laboratoire de Physique et Modélisation des  
Milieux Condensés, Président

**Monsieur Pol Forn-Díaz**

Professeur assistant, Barcelona Supercomputing Center, Membre

**Monsieur Julien Renard**

Chercheur, Institut Néel, Membre

**Monsieur Nicolas Roch**

Chargé de Recherche, Institut Néel, Co-directeur de thèse







# Acknowledgments

First of all I would like to thank the members of the committee: Prof. Gary Steele and Dr. Fabien Portier for accepting being *rapporteurs* and Dr. Pol Forn Díaz and Dr. Denis Basko for being *examineurs* of my thesis.

The results of any experimental work rely on hundreds of people working to maintain the equipment in good shape. I want to thank the Nanofab team at the Néel Institut and the PTA team for making it possible to fabricate all the samples present and not present in this manuscript. Thanks also to Benjamin Sacépé for the fabrication of the InOx resonator presented at the end of the manuscript. In addition I want to thank Eric Eyraud for his efforts installing the cryostat used in this work and Christophe Hoarau for his willingness to fabricate and re-fabricate several PCBs for this and future projects. In addition I want to thank the administrative staff, specially Florence Pois, for making things always easier.

This thesis would not have been possible without the funding of Laboratoire d'Alliances Nanosciences-Energies du futur (LANEF). It would not have been possible either without the permanent members of the Superconducting Quantum Circuits Team: Olivier Buisson, Wiebke Guichard, Cécile Naud, Nicolas Roch and Julien Renard, that although is not officially in the team, helped me as if he were. I want to thank specially Nicolas Roch and Olivier Buisson for their supervision. Nico helped me from the beginning to the end, guiding me whenever I needed to. He was very patient and helpful and there is no doubt he is the best supervisor one can have. Olivier is tied with Nico at the supervisor level. Discussing with him gave me a greater insight in the physics of my project. I greatly value his relaxed way of discussing any topic.

After doing an experiment one needs to understand the results and this is where these superheros enter the scene, the theoreticians. I was very lucky to work with Serge Florens and Izak Snyman who gave answers to all our questions. They helped us during the project and more personally, they helped me during the writing of this manuscript. I would also like to thank Duy Nguyen and Denis Basko for his help in understanding and deriving the remote ground model for the array of SQUIDS.

During my three years at the Néel Institut the members of the office Z-218 have been continuously changing. Everyone in that office has influenced somehow this work. The older member I met was Étienne. He started the now famous tradition of bringing our own food to the lab. In addition he helped me with Python, Git, KLayout, the fabrication of the magnetic screen . . . When I arrived Rémy was already there. We have grown together scientifically speaking sharing both the good and bad times of the PhD. The last original member was Clément; being from other group never stopped him from saying *bonjour* every morning. Then new members arrived. First Kitty, best partner for coffee breaks. Then Luca, from

whom I learned that no matter how bad your team plays, it won't be worse than PSG. Other members include Akansha, now in CEA and forgetting about us; Farshad, a very "happy" person; Doriane, who brings very sweet *québécois* desserts; Karthik, biggest LOTR fan and Sébastien. With his deep knowledge of mathematics, Sébastien helped in the last months of my work. He is now in charge of measuring *The Kondo*, I hope he succeeds.

Out of the office there were valuable people too: Yuriy, Jorge, Álvaro, Nico, Goutham, Ioanna, Ana, Bivas . . . Honorable mention to Jorge, who organizes everything at every moment. He is the kind of person you have to ask when you are doing paperwork and that's why he is in everybody's heart. Another honorable mention to Goutham's delicious indian food and to Yuriy for our homemade filters. Finally thanks to Nico, for sharing somehow with me the project and for the *randonnées* we did together.

Some people do not work with you but help you anyway, they are either friends or family. In my case, the first group can be classified in three subgroups: Grenoble, Munich and Moratalaz. Thanks to all of them for supporting me. Regarding my family, thanks for telling me at every time things like "You don't speak French after living there for three years?" or "What are these qubits for?". This gave me the strength for finishing my thesis as soon as possible.

Finally, this thesis would not have been possible at all if it weren't for Ana. She encouraged me to start it and encouraged me even further to finish it within three years. She supported me in the difficult times and she has been always present during my stay in Grenoble. She helped in a material way too. Not only did she bring *jamón*, *espetec* and *chorizo* to Grenoble, she also brought happiness in the form of *Napolitanas de Cuétara*. For all this and your love, thank you Ana.

*¿Tres razones para vivir?,  
me sobra con una, la curiosidad.*

LUIS GARCÍA BERLANGA



# Contents

INTRODUCTION AND SUMMARY	1
1 LIGHT-MATTER INTERACTION	13
1.1 One atom and one mode . . . . .	13
1.2 One atom and several modes . . . . .	19
2 CIRCUIT THEORY	23
2.1 Basics of superconducting circuits . . . . .	23
2.2 Linear circuits . . . . .	28
2.3 Nonlinear circuits . . . . .	44
3 COUPLING IN CIRCUITS	49
3.1 Coupling between two oscillators . . . . .	49
3.2 Coupling between an LC oscillator and a continuous environment .	53
3.3 Coupling of a transmon qubit to a linearized array . . . . .	59
3.4 The transmon phase shift . . . . .	62
4 CIRCUIT DESIGN AND FABRICATION	75
4.1 Circuit fabrication with e-beam lithography . . . . .	75
4.2 DC measurements . . . . .	92
4.3 Circuit parameters . . . . .	97
5 EXPERIMENTAL SETUP	103
5.1 The dilution refrigerator . . . . .	103
5.2 Microwave setup . . . . .	110
6 CHARACTERIZATION OF THE ARRAYS OF SQUIDS	117
6.1 Measured samples . . . . .	117
6.2 Transmission measurements . . . . .	118
6.3 Dispersion relation . . . . .	122
7 TRANSMON QUBIT COUPLED TO AN ARRAY OF SQUIDS	127
7.1 The sample . . . . .	127
7.2 Transmission measurements . . . . .	127
7.3 System-environment interaction . . . . .	133
CONCLUSION AND PERSPECTIVES	143
APPENDICES	149
A CALCULATIONS	151

A.1	Characteristic impedance of a periodic transmission line . . . . .	151
A.2	Linear Hamiltonian in eigenmodes . . . . .	152
A.3	SCHA derivation for the full system . . . . .	153
A.4	TPS calculations . . . . .	155
B	SCRIPTS . . . . .	161
B.1	NanoBeam files . . . . .	161
B.2	Python GDS . . . . .	163
B.3	Python DC measurements . . . . .	165
C	FABRICATION RECIPE . . . . .	167
D	ADDITIONAL TRANSMON PHASE SHIFT DATA . . . . .	169
	BIBLIOGRAPHY . . . . .	171

# Introduction and summary

## *Introduction*

### *Study of light-matter interaction with circuits*

Understanding the underlying mechanism in the interaction between light and matter has been a fundamental part of physics since its beginning. From geometrical optics to electromagnetism, every new discovery gave rise to a different way of understanding nature. In quantum physics the introduction of the idea of the *photon* and its role in the excitation and relaxation of atoms set the foundations of the study of light-matter coupling at its most fundamental level.

A system composed of an atom coupled to a single electromagnetic mode of frequency  $\omega_0$  represents the most standard model in quantum optics<sup>1</sup>. The research field treating this type of system is called Cavity Quantum ElectroDynamics (CQED) because of the optical cavities used in the experiments to “trap” photons inside. Whenever the mode is nearly resonant with one atomic transition of frequency  $\omega_q$ , the atom can be modeled as an effective two-level system whose energy splitting is given by  $\omega_q$ . There is an exchange of energy between the two systems, the atom and the EM mode. This energy exchange is related to the light-matter coupling strength  $g$ . The system dynamics is governed by the strength of this coupling  $g$  compared to the other energy scales in the system,  $\omega_0$  and  $\omega_q$ . In natural systems  $g$  is related to the fine structure constant  $\alpha \sim 1/137$  which, as a result, limits the strength of this coupling. Given its weakness, it is common in these systems to perform the Rotating Wave Approximation (RWA) where effects such as the simultaneous creation (annihilation) of a photon and the excitation (relaxation) of the atom can be neglected. Within this approximation and whenever the coupling strength  $g$  overcomes the losses in the system, it is possible to observe a coherent exchange of energy between the atom and the EM mode in an oscillatory fashion: the atom relaxes emitting a photon into the mode that eventually is absorbed back by the atom exciting it, the so called *Rabi oscillations*.

In the last decade, the study of light-matter interaction has seen an incredible development thanks to the introduction of superconducting circuits<sup>2</sup>. Natural atoms are replaced by superconducting qubits that couple to the EM field inside microwave transmission lines and resonators. Due to the similarity with CQED this field was called Circuit Quantum ElectroDynamics (Circuit QED). Apart from its wide use in quantum computation<sup>3</sup> and quantum information<sup>4</sup>, superconducting circuits enable the exploration of light-matter coupling beyond the RWA approximation, a regime unreachable with natural atoms. In this regime exotic phenomena such as quantum phase transitions<sup>5</sup> and photonic population



of the ground state<sup>6</sup> take place. There are three factors affecting the coupling strength  $g$ . First, the dipole moment of the atom. Superconducting circuits have a larger dipole moment than natural atoms due to their larger size. Second, the field dimension. In the integrated circuits used in Circuit QED the field propagates in one dimensional transmission lines which enhances the coupling compared to the three dimensional confinement of their CQED counterpart. Third, the vacuum fluctuations of the electromagnetic field. These fluctuations are related to the impedance of the environment  $Z_0$ . They scale as  $1/\sqrt{Z_0}$  for magnetic coupling and as  $\sqrt{Z_0}$  for electric coupling<sup>7,8</sup>. By engineering the proper impedance  $Z_0$  one can increase the coupling strength several orders of magnitude compared to CQED systems. First experiments showing coherent coupling within the RWA between a superconducting qubit and a photonic mode used microwave resonators to enhance this coupling<sup>9,10,11,12,13</sup>. Soon after, thanks to the optimization of the qubit-resonator coupling, experimental observations of the break down of the RWA were reported<sup>14,15,16</sup>. This coupling regime was named *ultra-strong coupling regime*. In addition, quantum simulations of these systems have shown the qubit-photon entanglement of the ground state<sup>17</sup> and the system dynamics<sup>18</sup> beyond the RWA. Despite the great advances obtained in these experiments, the use of microwave resonators limited the measured systems to a two-body problem where only two electromagnetic modes interact, the one from the qubit and the one from the microwave resonator.

### *Many-body systems in Circuit QED*

Many-body problems are ubiquitous in nature due to the fact that no system is ever fully isolated from its environment. Moreover, many-body systems are at the core of condensed matter physics. Therefore, understanding how these systems behave in a controlled environment is highly relevant for nowadays research. Given the versatility of Circuit QED architectures they are one of the best candidates to study these problems.

Until now we have introduced the idea of light-matter coupling with one atom and one electromagnetic mode. With an increasing number of modes we can enter the realm of many-body physics. More modes does not necessarily mean that the atom is interacting with several of them. If the coupling is weak, the atom will only interact with the mode it is resonant with. One would need a strong enough coupling for the atom to interact with more than one mode at once. Here we give some conditions that ensure that a system can be viewed as a many-body system.

In a multi-mode system, the atom couples to each of the modes of the environment  $\omega_k$  via a coupling strength  $g_k$ , where  $k$  indicates the mode index. Whenever the atom is resonant with any of the modes, a mode splitting of  $\sim 2g_k$  occurs. If this mode splitting is big enough it will involve several modes. Therefore, in order to have a many-body system it is necessary for the coupling strengths  $g_k$  to be in the order of the Free Spectral Range of the environment ( $\text{FSR} = \omega_k - \omega_{k-1}$ ). In addition, for the qubit to behave as a nonlinear system, it is important for its nonlinearity to be at least in the order of the FSR. In this way, the effect of the nonlinearity will not be seen as a perturbation to the system. Finally, in order to observe nontrivial effects, it is important for the system to be beyond RWA, that is, the coupling strength should be comparable to the qubit frequency. This regime

is named ultra-strong coupling regime. We can summarize these conditions as:

- The environment the qubit couples to contains several modes  $\omega_k$ .
- These modes are dense, i.e. the coupling strength is comparable to the Free Spectral Range of the environment,  $2g_k/\text{FSR} \sim 1$  with  $\text{FSR} = |\omega_k - \omega_{k-1}|$ .
- The qubit anharmonicity  $\tilde{\alpha}$  should be larger or in the order of the FSR,  $\tilde{\alpha}/\text{FSR} \geq 1$
- The system must be beyond the RWA, coupling strength comparable to the qubit frequency (ultra-strong coupling regime).

In a Circuit QED architecture we can obtain all these conditions. The first two can be obtained either with very long microwave resonators ( $\text{FSR} \propto 1/l$ ) or directly using open transmission lines ( $\text{FSR} = 0$ ). The third one can be obtained choosing the right qubit design. For the fourth one, the impedance of the environment  $Z_0$  and the dipole moment of the qubit, the most challenging of the two, should be designed to maximize the qubit-environment coupling.

First experiments on many-modes environments in Circuit QED consisted of a flux qubit inductively coupled to an open transmission line<sup>19,20</sup>. They observed resonance fluorescence of the flux qubit in a transmission line. In addition, well-known quantum optics effects such as the Mollow triplet, the Autler-Townes splitting and Electromagnetically Induced Transparency were measured, all within the RWA. With the same type of system but with an optimized coupling scheme<sup>21</sup>, a new experiment<sup>22,23</sup> measured quantum many-body effects from the spectroscopy of the circuit. When increasing the coupling  $g$  between the flux qubit and the transmission line, the bare qubit frequency  $\omega_q$  shifted to lower values. This renormalization of the qubit frequency is a well-known many-body effect related to the suppression of the tunneling rate in the Josephson junction<sup>24</sup>.

Regarding capacitive coupling, some experiments have been already performed where a transmon qubit is coupled to an open transmission line<sup>25,26</sup>. They showed the extinction of the qubit resonance with increasing microwave power, a signature of strong nonlinearity, and obtained the Mollow triplet and Autler-Townes splitting for this system. Following a different approach, a transmon qubit was capacitively coupled to a long resonator<sup>27</sup> ( $l \sim 0.68$  m). Given the length of the resonator, the obtained FSR is very small,  $\sim 92$  MHz, obtaining a ratio  $2g/\text{FSR} \sim 0.65$  for mode number 75. The hybridization of the transmon qubit mode with each of the modes of the environment was measured via the spectroscopy of the system. In addition, high power measurements showed multimode fluorescence in the resonator. Due to the fact that these measurements were performed in a low impedance environment,  $Z_0 = 50 \Omega$ , they did not show any non RWA effect. Recently, a new device was presented consisting of a transmon qubit coupled to a microwave resonator<sup>28</sup>. The coupling was optimized via a vacuum-gap capacitor between the transmon island and the center conductor of the resonator. Thanks to this optimized capacitor non RWA effects were measured despite working in a low impedance environment. They obtained a coupling strength of  $g = 897$  MHz. Comparing this to the qubit frequency  $\omega_q$  they obtained a ratio of  $g/\omega_q = 0.2$ , already far beyond RWA. Due to the short length of the microwave resonator, in their system they obtained  $2g/\text{FSR} \sim 0.4$ . Despite this, they fitted the spectrum

of the circuit with a multimode Rabi model proving the coupling of the qubit to up to 5 modes of the resonator. These experiments open exciting new possibilities and represent a first step towards many-body quantum optics. However, most of this field remains experimentally unknown: a quantitative understanding of this many-body renormalization remains to be given and countless theoretical predictions concerning the dynamics of such systems remain to be tested<sup>29,30,31,32</sup>.

The aim of this work is to enhance the qubit-light coupling by increasing the impedance of the environment the qubit is coupled to. A similar idea was experimentally implemented recently using a transmon qubit coupled to a standard microwave resonator in the CPW geometry<sup>33</sup>. In our case, following recent theoretical proposals<sup>29,30,34</sup>, we engineer a high impedance environment consisting of an array of Josephson junctions.

The use of arrays of Josephson junctions for the study of fundamental physics is not new. It has been an important topic in condensed matter physics for more than thirty years now. First experiments used two dimensional arrays for studying topological phase transitions<sup>35,36,37,38</sup>.

More recently, one dimensional arrays have been used in DC experiments showing the effects of large phase fluctuations on single Josephson junctions<sup>39,40</sup>. Contrary to the arrays used in this work, the ones used in these experiments were highly nonlinear ( $E_J \sim E_C$ ). These arrays have also been used for measuring phase slips<sup>41,42,43</sup>. It is only recently that the microwave properties of such arrays have been investigated in their linear regime ( $E_J \gg E_C$ )<sup>44,45</sup>. Given their large kinetic inductance, they are used as superinductors<sup>46,47</sup> and gave rise to the fluxonium qubit<sup>48</sup>. In applied physics they are used for fabricating Josephson Parametric Amplifiers<sup>49,50,51</sup>.

The circuit presented in this manuscript consists of a transmon qubit capacitively coupled to an array of SQUIDS. The aim is two fold: the transmon qubit is very resilient to noise and easy to model while the parameters of the arrays of SQUIDS can be adjusted in-situ making it possible to study the transmon-array system at different coupling regimes. Thanks to the high impedance of the array and its dense spectrum we observe a coupling between the transmon qubit and the array of SQUIDS involving several modes of the system. This makes this circuit a perfect platform for studying many-body physics in a tunable and controllable system.

Most theoretical predictions made for many-body systems<sup>52</sup> have not been proved experimentally yet. Therefore, near future experiments using our original circuit platform involve the measurement of some of these phenomena such as low power frequency conversion<sup>29,32,53</sup> or the many-body renormalization of the qubit frequency<sup>34</sup>. Long-term goals involve the study of well-known many-body problems in condensed matter physics such as the sine-Gordon model, the Dicke model or the Kondo model. In addition, taking advantage of the flexibility of the array of SQUIDS, one can think of shaping the dispersion relation by modulating the size of the junctions in the array<sup>54</sup> or designing Left Handed Transmission Lines that are predicted to show multimode entanglement and quantum phase transitions<sup>55,56</sup>.

## Summary

The purpose of this work is to study the interaction between a transmon qubit and a controlled environment for non-perturbative coupling strengths, i.e. for coupling strengths comparable to the qubit frequency. This regime has been achieved by increasing the impedance of the environment using an array of SQUIDS. Indeed, for capacitive coupling, this strength scales as  $\sqrt{Z_{\text{array}}}$ .

We perform spectroscopy measurements of a transmon qubit coupled to an array of SQUIDS and observe the hybridization of the transmon qubit mode with several modes of the array. Using an external magnetic field we tune the characteristic impedance of the array and study the system at different coupling strengths. This tuning of the coupling strength is seen by a modulation of the transmon qubit resonance width as a function of the applied magnetic flux. Finally we develop an effective linear model accounting for the transmon non-linearity and all the vacuum-quantum fluctuations that explains the experimental results with no fitting parameter for all the range of coupling strengths.

## The sample

The sample consists of a transmon qubit capacitively coupled to an array of 4700 Josephson junctions in a SQUID geometry. Its lumped element model is given in Fig. 1 (a). In red the transmon qubit is shown. It plays the role of the quantum system we want to study. On the other hand, in blue, the array plays the role of the environment the transmon is coupled to. Thanks to the large kinetic inductance of Josephson junctions the array behaves as a high impedance transmission line of characteristic impedance  $Z_{\text{array}} = \sqrt{L_J/C_g}$ . In addition, the SQUIDS in the array allow us to tune this impedance and therefore the transmon-array coupling strength. We include a SQUID with a larger loop area in the transmon qubit. This makes it possible to study the interaction between the system (the transmon qubit) and the environment (the array of SQUIDS) in different coupling regimes. An optical picture of the sample is shown in Fig. 1 (b). The circuit was fabricated in one step of e-beam lithography. It is made of aluminum deposited on a silicon substrate.

## Measurements

The characterization of the circuit is done via microwave transmission measurements performed at 20 mK in a dilution refrigerator. We measure the transmitted voltage  $S_{21}(\omega) = V_2/V_1$  as a function of the applied microwave frequency  $\omega$  using a Vector Network Analyzer (VNA). We obtain a peak in transmission at the eigenfrequencies of the system. Using an external superconducting coil we apply a magnetic field to the sample and obtain the transmission for several magnetic fields, Fig. 2 top. We denote by  $\Phi_C$  the flux in the SQUIDS loops of the array and by  $\Phi_T$  the flux in the transmon qubit SQUID loop. The magnetic flux is given in units of the magnetic flux quantum  $\Phi_0 = h/2e$ . The colormap represents the amplitude of the transmission through the circuit  $|S_{21}|(\omega)$ .

As it can be seen, we measure two different flux periods. This is due to the difference in area between the transmon SQUID loop (large area, short period) and

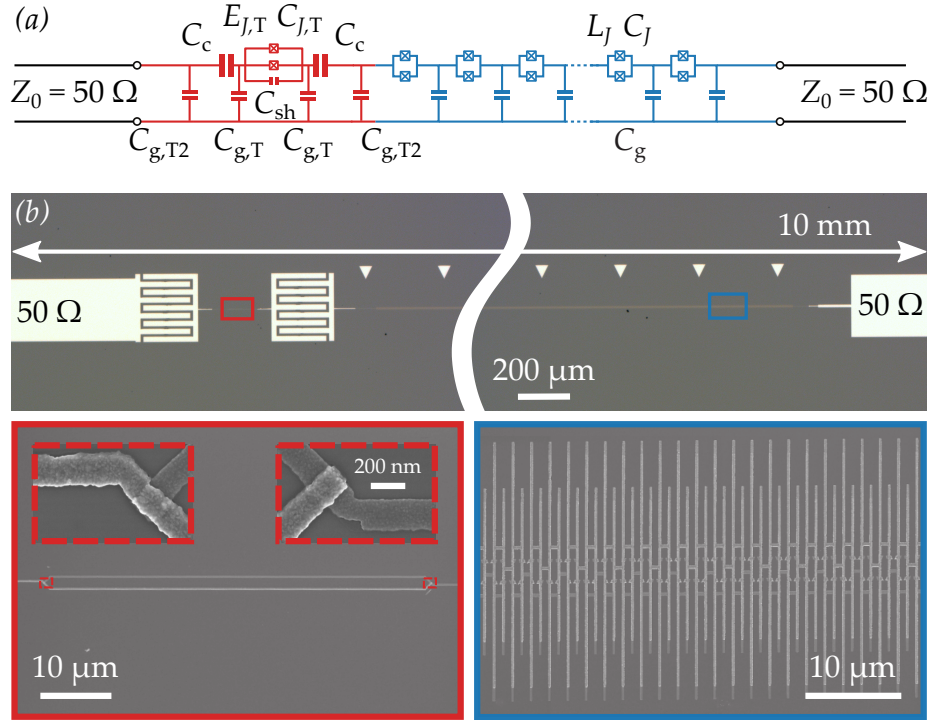


Figure 1 – The sample measured in this work. (a) Circuit diagram of the sample. In red the transmon qubit and in blue the array. Both the transmon qubit and the array of SQUIDs are flux tunable. We include the input and output ports of characteristic impedance  $Z_0 = 50 \Omega$ . (b) Optical image of the sample. Only a portion of the array of SQUIDs is shown. The insets show the SQUID in the transmon (red) and the SQUIDs in the array (blue). The Josephson junctions for the transmon are given as insets in the former (red dashed squares).



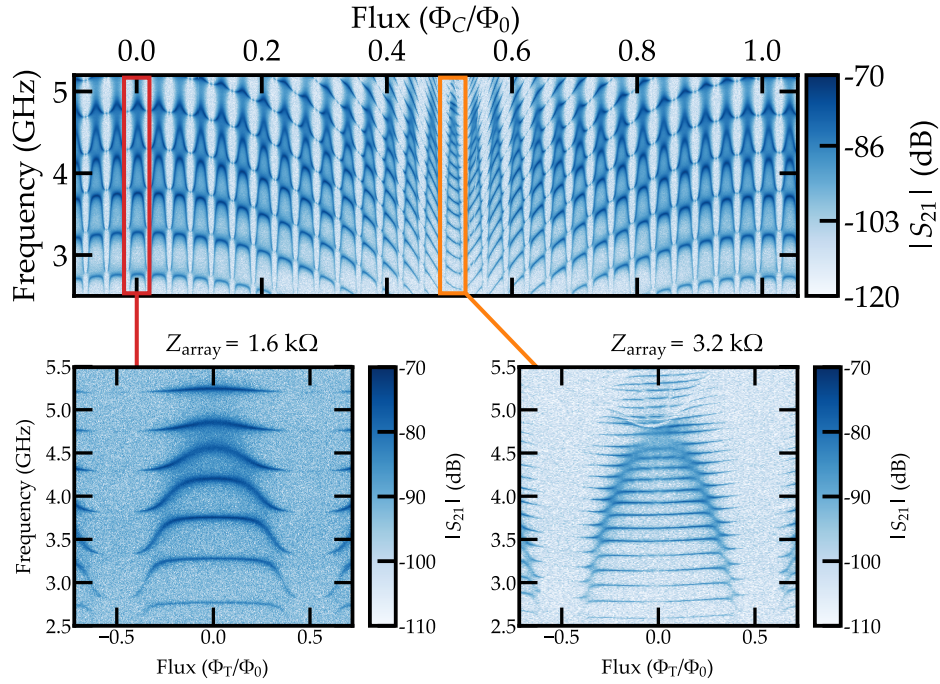


Figure 2 – Transmission of the circuit as a function of the magnetic flux in the array  $\Phi_C$  and the microwave frequency. The bottom plots show two qubit periods for the smallest (left) and the largest (right) array impedances.

the array SQUIDS loops (small area, long period). Thanks to this we can observe the system response at several array impedances  $Z_{\text{array}}(\Phi_C)$ . In Fig. 2 bottom we show a transmon period for the smallest impedance  $Z_{\text{array}}(0)$  (red square in the upper figure) and the largest impedance  $Z_{\text{array}}(\Phi_0/2)$  (orange square). These figures show qualitatively the high degree of tunability of the sample. At low  $Z_{\text{array}}$  the density of modes is lower and less modes are coupled to the transmon qubit. However at high  $Z_{\text{array}}$  the density of modes increases and more modes couple to the qubit.

## Results

The main results of this work are first the fabrication and characterization of several arrays of SQUIDS of various lengths,  $N \in (500, 5500)$ , and second the measurement of an ultra-strongly coupled transmon qubit to several photonic modes in a high impedance tunable environment.

### *Influence of the transmon in the environment*

From the transmission measurements shown in Fig. 2 it is clear that the transmon qubit is coupled to several modes at once. This is seen as a shift in the frequency of the modes due to the presence of the transmon qubit mode. To quantify this

effect we define the *frequency shift* as

$$\delta\phi_n(\Phi_T, \Phi_C) = \pi \frac{\overbrace{\omega_n(\Phi_0/2, \Phi_C)}^{\text{Mode for uncoupled transmon}} - \overbrace{\omega_n(\Phi_T, \Phi_C)}^{\text{Mode for coupled transmon}}}{\underbrace{\omega_n(\Phi_0/2, \Phi_C) - \omega_{n-1}(\Phi_0/2, \Phi_C)}_{\text{Mode spacing for uncoupled transmon}}}. \quad (1)$$

Here,  $\omega_n(\Phi_T, \Phi_C)$  is the mode number  $n$  of the system (transmon plus array). It depends on the flux in the SQUIDS of the array ( $\Phi_C$ ) and the flux in the SQUID of the transmon ( $\Phi_T$ ). For  $\Phi_T = \Phi_0/2$  the transmon frequency becomes zero and it decouples from the environment. Therefore, the frequency shift  $\delta\phi_n$  is a measure of the dispersion of the modes of the environment due to the presence of the transmon qubit. The experimentally obtained  $\delta\phi_n$  is given as dots in Fig. 3 for several values of  $\Phi_T$ . It is a step-like function that goes from 0 to  $\pi$ . The points in the step give the number of modes coupled to the transmon qubit. As we see, at least eight modes are affected by the presence of the transmon. In the inset the measurement where the data is taken from is shown.

The frequency shift is related to the phase shift induced by the qubit in the modes of the array. As explained in the manuscript, we linearize the lumped element circuit in Fig. 1 via a Self-Consistent Harmonic Approximation (SCHA) that accounts for the quantum-vacuum fluctuations in the circuit and the nonlinearity of the transmon. From the linearized system we can obtain the eigenmodes of the circuit. They are given by

$$\Phi_l \propto \cos[ka(l-1) - \phi] \quad \text{with } l = 1, 2, 3, \dots \quad (2)$$

Here  $\Phi_l$  is the flux at island  $l$ ,  $k$  is the wave number of the mode and  $a$  is the unit cell of the array. We included in the mode definition a phase  $\phi$ . This phase comes from the fact that the array is coupled to the measurement line via the transmon qubit. Therefore the boundary conditions for the eigenmodes of the circuit depend on the transmon. As already mentioned, when  $\Phi_T = \Phi_0/2$  the transmon frequency goes to zero and it decouples from the environment. Therefore, for monitoring the effect of the transmon qubit in the modes of the circuit, we define the *transmon phase shift*  $\delta\phi$  as the difference between the phase of the eigenmodes of the system when the transmon is uncoupled and when the transmon is coupled to the array,

$$\delta\phi = \underbrace{\phi(\Phi_T = \Phi_0/2)}_{\text{Transmon uncoupled}} - \underbrace{\phi(\Phi_T \neq \Phi_0/2)}_{\text{Transmon coupled}}. \quad (3)$$

In this thesis we demonstrate that from this phase shift we can obtain the width  $\Gamma_T$  and frequency  $\omega_T$  of the transmon qubit. The width  $\Gamma_T$  is directly related to the coupling strength between the qubit and the environment<sup>22,57</sup>.

The obtained  $\delta\phi$  in the thermodynamic limit i.e. when the number of SQUIDS in the array tends to infinity, is shown in Fig. 3 as solid lines. The agreement between the experimental points and the theoretical curves is very good taking into account that we did not use any fitting parameter. The transmon frequency  $\omega_T$  and width  $\Gamma_T$  are indicated in gray.

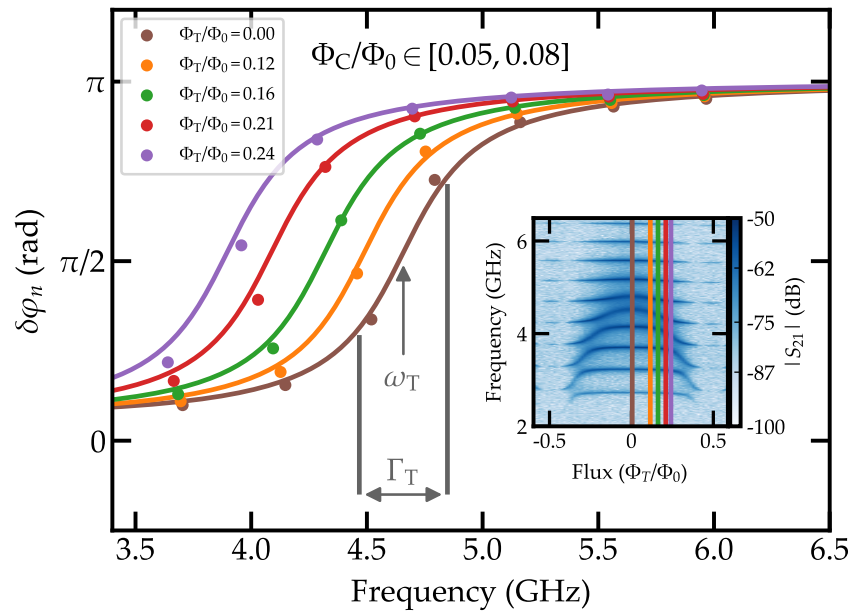


Figure 3 – Comparison between the experimental phase shift  $\delta\varphi_n$  and the theoretical one  $\delta\phi$  with no fitting parameter. The curves are taken for several values of  $\Phi_C$ . In gray the transmon width  $\Gamma_T$  and transmon frequency  $\omega_T$  obtained from  $\delta\varphi_n$  are given. In the inset the transmon period from where the data is taken is shown.



### Tunable environment

One of the strong points of our platform is that we can tune it exploring different coupling regimes. To do so we measure at different fluxes in the array,  $\Phi_C$ , and obtain the width  $\Gamma_T$  of the transmon qubit via the frequency shift defined in Eq. (1).

To get an estimation of the transmon width and frequency we fit both the experimental data and the theoretical curve with an arctangent. In Fig. 4 we plot the transmon width as a function of  $\Phi_C$ . The experimental values are given by the blue dots with the error bars coming from the fitting procedure. It is clear that thanks to the tunability of the circuit we can explore different coupling regimes, reaching a variation in the transmon width of almost 40%. The theoretical prediction is included as a shaded area giving by the error in the estimation of the parameters of the circuit. Once again despite not using any fitting parameter the agreement between the experiment and the theory is very good. Contrary to the expected behavior, we observe in Fig. 4 that the coupling

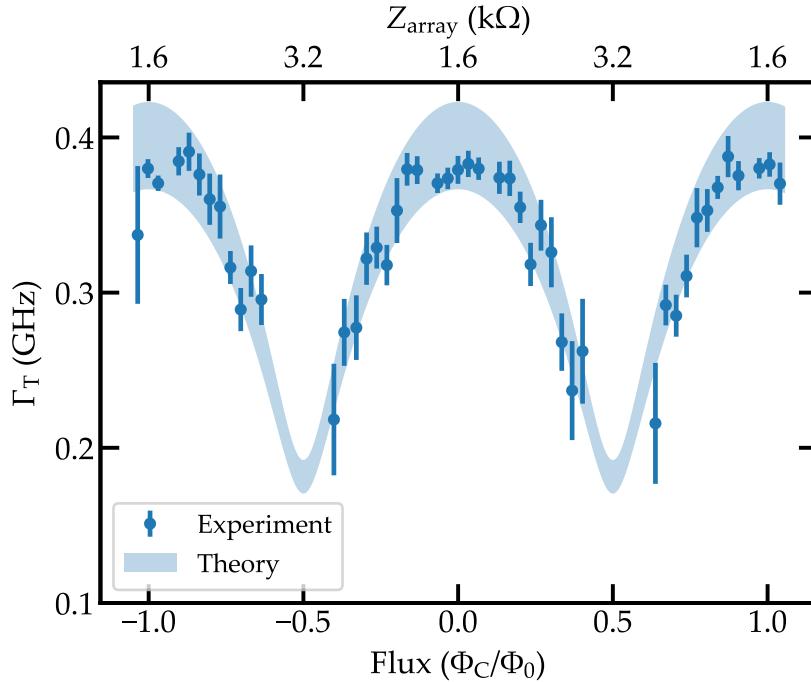


Figure 4 – Transmon qubit maximum width as a function of the flux in the array  $\Phi_C$ . The blue dots are experimental data. The error bars come from the error in the fitting procedure. The blue shaded area is the theoretical curve. The area represents the error in the estimation of the system parameters.

is reduced with increasing impedance. As explained in the main text, this effect comes from the fact that the ground capacitances shunt the array for very high impedances and is directly linked to the impedance matching condition in circuit theory<sup>58</sup>. At  $Z_{\text{array}}(\Phi_C = 0) = 1.6 \text{ k}\Omega$  the transmon is more impedance matched than at  $Z_{\text{array}}(\Phi_C = \Phi_0/2) = 3.2 \text{ k}\Omega$ . At the maximum coupling strength we obtain  $\Gamma_T/\omega_T \sim 10\%$  which is already in the so called *ultra strong coupling regime*<sup>14,15</sup>.

### *Conclusion*

During my PhD we fabricated and characterized several arrays of SQUIDS of different lengths  $N \in (500, 5500)$  in the linear regime ( $E_J/E_C \gg 1$ ) using microwave transmission measurements. Then we coupled a transmon qubit to an array with  $N = 4700$  and observe the hybridization of the qubit with several modes in the array. We prove the in situ tunability of the qubit-array interaction and reach a coupling strength of 10% the qubit frequency. We obtain a good agreement between experiment and theory using an effective linear model in the thermodynamic limit ( $N \rightarrow \infty$ ) with no fitting parameter. Then we could confirm that the four above-mentioned criteria are fulfilled: an environment that contains several modes, the coupling strength is comparable to the FSR of the environment, the qubit anharmonicity in the order of the FSR and the system is beyond the RWA.

Therefore the circuit behaves as a many-body system where the array of SQUIDS can be seen as the high impedance dissipative environment the transmon qubit is coupled to.

### *Manuscript organization*

This manuscript contains seven chapters organized as follows. The first three chapters give the necessary theoretical background to understand the experimental results. The first chapter contains a brief introduction on the different light-matter interaction models. The second one introduces the basic concepts related to superconducting circuits. The third one treats in detail the different variables involved in the coupling between electrical circuits. The next two chapters are focused on the most experimental aspects of this work. In chapter four we describe the fabrication process in detail as well as the estimation of the system parameters. Chapter five contains a brief description of the experimental setup used in all the measurements. Finally, the last two chapters contain all the experimental results for the arrays of SQUIDS, chapter six, and for the transmon qubit coupled to one of these arrays, chapter seven.



# Light-matter interaction

# 1

Light-matter interaction is at the heart of many phenomena in nature. That is the reason why it remains a key topic in fundamental physics. In this section we briefly introduce the most important models dealing with it. We start with the Jaynes-Cummings and Rabi model treating a two-level system interacting with a single photonic (bosonic) mode. Then we increase the number of modes and enter into the realm of many-body physics introducing the spin-boson model. This model is seen as the simplest quantum many-body problem. Despite its apparent simplicity, finding its solution is far from trivial and therefore it still represents a challenge both experimental and theoretical in nowadays research.

## 1.1 One atom and one mode

As a first approach to light-matter interaction it is important to introduce the models that treat only one electromagnetic mode interacting with a two-level system.

We start by obtaining a quantum mechanical description of the electromagnetic field. The Hamiltonian for the electromagnetic field can be written in SI units as<sup>1</sup>

$$\mathcal{H}_{\text{EM}} = \frac{1}{2} \int_V \left( \epsilon |\vec{E}(\vec{r})|^2 + \mu |\vec{H}(\vec{r})|^2 \right) d\vec{r}. \quad (1.1)$$

Here  $\vec{E}(\vec{r})$  and  $\vec{H}(\vec{r})$  are the electric and magnetic fields respectively. The constants  $\epsilon$  and  $\mu$  are the electric permittivity and the magnetic permeability of the medium. The integration is taken over an arbitrary volume  $V$ .

To treat this Hamiltonian quantum mechanically we promote the fields  $\vec{E}$  and  $\vec{H}$  to operators  $\hat{E}$  and  $\hat{H}$ . There is a clear correspondence between Eq. (1.1) and the Hamiltonian for a quantum harmonic oscillator. We therefore define the operators  $\hat{E}$  and  $\hat{H}$  as a function of the creation and annihilation operators  $a_k^\dagger$  and  $a_k$  as in Eq. (1.2),

$$\begin{aligned} \hat{E} &= \sum_k \sqrt{\frac{\hbar\omega_k}{2\epsilon V}} (a_k + a_k^\dagger) \\ \hat{H} &= i \sum_k \sqrt{\frac{\hbar\omega_k}{2\mu V}} (a_k - a_k^\dagger). \end{aligned} \quad (1.2)$$

where  $k$  is the mode index.

Operators  $a_k^\dagger$  and  $a_k$  satisfy the following commutation relations,

$$\begin{aligned} [a_n, a_m^\dagger] &= \delta_{n,m} \\ [a_n, a_m] &= 0 \\ [a_n^\dagger, a_m^\dagger] &= 0. \end{aligned} \quad (1.3)$$

If we insert the operators definition from Eq. (1.2) in Eq. (1.1) we obtain for  $\mathcal{H}_{\text{EM}}$

$$\mathcal{H}_{\text{EM}} = \frac{1}{2} \int_V \left( \epsilon \hat{\mathbf{E}}(\vec{r})^2 + \mu \hat{\mathbf{H}}(\vec{r})^2 \right) d\vec{r} = \sum_k \hbar \omega_k \left( a_k^\dagger a_k + \frac{1}{2} \right). \quad (1.4)$$

This is the Hamiltonian for several uncoupled harmonic oscillators. For a detailed derivation of this result refer to D.F. Walls<sup>1</sup>, Meystre and Sargent<sup>59</sup>.

This Hamiltonian has as eigenstates the Fock states  $|n_k\rangle$ . Application of operators  $a_k^\dagger$  and  $a_k$  on the Fock state  $|n_k\rangle$  gives

$$a_k^\dagger |n_k\rangle = \sqrt{n_k + 1} |n_k + 1\rangle \quad a_k |n_k\rangle = \sqrt{n_k} |n_k - 1\rangle. \quad (1.5)$$

At first, we are interested only in one of the modes of  $\mathcal{H}_{\text{EM}}$  of frequency  $\omega_0$ . Therefore we write

$$\mathcal{H}_{\text{mode}} = \hbar \omega_0 \left( a^\dagger a + \frac{1}{2} \right), \quad (1.6)$$

which is the Hamiltonian for a single harmonic oscillator.

Now that we have a proper definition for the electromagnetic field we can turn into the problem of describing the material system interacting with it. Here we will treat the simplest material system, a quantum two-level system. This two-level system has a ground state  $|\downarrow\rangle$  and an excited state  $|\uparrow\rangle$ . We denote the energy difference between these two levels as  $\hbar \omega_q$ . Under these assumptions the Hamiltonian for such a system can be written as

$$\mathcal{H}_{\text{atom}} = \frac{\hbar}{2} \omega_q \sigma_z \quad \text{with} \quad \sigma_z = |\uparrow\rangle \langle \uparrow| - |\downarrow\rangle \langle \downarrow|. \quad (1.7)$$

The last term we need to include is the interaction between light and matter. Once again this is simple if we make some approximation. If the system, e.g. an atom, is much smaller than the wavelength of the electromagnetic field we can perform the *dipolar approximation*<sup>1</sup>. Under this approximation we can write the interaction term as in Eq. (1.8),

$$\mathcal{H}_{\text{int}} = \vec{p} \cdot \vec{E}. \quad (1.8)$$

Here  $\vec{p}$  is the dipole moment of the system. For a two-level system this dipole moment is proportional to the raising and lowering operators  $\sigma_+$  and  $\sigma_-$ ,

$$\vec{p} \propto (\sigma_+ + \sigma_-) \quad \text{with} \quad \sigma_+ = |\uparrow\rangle \langle \downarrow|, \quad \sigma_- = |\downarrow\rangle \langle \uparrow|. \quad (1.9)$$

Combining the expression in Eqs. (1.2) and (1.9) we obtain for the interaction term,

$$\mathcal{H}_{\text{int}} = \vec{p} \cdot \vec{E} = \hbar g (\sigma_+ + \sigma_-) (a^\dagger + a). \quad (1.10)$$

Here  $g$  is a measure of the strength of the interaction. As already seen in Eq. (1.8), there are two different contributions in  $g$ . One contribution comes from the electric dipolar moment of the atom. This can be considered a geometrical factor related to the exact shape of the atomic orbital. The second term comes from the strength of the electric field, which is given by its quantum r.m.s fluctuations. For harmonic modes in optical systems this fluctuations are proportional to the impedance of the vacuum  $Z_{\text{vac}} \sim 377 \Omega$ <sup>7</sup>. As will be discussed in detail in Chapter 3, in capacitively coupled superconducting circuits the geometrical factor is given by a capacitance ratio and the electric field fluctuations are related to the characteristic impedance of the environment the qubit is coupled to.

Adding Eqs. (1.6), (1.7) and (1.10) we arrive to the Rabi Hamiltonian<sup>60</sup> given in Eq. (1.11), which represents a two-level system interacting with an electromagnetic mode.

$$\begin{aligned} \mathcal{H}_{\text{Rabi}} &= \mathcal{H}_{\text{mode}} + \mathcal{H}_{\text{atom}} + \mathcal{H}_{\text{int}} \\ &= \hbar\omega_0 \left( a^\dagger a + \frac{1}{2} \right) + \frac{\hbar}{2} \omega_q \sigma_z + \hbar g (\sigma_+ + \sigma_-) (a^\dagger + a). \end{aligned} \quad (1.11)$$

### 1.1.1 The Rotating Wave Approximation

Finding an analytical solution for the Rabi Hamiltonian in Eq. (1.11) is not trivial<sup>61</sup>. However, for most regimes of light-matter interaction found in nature one can perform an approximation that simplifies it and makes it easier to solve. This is the Rotating Wave Approximation (RWA).

If we assume that the coupling strength is much smaller than the system frequency,  $g \ll \omega_q$  and the electromagnetic mode is near resonant with the system,  $|\omega_q - \omega_0| \ll \omega_q$ , we can get rid of the terms containing  $a^\dagger \sigma_+$  and  $a \sigma_-$  in Eq. (1.11) and arrive to the Jaynes-Cummings Hamiltonian<sup>62</sup>  $\mathcal{H}_{\text{JC}}$  in Eq. (1.12).

$$\mathcal{H}_{\text{JC}} = \hbar\omega_0 \left( a^\dagger a + \frac{1}{2} \right) + \frac{\hbar}{2} \omega_q \sigma_z + \hbar g (\sigma_+ a + \sigma_- a^\dagger). \quad (1.12)$$

The effect of the coupling term now becomes clear. The term  $\sigma_+ a$  absorbs one photon and excites the atom. On the other hand, the term  $\sigma_- a^\dagger$  creates a photon by relaxing the atom.

To get some insight into this Hamiltonian we can write it in matrix form. To do so we use the following basis;

- $|0, \downarrow\rangle$ : No photons and the qubit in the ground state,
- $|n + 1, \downarrow\rangle$ :  $n + 1$  photons and the qubit in the ground state,
- $|n, \uparrow\rangle$ :  $n$  photons and the qubit in the excited state.

Recalling the application of the operators on the different states  $|n\rangle$ ,  $|\downarrow\rangle$  and  $|\uparrow\rangle$  we obtain the matrix in Eq. (1.13).

$$\mathcal{H}_{\text{JC}} = \hbar \begin{pmatrix} \frac{1}{2}\omega_0 - \frac{1}{2}\omega_q & & & & \\ & M_0 & & & \\ & & M_1 & & \\ & & & \ddots & \\ & & & & \ddots \end{pmatrix} \quad (1.13)$$

where each block  $M_n$  is given by

$$M_n = \begin{pmatrix} \omega_0 \left(n + \frac{3}{2}\right) - \frac{1}{2}\omega_q & \sqrt{n+1}g \\ \sqrt{n+1}g & \omega_0 \left(n + \frac{1}{2}\right) + \frac{1}{2}\omega_q \end{pmatrix}. \quad (1.14)$$

Thanks to the RWA the obtained Hamiltonian is block diagonal. This means that we can diagonalize each of the blocks independently to obtain the eigenenergies and the eigenstates of the system. The eigenenergies are given by

$$E_g = -\frac{\delta}{2} \quad (1.15)$$

$$E_{n,\pm} = (n+1)\omega_0 \pm \frac{1}{2}\sqrt{4g^2(n+1) + \delta^2}$$

where  $\delta = \omega_q - \omega_0$ . The associated eigenstates are

$$|0\rangle = |0, \downarrow\rangle \quad (1.16)$$

$$|n, +\rangle = \cos(\theta_n) |n, \uparrow\rangle + \sin(\theta_n) |n+1, \downarrow\rangle \quad (1.17)$$

$$|n, -\rangle = -\sin(\theta_n) |n, \uparrow\rangle + \cos(\theta_n) |n+1, \downarrow\rangle \quad (1.18)$$

where  $\theta_n$  is given by

$$\tan(2\theta_n) = \frac{2g\sqrt{n+1}}{\delta}. \quad (1.19)$$

There are several things to notice in this solution. First, the ground state of the Hamiltonian is  $|\downarrow, 0\rangle$  i.e. the two-level system in the ground state and no photon in the electromagnetic mode. This is an expected result. However, we will see later that beyond the RWA it is not true. Second, the interaction terms mix the states  $|\downarrow, n+1\rangle$  and  $|\uparrow, n\rangle$  showing the hybridization between the photon states and the two-level system states.

If we think in energy transitions we see from Eqs. (1.16) to (1.18) that we obtain two transitions per Fock state  $|n\rangle$ , Eq. (1.21).

$$E_{n,-} - E_g = (n+1)\omega_0 - \frac{1}{2}\sqrt{4g^2(n+1) + \delta^2} + \frac{\delta}{2} \quad (1.20)$$

$$E_{n,+} - E_g = (n+1)\omega_0 + \frac{1}{2}\sqrt{4g^2(n+1) + \delta^2} + \frac{\delta}{2} \quad (1.21)$$

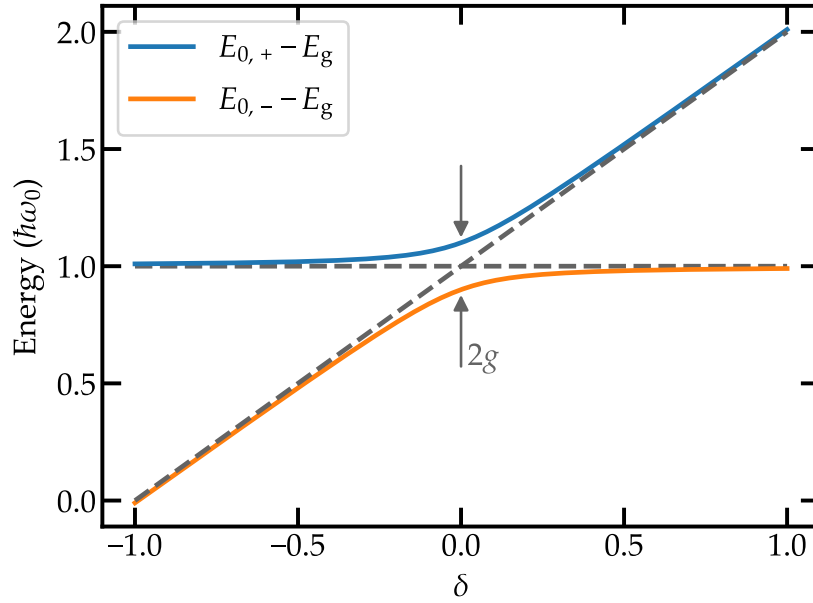


Figure 1.1 – Energy spectrum in units of  $\hbar\omega_0$  of the Jaynes-Cummings Hamiltonian for  $n = 0$ . The gray dashed lines indicate the uncoupled values for  $\omega_0$  and  $\omega_q$ .

These two transitions are shown in Fig. 1.1 for different  $\delta$  values and for  $n = 0$ . We see an avoided crossing for  $\delta = 0$ , the vacuum Rabi splitting. The value of this splitting depends on the number of photons  $n$  as

$$E_{n,+} - E_{n,-} = 2g\sqrt{n+1}. \quad (1.22)$$

This gives a direct measure of the coupling strength  $g$  from the spectroscopy. We see that when the absolute value of the detuning increases, one energy transition tends towards  $\hbar\omega_q$  and the other towards  $\hbar\omega_0$ .

When performing real experiments to probe this model one needs to take into account the losses inherent to any experimental setup. If we imagine the setup as a “photon box” where we introduce our two-level system we can think of two contributions for the losses. First the rate  $\kappa$  at which photons leak out of the box and second the decay rate  $\gamma$  at which the atom releases energy to the environment. Therefore in order to see a coherent interaction between the photons and the system it is necessary to fulfill the condition  $\kappa, \gamma \ll g$ . The fulfillment of this condition is called *strong coupling regime*.

The first experiments probing this model experimentally were performed during the last two decades of the twentieth century<sup>63</sup>. They involved real atoms inside optical cavities. The first experimental evidence of the strong coupling regime at the single-atom level was obtained in 1992<sup>64</sup>. This field of research was called Cavity Quantum Electrodynamics (CQED) due to the optical cavities used in the experiments. Later on, between 2001 and 2004, it was proposed<sup>65,66</sup> to use superconducting circuits as building blocks for the same type of experiments. Microwave resonators were proposed as substitutes for optical cavities and nonlinear circuits as substitutes for the atoms. The use of superconducting circuits presents sev-



eral advantages over the previous setups<sup>7,8</sup>; they can be fabricated using existing lithography techniques, electromagnetic field can be confined to one dimension which increases the dipole coupling and superconducting qubits are much bigger than real atoms giving rise to a stronger dipole moment. To highlight the proximity to the previous experiments, this field was called Circuit Quantum Electrodynamics (Circuit QED).

The first experiments reaching the strong coupling regime in a Circuit QED architecture were done in 2004 and consisted of a charge qubit capacitively coupled to a microwave resonator<sup>9</sup> and a flux qubit inductively coupled to a Superconducting QUantum Interference Device (SQUID)<sup>10</sup>. Thanks to the strong coupling and the low losses of superconducting circuits, coherent energy exchange between the electromagnetic mode and the qubit mode could be measured. Later on, other experiments explored the non-linear scaling<sup>67,68</sup> of Eq. (1.22) and the system dynamics<sup>11,12</sup>.

### 1.1.2 Beyond the RWA approximation

As pointed out before, thanks to the use of circuits in the study of light-matter interaction the coupling  $g$  between light and matter could be further increased reaching limits unreachable with natural atoms<sup>7</sup>. Therefore it was not long before the RWA had to be dropped and the full Rabi Hamiltonian in Eq. (1.11) needed to be used. This involves the counter-rotating terms  $a^\dagger \sigma_+$  and  $a \sigma_-$  which excite the qubit and create a photon and relax the qubit and annihilates a photon respectively.

We can write the Rabi Hamiltonian  $\mathcal{H}_{\text{Rabi}}$  in Eq. (1.11) in matrix form using the same basis as before. We obtain

$$H = \hbar \begin{pmatrix} |0, \downarrow\rangle & |0, \uparrow\rangle & |1, \downarrow\rangle & |1, \uparrow\rangle & \dots \\ \frac{1}{2}\omega_0 - \frac{1}{2}\omega_q & 0 & 0 & g & \dots \\ 0 & \frac{1}{2}\omega_0 + \frac{1}{2}\omega_q & g & 0 & \dots \\ 0 & g & \frac{3}{2}\omega_0 - \frac{1}{2}\omega_q & 0 & \dots \\ g & 0 & 0 & \frac{3}{2}\omega_0 + \frac{1}{2}\omega_q & \dots \\ \vdots & \vdots & \vdots & \vdots & \ddots \end{pmatrix}. \quad (1.23)$$

This matrix is no longer block diagonal due to the matrix elements coupling states  $|n, \downarrow\rangle$  and  $|n + 1, \uparrow\rangle$ . It is possible to obtain the eigenenergies of this Hamiltonian analytically<sup>61</sup>. However, obtaining its eigenvectors and its dynamics remains a modern theoretical challenge. In Fig. 1.2 we see a comparison between the Jaynes-Cummings model and the Rabi model as a function of the coupling strength for several  $n$  values. The curve for the Rabi model was obtained by numerical diagonalization of Eq. (1.23). As it can be seen, for low coupling both models coincide. However when the coupling is increased the Jaynes-Cummings model is not correct anymore and the counter-rotating terms start to play a role.

Regarding the eigenstates, there are some approximated solutions based on polarons and antipolarons<sup>6,69</sup>. Here we will only point out that the ground state is not  $|0\rangle = |0, \downarrow\rangle$  anymore. Due to the counter-rotating terms the expected number of photons in the ground state is not zero. This is a striking result that serves as

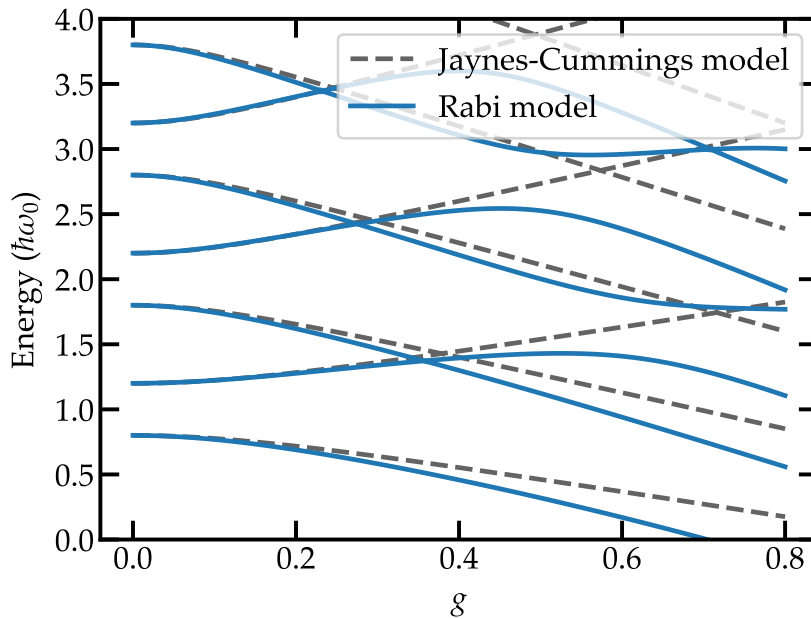


Figure 1.2 – Numerical simulation of the energy spectrum in units of  $\hbar\omega_0$  as a function of the coupling strength  $g$  for the Jaynes-Cummings model (dashed gray lines) and the Rabi model (blue lines). We set  $\delta = 0.4$ .

an example of the new physics that can be found when the light-matter coupling strength is increased. For a recent review on the Rabi model see Xie et al.<sup>70</sup>

In 2010 the first Circuit QED system in the ultra strong coupling regime was measured<sup>14</sup>. It consisted of a flux qubit galvanically coupled to a microwave resonator. Shortly after the same regime was reached but this time coupling a flux qubit to a lumped element  $LC$  resonator<sup>15</sup>. These works showed a qualitative difference between the measured spectrum and the spectrum obtain from the Jaynes-Cummings model. This difference was explained using the Rabi model. Recently the Rabi model with coupling strength  $g$  in the order of  $\omega_q$  was simulated experimentally. This experiments showed the Schrödinger-cat-like structure of the ground state in the Rabi model<sup>17</sup> and the system dynamics beyond the RWA approximation<sup>18</sup>.

## 1.2 One atom and several modes

Until now we treated the interaction between a two-level system and a single electromagnetic mode. In order to enter the realm of many-body physics we can include several modes in the model. In the Rabi Hamiltonian we substitute the Hamiltonian for one mode in Eq. (1.6) by the one in Eq. (1.4) for several modes. The resulting Hamiltonian is given in Eq. (1.24). It is known in literature as the *spin boson Hamiltonian*<sup>24,52,71</sup>.

$$\mathcal{H}_{\text{SB}} = \frac{\hbar}{2}\omega_q\sigma_z + \sum_k \hbar\omega_k \left( a_k^\dagger a_k + \frac{1}{2} \right) + \hbar g_k (\sigma_+ + \sigma_-) (a_k^\dagger + a_k) \quad (1.24)$$

As we see now the frequency of the modes  $\omega_k$  and the coupling strength  $g_k$  depend on the mode index  $k$ . The modes  $\omega_k$  can be seen as the environment to which the two-level system couples. The frequencies  $\omega_k$  are given by the dispersion relation of the modes of the environment  $\omega(k)$ . Usually a cut-off frequency  $\omega_{\text{cut-off}}$  is included to give the system a finite size<sup>72</sup>. The  $g_k$  are given by the spectral function  $J(\omega)$ ,

$$J(\omega) = \frac{2\pi}{\hbar^2} \sum_k g_k^2 \delta(\omega - \omega_k). \quad (1.25)$$

The spectral function relates the dispersion relation  $\omega_k$  to the coupling terms  $g_k$ . The different environments can be classified according to  $J(\omega)$ . In the continuous limit, if we assume<sup>24</sup> that  $J(\omega) \propto \omega^s$  we can classify the environments as *subohmic* ( $s < 1$ ), *ohmic* ( $s = 1$ ) and *superohmic* ( $s > 1$ ).

This Hamiltonian is strongly linked to dissipation in quantum systems<sup>24,73,74</sup>. The bath of harmonic oscillators plays the role of friction in the system as long as the number of oscillators tends to infinity. For circuits the dissipation by a resistor has  $s = 1$  and therefore the name ohmic<sup>71</sup>. In this case it is common to write  $J(\omega) = \alpha\omega$  where  $\alpha$  is a dimensionless parameter that gives the strength of the coupling.

An example of the energy spectrum for the spin-boson model is shown in Fig. 1.3 for two different coupling strengths  $\alpha$ . As it can be seen, with increasing coupling strength more modes disperse due to the two-level system. These figures are meant to give a qualitative idea of the energy spectrum for the spin-boson model. Therefore we truncated the Hilbert space to one excitation per mode. This discards any many-body effect in the system. Obtaining the exact spectrum of the full spin-boson Hamiltonian is currently an intensive subject of research<sup>69</sup>.

When  $\alpha$  is large or equivalently the dissipation is strong, one of the predicted effects is the renormalization of  $\omega_q$  due to the interaction with the environment<sup>24,52</sup>. For a coupling strength  $\alpha < 1$  this renormalized frequency is given by<sup>24,34</sup>

$$\omega_{q,r} = \omega_q \left( \frac{\omega_q}{\omega_{\text{cut-off}}} \right)^{\frac{\alpha}{1-\alpha}}. \quad (1.26)$$

This expression is plotted in Fig. 1.4 for several values of  $\omega_{\text{cut-off}}$ . As it can be seen, with increasing coupling strength the frequency of the qubit is renormalized. This effect is clearly suppressed for  $\omega_q \sim \omega_{\text{cut-off}}$  due to the drop of the coupling strength close to this frequency. Some other predicted effects in this regime include spontaneous Schrödinger cat emission<sup>31</sup> and low power frequency conversion<sup>29,32</sup>.

The Hamiltonian in Eq. (1.24) can be further expanded if we substitute the two-level system by a multilevel one with Hamiltonian  $\mathcal{H}_{\text{system}}$ ,

$$\mathcal{H}_{\text{multi-level}} = \mathcal{H}_{\text{system}} + \sum_k \hbar\omega_k \left( a_k^\dagger a_k + \frac{1}{2} \right) + \hbar g_k \hat{C}_{\text{system}} \left( a_k^\dagger + a_k \right). \quad (1.27)$$

Here  $\hat{C}_{\text{system}}$  represents the coupling degree of freedom between  $\mathcal{H}_{\text{system}}$  and the bath.

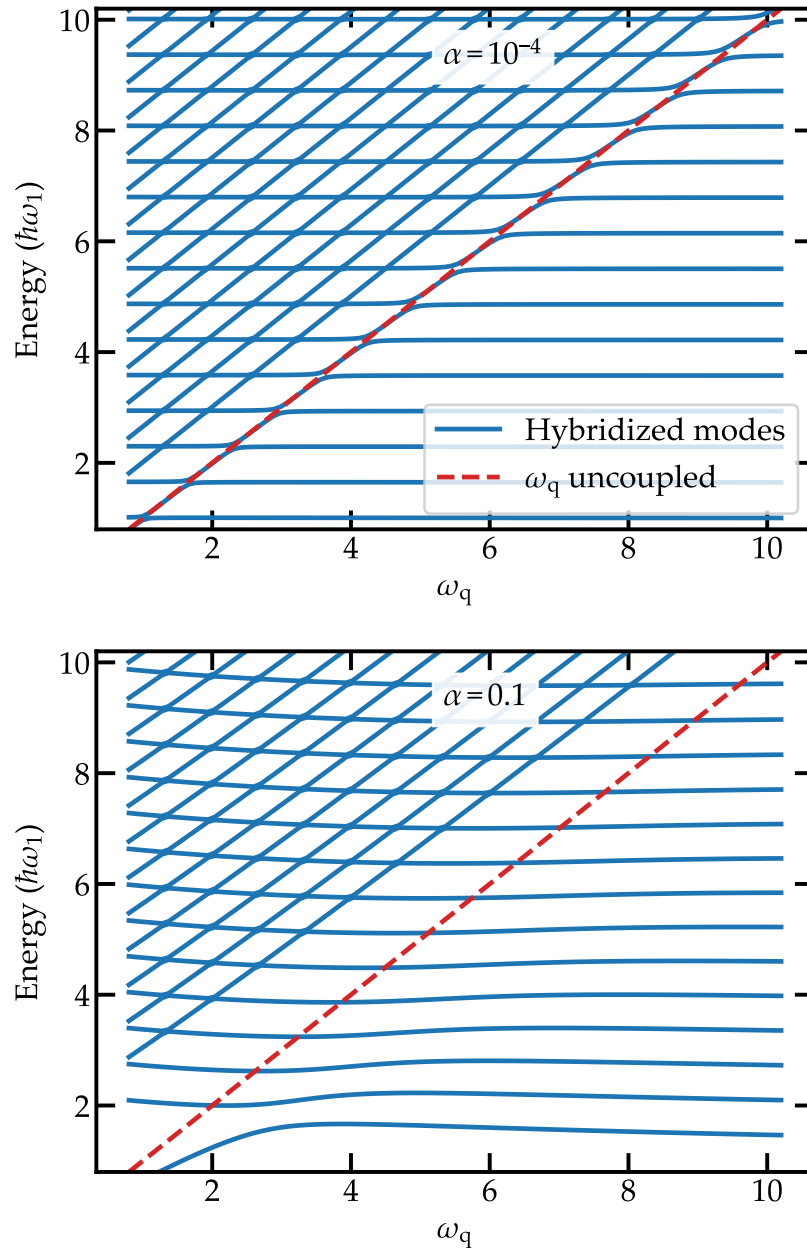


Figure 1.3 – Spin boson model spectrum as a function of  $\omega_q$  for two different coupling strengths  $\alpha$ . In blue the eigenenergies of the Hamiltonian are given. The dashed red line indicates the value of  $\omega_q$ . The same linear dispersion relation was used for both plots with an ohmic spectral density, i.e.  $g_k = \sqrt{\alpha\omega_k}$ . In both cases the Hilbert space was truncated to one excitation per mode. These plots show qualitatively how with an increasing coupling strength the number of modes coupled to the qubit increases.

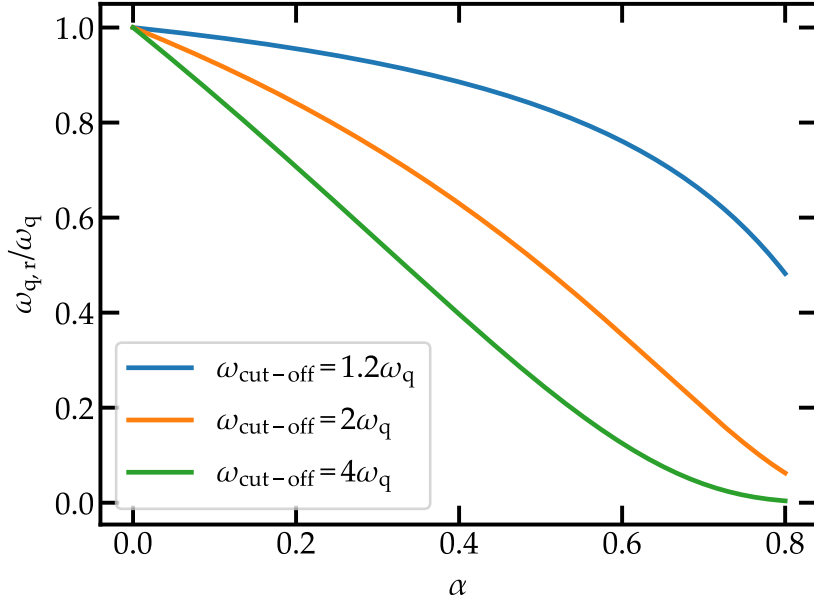


Figure 1.4 – Ratio between the renormalized qubit frequency  $\omega_{q,r}$  and  $\omega_q$  as a function of the coupling strength  $\alpha$ . We set  $\omega_q = 4.65$  GHz which is the value obtained in the experiment.

Both the spin-boson Hamiltonian  $\mathcal{H}_{\text{SB}}$  and its multilevel version  $\mathcal{H}_{\text{multi-level}}$  require a huge Hilbert space whenever we include several modes, several excitations per mode and large coupling. This makes brute force diagonalization hopeless. However, some alternative tools have been presented to make the problem tractable<sup>69</sup>. Regarding the experimental implementation of this model in a Circuit QED architecture there have been several attempts<sup>27,75</sup>. As previously explained, in 2016 a flux qubit was coupled to an open transmission line and the renormalization of the qubit frequency due to many-body effects was first measured<sup>22</sup>. This represents an important first step towards the study of many-body systems in superconducting circuits.

In this chapter we present the theoretical methods used along the manuscript to model the different circuits. First we give a brief introduction of the basic notions in superconducting circuits. Then we introduce the transmission line theory and the Lagrangian and Hamiltonian formalism for linear circuits. Finally, we introduce the Self Consistent Harmonic Approximation (SCHA) as a way of treating circuits embedding intermediate non-linearities such as a transmon qubit.

## 2.1 Basics of superconducting circuits

For understanding the physics in Circuit QED it is required to introduce the Josephson effect and the quantization of electrical circuits. Here we introduce both and explain the superconducting qubit used in this work, the transmon qubit.

### 2.1.1 The Josephson effect

Most of the results included in this work depend fundamentally on the existence of the Josephson effect. It allows to create lossless nonlinear elements that can be used as the building blocks of superconducting qubits and high impedance environments.

#### *The Josephson junction*

A Josephson junction consists of two superconducting electrodes separated by a thin insulating barrier. In 1962 Josephson predicted<sup>76</sup> that a zero voltage supercurrent can flow between them. This supercurrent  $I_s$  is given by the first Josephson equation

$$I_s = I_c \sin \varphi. \quad (2.1)$$

Here  $\varphi$  is the gauge invariant phase difference between the two superconducting electrodes and the *critical current*  $I_c$  is the maximum supercurrent that can flow through the junction. Moreover, when a constant voltage difference  $V$  is applied to a junction, the phase difference  $\varphi$  evolves according to the second Josephson equation:

$$\frac{d\varphi}{dt} = \frac{2e}{\hbar} V = \frac{1}{\varphi_0} V, \quad (2.2)$$

where  $\varphi_0 = \hbar/2e$  is the reduced magnetic flux quantum.

From Eqs. (2.1) and (2.2) we can obtain the Josephson inductance  $L_J$ ,

$$L_J = \frac{V}{dI/dt} = \frac{\varphi_0}{I_c \cos \varphi}. \quad (2.3)$$

The Josephson inductance plays a crucial role in this work. First, as it can be seen from Eq. (2.3), it is nonlinear. Second, it is several orders of magnitude larger than any other linear magnetic inductance per unit length. We make use of this large inductance to build high impedance environments. We can rewrite Eq. (2.3) as a function of the bias current  $I$  as

$$L_J = \frac{\varphi_0}{I_c \sqrt{1 - \left(\frac{I}{I_c}\right)^2}}. \quad (2.4)$$

In this form it is clear that  $L_J$  is a function of the bias current  $I$ . However, when we take the limit  $I_c \gg I$  we eliminate the dependence in  $I$  and obtain a constant inductance  $L_J = \varphi_0/I_c$ . Therefore, by increasing the critical current of the Josephson junction we can find a regime where it becomes a linear inductor. This is going to be important when designing high impedance transmission lines.

From Eqs. (2.1) and (2.2) we can obtain the energy stored in a Josephson junction by integrating the electrical power stored in the junction with respect to time,

$$\begin{aligned} U &= \int_0^t V I_s dt = \varphi_0 \int_0^t I_s \frac{d\varphi}{dt} dt = \varphi_0 \int_0^t I_c \sin \varphi d\varphi = \\ &= \varphi_0 I_c (1 - \cos \varphi) = E_J (1 - \cos \varphi). \end{aligned} \quad (2.5)$$

Here  $E_J = \varphi_0 I_c$  is the Josephson energy. It gives the right scale for the energy stored in the junction.

Another important aspect of the Josephson junction is its self-capacitance  $C_J$ , see Fig. 2.1. This capacitance comes from the fact that the junction consists of two electrodes separated by an insulator. From this capacitance we define a charging energy for the junction  $E_C = e^2/C_J$ . Nonlinear effects such as phase slips can occur in the junction for small  $E_C$ . The rate at which these phase slips occur scales as<sup>77</sup>  $\exp\{-8\sqrt{E_J/E_C}\}$ . Therefore, for large  $E_J/E_C$  ratio these phase slips can be neglected.  $L_J$  and  $C_J$  in parallel create an  $LC$  oscillator. As we said, for large  $I_c$  we can assume that the Josephson junction is a linear inductor. In this regime the junction has a resonance frequency given by

$$\omega_p = \frac{1}{\sqrt{L_J C_J}}. \quad (2.6)$$

This frequency is the *plasma frequency* of the junction. It can be shown that the plasma frequency is independent of the junction area and only depends on the thickness of the insulating barrier  $t$ , see Section 4.2.4.

### The SQUID

The Superconducting QUantum Interference Device<sup>78,79</sup> (SQUID) consists of two Josephson junctions connected in parallel forming a loop. By applying a magnetic

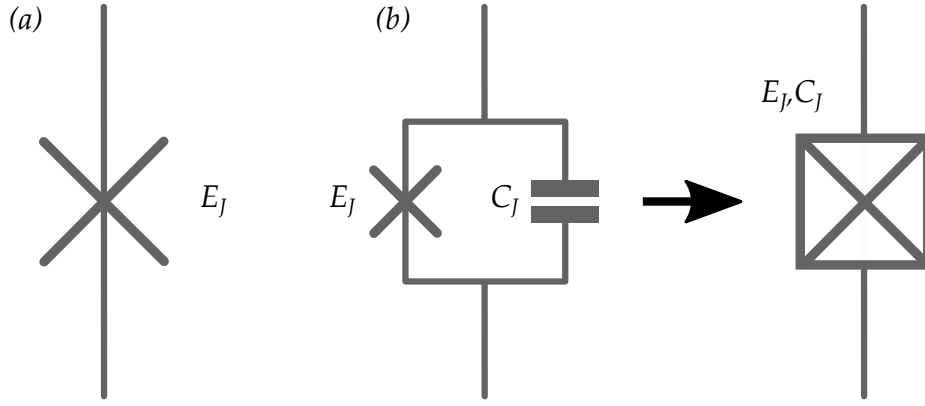


Figure 2.1 – Symbols for the Josephson junction. (a) A single Josephson junction without the Josephson capacitance. (b) The Josephson capacitance is included. To simplify the notation the last symbol is used.

flux to the loop the supercurrents flowing in each arm acquire a different phase. This leads to an interference phenomenon that modulates the outgoing supercurrent  $I_{\text{total}}$ .

The total outgoing supercurrent is the sum of the supercurrent coming from the left branch ( $I_L$ ) and the supercurrent coming from the right branch ( $I_R$ ). Assuming that both junctions are identical with critical current  $I_c$  we have

$$I_{\text{total}} = I_L + I_R = I_c (\sin \varphi_L + \sin \varphi_R) = 2I_c \cos \left( \frac{\varphi_L - \varphi_R}{2} \right) \sin \left( \frac{\varphi_L + \varphi_R}{2} \right). \quad (2.7)$$

If both junctions are the same and there is no applied magnetic flux then  $\varphi_L = \varphi_R = \varphi$  and  $I_{\text{total}} = 2I_c \sin \varphi$ . However when an external magnetic field  $\Phi$  is applied the fluxoid quantization<sup>79</sup> leads to

$$\varphi_L - \varphi_R = 2\pi \frac{\Phi}{\Phi_0}. \quad (2.8)$$

Here  $\Phi_0 = h/2e$  is the magnetic flux quantum. This condition gives a flux dependent total critical current given by

$$I_{c,\text{total}}(\Phi) = 2I_c \left| \cos \left( \pi \frac{\Phi}{\Phi_0} \right) \right|. \quad (2.9)$$

This result can be generalized to take into account an asymmetry between the junctions<sup>80</sup>. The expression in this case is

$$I_{c,\text{total}}(\Phi) = I_{c,\Sigma} \left| \cos \left( \pi \frac{\Phi}{\Phi_0} \right) \right| \sqrt{1 + d^2 \tan^2 \left( \pi \frac{\Phi}{\Phi_0} \right)}. \quad (2.10)$$

Here  $I_{c,\Sigma} = I_{c,1} + I_{c,2}$  is the maximum current through the SQUID and  $d = (I_{c,1} - I_{c,2}) / (I_{c,1} + I_{c,2})$  gives the asymmetry between the junctions. In Fig. 2.2  $I_{c,\text{total}}(\Phi)$  is plotted for several asymmetry values. From the tunability of the critical current we have a tunable inductance, see Eq. (2.3). As explained later, this allows to



have a tunable impedance for a transmission line made of SQUIDS and a tunable frequency for the superconducting qubits.

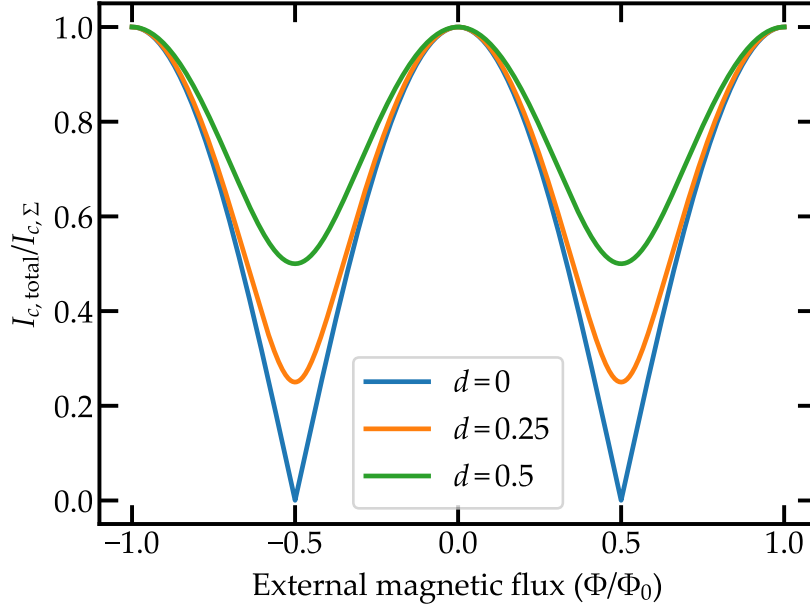


Figure 2.2 – Total critical current in a SQUID  $I_{c,\text{total}}$  as a function of the external magnetic flux for several asymmetries  $d$  between the junctions.

### 2.1.2 Circuit quantization

Here we give a brief introduction of the different operators used to quantize electrical circuits. For a rigorous treatment refer to Devoret<sup>81</sup>. Any electrical circuit can be seen as a group of nodes connected via electrical components. We use the charge  $Q_n$  and flux  $\Phi_n$  at each node  $n$  as variables to describe the dynamics of the system. Here, the node flux is given by<sup>a</sup>  $\Phi_n = \int_{-\infty}^t V_b(t') dt'$ . To perform the circuit quantization we promote the classical variables to operators; the charge operator at node  $n$ ,  $\hat{Q}_n$  and the flux operator at node  $n$ ,  $\hat{\Phi}_n$ . They satisfy the commutation relation  $[\hat{\Phi}_n, \hat{Q}_m] = i\hbar\delta_{n,m}$ , where  $\delta_{n,m}$  is the Kronecker delta.

When treating a Josephson junction in the superconducting state Cooper pairs tunnel through the barrier and therefore the charge is quantized in units of  $2e$ . It is then useful to define the Cooper pair number operator as

$$\hat{n}_n = \frac{\hat{Q}_n}{2e}. \quad (2.11)$$

In addition we define an operator for the superconducting phase. To do so we use the second Josephson equation in Eq. (2.2) and Faraday's law to relate the

<sup>a</sup>In this expression the orientation of the branch should be taken into account according to Kirchhoff's laws<sup>81</sup>.

superconducting phase operator to the flux operator for a Josephson junction as

$$\hat{\varphi}_n = \frac{2e}{\hbar} \hat{\Phi}_n = \frac{1}{\varphi_0} \hat{\Phi}_n. \quad (2.12)$$

These operators satisfy the commutation relation  $[\hat{\varphi}_n, \hat{n}_m] = i\delta_{n,m}$ .

### 2.1.3 The transmon qubit

The first implementation of a superconducting qubit was the Single Cooper Pair Box<sup>82</sup> (SCPB). It consists of a superconducting island coupled via a Josephson junction to a superconducting reservoir, Fig. 2.3 (a). Using an external voltage source

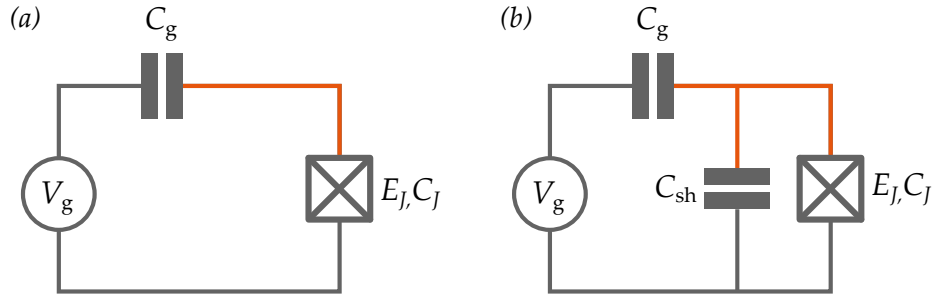


Figure 2.3 – Circuit scheme for the (a) SCPB and (b) the transmon qubit. In orange the superconducting island is shown.

a gate voltage  $V_g$  is applied to tune the energy levels of the SCPB. Using the operators defined in Eqs. (2.11) and (2.12) the Hamiltonian for the SCPB can be written as

$$\mathcal{H} = \frac{E_C}{2} (\hat{n} - n_g)^2 + E_J [1 - \cos(\hat{\varphi})]. \quad (2.13)$$

Note that we use a different but equivalent definition for the Hamiltonian from the usual one<sup>80,81</sup>. The first term with  $E_C = (2e)^2/C_\Sigma$  represents the charging energy of the island, where  $C_\Sigma = C_g + C_J$ . The cosine term is the potential energy of the Josephson junction with  $E_J$  its Josephson energy. Finally,  $n_g = C_g V_g / 2e$  is the induced charge via the gate voltage  $V_g$  in  $2e$  units. This Hamiltonian can be exactly solved in the phase basis in terms of Mathieu functions<sup>83</sup>. In the charge basis it can be numerically solved. To do so we rewrite the Hamiltonian in the charge basis<sup>81</sup>, Eq. (2.14) and diagonalize it. Here we dropped the constant term  $E_J$ .

$$\langle n | \mathcal{H} | n' \rangle = \frac{E_C}{2} (\delta_{n,n'} - n_g)^2 - \frac{E_J}{2} [\delta_{n+1,n'} + \delta_{n,n'+1}] \quad (2.14)$$

The energy levels normalized by the first transition frequency at  $n_g = 1/2$  are shown in Fig. 2.4 (a) as a function of the gate charge  $n_g$ . The spectrum consists on charging parabolas with periodicity  $2e$ . The Josephson term opens a gap where this parabolas intercept. Two features of the spectrum should be noticed. First, the spectrum is fully anharmonic i.e. the energy levels are not equally spaced. This is crucial if the system is meant to be used as a qubit. Second, the spectrum is not flat. This means that the system's coherence time is greatly reduced due to

fluctuations in the gate charge  $n_g$  that lead to fluctuations in the SCPB transition frequencies<sup>57</sup>. In order to reduce this effect, one can tune  $n_g$  to  $1/2$  where the first derivative with respect to  $n_g$  is suppressed. However, this calls for a high level of control over the gate voltage and does not protect the system from large amplitude noise (e.g.  $1/f$  charge noise) and quasiparticles in the Josephson junction.

In order to overcome this difficulty, in 2007 a modified version of the SCPB was presented under the name of *transmon qubit*<sup>13,80</sup>, Fig. 2.3 (b). The idea behind the transmon qubit is to increase the  $E_J/E_C$  ratio. To do so an additional capacitance  $C_{sh}$  is included in parallel with the Josephson junction, see Fig. 2.3 (b). This capacitance lowers the charging energy  $E_C$  increasing the  $E_J/E_C$  ratio. The effect of the increment of this ratio can be seen in Fig. 2.4. For low  $E_J/E_C$  ratio, the energy levels are not flat. However, with increasing  $E_J/E_C$  the levels become flatter. This improves the SCPB coherence time by several orders of magnitude<sup>13</sup>. The increment of the  $E_J/E_C$  ratio comes with a drawback, the anharmonicity of the system is reduced. However it can be shown<sup>80</sup> that the reduction in the charge dispersion overcomes the reduction in the anharmonicity.

## 2.2 Linear circuits

A linear circuit is a circuit whose components relate voltage and current linearly. It can easily be treated due to the fact that its equations of motion are the same as the ones for the harmonic oscillator.

### 2.2.1 Homogeneous systems

First we treat translational invariant systems. These are circuits that can be defined by a unit cell that repeats periodically in one dimension.

#### *Transmission line*

A transmission line is a circuit element that can propagate electromagnetic waves. This means that, contrary to lumped elements, the voltage and current magnitude and phase vary over its length. The most common way of representing a transmission line is with two conductors, Fig. 2.5 (a). The reason for this is that TEM modes need at least two conductors to propagate.

A portion of infinitesimal length  $dx$  can be modeled using the following lumped elements:

- $R_x$  : series resistance per unit length for both conductors.
- $L_x$  : series inductance per unit length for both conductors.
- $G_x$  : shunt conductance per unit length.
- $C_x$  : shunt capacitance per unit length.

The series inductance  $L_x$  is the inductance of both conductors and the shunt capacitance  $C_x$  comes from the proximity between the conductors. The series resistance  $R_x$  represents the finite conductivity of the conductors and the shunt conductance

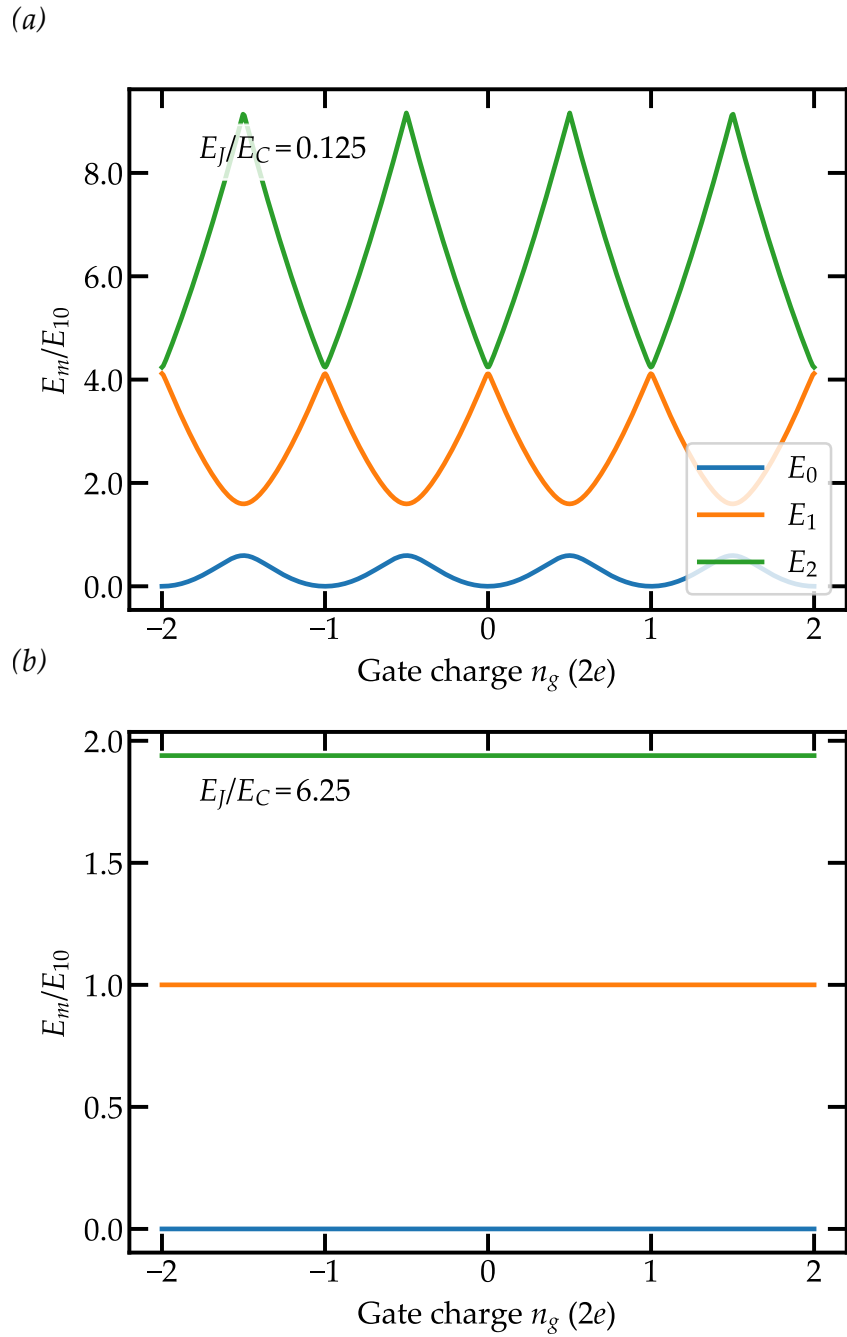


Figure 2.4 – First three energy levels as a function of  $n_g$  for the (a) SCPB and (b) the transmon qubit. The energy is normalized to the  $0 \rightarrow 1$  transition energy at  $n_g = 1/2$ ,  $E_{10}$ .

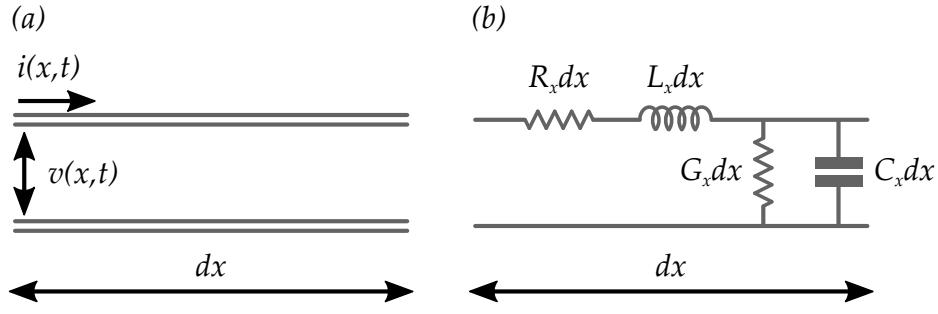


Figure 2.5 – (a) Voltage and current definitions. (b) Lumped element model.

$G_x$  the losses in the dielectric between the two conductors.  $R_x$  and  $G_x$  therefore represent the losses in the transmission line.

The equations of motion of the transmission line can be obtained applying Kirchhoff's laws to the circuit in Fig. 2.5 (b)<sup>58</sup>. This results in the *telegrapher equations*, Eq. (2.15).

$$\begin{aligned}\frac{\partial v(x, t)}{\partial x} &= -R_x i(x, t) - L_x \frac{\partial i(x, t)}{\partial t}, \\ \frac{\partial i(x, t)}{\partial x} &= -G_x v(x, t) - C_x \frac{\partial v(x, t)}{\partial t}.\end{aligned}\tag{2.15}$$

We can simplify the expression assuming sinusoidal solutions of the form  $v(x, t) = V(x)e^{j\omega t}$  for both voltage and current. Introducing this expression in Eq. (2.15) we obtain

$$\frac{dV(x)}{dx} = -(R_x + j\omega L_x) I(x)\tag{2.16}$$

$$\frac{dI(x)}{dx} = -(G_x + j\omega C_x) V(x)\tag{2.17}$$

Combining these two expressions we get a wave equation for the voltage and the current, Eq. (2.19).

$$\frac{\partial^2 V(x, t)}{\partial x^2} - \gamma^2 V(x, t) = 0\tag{2.18}$$

$$\frac{\partial^2 I(x, t)}{\partial x^2} - \gamma^2 I(x, t) = 0\tag{2.19}$$

Here  $\gamma$  is the propagation constant of the line. It is given by

$$\gamma = \alpha + jk = \sqrt{(R_x + j\omega L_x)(G_x + j\omega C_x)}\tag{2.20}$$

The solutions for Eq. (2.19) are incoming and outgoing voltage and current waves;

$$V(x, t) = |V_0^+| e^{j\omega t - \gamma x} + |V_0^-| e^{j\omega t + \gamma x},\tag{2.21}$$

$$I(x, t) = |I_0^+| e^{j\omega t - \gamma x} + |I_0^-| e^{j\omega t + \gamma x}.\tag{2.22}$$

From Eqs. (2.16), (2.21) and (2.22) we see that the current and the voltage in the line are related via

$$\frac{V_0^+}{I_0^+} = \frac{-V_0^-}{I_0^-} = Z_0 = \sqrt{\frac{R_x + j\omega L_x}{G_x + j\omega C_x}} \quad (2.23)$$

This quantity  $Z_0$  is the *characteristic impedance* of the transmission line. It plays a role similar to the index of refraction in optical media. When connecting two transmission lines in series they must have the same characteristic impedance  $Z_0$  in order to avoid reflections at the interface between them. For most electrical circuits it is fixed to  $50 \Omega$ .

We can rewrite Eq. (2.21) taking the real part to show explicitly the space dependence,

$$v(x, t) = |V_0^+| \cos(\omega t - kx + \phi^+) e^{-\alpha x} + |V_0^-| \cos(\omega t + kx - \phi^-) e^{\alpha x}. \quad (2.24)$$

Here  $\omega$  and  $k$  are related via the dispersion relation of the line imposed by Eq. (2.20).

In this work we use superconductors and measure at cryogenic temperatures, therefore we neglect both  $R_x$  and  $G_x$  and work with a lossless line. In this case we can simplify the expressions for the propagation constant  $\gamma$  and the characteristic impedance  $Z_0$  of the line as

$$\gamma = j\omega\sqrt{L_x C_x} \rightarrow k = \omega\sqrt{L_x C_x}, \quad (2.25)$$

$$Z_0 = \sqrt{\frac{L_x}{C_x}}, \quad (2.26)$$

As it can be seen, now  $Z_0$  is frequency independent. From Eq. (2.25) we obtain a linear dispersion relation

$$\omega(k) = v_p k. \quad (2.27)$$

where the phase velocity  $v_p$  is given by

$$v_p = \frac{1}{\sqrt{L_x C_x}} \quad (2.28)$$

Therefore, in a transmission line waves propagate in the same way as optical light does in a linear medium of refractive index  $n = c/v_p$ .

### *The array of SQUIDS*

In circuits the coupling strength is given by the *impedance matching condition*<sup>58</sup> which basically states that the coupling between two circuits is maximal whenever their impedances are the same. This idea is treated in detail in Chapter 3. For the superconducting qubits the impedance is in the  $k\Omega$  range. Therefore to improve the coupling between the qubit and the transmission line we need to increase  $Z_0$ . From Eq. (2.26) it follows that it is necessary to increase  $L_x$  and to decrease  $C_x$ .

As mentioned in Section 2.1.1, a Josephson junction has a large inductance while being dissipation less. In addition, due to its reduced size ( $\sim \mu\text{m}^2$ ) its capacitance to ground can be very small ( $\leq 1\text{fF}$ ). In order to fabricate this high impedance transmission line we connect several junctions in series<sup>39,46,47,84</sup>. The lumped element model for this array is shown in Fig. 2.6 (a). Each site consists of a Josephson junction with inductance  $L_J$  and self capacitance  $C_J$ . In addition each site has a capacitance to ground  $C_g$ . We are interested in the linear properties of this array, therefore we use junctions with a large  $E_J/E_C$  ratio (large  $I_C$ ) to be sure that they behave as linear inductors, see Eq. (2.4). Moreover, instead of single junctions we use SQUIDS that allow to tune the inductance of the junctions  $L_J$  and therefore the characteristic impedance of the line  $Z_0$  via an external magnetic flux  $\Phi$ . The circuit scheme for the array in the linear regime is shown in Fig. 2.6 (b). To represent the tunable linear inductors we use the usual inductor symbol with an arrow across it.

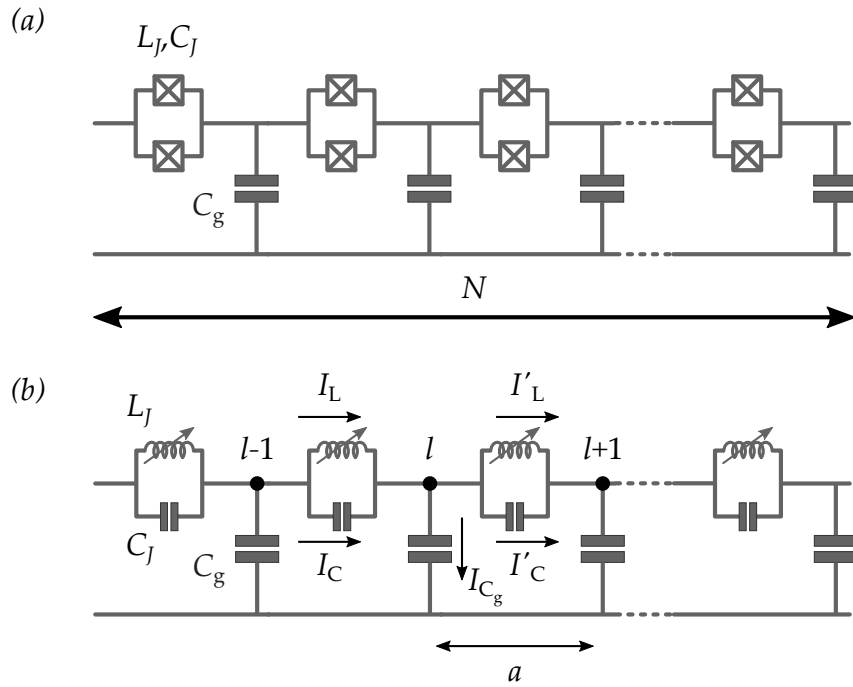


Figure 2.6 – Lumped element model for an array of SQUIDS. (a) Full nonlinear model. (b) Linearized model. The different nodes in the circuit and different currents are shown. The length of each unit cell is  $a$ .

Using the linear model of Fig. 2.6 (b) we obtain the dispersion relation of the modes in the chain. We apply Kirchhoff's current law to one chain cell of length  $a$ ,

$$I_L + I_C - I'_L - I'_C - I'_{C_g} = 0. \quad (2.29)$$

We rewrite this expression using the flux  $\Phi_l$  at node  $l$  and the parameters of the

array,  $L_J, C_J$  and  $C_g$ . We obtain

$$\begin{aligned} & \frac{1}{L_J} (\Phi_{l-1} - \Phi_l) + C_J (\ddot{\Phi}_{l-1} - \ddot{\Phi}_l) \\ & - \frac{1}{L_J} (\Phi_l - \Phi_{l+1}) - C_J (\ddot{\Phi}_l - \ddot{\Phi}_{l+1}) - C_g \ddot{\Phi}_l = 0. \end{aligned} \quad (2.30)$$

It is convenient for this system to denote the length of a unit cell as  $a$ . Therefore the position along the  $x$  axis can be written as  $x = la$  with  $l$  an integer denoting the node in the circuit. To solve Eq. (2.30) we use as ansatz a plane wave  $\Phi_l = A \exp j(\omega t - kla)$  and solve for  $\omega$ . In this way we obtain the dispersion relation for an array of SQUIDS in the linear regime, Eq. (2.31).

$$\omega(k) = \frac{1}{\sqrt{L_J C_J}} \sqrt{\frac{1 - \cos(ka)}{1 - \cos(ka) + \frac{C_g}{2C_J}}}. \quad (2.31)$$

In Fig. 2.7 we plot  $\omega(k)$  in blue. We distinguish two different regimes in this dispersion relation. When  $ka \ll 1$  and  $ka \ll \sqrt{C_g/C_J}$  we can Taylor expand the cosine term  $\cos(ka) \sim 1 - (ka)^2/2$  obtaining a linear dispersion relation

$$\omega(k) = \frac{a}{\sqrt{L_J C_g}} k = v_p k. \quad (2.32)$$

We recover the linear behavior for the infinite continuous transmission line in Eq. (2.27). This linear regime is shown in orange in Fig. 2.7. For usual values of  $a = 1 \mu\text{m}$ ,  $L_J = 1 \text{ nH}$  and  $C_g = 0.1 \text{ fF}$  we obtain a phase velocity of  $v_p = 3 \times 10^6 \text{ m/s}$ . This means that with such arrays of SQUIDS we can get refractive indexes in the order of  $n = c/v_p = 100$ . For  $ka \rightarrow \pi$  the dispersion relation becomes flat approaching a constant value given by

$$\omega_p = \frac{1}{\sqrt{L_J (C_J + C_g/4)}}. \quad (2.33)$$

This is the plasma frequency of the single junctions. It is shown in Fig. 2.7 with a dashed gray line. As it can be seen, for  $C_J \gg C_g/4$  the dispersion relation is already almost flat for  $ka = 0.2$ .

This plasma frequency comes from two different characteristics of the array. The most intuitive one is the Josephson capacitance  $C_J$ . At low frequencies this capacitance is an open and the array behaves as a regular transmission line. However, at high frequencies it becomes a short. No current flows through the inductors and therefore no mode propagates. There is however some transmission through the array via capacitances  $C_J$  and  $C_g$ . The boundary between these two limits is the resonance frequency of the  $LC$  circuit formed by each cell. At this frequency the impedance of each cell becomes infinite and there is no transmission through the array.

The second characteristic is that we assumed a discrete model for the array, i.e. we divided its length in unit cells of length  $a$ . Within this model, the shortest



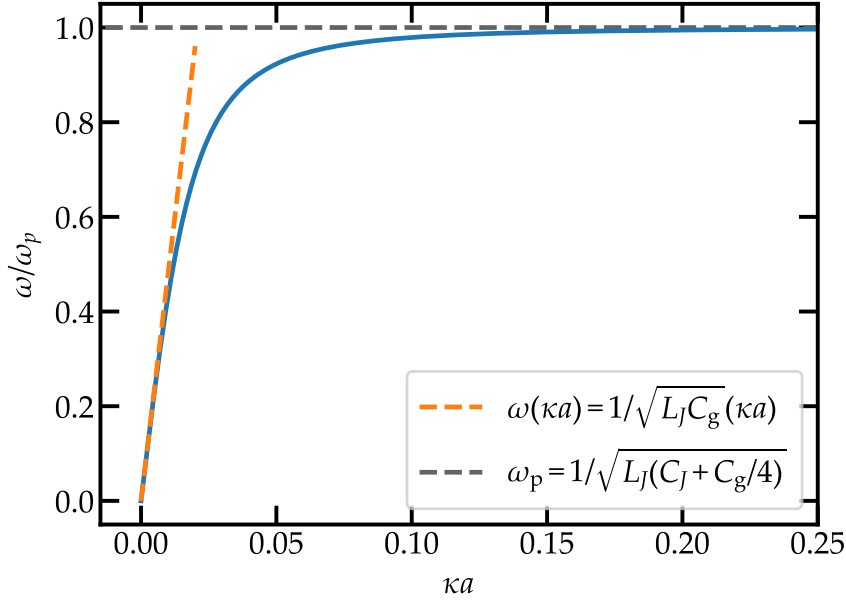


Figure 2.7 – Dispersion relation for an infinite chain. In orange the linear regime is shown. The plasma frequency is given in grey. The chosen parameters are similar to the ones in the experiment,  $L_J = 0.33$  nH,  $C_J = 259$  fF and  $C_g = 0.13$  fF.

possible wavelength  $\lambda$  is when each unit cell oscillates with a  $\pi$  shift from its neighbors, i.e. when  $\lambda = 2a$ . This corresponds to  $k = 2\pi/\lambda = \pi/a$  which gives  $ka = \pi$ . Using Eq. (2.31) and  $ka = \pi$  the maximum mode frequency is given by  $\omega_{\max} = \omega_p$ .

Regarding the wave number  $k$ , its values depend on the boundary conditions imposed in the array. For an infinite array,  $k$  takes any value. All waves propagate and there are no standing waves. However, whenever we make a finite size array with islands  $l \in [0, \dots, N]$ , the two sites at the extremity have different boundary conditions than the sites in the middle. Therefore the value of  $k$  will be restricted.

The general form of the eigenmodes of a chain is a superposition of right-moving and left-moving plane waves,

$$\Phi_l = A \exp j(\omega t - kla) + B \exp j(\omega t + kla). \quad (2.34)$$

If we ground both ends of the chain the voltage at nodes 0 and  $N$  becomes zero,

$$\dot{\Phi}_0 = 0 \quad \dot{\Phi}_N = 0. \quad (2.35)$$

Plugging this condition into Eq. (2.34) gives the allowed  $k$  values,

$$k = \frac{n\pi}{Na} \quad \text{for } n = 1, 2, \dots, N-1. \quad (2.36)$$

For both ends open the voltage reaches a maximum at nodes 0 and  $N$ . This

imposes the following condition on the flux,

$$\begin{aligned}\frac{\partial V_l}{\partial (la)} \Big|_{l=0} &= \frac{\partial \dot{\Phi}_l}{\partial (la)} \Big|_{l=0} = j\omega \frac{\partial \Phi_l}{\partial (la)} \Big|_{l=0} = 0 \\ \frac{\partial V_l}{\partial (la)} \Big|_{l=N} &= \frac{\partial \dot{\Phi}_l}{\partial (la)} \Big|_{l=N} = j\omega \frac{\partial \Phi_l}{\partial (la)} \Big|_{l=N} = 0.\end{aligned}\tag{2.37}$$

With these boundary conditions we obtain the same expression for the  $k$  as in Eq. (2.36).

Another configuration is to keep one side open and the other grounded. This gives mixed boundary conditions,

$$\frac{\partial \Phi_l}{\partial (la)} \Big|_{l=0} = 0 \quad \Phi_N = 0.\tag{2.38}$$

For this case the allowed values for  $k$  are

$$k = \frac{(n - 1/2)\pi}{Na} \quad \text{for } n = 1, 2, \dots, N.\tag{2.39}$$

The characteristic impedance of the array of SQUIDS can be obtained in a similar way to the dispersion relation, see Appendix A.1. The result is

$$Z_0(\omega) = \sqrt{\frac{L_J}{C_g(1 - L_J C_J \omega^2)}}.\tag{2.40}$$

For frequencies far away from the plasma frequency of the junctions, the array of SQUIDS behaves as a lossless transmission line of characteristic impedance

$$Z_0 = \sqrt{\frac{L_J}{C_g}} \quad \text{for } \omega \ll 1/\sqrt{L_J C_J}.\tag{2.41}$$

Regular Josephson junctions have an inductance in the nH range. The capacitance to ground depends on the specific geometry of the circuit but it is usually in the fF range. This means that the characteristic impedance for these arrays is in the k $\Omega$  range, much larger than the usual 50  $\Omega$  in microwave systems. Thanks to the SQUIDS in the array we can tune the impedance with an external flux via the Josephson inductance,

$$Z_0(\Phi_{\text{ext}}) = \sqrt{\frac{L_J(\Phi_{\text{ext}})}{C_g}}.\tag{2.42}$$

To sum up, the array of SQUIDS is a high impedance transmission line whose impedance is flux tunable. This allows us to study the qubit-array system at different interaction regimes.

### 2.2.2 Non-homogeneous systems

Most circuits are not homogeneous i.e. they cannot be described by a unit cell that repeats periodically over a finite length. Here we introduce two different

formalisms to treat these circuits.

### *Lagrangian and Hamiltonian for a linear circuit*

In this section we describe the formalism to obtain the eigenmodes and eigenfrequencies for any given linear circuit. The useful variables to describe the circuit are the flux  $\Phi_n$  and the voltage  $\dot{\Phi}_n$  at node  $n$ . We are going to work only with linear elements: capacitors ( $C$ ) and inductors ( $L$ ). Each of these elements have the following constitutive relations<sup>81</sup>;

$$Q = C (V_m - V_n) = C (\dot{\Phi}_m - \dot{\Phi}_n), \quad (2.43)$$

$$I = \frac{(\Phi_m - \Phi_n)}{L}. \quad (2.44)$$

The energy stored in each component integrating the electrical power with respect to time is given by Eqs. (2.45) and (2.46).

$$E_C = \frac{C (\dot{\Phi}_m - \dot{\Phi}_n)^2}{2}, \quad (2.45)$$

$$E_L = \frac{(\Phi_m - \Phi_n)^2}{2L}. \quad (2.46)$$

A Lagrangian containing only linear elements is quadratic in  $\Phi_n$  and  $\dot{\Phi}_n$  for all  $n$ . This means that it can be written in the form

$$\mathcal{L} = \frac{1}{2} \dot{\vec{\Phi}}^T \hat{C} \dot{\vec{\Phi}} - \frac{1}{2} \vec{\Phi}^T \hat{L}^{-1} \vec{\Phi}, \quad (2.47)$$

where we defined vectors  $\dot{\vec{\Phi}}$  and  $\vec{\Phi}$  as

$$\dot{\vec{\Phi}} = \begin{pmatrix} \dot{\Phi}_0 \\ \dot{\Phi}_1 \\ \vdots \\ \dot{\Phi}_N \end{pmatrix}, \quad \vec{\Phi} = \begin{pmatrix} \Phi_0 \\ \Phi_1 \\ \vdots \\ \Phi_N \end{pmatrix}. \quad (2.48)$$

The matrices  $\hat{C}$  and  $\hat{L}$  are symmetric matrices.  $\hat{C}$  is the capacitance matrix and  $\hat{L}$  is the inductance matrix of the circuit. For this Lagrangian the Euler-Lagrange equation is given by<sup>85,86</sup>

$$\ddot{\vec{\Phi}} = -\hat{C}^{-1} \hat{L}^{-1} \vec{\Phi}. \quad (2.49)$$

From this expression it is clear that the positive square root of the eigenvalues of  $\hat{C}^{-1} \hat{L}^{-1}$  gives the resonance frequencies of the circuit.

From the Lagrangian in Eq. (2.47) we can obtain directly the Hamiltonian of any linear circuit. To do so we perform a Legendre transformation obtaining<sup>86</sup>

$$\mathcal{H} = \frac{1}{2} \vec{Q}^T \hat{C}^{-1} \vec{Q} + \frac{1}{2} \vec{\Phi}^T \hat{L}^{-1} \vec{\Phi}, \quad (2.50)$$

where the  $\vec{Q}$  contains the conjugate momenta of node fluxes, the node charges  $Q_n$ . The relation between  $\vec{\Phi}$  and  $\vec{Q}$  is given by

$$\vec{Q} = \hat{C} \vec{\Phi}. \quad (2.51)$$

To move to the quantum mechanical problem we replace the variables  $Q$  and  $\Phi$  by the operators  $\hat{Q}$  and  $\hat{\Phi}$  defined in Section 2.1.2. Following the method in Snyman and Florens<sup>30</sup> we write the linear Hamiltonian in Eq. (2.50) in its normal-mode basis. To do so we first impose the following relation between the charge and flux operators and the bosonic creation and annihilation operators,

$$\hat{Q}_n = \sqrt{\frac{\hbar}{2}} \sum_{k=1}^N \zeta_{n,k} (a_k + a_k^\dagger) \quad \hat{\Phi}_n = i \sqrt{\frac{\hbar}{2}} \sum_{k=1}^N \pi_{n,k} (a_k - a_k^\dagger). \quad (2.52)$$

The inverse relation reads,

$$a_k = \frac{1}{\sqrt{2\hbar}} \sum_{n=1}^N [\zeta_{k,n} \hat{\Phi}_n + i\pi_{k,n} \hat{Q}_n] \quad a_k^\dagger = \frac{1}{\sqrt{2\hbar}} \sum_{n=1}^N [\zeta_{k,n} \hat{\Phi}_n - i\pi_{k,n} \hat{Q}_n]. \quad (2.53)$$

Here, matrices  $\zeta$  and  $\pi$  need to be determined. By imposing the standard commutation relations for the bosonic operators,  $[a_n, a_m^\dagger] = \delta_{n,m}$  and  $[a_n, a_m] = 0$ , and the commutation relations for charge and flux operators,  $[\hat{\Phi}_n, \hat{Q}_m] = i\hbar\delta_{n,m}$  we obtain an important relation for matrices  $\zeta$  and  $\pi$  (see Appendix A.2 for the derivation),

$$\zeta \pi^T = I. \quad (2.54)$$

The units for the elements of the matrices are  $[\zeta] = 1/\sqrt{\Omega}$  and  $[\pi] = \sqrt{\Omega}$ . If we introduce Eq. (2.52) in the Hamiltonian in Eq. (2.50) we obtain

$$\begin{aligned} \mathcal{H} &= \frac{1}{2} \vec{\tilde{Q}}^T \hat{C}^{-1} \vec{\tilde{Q}} + \frac{1}{2} \vec{\tilde{\Phi}}^T \hat{L}^{-1} \vec{\tilde{\Phi}} \\ &= \frac{1}{2} \sum_{j,k=1}^N [\hat{Q}_j \hat{C}_{j,k}^{-1} \hat{Q}_k + \hat{\Phi}_j \hat{L}_{j,k}^{-1} \hat{\Phi}_k] \\ &= \frac{\hbar}{4} \sum_{j,k=1}^N [(a_j^\dagger + a_j) [\zeta^T \hat{C}^{-1} \zeta] (a_k^\dagger + a_k) \\ &\quad - (a_j^\dagger - a_j) [\pi^T \hat{L}^{-1} \pi] (a_k^\dagger - a_k)]. \end{aligned} \quad (2.55)$$

In order to recover the expression for an harmonic Hamiltonian the terms in brackets must fulfill

$$[\zeta^T \hat{C}^{-1} \zeta] = \hat{\Omega}, \quad (2.56)$$

$$[\pi^T \hat{L}^{-1} \pi] = \hat{\Omega}, \quad (2.57)$$

where  $\widehat{\Omega}$  is a diagonal matrix whose entries are the frequencies of the normal modes  $\omega_k$ . Therefore, from Eq. (2.49),  $\widehat{\Omega}$  contains the positive square root of the eigenvalues of matrix  $\widehat{C}^{-1}\widehat{L}^{-1}$ .

To fulfill these conditions the components of matrix  $\pi$  must be the eigenvectors of matrix  $\widehat{C}^{-1}\widehat{L}^{-1}$ . If we multiply on the left Eq. (2.56) by  $\pi$  and Eq. (2.57) by  $\zeta$  we obtain

$$\pi\zeta^T\widehat{C}^{-1}\zeta = \widehat{C}^{-1}\zeta = \pi\widehat{\Omega}, \quad (2.58)$$

$$\zeta\pi^T\widehat{L}^{-1}\pi = \widehat{L}^{-1}\pi = \zeta\widehat{\Omega}. \quad (2.59)$$

Now we substitute the expression for  $\zeta$  in Eq. (2.59),  $\zeta = \widehat{L}^{-1}\pi\widehat{\Omega}^{-1}$ , into Eq. (2.58). We get an eigenvalue equation for  $\pi$ ,

$$\widehat{C}^{-1}\widehat{L}^{-1}\pi\widehat{\Omega}^{-1} = \pi\widehat{\Omega} \quad \rightarrow \quad \widehat{C}^{-1}\widehat{L}^{-1}\pi = \pi\widehat{\Omega}^2. \quad (2.60)$$

This means that the columns of matrix  $\pi$  are the right eigenvectors of matrix  $\widehat{C}^{-1}\widehat{L}^{-1}$ .

Taking all this into account we can finally write the Hamiltonian as:

$$\begin{aligned} \mathcal{H} &= \frac{\hbar}{4} \sum_{j,k=1}^N \left[ (a_j^\dagger - a_j) \left[ \widehat{\zeta}^T \widehat{C}^{-1} \widehat{\zeta} \right] (a_k^\dagger - a_k) \right. \\ &\quad \left. - (a_j^\dagger + a_j) \left[ \widehat{\pi} \widehat{L}^{-1} \widehat{\pi}^T \right] (a_k^\dagger + a_k) \right] \\ &= \frac{\hbar}{4} \sum_{j=1}^N \left[ (a_j^\dagger - a_j) \omega_j (a_j^\dagger - a_j) - (a_j^\dagger + a_j) \omega_j (a_j^\dagger + a_j) \right] \\ &= \sum_{j=1}^N \hbar \omega_j \left( a_j^\dagger a_j + \frac{1}{2} \right). \end{aligned} \quad (2.61)$$

This method is valid for any system whose Lagrangian can be written as in Eq. (2.47) for any form of matrices  $\widehat{C}$  and  $\widehat{L}$  i.e. for any quadratic Lagrangian. This means that the system must be linear.

### ABCD matrices

Here we present a method to obtain the scattering parameters of a circuit for any given frequency. The circuits treated in this work are two port circuits. They have an input port, port 1, and output port, port 2. We can relate the incident voltage in both ports  $V_1^-, V_2^-$  to the reflected voltage  $V_1^+, V_2^+$  via the scattering matrix as

$$\begin{pmatrix} V_1^- \\ V_2^- \end{pmatrix} \begin{pmatrix} S_{11} & S_{12} \\ S_{21} & S_{22} \end{pmatrix} = \begin{pmatrix} V_1^+ \\ V_2^+ \end{pmatrix}. \quad (2.62)$$

Although the scattering matrix can in principle be obtained for any circuit, it is not very convenient when using several elements in series. A much more suitable description of the circuit is given by the  $ABCD$  matrix<sup>58</sup>. This matrix relates the total voltage  $V_i = V_i^+ + V_i^-$  and current  $I_i = I_i^+ - I_i^-$  in any of the ports to the voltage and current in the other port, Eq. (2.63).

$$\begin{pmatrix} V_1 \\ I_1 \end{pmatrix} \begin{pmatrix} A & B \\ C & D \end{pmatrix} = \begin{pmatrix} V_2 \\ I_2 \end{pmatrix} \quad (2.63)$$

It can be easily shown that the  $ABCD$  matrix of two subsystems coupled in cascade is given by the multiplication of the two subsystems  $ABCD$  matrices. Therefore for modeling an array of  $N$  SQUIDS we can obtain the  $ABCD$  matrix of a single cell to the power  $N$ .

We can relate the  $ABCD$  matrix to the transmission coefficient  $S_{21}$  via<sup>58</sup>:

$$S_{21} = \frac{2}{A + B/Z_0 + CZ_0 + D}. \quad (2.64)$$

Here  $Z_0$  is the impedance of the input and output ports. For asymmetric ports with characteristic impedances  $Z_1$  and  $Z_2$  given by

$$Z_1 = R_1 + jX_1, \quad (2.65)$$

$$Z_2 = R_2 + jX_2, \quad (2.66)$$

an expression for  $S_{21}$  can be obtained<sup>87</sup>,

$$S_{21} = \frac{2\sqrt{R_1 R_2}}{AZ_2 + B + CZ_1 Z_2 + DZ_1}. \quad (2.67)$$

This expression reduces to Eq. (2.64) when  $Z_1 = Z_2 = Z_0$ .

Using this method it is easy to obtain the transmission of a circuit  $S_{21}$  for any component configuration and at any frequency via the multiplication of each of the components'  $ABCD$  matrices.

### Comparison

It is interesting to get an understanding of both methods to compare them in different regimes. For doing so we are going to simulate the linearized array of SQUIDS shown in Fig. 2.6 (b). We reproduce the circuit diagram in Fig. 2.8. We include the different nodes that are going to be used to obtain the Lagrangian of the circuit. In addition, we include an input port of impedance  $Z_{\text{in}}$  and an output port of impedance  $Z_{\text{out}}$ . The values for the capacitances and the inductances of the system are given in Table 2.1. We use the same values as the ones in the experiment. However, in order to speed up the computation, we use a shorter chain of 1000 sites.

To write the Lagrangian of the circuit we use as coordinates the flux  $\Phi_n$  and the electric voltage  $\Phi_n$  in each of the islands of the circuit,  $n \in 0, 1, \dots, N$ . However, the Lagrangian formalism cannot deal with the impedances  $Z_{\text{in}}$  and  $Z_{\text{out}}$ . We can take two limits on each of these impedances, one when they tend to zero and the

$L_J$	0.33 nH
$C_g$	0.13 fF
$C_J$	259 fF
$d(\text{asymmetry})$	0.25
$N$	1000

Table 2.1 – Array parameters for the Lagrangian and the ABCD simulations.

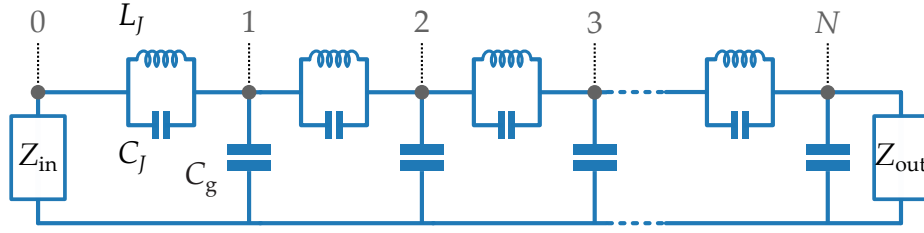


Figure 2.8 – Linearized model for the array. In gray we include the different nodes used to obtain the Lagrangian of the circuit. We include the input and output ports  $Z_{\text{in}}$  and  $Z_{\text{out}}$ .

other when they tend to infinity. These two limits change the boundary conditions at sites 0 and  $N$ . If  $Z_{\text{in}} = 0$  node 0 will be grounded and  $\Phi_0 = \dot{\Phi}_0 = 0$ . The same would happen for  $Z_{\text{out}}$  and node  $N$ . The Lagrangian for the array for open boundary conditions, i.e.  $Z_{\text{in}}, Z_{\text{out}} \rightarrow \infty$  is given by<sup>b</sup>

$$\mathcal{L}_{\text{array}} = \sum_{n=1}^N \left[ \frac{C_J (\Phi_n - \Phi_{n-1})^2}{2} + \frac{(\Phi_n - \Phi_{n-1})^2}{2L_J} + \frac{C_g \Phi_n^2}{2} \right]. \quad (2.68)$$

We can write it using the capacitance  $\hat{C}$  and inductance  $\hat{L}$  matrices of the array,

$$\mathcal{L}_{\text{array}} = \frac{1}{2} \dot{\vec{\Phi}}^T \hat{C} \dot{\vec{\Phi}} - \frac{1}{2} \vec{\Phi}^T \hat{L}^{-1} \vec{\Phi}. \quad (2.69)$$

<sup>b</sup>One can always set  $\Phi_0 = \dot{\Phi}_0 = 0$  or  $\Phi_N = \dot{\Phi}_N = 0$  in this expression to obtain the desired boundary conditions.





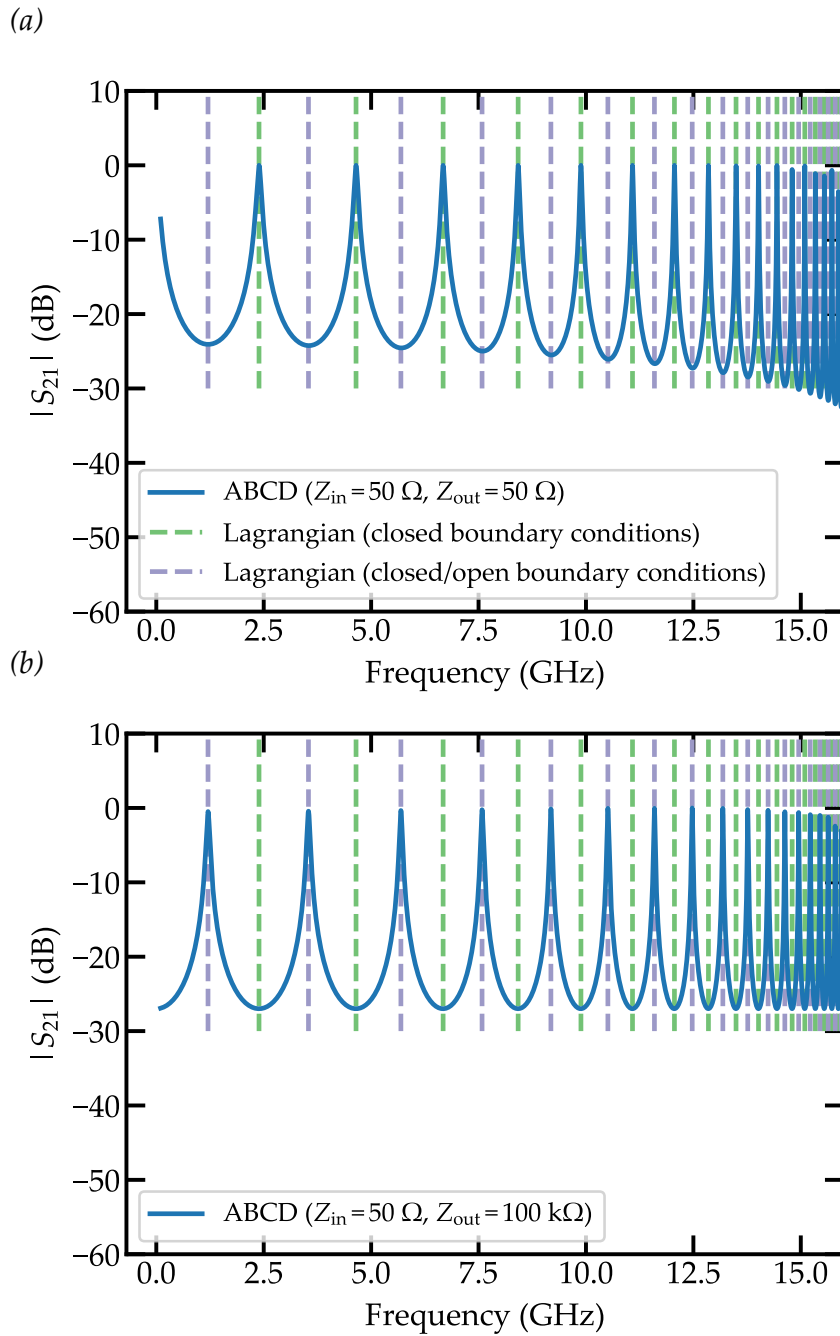


Figure 2.9 – Comparison between the ABCD matrices and the Lagrangian formalism for the linearized array. The dashed lines in both figures indicate the eigenfrequencies obtained from the Lagrangian formalism with closed boundary conditions (green) and close/open boundary conditions (purple). The blue curve is the result obtained from the ABCD matrices for (a)  $Z_{in} = 50 \Omega$  and  $Z_{out} = 50 \Omega$  and (b)  $Z_{in} = 50 \Omega$  and  $Z_{out} = 100 \text{ k}\Omega$ .

boundary conditions. This means that  $50\ \Omega$  ports can effectively be seen as shorts to ground. When we change the value of  $Z_{\text{out}}$  to  $100\ \text{k}\Omega$  the peaks shift to the eigenvalues in the closed/open configuration. Now the impedance of the output port is too high and the last site of the circuit can be seen as an open. In both cases the plasma frequency of the array can be seen as the resonances pack together at high frequencies.

The boundary between the two is the point where  $Z_{\text{out}} = Z_{\text{array}} = \sqrt{L_J/C_g}$ . At this point the spectrum is almost flat due to the fact that the array is impedance matched with the input and output ports, see Fig. 2.10. For low frequencies the

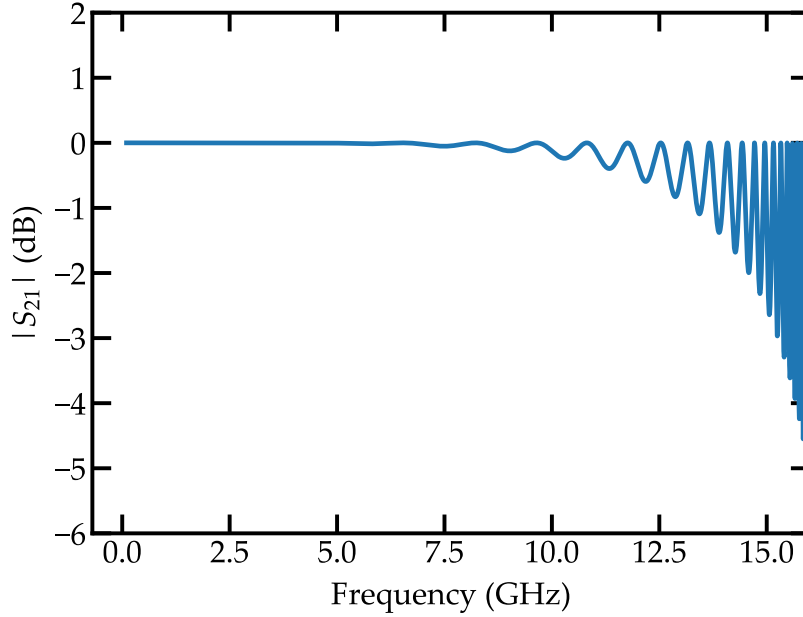


Figure 2.10 – Transmission as a function of frequency for a linearized array. Here  $Z_{\text{out}} = Z_{\text{array}} = \sqrt{L_J/C_g}$ .

array behaves as a transmission line of impedance  $\sqrt{L_J/C_g}$  giving a flat transmission. However, for high frequencies some oscillations appear. This is because close to the plasma frequency the array is not impedance matched with the ports anymore. In this work we are interested in the low frequency regime where the impedance of the array is almost constant with frequency.

As mentioned in Section 2.1.1 we can use an external magnetic flux  $\Phi$  to tune the total critical current of a SQUID. We can get an idea of the effect of this flux tunability using both the Lagrangian and the  $ABCD$  matrices. We perform the same simulations performed before varying  $L_J$  according to the flux modulation of an asymmetric SQUID,

$$L_J(\Phi) = \frac{L_J(0)}{\left| \cos\left(\pi \frac{\Phi}{\Phi_0}\right) \right| \sqrt{1 + d^2 \tan^2\left(\pi \frac{\Phi}{\Phi_0}\right)}}, \quad (2.74)$$

where  $L_J(0) = L_J$ . The result is shown in Fig. 2.11. The color map is the transmission obtained with  $ABCD$  matrices. The red dashed lines are the eigenfrequencies

from the Lagrangian.

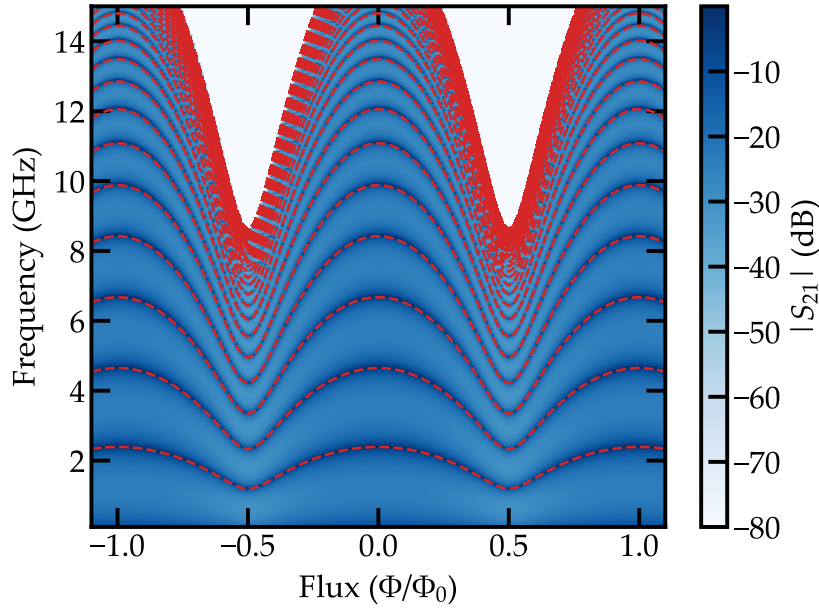


Figure 2.11 – Simulated flux sweep. The color code is the transmission obtained from the ABCD matrix simulation. The dashed red lines are the eigenfrequencies obtained from the Lagrangian.

### 2.3 Nonlinear circuits

The theoretical derivations presented here were made by Dr. Izak Snyman and Dr. Serge Florens with whom I have closely collaborated.

When dealing with nonlinear elements, such as the Josephson junctions, one cannot write the Lagrangian of a circuit as a matrix product (Eq. (2.47)) and obtain the Euler-Lagrange equation in Eq. (2.49). It is then very convenient to approximate this nonlinear elements by linear ones.

A common approach for linearizing a circuit with Josephson junctions of energy  $E_J$  is to replace them by linear inductors of inductance  $L_J = \varphi_0^2/E_J$ . This is the approach we follow with the array of SQUIDS. One could in principle make the same approximation for the transmon qubit. However, this approach does not give the best possible harmonic approximation for the system since it does not count for the strong vacuum fluctuations within the transmon potential. To obtain the closest harmonic Hamiltonian one has to use the Self Consistent Harmonic Approximation (SCHA). Although the SCHA could in principle be used to treat all the nonlinearities in any circuit, in this work we use it only to linearize the transmon qubit.

We start with the transmon qubit Hamiltonian from Eq. (2.13);

$$\mathcal{H}_T = \frac{E_C}{2} \hat{n}^2 + E_J [1 - \cos(\hat{\varphi})]. \quad (2.75)$$

Keeping the system in a potential minimum is needed in order to perform the SCHA. For this reason in this Hamiltonian we set  $n_g = 0$ . Taking into account that we work in the transmon regime, the effect of  $n_g$  in the Hamiltonian is negligible. We would like to write this Hamiltonian as an harmonic Hamiltonian of the form

$$\mathcal{H}_{\text{ho}} = \frac{E_C}{2} \hat{n}^2 + \frac{E_S}{2} \hat{\varphi}^2. \quad (2.76)$$

Here the parameter  $E_S$  is the parameter we would like to optimize in order to obtain the closest harmonic solution to the exact solution. The criterion we use is that the chosen  $E_S$  should minimize  $\langle \mathcal{H}_T \rangle$  where the expectation value is taken with respect to the ground state of  $\mathcal{H}_{\text{ho}}$ .

For a given  $E_S$ , the eigenstates and eigenenergies of  $\mathcal{H}_{\text{ho}}$  are the ones for a quantum harmonic oscillator,

$$|n\rangle = \frac{(\mathbf{B}^\dagger)^n}{\sqrt{n!}} |0\rangle, \quad (2.77)$$

$$E_n^0 = \hbar\omega_{\text{ho}} \left( n + \frac{1}{2} \right) \quad \text{for } n = 0, 1, 2, \dots \quad (2.78)$$

with the resonance frequency given by  $\omega_{\text{ho}} = \sqrt{E_C E_S} / \hbar$  and operator  $\mathbf{B}$  defined as

$$\mathbf{B} = \frac{1}{2\lambda} \hat{\varphi} - i\lambda \hat{n}, \quad \lambda = \frac{1}{\sqrt{2}} \left( \frac{E_C}{E_S} \right)^{\frac{1}{4}}. \quad (2.79)$$

With this definition, operators  $\hat{n}$  and  $\hat{\varphi}$  can be written as

$$\hat{n} = \frac{i}{2\lambda} (\mathbf{B} - \mathbf{B}^\dagger) \quad (2.80)$$

$$\hat{\varphi} = \lambda (\mathbf{B} + \mathbf{B}^\dagger). \quad (2.81)$$

Now we express the full Hamiltonian  $\mathcal{H}_T$  using these operators. First we rewrite it in the form

$$\mathcal{H}_T = \frac{E_C}{2} \hat{n}^2 + \frac{E_S}{2} \hat{\varphi}^2 + E_J [1 - \cos(\hat{\varphi})] - \frac{E_S}{2} \hat{\varphi}^2. \quad (2.82)$$

The first two terms are just the harmonic part. Now we can substitute expressions Eqs. (2.80) and (2.81) in Eq. (2.82) obtaining

$$\begin{aligned} \mathcal{H}_T = & \hbar\omega_{\text{ho}} \left( \mathbf{B}^\dagger \mathbf{B} + \frac{1}{2} \right) + E_J \left[ 1 - \frac{e^{-\lambda^2/2}}{2} \left( e^{i\lambda \mathbf{B}^\dagger} e^{i\lambda \mathbf{B}} + e^{-i\lambda \mathbf{B}^\dagger} e^{-i\lambda \mathbf{B}} \right) \right] \\ & - \frac{E_S}{2} \lambda^2 \left[ (\mathbf{B}^\dagger)^2 + \mathbf{B}^2 + 2\mathbf{B}^\dagger \mathbf{B} + 1 \right]. \end{aligned} \quad (2.83)$$

Here we used the Baker-Campbell-Hausdorff formula<sup>c</sup>. The expectation value  $\langle 0 | \mathcal{H}_T | 0 \rangle$  is given by

$$\langle 0 | \mathcal{H}_T | 0 \rangle = \frac{\hbar\omega_{\text{ho}}}{4} + E_J \left( 1 - e^{-\lambda^2/2} \right) = \frac{\sqrt{E_C E_S}}{4} + E_J \left[ 1 - e^{-\frac{1}{4}\sqrt{E_C/E_S}} \right]. \quad (2.84)$$

The minimal value for  $\langle 0 | \mathcal{H}_T | 0 \rangle$  is

$$\frac{\partial \langle 0 | \mathcal{H}_T | 0 \rangle}{\partial E_S} = 0 \quad \rightarrow \quad E_S = E_J e^{-\frac{1}{4}\sqrt{E_C/E_S}}, \quad (2.85)$$

or rewriting it using the harmonic oscillator resonance frequency

$$\hbar\omega_{\text{ho}} = \sqrt{E_J E_C} e^{-E_C/8\omega_{\text{ho}}}. \quad (2.86)$$

One needs to solve Eq. (2.85) self-consistently to get  $E_S$ . However we can solve it approximately performing a Taylor expansion of the exponential and assuming  $E_S \sim E_J$ ,

$$E_S = E_J - \frac{1}{4}\sqrt{E_C E_J}. \quad (2.87)$$

The same expression for the harmonic oscillator resonance frequency is

$$\hbar\omega_{\text{ho}} = \sqrt{E_J E_C} - \frac{E_C}{8}. \quad (2.88)$$

In Fig. 2.12 we compare the numerical diagonalization of the exact Hamiltonian in Eq. (2.75) with the approximate solutions given in Eqs. (2.86) and (2.88). As we see, for  $E_J/E_C \geq 2$  both approximations are indistinguishable from the exact solution. This means that for this regime we can approximate the transmon qubit by an harmonic oscillator characterized by  $E_C$  and  $E_S$ .

### 2.3.1 General formula

The strength of the SCHA compared to the usual linearizations of the transmon qubit performed in e.g. Koch et al.<sup>80</sup> is easier to see if we deal with the whole system, a transmon qubit capacitively coupled to an array of linearized SQUIDS. The Hamiltonian of this system is

$$\mathcal{H} = \frac{(2e)^2}{2} \sum_{l,s} \widehat{C}_{l,s}^{-1} \widehat{n}_l \widehat{n}_s + \sum_l \frac{E_J}{2} (\widehat{\varphi}_l - \widehat{\varphi}_{l+1})^2 - E_{J,T} \cos \widehat{\varphi}_T. \quad (2.89)$$

Here the operator  $\widehat{n}_l$  is the Cooper pair number operator at island  $l$  and the operator  $\widehat{\varphi}_l$  is the superconducting phase operator at island  $l$ . The only nonlinear term in the Hamiltonian is the last one which contains  $\widehat{\varphi}_T$ , the superconducting phase difference through the Josephson junction in the transmon qubit. We rewrite the Hamiltonian as

$$\mathcal{H} = \mathcal{H}_0 - E_{J,T} \cos \widehat{\varphi}_T. \quad (2.90)$$

<sup>c</sup>For creation and annihilation operators  $B$  and  $B^\dagger$  with commutation relation  $[B, B^\dagger] = 1$  and a scalar  $\lambda$  it follows that  $e^{\lambda(B - B^\dagger)} = e^{\lambda B} e^{\lambda B^\dagger} e^{-\lambda^2/2}$

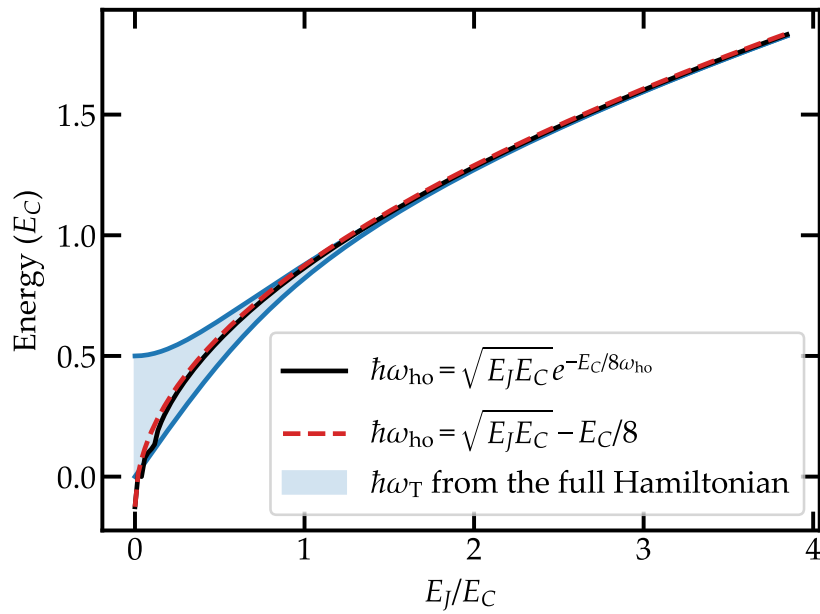


Figure 2.12 – Comparison between the exact transmon frequency  $\omega_{\text{T}}$  and its harmonic approximation  $\omega_{\text{ho}}$  for  $E_C = 2.6$  GHz. The blue area represents  $\omega_{\text{T}}$  for  $n_{\text{g}} \in [0, \dots, 1/2]$ . The black line is the self-consistent solution from the SCHA. The red dashed line is the approximate solution for the self-consistent equation.

Our goal is to obtain an harmonic Hamiltonian to approximate the original one. This harmonic trial Hamiltonian is given by

$$\mathcal{H}_{\text{trial}} = \mathcal{H}_0 + \frac{E_S}{2} \hat{\varphi}_T^2. \quad (2.91)$$

We use as a trial state  $|\Psi\rangle$  the ground state of  $\mathcal{H}_{\text{trial}}$ . From the variational principle we obtain the condition

$$\frac{\partial}{\partial E_S} \langle \Psi | \mathcal{H} | \Psi \rangle = 0. \quad (2.92)$$

After some calculations, see Appendix A.3, this condition gives the following expression for  $E_S$ ,

$$E_S = E_J e^{-\frac{1}{2} \langle \Psi | \hat{\varphi}_T^2 | \Psi \rangle}. \quad (2.93)$$

The meaning of this expression is clear, the self-consistent energy  $E_S$  depends strongly on the vacuum fluctuations of the superconducting phase at the transmon island. This vacuum fluctuations have contributions from all the modes in the array, see the mode decomposition given in Eq. (2.52). Therefore, contrary to the usual linearization of the Josephson junction energy, this method properly takes into account the contribution to  $E_S$  from the modes of the environment. The full procedure was implemented for the full system in this work but it gave negligible contributions and therefore we took into account the vacuum fluctuations coming from the transmon qubit only and their strong effect given its nonlinear potential.

# Coupling in circuits

# 3

In this chapter we give a detailed description of the capacitive coupling between circuits. First we study the case of two oscillators capacitively coupled. We obtain the coupling strength as a function of the circuit parameters for the linear case, two  $LC$  linear oscillators, and the non-linear case, a Single Cooper Pair Box (SCPВ) and an  $LC$  oscillator. Then we show how the coupling between an  $LC$  circuit and a continuous environment of characteristic impedance  $Z_0$  depends on this impedance. Finally we substitute the environment by an array of SQUIDS and the  $LC$  oscillator by a transmon qubit and introduce a way of obtaining the coupling strength between them by looking at the frequency shift of the modes of the array. This method allows to account for the many modes of the array of SQUIDS and for the nonlinearity of the transmon qubit, which is comparable to the Free Spectral Range (FSR) of the array.

## 3.1 Coupling between two oscillators

Most of the results in this work are based on the coupling of one system to an environment composed of several modes. Here we briefly treat a simpler case, a linear  $LC$  oscillator coupled to another  $LC$  oscillator via a capacitor. The lumped element model of this system is shown in Fig. 3.1. The first oscillator, in red, has inductance  $L_1$  and capacitance  $C_1$ . The second one, in blue, has inductance  $L_2$  and capacitance  $C_2$ . They are coupled via capacitance  $C_c$ . In the following, we relate the oscillator 1 to the system and oscillator 2 to the environment.

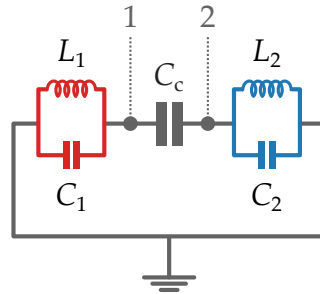


Figure 3.1 – Two coupled  $LC$  oscillators. In grey the nodes used for describing the circuit are shown. The third node is grounded.

The Lagrangian of this system can be easily obtained,

$$\mathcal{L} = \frac{C_1 \Phi_1^2}{2} + \frac{\Phi_1^2}{2L_1} + \frac{C_2 \Phi_2^2}{2} + \frac{\Phi_2^2}{2L_2} + \frac{C_c (\Phi_2 - \Phi_1)^2}{2}. \quad (3.1)$$



In order to study the coupling between the two oscillators it is useful to obtain a Hamiltonian in terms of creation and annihilation operators. The Hamiltonian of the system can be directly obtained via a Legendre transformation of the Lagrangian. It is given by

$$\mathcal{H} = \frac{Q_1^2}{2C_{\Sigma,1}} + \frac{\Phi_1^2}{2L_1} + \frac{Q_2^2}{2C_{\Sigma,2}} + \frac{\Phi_2^2}{2L_2} + \frac{Q_1Q_2}{C_{\Sigma,c}}. \quad (3.2)$$

Here we defined the following capacitances;

$$C_{\Sigma,1} = C_1 + \left( \frac{1}{C_2} + \frac{1}{C_c} \right)^{-1}, \quad (3.3)$$

$$C_{\Sigma,2} = C_2 + \left( \frac{1}{C_1} + \frac{1}{C_c} \right)^{-1}, \quad (3.4)$$

$$C_{\Sigma,c} = C_1 + C_2 + \frac{C_1C_2}{C_c}. \quad (3.5)$$

In Eq. (3.2) we can clearly differentiate three terms: two harmonic oscillators and one coupling term. This coupling term contains the charge associated to each of the oscillators. Now we can promote all variables to operators and introduce as usual the creation and annihilation operators. The charge and flux operators in this basis are given by

$$\hat{Q}_j = \sqrt{\frac{\hbar}{2}} \frac{1}{\sqrt{Z_j}} (a_j + a_j^\dagger), \quad (3.6)$$

$$\hat{\Phi}_j = i\sqrt{\frac{\hbar}{2}} \sqrt{Z_j} (a_j - a_j^\dagger) \quad \text{for } j = 1, 2. \quad (3.7)$$

We defined the impedances of the oscillators as  $Z_j = \sqrt{L_j/C_{\Sigma,j}}$ . The quantum vacuum oscillations for the flux  $\hat{\Phi}_j$  are then given by  $\langle 0 | \hat{\Phi}_j | 0 \rangle = \hbar/2Z_j$  which is proportional to the impedance of the oscillator.

Using these operators we obtain a linear Hamiltonian for two coupled LC oscillators, Eq. (3.8).

$$\begin{aligned} \mathcal{H} = & \hbar\omega_1 \left( a_1^\dagger a_1 + \frac{1}{2} \right) + \hbar\omega_2 \left( a_2^\dagger a_2 + \frac{1}{2} \right) + \\ & \hbar g \left( a_1 + a_1^\dagger \right) \left( a_2 + a_2^\dagger \right). \end{aligned} \quad (3.8)$$

The first two terms are the usual Hamiltonian for an harmonic oscillator. The frequencies  $\omega_j$  are given by  $1/\sqrt{L_jC_{\Sigma,j}}$ . The third term gives the coupling between the oscillators. The coupling strength  $g$  is given by

$$g = \frac{1}{2C_{\Sigma,c}} \frac{1}{\sqrt{Z_1}} \frac{1}{\sqrt{Z_2}} = \frac{C_c}{2(C_c(C_1 + C_2) + C_1C_2)} \frac{1}{\sqrt{Z_1}} \frac{1}{\sqrt{Z_2}}. \quad (3.9)$$

It has two parts. The first one is a term that contains a ratio of the coupling capacitance  $C_c$  to the other capacitances. This is expected, with increasing  $C_c$  the coupling between the oscillators increases. The second part contains the impedances  $Z_1$  and  $Z_2$  of the oscillators. At first glance one would think that in order to increase the coupling we need to decrease this impedances. This is the total opposite to what one would expect. As already shown several times<sup>7,8,39,85</sup>, to get the proper scaling for the coupling we need to compare it to the energy scales of the system. In this case we take the energy of the environment,  $\hbar\omega_2$ , and write the coupling term as

$$\frac{g}{\omega_2} = \frac{1}{2} \frac{C_c}{C_1 + C_c} \sqrt{\frac{Z_2}{Z_1}}. \quad (3.10)$$

We can distinguish two contributions in this coupling term. The first one is a ratio of capacitances. It is a purely geometrical factor and can be increased with the proper design for the coupling capacitors. The second one is related to the vacuum fluctuations of  $\hat{\Phi}$ <sup>7</sup>. It is clear that we need  $Z_2/Z_1 \gg 1$ . This states that we need the impedance of the environment to be at least as high as the impedance of the system if we want a coupling in the order of the frequencies of the environment. Of course, given the relation between the impedance and the frequency of each of the oscillators, the condition  $Z_2/Z_1 \gg 1$  might not be experimentally relevant if, for example, one wants to keep the resonance condition  $\omega_1 = \omega_2$ .

### 3.1.1 Nonlinear model

The results in previous section were obtained assuming two linear LC oscillators. In a way similar than the one followed in Manucharyan et al.<sup>8</sup> we replace now the linear inductor  $L_1$  with a Josephson junction of Josephson energy  $E_{J,T} = \varphi_0^2/L_{J,T}$ , see Fig. 3.2. To keep a consistent notation we rename  $C_1$  as  $C_{J,T}$  and relabel the

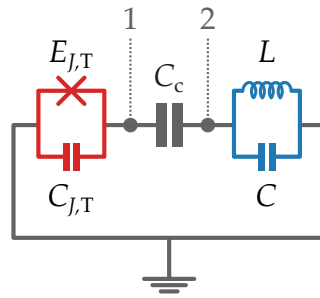


Figure 3.2 – One SCPB in red coupled to an LC oscillator in blue via a coupling capacitor  $C_c$ . The nodes of the circuit are given in gray.

inductance and capacitance of oscillator 2 as  $L$  and  $C$ . The Hamiltonian of the system is then

$$\mathcal{H} = \frac{E_{C,T}}{2} \hat{n}^2 - E_{J,T} \cos \hat{\varphi} + \frac{\hat{Q}^2}{2C_\Sigma} + \frac{\hat{\Phi}^2}{2L} + \frac{(2e) \hat{n} \hat{Q}}{C_{\Sigma,c}}. \quad (3.11)$$

Here  $\hat{n}$  and  $\hat{\varphi}$  are the Cooper pair number operator and the superconducting phase operator respectively. We defined  $E_{C,T} = (2e)^2/C_{\Sigma,J}$  as the charging energy of the Cooper pair box. The capacitances  $C_{\Sigma,J}$  and  $C_{\Sigma}$  are given by  $C_{\Sigma,1}$  and  $C_{\Sigma,2}$  respectively. Contrary to Eq. (3.2), this Hamiltonian is not linear due to the Josephson energy term. We can introduce the creation and annihilation operators for the harmonic oscillator as in Eq. (3.8). This gives the following Hamiltonian,

$$\mathcal{H} = \frac{E_{C,T}}{2} \hat{n}^2 - E_{J,T} \cos \hat{\varphi} + \hbar\omega_r \left( a^\dagger a + \frac{1}{2} \right) + \hbar \frac{2e}{C_{\Sigma,c}} \sqrt{\frac{1}{2\hbar}} \frac{1}{\sqrt{Z_r}} \hat{n} (a^\dagger + a). \quad (3.12)$$

Here we defined  $Z_r = \sqrt{L/C_{\Sigma}}$ . The last term is the coupling term and depends on the value of  $\hat{n}$ . As previously we can rewrite it taking out the resonance frequency of the  $LC$  resonator  $\omega_r = 1/\sqrt{LC}$ . In addition we introduce the quantum of resistance  $R_q = h/(2e)^2 \sim 6.5 \text{ k}\Omega$ . This gives

$$\mathcal{H}_{\text{coupling}} = \hbar\omega_r \frac{C_c}{C_c + C_{J,T}} \sqrt{\frac{\pi Z_r}{R_q}} \hat{n} (a^\dagger + a). \quad (3.13)$$

As we see we obtain an expression similar to the one obtained for linear circuits. We have to keep in mind that the strength of the coupling depends on the operator  $\hat{n}$ .

For a linear circuit we could easily introduce the creation and annihilation operators to obtain the final expression for the coupling between the circuits. In this case we can take two limits, small and large  $E_{J,T}/E_{C,T}$ . For small  $E_{J,T}/E_{C,T}$  we can assume that the SCPB is an effective two-level system and write<sup>8</sup>

$$\mathcal{H}_{\text{coupling}} = \hbar\omega_r \frac{C_c}{C_c + C_{J,T}} \sqrt{\frac{\pi Z_r}{R_q}} (\sigma_+ + \sigma_-) (a^\dagger + a). \quad (3.14)$$

This is the expression for the coupling in the Rabi model, see Section 1.1. We can identify the coupling strength  $g$  as

$$\frac{g}{\omega_r} = \frac{C_c}{C_c + C_{J,T}} \sqrt{\frac{\pi Z_r}{R_q}}. \quad (3.15)$$

This shows that in this regime the impedance of the environment needs to be quite large, in the  $\text{k}\Omega$  range. That is a clear justification for using an array of SQUIDS as the environment.

We can take now the limit of large  $E_{J,T}/E_{C,T}$  in Eq. (3.13) and obtain the coupling in the transmon regime. First we introduce the Cooper pair number operator  $\hat{n}$  for a transmon qubit<sup>80</sup>

$$\hat{n} = \sqrt{\frac{1}{2}} \left( \frac{E_{J,T}}{E_{C,T}} \right)^{\frac{1}{4}} (B^\dagger + B), \quad (3.16)$$

where  $B^\dagger$  and  $B$  are the creation and annihilation operators for the harmonic oscillator approximating the transmon qubit. Introducing this in Eq. (3.13) we obtain an expression similar to the one of the harmonic oscillators,

$$\frac{g}{\omega_r} = \frac{C_c}{C_c + C_{J,T}} \frac{1}{\sqrt{2}} \left( \frac{E_{J,T}}{E_{C,T}} \right)^{\frac{1}{4}} \sqrt{\frac{\pi Z_r}{R_q}}. \quad (3.17)$$

Once again we need to increase the impedance  $Z_r$  to enhance the coupling between the transmon and the  $LC$  oscillator.

### 3.2 Coupling between an $LC$ oscillator and a continuous environment

It is now clear that in order to couple strongly a charge qubit or a transmon qubit to a resonator one needs to increase the impedance of the latter. Now we are going to continue increasing the complexity of the problem. Here we study the coupling between a linear  $LC$  oscillator and a continuous environment of characteristic impedance  $Z_0$ . By continuous environment we mean that the dispersion relation of the environment is continuous.

First of all we need to discuss what we understand for coupling strength when dealing with a continuous environment. Until now the coupling strength was given by a number  $g$ . When dealing with several modes we have a  $g_k$  per mode. In this case it is more convenient to measure the coupling strength via the width  $\Gamma_0$  of the resonance frequency of the qubit. This width  $\Gamma_0$  can be seen as the relaxation rate of the system to the environment. We can obtain the relation between  $\Gamma_0$  and the  $g_k$  via the bath spectral function  $J(\omega)$ ,

$$\Gamma_0 = \frac{2\pi}{\hbar^2} \sum_k g_k^2 \delta(\omega_q - \omega_k) = J(\omega_q). \quad (3.18)$$

This expression is obtained via the Born-Markov and rotating-wave approximations. However, up to  $\Gamma_0/\omega_q \sim 1$  the equation is still correct<sup>22</sup>. Therefore we can use  $\Gamma_0$  as a direct measure of the coupling strength. According to the previous results,  $g \propto \sqrt{Z_0}$ , we expect  $\Gamma_0$  to be proportional to the impedance of the environment.

#### 3.2.1 Intuitive explanation

The behavior of an  $LC$  circuit coupled to an environment with impedance  $Z_0$  can be intuitively obtained using the circuit depicted in Fig. 3.3. We model the environment with a resistor of resistance  $R$  and couple the  $LC$  circuit via two coupling capacitors of capacitance  $C_c$ . From the impedance  $Z_{AB}$  between points  $A$  and  $B$  we can obtain the frequency  $\omega_0$  and the width  $\Gamma_0$  of the resonance of the

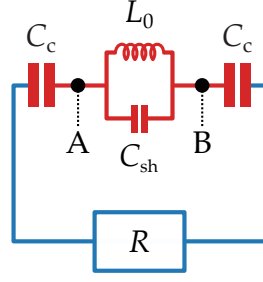


Figure 3.3 – A parallel LC circuit capacitively coupled to a resistor of resistance  $R$ . The impedance of the system  $Z_{AB}$  is obtained between nodes A and B.

system. From the circuit in Fig. 3.3 we see that this impedance is given by

$$\begin{aligned} \frac{1}{Z_{AB}(\omega)} &= \left( R + \frac{2}{j\omega C_c} \right)^{-1} + j\omega C_{sh} + \frac{1}{j\omega L_0} \\ &= \frac{(2 + iC_c R\omega)(1 - L_0 C_{sh} \omega^2) - L_0 C_c \omega^2}{iL_0 \omega (2 + iC_c R\omega)}. \end{aligned} \quad (3.19)$$

The real part of the poles of this impedance gives the resonance frequency of the system  $\omega_0$ . The imaginary part gives the resonance width  $\Gamma_0$ <sup>88</sup>.

The behavior of  $\omega_0$  with respect to  $R$  is easy to understand. If we set  $R = 0$  we simplify Eq. (3.19) and obtain

$$\frac{1}{Z_{AB}(\omega)} = 1 - \omega^2 L_0 \left( C_{sh} + \frac{C_c}{2} \right). \quad (3.20)$$

This gives a resonance frequency of  $\omega_{0,R=0} = 1/\sqrt{L_0(C_{sh} + C_c/2)}$ . This makes sense, the current oscillates through the whole circuit. However, at large  $R$  the first term in Eq. (3.19) disappears and we obtain  $\omega_{0,R \rightarrow \infty} = 1/\sqrt{L_0 C_{sh}}$ . In this case the resistor behaves as an open and the current oscillates only in the parallel LC formed by  $C_{sh}$  and  $L_0$ . Regarding the width, we obtain analytically two asymptotic expressions for small and large  $R$ ,

$$\Gamma_{0,R \rightarrow 0} = \frac{C_c^2 R}{8(C_{sh} + C_c/2)^2 L_0} \quad (3.21)$$

$$\Gamma_{0,R \rightarrow \infty} = \frac{1}{2C_{sh} R}. \quad (3.22)$$

In Fig. 3.4 the width  $\Gamma_0$  is plotted as a function of  $R$  including the asymptotic expressions. For the calculation we used  $L_0 = 18.1$  nH,  $C_c = 119$  fF and  $C_{sh} = 80$  fF. As it can be seen, for small  $R$  the width  $\Gamma_0$  is linear with  $R$ . This is an expected behavior consistent with the results derived in the previous section and the fact that  $\Gamma_0 \propto g^2$ . However, at large  $R$  it is proportional to  $1/R$ . This is because with an increasing  $R$  less and less current goes through capacitances  $C_c$  and therefore the coupling is reduced.

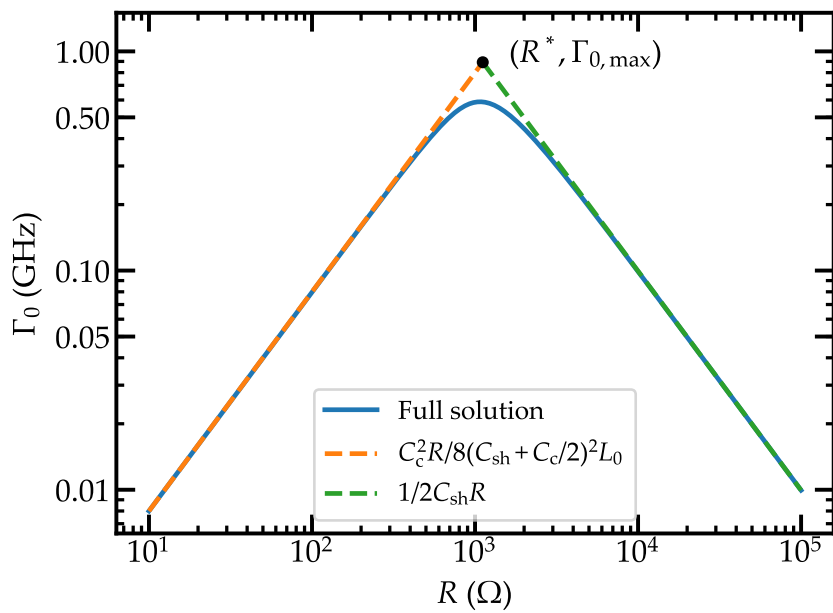


Figure 3.4 – Resonance width  $\Gamma_0$  as a function of the resistance  $R$ . We take  $L_0 = 18.1$  nH,  $C_c = 119$  fF and  $C_{sh} = 80$  fF. The dashed lines give the two asymptotic expressions. The black dot where both asymptotic expressions cross gives an estimation of the maximum value of  $\Gamma_0$  and the respective resistance  $R^*$ .

We can get a good estimation of the maximum value of  $\Gamma_0$  and its related resistance  $R^*$  from the intersection of the two asymptotic expressions,

$$\Gamma_{0,\max} = \frac{1}{2} \frac{C_c}{2C_{\text{sh}} + C_c} \omega_{0,R \rightarrow \infty}, \quad (3.23)$$

$$R^* = \left(1 + \frac{2C_{\text{sh}}}{C_c}\right) Z_{LC}. \quad (3.24)$$

Here we defined  $Z_{LC}$  as the impedance of the  $LC$  oscillator. The point  $(R^*, \Gamma_{0,\max})$  is given in Fig. 3.4 in black. This analysis shows intuitively that despite needing a high impedance to increase the coupling between a circuit and its environment, one should take care of parasitic capacitances that might shunt the environment for too high impedances. This effect of shunting a high impedance environment via parasitic capacitances has been studied recently in several publications<sup>72,89,90</sup> relating it to  $A^2$  terms in CQED.

### 3.2.2 Quantitative results

In this section we obtain more quantitative results regarding the coupling of an  $LC$  oscillator to an environment of characteristic impedance  $Z_0$ . We are going to treat the circuit shown in Fig. 3.5. This capacitance network describes the experiment, see Section 4.3.2 for a detailed description of the capacitors used in the sample. The value of the capacitances used in these simulations is the same as the ones in the sample measured in the experiment. They are given in Table 3.1. Using

Capacitance	Value (fF)
$C_{g,T2}$	33
$C_{g,T}$	48
$C_c$	119
$C_{\text{sh}}$	12.1
$L_0$	18.1 nH

Table 3.1 –  $LC$  oscillator parameters for the ABCD simulations.

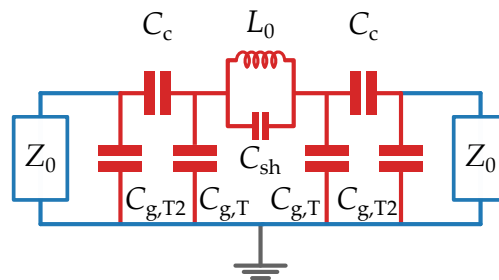


Figure 3.5 –  $LC$  oscillator (red) coupled to two transmission lines of characteristic impedance  $Z_0$  (blue). The capacitance network is the one used in the experiment.

ABCD matrices it is easy to obtain the transmission of this circuit as a function of the impedance of the ports  $Z_0$ .

To obtain the ABCD matrix for the circuit we decompose it in three submatrices. Two of them are given by capacitances  $C_{g,T2}$ ,  $C_c$  and  $C_{g,T}$ ,

$$M_1 = \begin{pmatrix} 1 + \frac{C_{g,T}}{C_c} & \frac{1}{j\omega C_c} \\ j\omega \left( C_{g,T2} + C_{g,T} + \frac{C_{g,T2}C_{g,T}}{C_c} \right) & 1 + \frac{C_{g,T2}}{C_c} \end{pmatrix}. \quad (3.25)$$

The third one contains the parallel LC circuit formed by  $L_0$  and  $C_{sh}$ ,

$$M_{LC,0} = \begin{pmatrix} 1 & j \left( \frac{\omega L_0}{1 - \omega^2 L_{J,T} C_{sh}} \right) \\ 0 & 1 \end{pmatrix}. \quad (3.26)$$

The total ABCD matrix is obtained multiplying these three matrices,

$$M_{LC} = M_1 M_{LC,0} M_1. \quad (3.27)$$

Now we can use the expression in Eq. (2.67) to obtain the transmission of the circuit as a function of frequency. First we set  $Z_0 = 50 \Omega$  and obtain the curve in Fig. 3.6. As it can be seen the transmission has a resonance peak and

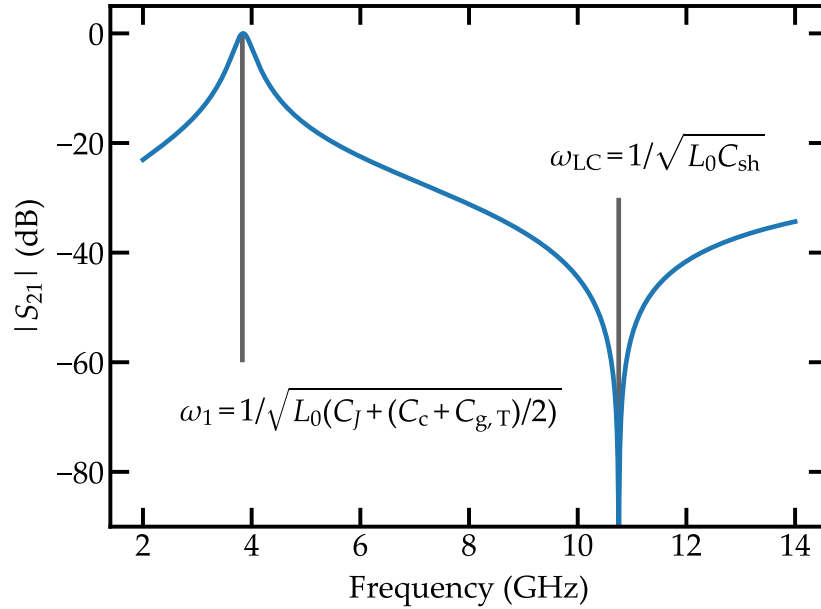


Figure 3.6 – Transmission of the circuit in Fig. 3.5 for  $Z_0 = 50 \Omega$ . In gray the resonance and the antiresonance are given.

a dip. The dip occurs at frequency  $\omega_{LC} = 1/\sqrt{L_0 C_{sh}}$ . It is an antiresonance that comes from the parallel LC circuit formed by  $L_0$  and  $C_{sh}$ . When the microwave frequency is  $\omega_{LC}$  the impedance of the LC circuit becomes infinite and no signal is transmitted through it. A very important feature of this antiresonance is



that it does not depend on any other parameters but  $L_0$  and  $C_{sh}$ . This is an important property that will be used in Section 4.3.2 to obtain the system capacitances. Regarding the peak in transmission, it comes from the  $LC$  circuit formed by the whole capacitance network and  $L_0$ . For low impedances its frequency is  $\omega_1 = 1/\sqrt{L_0(C_{sh} + (C_c + C_{g,T})/2)}$  which does not depend on  $C_{g,T2}$ . This is expected, for low impedances  $C_{g,T2}$  is totally shunted by impedances  $Z_0$  and therefore no current flows through it.

In Fig. 3.7 we plot the transmission for four different port impedances  $Z_0$ . As mentioned before, the dip in transmission is not affected by the impedance

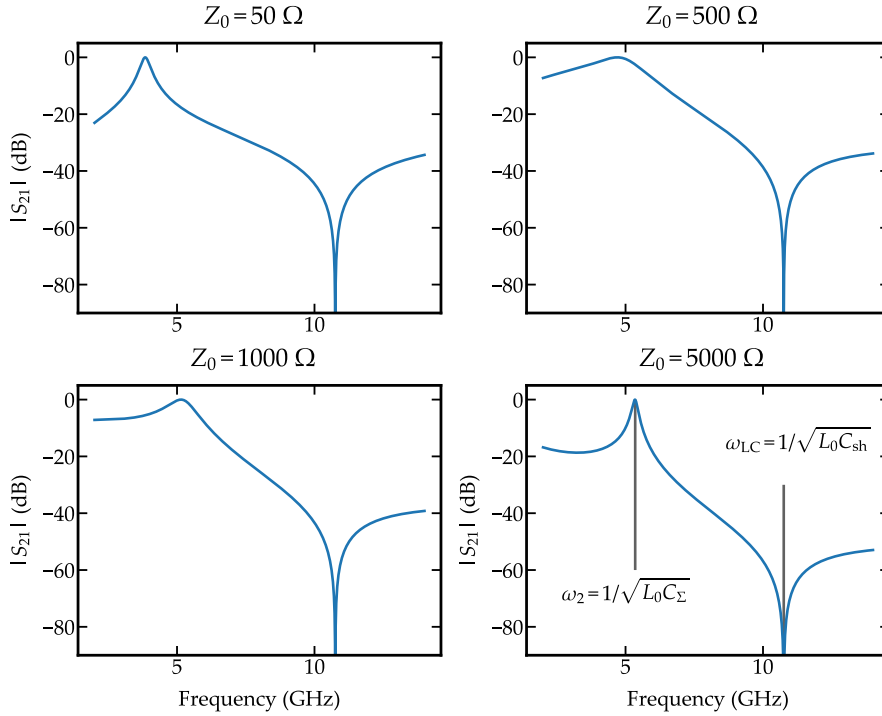


Figure 3.7 – Transmission of the circuit in Fig. 3.5 for different values of  $Z_0$ . For  $Z_0 = 5000 \Omega$  the resonance and antiresonance are indicated in gray.

$Z_0$ . However, the width and position of the resonance peak changes as a function of  $Z_0$ . The behavior is similar to the one described in Section 3.2.1. For low impedances the width of the resonance increases with increasing impedance. This is expected because the oscillator and the port impedances become impedance matched. However for too high impedances the width is reduced due to the capacitances  $C_{g,T}$  and  $C_{g,T2}$  which shunt impedances  $Z_0$ .

Interestingly, by increasing the impedance  $Z_0$  the position of the peak shifts to higher frequencies. It goes from  $\omega_1 = 1/\sqrt{L_0(C_{sh} + (C_c + C_{g,T})/2)}$  in the low impedance limit to

$$\omega_2 = \frac{1}{\sqrt{L_0 C_\Sigma}} \quad (3.28)$$

$$\text{with } C_\Sigma = \left( \frac{2}{C_c} + \frac{2}{C_{g,T2}} \right)^{-1} + C_{sh} + \frac{C_{g,T}}{2}.$$

in the high impedance limit. It is obvious that for high impedances the effective capacitance  $C_\Sigma$  is the parallel combination of  $C_{g,T}$ ,  $C_{sh}$  and  $C_c, C_{g,T2}$  in series. This makes sense because in this regime the ports can be seen as opens and the current needs to go through all these capacitances.

In conclusion, whenever we are dealing with a complex capacitance network that includes capacitances to ground, both the resonance frequency and width depend on the impedance of the environment. Moreover, if we want to optimize the coupling between the  $LC$  oscillator and this impedance we need to design coupling capacitors to reduce the capacitances to ground and increase the coupling capacitances.

### 3.3 Coupling of a transmon qubit to a linearized array

Following what we did in Section 3.1 we can obtain the expression for the coupling between a transmon qubit and a linearized array of SQUIDS. We consider the same

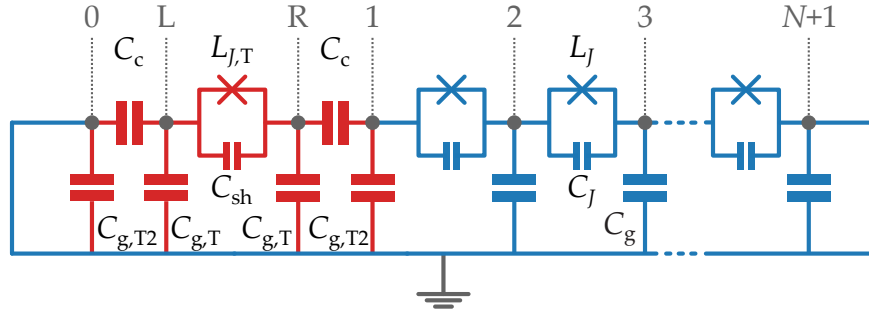


Figure 3.8 – Circuit diagram of the sample measured in the experiment, a transmon qubit (red) capacitively coupled to an array of SQUIDS (blue). In gray the different islands in the circuit are given. Both ends of the circuit are shunted to ground.

circuit as the one in the experiment, but the method presented here can be used in principle with any circuit. The circuit diagram is given in Fig. 3.8. We replaced the  $50\ \Omega$  input and output pads by shorts to ground. As we have seen in Section 2.2.2, this is a good approximation.

The Hamiltonian of the system can be written as

$$\mathcal{H} = \frac{(2e)^2}{2} \sum_{l,s \in L,R,1,2,\dots} \hat{n}_l \hat{C}_{l,s}^{-1} \hat{n}_s + \frac{\varphi_0^2}{2} \sum_{l,s \in L,R,1,2,\dots} \hat{\varphi}_l \hat{L}_{l,s}^{-1} \hat{\varphi}_s - E_{J,T} \cos(\hat{\varphi}_R - \hat{\varphi}_L). \quad (3.29)$$

Matrices  $\hat{C}$  and  $\hat{L}$  are the inductance and capacitance matrices of the circuit. They



given by

$$E_{C,T} = (2e)^2 \left\{ \left[ \widehat{C}^{-1} \right]_{L,L} + \left[ \widehat{C}^{-1} \right]_{R,R} - 2 \left[ \widehat{C}^{-1} \right]_{R,L} \right\}. \quad (3.34)$$

The coupling between  $\widehat{n}_T$  and  $\widehat{n}_l$  is given by the term  $\nu_l$  defined by

$$\nu_l = (2e)^2 \left\{ \left[ \widehat{C}^{-1} \right]_{R,l} - \left[ \widehat{C}^{-1} \right]_{L,l} \right\}. \quad (3.35)$$

In order to obtain the values for the  $g_k$  of the system we first need to diagonalize the array of SQUIDS using the method described in Section 2.2.2. In this case, we need to remove the sites in  $\widehat{C}^{-1}$  and  $\widehat{L}^{-1}$  that contain any of the transmon islands, L or R. Then we write the Cooper pair number operator and the superconducting phase operator as a function of creation and annihilation operators,

$$\widehat{n}_n = \frac{1}{2e} \sqrt{\frac{\hbar}{2}} \sum_{k=1}^N \zeta_{n,k} (a_k + a_k^\dagger), \quad \widehat{\varphi}_n = \frac{1}{\varphi_0} i \sqrt{\frac{\hbar}{2}} \sum_{k=1}^N \pi_{n,k} (a_k - a_k^\dagger). \quad (3.36)$$

We need to keep in mind that in this case the matrices  $\zeta$  and  $\pi$  are obtained from matrices  $\widehat{C}^{-1}$  and  $\widehat{L}^{-1}$  without the transmon islands. With this definition the coupling term is given by

$$\widehat{n}_T \sum_{l=1}^N \nu_l \widehat{n}_l = \widehat{n}_T \sum_{k=1}^N \tilde{g}_k (a_k + a_k^\dagger), \quad (3.37)$$

where the  $\tilde{g}_k$  are given by

$$\tilde{g}_k = \sqrt{\frac{\hbar}{2}} \sum_{l=1}^N \nu_l \zeta_{l,k} \quad (3.38)$$

By using the expression in Eq. (3.16) for the transmon qubit charge operator we obtain

$$g_k = \sqrt{\frac{1}{2}} \left( \frac{E_{J,T}}{E_{C,T}} \right)^{\frac{1}{4}} \tilde{g}_k. \quad (3.39)$$

Here  $E_{J,T}$  is the Josephson energy obtained from the Self Consistent Harmonic Approximation (SCHA) for the sample in the experiment which is  $E_{J,T} = 9.0$  GHz at zero flux. The charging energy is obtained from the estimated capacitances in the circuit,  $E_{C,T} = 2.4$  GHz, see Chapter 7. In Fig. 3.9  $g_k$  is plotted as a function of the modes in the array  $\omega_k$ . We used the array parameters and the qubit capacitances for the real sample, see Tables 2.1 and 3.1 with  $N = 4700$ . As we see, for low frequencies the coupling grows as  $\sqrt{\omega_k}$ , gray dashed line. This is expected for an ohmic environment. However, at high frequencies the coupling decays due to the effect of the capacitances to ground of the system and the plasma frequency of the array. In blue we give the frequency range where we can measure the hybridization between the transmon qubit and the modes of the array. As we can see, with this sample design we get a coupling strength between 200 MHz and 150 MHz for the transmon-array coupling. This gives a  $2g_k$  which is comparable to the FSR of

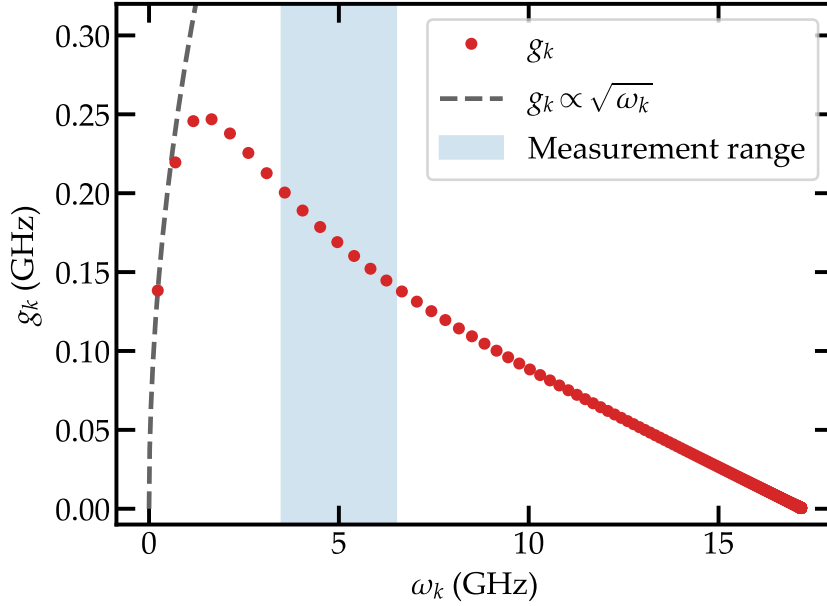


Figure 3.9 – The coupling strength  $g_k$  as a function of the mode frequency  $\omega_k$  for the parameters of the measured sample. The gray dashed line shows the  $\sqrt{\omega_k}$  scaling characteristic of an ohmic bath. In blue the frequency range where the measurements are performed is shown.

the environment,  $\text{FSR} \sim 400$  MHz. It is interesting to obtain  $g_k$  for different values of the capacitances to ground,  $C_{g,T}$  and  $C_{g,T2}$ . In Fig. 3.10 we compare three cases, the one in the experiment, one with  $C_{g,T} = 0$  and one with  $C_{g,T} = C_{g,T2} = 0$ . As shown in Fig. 3.10 these capacitances reduce the coupling drastically. We still see the effect of the plasma frequency in the coupling strength since  $g_k$  decays for  $\omega_k$  close to the plasma frequency. However it is clear, as shown previously in Section 3.2.2, that the most limiting factor are the capacitances to ground that shunt the environment.

### 3.4 The transmon phase shift

As previously discussed, the coupling strength  $g_k$  between each mode and the transmon qubit are obtained from the capacitance and inductance matrix of the circuit. However this requires the diagonalization of the Hamiltonian in Eq. (3.33) which is not possible given its size. For  $m = 10$  modes with  $n = 4$  photons each and a transmon qubit with  $q = 3$  levels the size of the Hamiltonian is already  $3 \times 10^4$ . Therefore we follow a different approach. The coupling strength between the array and the transmon qubit can be described by a phase shift amplitude induced by the transmon qubit on the modes of the array. We call this effect *the transmon phase shift*. This phase shift informs on the strength of the coupling between the transmon and the array as well as the number of modes coupled to the transmon.

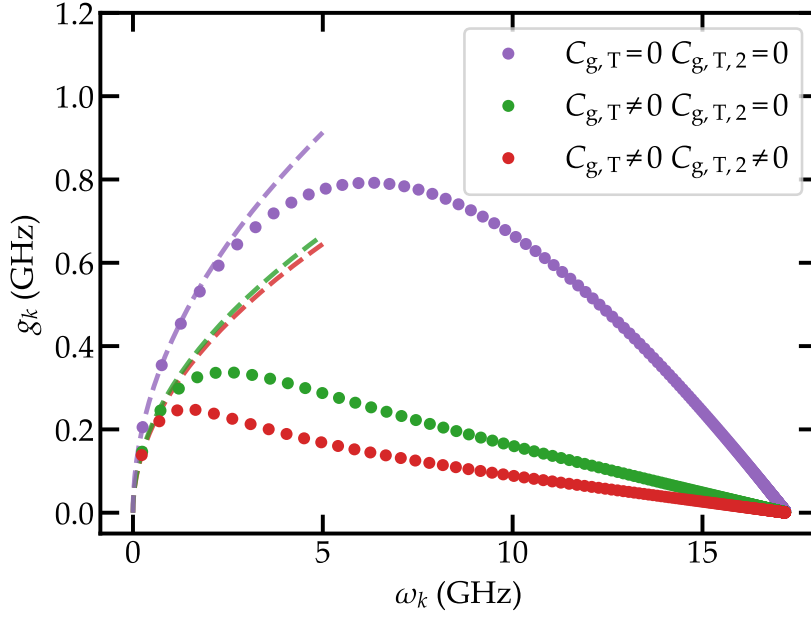


Figure 3.10 – Coupling strength  $g_k$  as a function of the mode frequency  $\omega_k$  for three cases,  $(C_{g,T} \neq 0, C_{g,T2} \neq 0)$ ,  $(C_{g,T} \neq 0, C_{g,T2} = 0)$  and  $(C_{g,T} = 0, C_{g,T2} = 0)$ . The dashed lines represent the scaling  $g_k \propto \sqrt{\omega_k}$ .

### 3.4.1 Derivation of the expression

First we need to obtain the eigenmodes of the circuit as a function of the circuit parameters. We start with the lumped element model for the real system, see Fig. 3.11 (a). It consists of a transmon qubit (red) coupled to an array of SQUIDS (blue). Both ends of the circuit are terminated with two  $Z_0 = 50 \Omega$  ports. As a first step we linearize the system. We can treat the array directly as a linear system due to its large  $E_J/E_C$  ratio,  $E_J/E_C \sim 8000$  in the experiment. Regarding the transmon qubit, in order to linearize it we perform the SCHA as explained in Section 2.3. This allows to replace the Josephson junction in the transmon qubit by a linear inductor of inductance  $L_{J,TS} = \varphi_0^2/E_S$ . Another approximation we make is to replace the  $50 \Omega$  port on the left by a short to ground. This is a valid approximation as explained in Section 2.2.2. Finally, in order to obtain analytical expressions, we assume that the array is semi-infinite therefore working in the thermodynamic limit. In conclusion, we go from the circuit in Fig. 3.11 (a) to the circuit in Fig. 3.11 (b) by embedding the phase fluctuations and the nonlinear potential of the transmon in an effective inductance.

We can obtain the equations of motion from the Euler-Lagrange equation in Eq. (2.49). However, we rewrite this expression in the following way to avoid having to invert the capacitance matrix  $\hat{C}_0$ <sup>30</sup>,

$$\hat{L}_0^{-1} \vec{\Phi} = \omega^2 \hat{C}_0 \vec{\Phi}. \quad (3.40)$$



In this expression  $a$  is the length of the unit cell of the array,  $\varphi_0$  is the reduced flux quantum,  $N$  is the amplitude of the wave and  $k$  is the wave number of a wave that propagates in the chain at a frequency  $\omega$ . We include a phase shift  $\phi$  that is sensitive to the transmon at one end of the chain. From this phase shift  $\phi$  we are going to obtain all the information about the coupling between the transmon and the array as well as about the transmon itself.

The wave number  $k$  can be obtained from the dispersion relation for a bare array, Eq. (3.43). For a detailed derivation of this expression see Appendix A.4.1.

$$k = \frac{2}{a} \operatorname{arccot} \sqrt{\left(\frac{4C_J}{C_g} + 1\right) \left[\left(\frac{\omega_p}{\omega}\right)^2 - 1\right]}. \quad (3.43)$$

Here  $\omega_p = 1/\sqrt{L_J(C_J + C_g/4)}$  is the plasma frequency of the array. In order to obtain the phase shift  $\phi$  as a function of the circuit parameters we need to solve the equations in Eq. (3.40) involving the transmon islands. These are

$$\frac{1}{L_{J,TS}} (\Phi_L - \Phi_R) = \omega^2 (C_1 \Phi_L - C_{sh} \Phi_R), \quad (3.44)$$

$$\frac{1}{L_{J,TS}} (\Phi_R - \Phi_L) = \omega^2 (-C_{sh} \Phi_L + C_1 \Phi_R - C_c \Phi_1), \quad (3.45)$$

$$\frac{1}{L_J} (\Phi_1 - \Phi_2) = \omega^2 (-C_c \Phi_R + C_2 \Phi_1 - C_J \Phi_2). \quad (3.46)$$

First from Eqs. (3.44) and (3.45) we eliminate  $\Phi_L$  and obtain  $\Phi_R$  as a function of  $\Phi_1$ .

$$\Phi_R = \frac{C_c [\omega^2 C_1 - 1/L_{J,TS}]}{(C_1 - C_{sh}) [(C_1 + C_{sh}) \omega^2 - 2/L_{J,TS}]} \Phi_1 \quad (3.47)$$

Substituting this into Eq. (3.46) and using the expression for  $k$  in Eq. (3.43) we arrive to

$$\frac{C_g}{2[1 - \cos(ka)]} (\Phi_1 - \Phi_2) = C_{\text{eff}} \Phi_1, \quad (3.48)$$

where  $C_{\text{eff}}$  is given by

$$C_{\text{eff}}(\omega) = C_2 - C_J - \frac{C_c^2 (\omega^2 C_1 - 1/L_{J,TS})}{(C_1 - C_{sh}) [(C_1 + C_{sh}) \omega^2 - 2/L_{J,TS}]}. \quad (3.49)$$

In Appendix A.4.2 the different steps followed to arrive to these expressions are given. This effective capacitance  $C_{\text{eff}}$  is related to the impedance to ground seen by the first site of the chain, island 1. This is directly related to the linearized transmon qubit. Depending of the parameters of the qubit this capacitance will have a different value.

Using the mode definition in Eq. (3.42) for  $\Phi_1$  and  $\Phi_2$  in Eq. (3.48) we obtain

$$\tan \phi = \left[1 - \frac{2C_{\text{eff}}(\omega)}{C_g}\right] \tan\left(\frac{ka}{2}\right). \quad (3.50)$$



Finally using again the expression for  $k$  in Eq. (3.43) we get to the final expression for the phase shift  $\phi$ ,

$$\tan \phi = \left[ 1 - \frac{2C_{\text{eff}}(\omega)}{C_g} \right] \sqrt{\frac{C_g}{C_g + 4C_J}} \frac{1}{\sqrt{\left(\frac{\omega_p}{\omega}\right)^2 - 1}}. \quad (3.51)$$

The first term including  $C_{\text{eff}}$  is related to the transmon qubit. It is the only part in the expression where the transmon qubit parameters appear. The second term is related to the array and does not depend on the transmon qubit parameters.

### 3.4.2 Effect of the transmon in the mode phase

The value of  $\phi$  is directly related to the presence of the transmon qubit. We can see that if  $L_{J,T,S} \rightarrow \infty$  in Eq. (3.49) the effective capacitance  $C_{\text{eff}}$  does not depend on frequency anymore. It is given by the effective capacitance to ground formed by capacitors  $C_{g,T2}$ ,  $C_{g,T}$ ,  $C_c$  and  $C_{\text{sh}}$  in Fig. 3.11 (b). This makes sense because in this regime the transmon does not contribute to the dynamics of the system.

Experimentally we can tune the transmon inductance  $L_{J,T,S}$  via an external magnetic flux  $\Phi_T$  by using a SQUID. For  $\Phi_T = \Phi_0/2$  the transmon inductance goes to infinity and it decouples from the array. For  $\Phi_T \neq \Phi_0/2$  it has a finite inductance and couples to the chain via  $C_{\text{eff}}$ . To measure the influence of the transmon qubit in the circuit we define the transmon phase shift  $\delta\phi$  as

$$\delta\phi = \phi(\Phi_T \neq \Phi_0/2) - \phi(\Phi_T = \Phi_0/2). \quad (3.52)$$

We can get some insight into the meaning of  $\delta\phi$  by comparing the system eigenmodes for  $\Phi_T = \Phi_0/2$  and  $\Phi_T \neq \Phi_0/2$ . In Fig. 3.12 we plot the eigenmodes given by Eq. (3.42) at the transmon frequency for the two different cases. In blue we plot the uncoupled eigenmode ( $\Phi_T = \Phi_0/2$ ) and in red the coupled one ( $\Phi_T \neq \Phi_0/2$ ). It is clear that the presence of the transmon qubit induces a phase shift  $\delta\phi$  in the eigenmodes of the system.

It is expected for the phase shift  $\delta\phi$  to be smaller when the mode frequency is far detuned from the transmon frequency. In Fig. 3.13 (a) the phase shift is plotted as a function of the mode frequency. It is a step-like function that goes from 0 to  $\pi$ . This behavior can be understood if we observe the eigenmodes of the system for different detunings  $\delta = \omega_T - \omega_k$ , see Fig. 3.13 (b). The lower plot shows an eigenmode with a lower frequency than  $\omega_T$  (orange dot in Fig. 3.13 (a)). As it can be seen, the coupled and uncoupled modes overlap, i.e. the phase shift  $\phi$  is almost zero. However, whenever the mode frequency becomes closer to the transmon frequency a phase shift appears (middle plot and green dot in Fig. 3.13 (a)). At this point the hybridization between the transmon and the modes in the array is maximum. Finally, for modes with frequencies above the transmon frequency the transmon phase shift converges to  $\pi$  (top plot and purple dot in Fig. 3.13 (a)). The two modes in the upper plot in Fig. 3.13 (b) are exactly the same mode but with a  $\pi$  shift. Therefore for frequencies far above the transmon qubit frequency we recover the bare modes of the array. This shows intuitively that the width of the step-like function of  $\delta\phi(\omega)$  is a measure of the number of modes hybridized with the transmon.

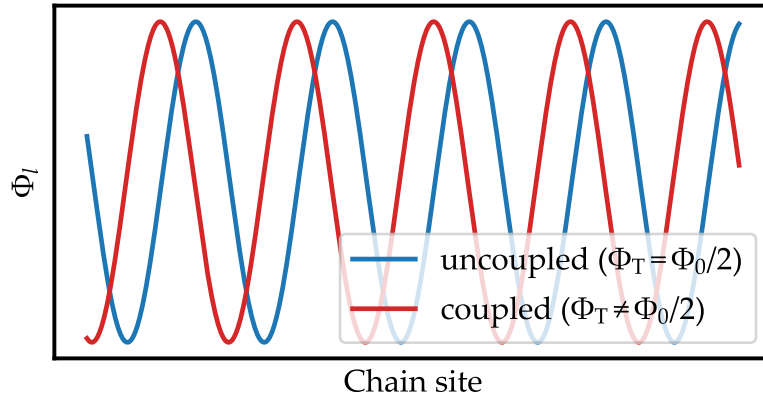


Figure 3.12 – Eigenmode of the system for  $\Phi_T = \Phi_0/2$  (blue) and  $\Phi_T \neq \Phi_0/2$  (red). The parameters for the simulation are given in Tables 2.1 and 3.1 taking  $L_0 = L_{J,T,S}$ .

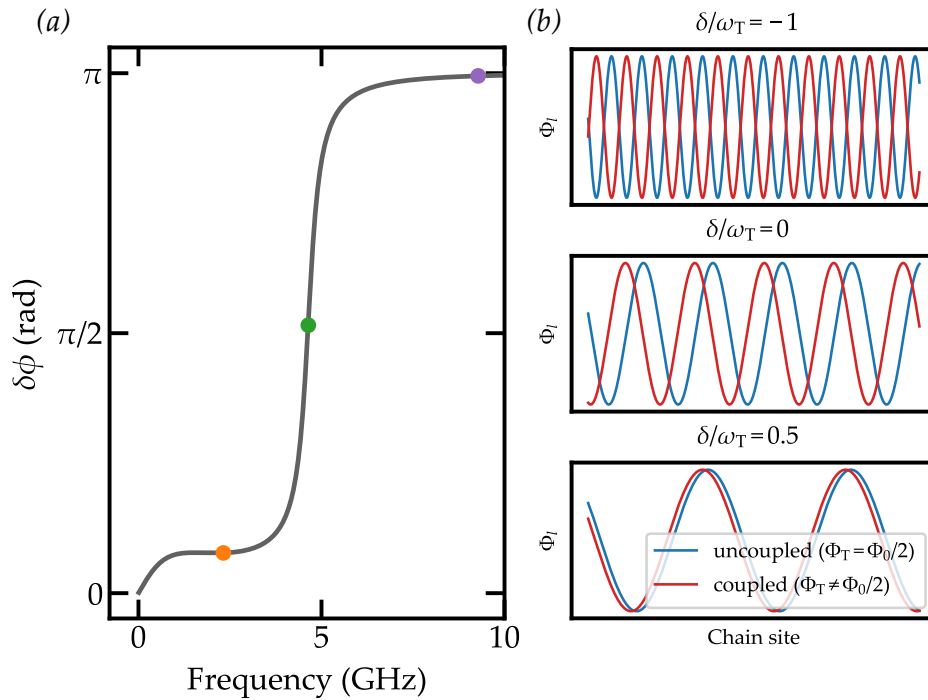


Figure 3.13 – (a) Phase shift  $\delta\phi$  as a function of frequency. Each of the dots correspond to a mode in (b). (b) Comparison between  $\Phi_T = \Phi_0/2$  (blue) and  $\Phi_T \neq \Phi_0/2$  (red) for several detunings  $\delta$ .

In Fig. 3.14 we plot  $\delta\phi$  as a function of frequency for several values of the coupling capacitance  $C_c$ . We change  $L_{J,T,S}$  to keep the transmon frequency  $\omega_T$  constant. It is clear that by increasing  $C_c$  the width of the phase shift becomes larger, i.e. the transmon influences modes far away from its resonance frequency. This is a clear signature of the increment in the coupling.

Another interesting feature is the low frequency tail of  $\delta\phi(\omega)$ . This tail is a combination of two effects: a large coupling capacitance  $C_c$  and an array with high characteristic impedance  $Z_0 = \sqrt{L_J/C_g}$ . At frequencies far detuned from the resonance frequency of the transmon there should be no phase shift. The coupling capacitors  $C_c$  have a high impedance at this frequencies and therefore the whole transmon qubit behaves as an open. This can be seen from the Taylor expansion of  $C_{\text{eff}}$  for low frequencies,

$$C_{\text{eff}} = C_c + C_{g,T2} - \frac{C_c^2}{2(C_c + C_{g,T})} + \frac{1}{4}C_c^2 L_{J,T,S} \omega^2 + \tilde{C}(\omega). \quad (3.53)$$

Here  $\tilde{C}(\omega) \leq 3$  fF for frequencies up to 2 GHz. It is clear that at low frequencies if  $C_c$  is small then  $C_{\text{eff}}$  is independent of frequency and  $\delta\phi = 0$ . However when the value of  $C_c$  is increased its impedance is reduced and  $C_{\text{eff}}$  depends on frequency via the last term proportional to  $L_{J,T,S}$ . Therefore  $\delta\phi \neq 0$ . However for this to happen, we need to impedance match the transmon qubit to the array. Otherwise all the signal would be reflected at the transmon-array interface and no phase shift would occur.

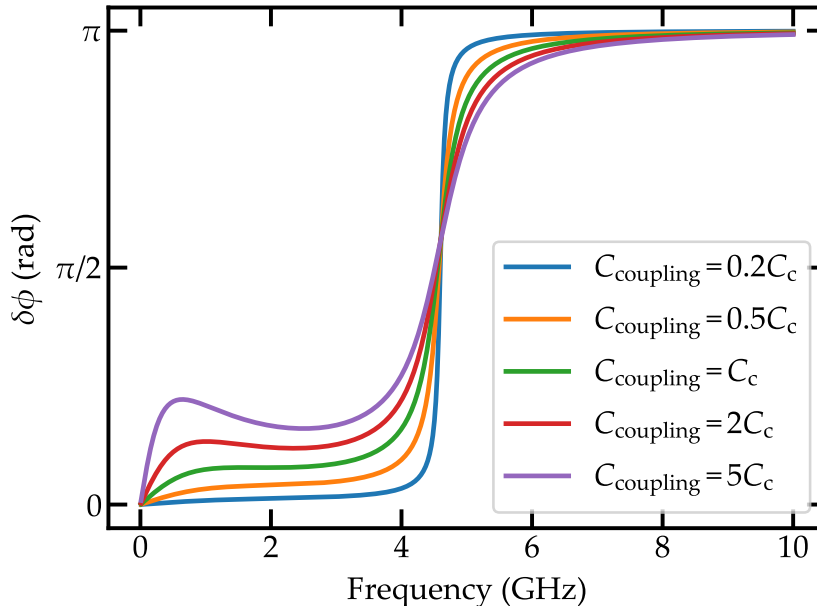


Figure 3.14 – Phase shift  $\delta\phi$  for several coupling capacitances. The value of  $C_c = 119$  fF is the one of the experiment. The value of  $L_{J,T,S}$  is changed to keep the same resonance frequency for all curves.

### 3.4.3 Link between the transmon phase shift and the relative frequency shift

Until now we have shown how we can obtain qualitative information about the coupling between the array and the transmon qubit via the phase shift that the latter induces in the eigenmodes of the system. Measuring this phase shift directly would be a difficult task. That is why in this section we are going to link the phase shift to an easily measurable quantity, the *relative frequency shift*.

#### *Intuitive explanation*

If we come back to the plot in Fig. 3.12 we see that the mode shifts in the  $x$ -axis as a function of  $E_{J,T}$  due to a phase shift. However, the frequency of the mode is not altered. This is possible because the model we used to obtain these curves assumes a semi-infinite chain, i.e. it can propagate modes at all frequencies. In other words, all wave numbers  $k$  are allowed. However, when dealing with a finite size chain this cannot happen, only the modes with specific  $k_n$  can propagate. Therefore the phase shift induces a shift in the resonance frequency of the mode. In order

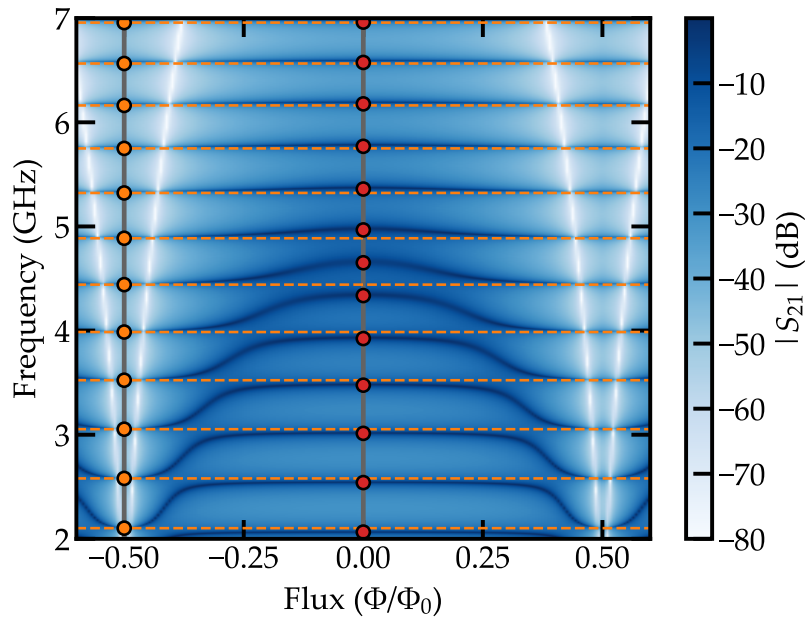


Figure 3.15 – Explanation of the relative frequency shift. The color map gives the transmission of the system obtained with ABCD matrices and the parameters in Tables 2.1 and 3.1. In this case we use  $N = 4700$ . The orange dots show the modes at  $\Phi_T = -\Phi_0/2$ . The red dots show the modes at  $\Phi_T = 0$ . The horizontal dashed lines are just a guide to the eye for the bare spectrum, i.e. if the transmon qubit were not present.

to measure this frequency shift at  $\Phi_T = 0$  first we measure the frequency of the modes at  $\Phi_T = \Phi_0/2$  as a reference. Then we compare the frequency of the modes

at this flux with the frequency of the modes at  $\Phi_T = \Phi_0/2$  (in the example we take  $\Phi = -\Phi_0/2$  which is the same because the system is periodic). As it can be seen in Fig. 3.15, due to the presence of the transmon qubit the modes are shifted in frequency. We define the relative frequency shift as

$$\delta\phi_n = \pi \frac{\omega_n(\Phi_0/2) - \omega_n(\Phi_T)}{\omega_n(\Phi_0/2) - \omega_{n-1}(\Phi_0/2)}. \quad (3.54)$$

This quantity goes to zero for  $\omega \ll \omega_T$  and to  $\pi$  for  $\omega \gg \omega_T$ . It is straightforward to obtain this quantity experimentally. As shown in Fig. 3.15 we only need to obtain the eigenfrequencies at  $\Phi_T = -\Phi_0/2$  and  $\Phi_T \neq \Phi_0/2$  and introduce these values in Eq. (3.54). We will show now that this quantity is equivalent to the phase shift given in Eqs. (3.51) and (3.52).

*Proof*

First we assume that the array is grounded to the right hand side although this is not important in the thermodynamic limit. Second, we introduce the transmon at the left end modifying the modes of the system. They are given by

$$\varphi_n \propto \cos(k_n a l - \phi_n) \quad \text{for } l = 1, 2, 3, \dots, N. \quad (3.55)$$

Here the  $\phi_n$  is the phase shift introduced by the transmon in mode  $n$ . As the array is grounded at site  $l = N$ , we obtain the following expression for the  $k_n$ ,

$$k_n a N - \phi_n = \pi(n - 1/2) \rightarrow k_n a = k_n^0 a + \frac{\phi_n}{N}, \quad (3.56)$$

where the  $k_n^0$  is the wavenumber for the eigenmode  $n$  of the bare array. In order to obtain the different frequencies in Eq. (3.54) we consider a dispersion relation of the form  $\omega_n = \omega(k_n a)$ . For sufficiently large  $N$  we can expand the dispersion relation around  $k_n^0 a$ ,

$$\omega_n = \omega(k_n^0 a) + \frac{\phi_n}{N} \left. \frac{\partial \omega(k a)}{\partial(k a)} \right|_{k=k_n^0} + \mathcal{O}(N^{-2}). \quad (3.57)$$

Similarly we can expand  $\omega_{n-1}$  around  $k_n^0 a$ . First we write

$$\omega_{n-1} = \omega\left(k_n^0 a - \frac{\pi}{Na} + \frac{\phi_{n-1}}{N}\right). \quad (3.58)$$

Here we used the fact that  $k_{n-1}^0 = k_n^0 - \pi/Na$ . Now if we expand this expression around  $k_n^0 a$  we obtain

$$\omega_{n-1} = \omega(k_n^0 a) + \left(\frac{\phi_{n-1}}{N} - \frac{\pi}{Na}\right) \left. \frac{\partial \omega(k a)}{\partial(k a)} \right|_{k=k_n^0} + \mathcal{O}(N^{-2}). \quad (3.59)$$

Keeping in mind that we are obtaining these expressions with an error of  $\mathcal{O}(N^{-2})$  we can write  $\phi_{n-1} = \phi_n$  introducing an error that can be ignored for large  $N$ . We

can therefore write Eq. (3.59) in the following form

$$\omega_{n-1} = \omega_n - \frac{\pi}{Na} \left. \frac{\partial \omega(k)}{\partial(ka)} \right|_{k=k_n^0}. \quad (3.60)$$

We finally obtain the terms in Eq. (3.54),

$$\omega_n(\Phi_T = \Phi_0/2) = \omega(k_n^0 a) + \frac{\phi_n(\Phi_T = \Phi_0/2)}{N} \left. \frac{\partial \omega(k)}{\partial(ka)} \right|_{k=k_n^0} \quad (3.61)$$

$$\omega_n(\Phi_T \neq \Phi_0/2) = \omega(k_n^0 a) + \frac{\phi_n(\Phi_T \neq \Phi_0/2)}{N} \left. \frac{\partial \omega(k)}{\partial(ka)} \right|_{k=k_n^0} \quad (3.62)$$

$$\omega_{n-1}(\Phi_T = \Phi_0/2) = \omega_n(\Phi_T = \Phi_0/2) - \frac{\pi}{N} \left. \frac{\partial \omega(k)}{\partial(ka)} \right|_{k=k_n^0}. \quad (3.63)$$

Introducing these three equations into Eq. (3.54) and recalling that  $\phi_n = \phi(\omega_n)$  we obtain the expression in Eq. (3.52). Therefore for sufficiently large  $N$  the phase shift and the relative frequency shift are the same. To get an idea of how large  $N$  needs to be we plot in Fig. 3.16 the expression for the frequency shift in Eq. (3.54) for different  $N$  values. The points are obtained from  $ABCD$  matrices simulations and give a step-like function similar to the analytical transmon phase shift  $\delta\phi$ . From these curves we can directly see the number of modes coupled to the linearized transmon. These are the points in  $\delta\phi_n$  in the step, between the two flat regions. As it can be seen, as  $N$  increases we have more modes coupled.

In addition, we observe that the frequency shift approaches the analytical expression in Eq. (3.52) for an infinite array. It is important to point out that the shape of the frequency shift  $\delta\phi_n$  is already the same as the one of the transmon phase shift  $\delta\phi$  for  $N = 5000$ . The only difference is a shift in the transmon qubit frequency. As will be shown later, we are mainly interested in the width  $\omega_T$  of the transmon qubit and we can assume that for the array in the experiment ( $N = 4700$ ) we are already in the thermodynamic limit.

#### 3.4.4 Relation between the phase shift and the impurity response function

Usually what is measured in Circuit QED experiments is the spectroscopic line shape  $S(\omega)$  of the qubit, see e.g. Schuster et al.<sup>12</sup>.  $S(\omega)$  gives the qubit response to a driving field of frequency  $\omega$ . This line shape can be obtained via the Fourier transform of the charge-charge, charge-phase and phase-phase correlation functions. In this section we link the transmon phase shift  $\delta\phi$  to its spectroscopic line shape. To do so we are going to focus on the correlation function of the superconducting phase given by

$$C_{[\varphi, \varphi]} = \langle [\widehat{\varphi}_T(t), \widehat{\varphi}_T(0)] \rangle. \quad (3.64)$$

Its Fourier transform gives the spectral density  $\tilde{C}_{[\varphi, \varphi]}$ ,

$$\tilde{C}_{[\varphi, \varphi]} = \frac{2E_S}{\hbar\omega_T} \text{Re} \int_0^\infty \frac{dt}{2\pi} e^{i\omega t} \langle [\widehat{\varphi}(t), \widehat{\varphi}(0)] \rangle, \quad (3.65)$$

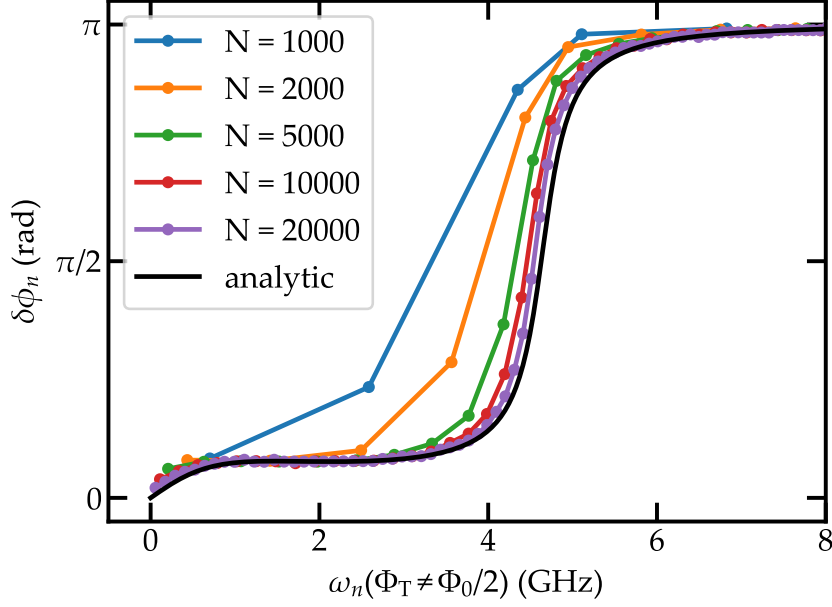


Figure 3.16 – Frequency shift for different number of sites in the array  $N$ . The points are obtained from ABCD matrices simulations. The solid black line shows the phase shift  $\delta\phi$  in the thermodynamic limit given by Eq. (3.52).

where we chose the unitless prefactor for later convenience.

In order to obtain this quantity we turn to the quantum mechanical problem. With each mode  $\omega$  we define a canonical creation and annihilation operator  $b_\omega$  and  $b_\omega^\dagger$ . They are related to the phase operator in each of the islands as

$$\hat{\varphi}_l = \frac{1}{\sqrt{2}} \int_0^{\omega_p} d\omega \varphi_l(\omega) (b_\omega + b_\omega^\dagger). \quad (3.66)$$

The profile  $\varphi_l(\omega)$  is given in Eq. (3.42). The spectral density  $\tilde{C}_{[\varphi,\varphi]}$  for this operator is given by (see Appendix Section A.4.3)

$$\tilde{C}_{[\varphi,\varphi]} = \frac{E_S}{\omega_T} \varphi(\omega)^2. \quad (3.67)$$

We define the operator  $\hat{\varphi}_T$  related to the transmon dynamics,

$$\hat{\varphi}_T = \hat{\varphi}_R - \hat{\varphi}_L. \quad (3.68)$$

In this case the spectral density is given by

$$\tilde{C}_{[\varphi,\varphi]} = \frac{E_S}{\omega_T} (\varphi_R(\omega) - \varphi_L(\omega))^2. \quad (3.69)$$

We can obtain  $\varphi_R(\omega) - \varphi_L(\omega)$  using Eqs. (3.44) to (3.46),

$$\varphi_R(\omega) - \varphi_L(\omega) = N \frac{L_{J,T,S} C_c \omega^2}{L_{J,T,S} (C_1 + C_{sh}) \omega^2 - 2} \cos \phi. \quad (3.70)$$

The only missing part is the normalization factor  $N$ . It can be obtained (see Appendix A.4.3) imposing the following normalization condition in the modes  $\varphi_l(\omega)$ ,

$$\sum_{l,s=L,R,1,2,\dots} \varphi_0^2 \varphi_l(\omega) \hat{L}_0^{-1}[l,s] \varphi_s(\omega') = \omega \delta(\omega - \omega'). \quad (3.71)$$

It is given by

$$N = \sqrt{\frac{\hbar\omega}{\pi E_J [1 - \cos(ka)]} \frac{\partial ka}{\partial \omega}}. \quad (3.72)$$

In Fig. 3.17 we compare the spectral density  $\tilde{C}_{[\varphi,\varphi]}$  with the derivative of  $\delta\phi$ . As it can be seen they overlap near the transmon resonance frequency. This means that the derivative of  $\delta\phi$  is a good estimate of  $\Gamma_T$  and  $\omega_T$ .

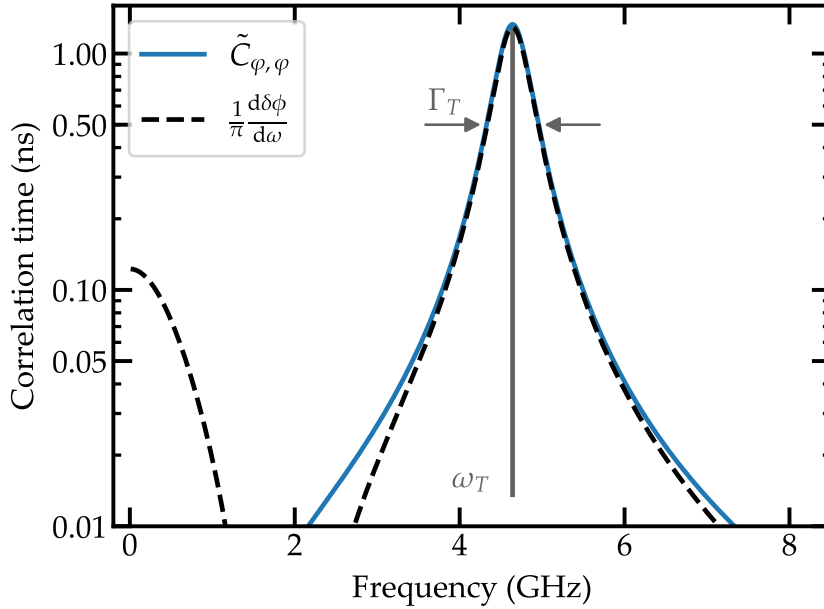


Figure 3.17 – Comparison between the spectral density  $\tilde{C}_{[\varphi,\varphi]}$  and the derivative of the transmon phase shift  $\delta\phi$ . In gray the transmon resonance frequency  $\omega_T$  and width  $\Gamma_T$  are given. For the calculation the real sample parameters were used.





# Circuit design and fabrication

# 4

This chapter is dedicated to the design and fabrication of the samples presented in this work. First we give a general description of the electron beam lithography. We introduce the Bridge Free Fabrication technique used to produce Josephson junctions and discuss the major technical problems that we met in the lithography process and their solutions. Second we present a detailed study of the reproducibility of the fabrication process and the aging of the Josephson junctions. Finally we discuss the circuit geometry and the simulation of the circuit parameters.

## 4.1 *Circuit fabrication with e-beam lithography*

The electron beam lithography (e-beam lithography) consists on using an electron beam to write a structure on top of a substrate. First the sample is covered with a resist. Then the resist is exposed to the electron beam to create the desired pattern. Afterward it is immersed in a developer. This gives the desired mask. Then some metal is deposited over the mask and finally, in a process known as *lift-off*, the resist is removed leaving the desired structure on top of the substrate. For a detailed description of the lithography process refer to Levinson<sup>91</sup>. In this work, in order to speed up the fabrication process, all samples were fabricated in a single step of e-beam lithography.

The e-beam writer used during this work is the model *nB5* from [NANOBEAM LTD](#). It is shown in Fig. 4.1. It was acquired by the Néel Institute at the beginning of my PhD. An important part of my PhD work has been to develop all the fabrication process for this e-beam writer. This includes performing dose tests for the arrays of SQUIDS and capacitors and solving focus problems.

### 4.1.1 *The Bridge Free Fabrication technique*

Among the different structures present in our superconducting circuits, Josephson junctions are the most important ones. Josephson junction fabrication requires that two metal layers overlap with a thin oxide barrier in between.

In order to have a high control over the barrier thickness the bottom layer needs to be oxidized in a controlled way. This means that the sample must be kept under vacuum between the first and the second metal depositions to avoid native oxidation of the metal or external pollution. The best way to do this is to perform the two metal depositions using the same mask, i.e. to perform only one lithography step. In order to do so an angle evaporation is needed. First one

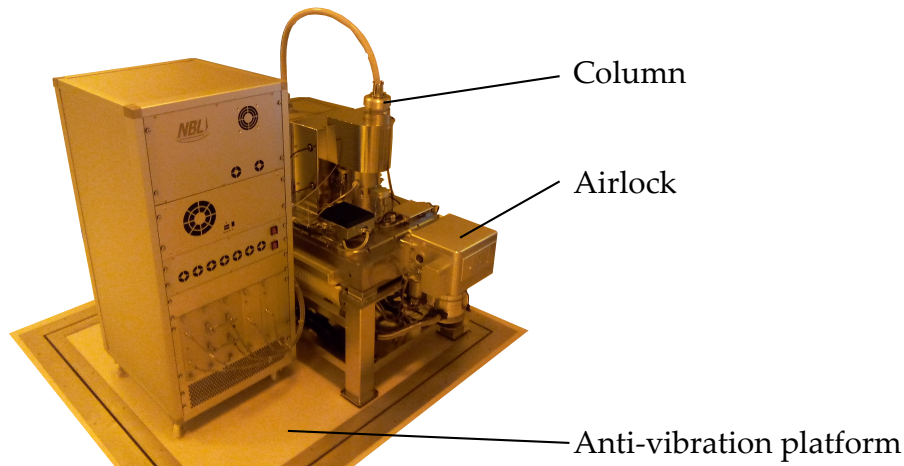


Figure 4.1 – E-beam writer used in this work. Picture taken at the Nanofab cleanroom at the Néel Institut.

aluminum layer is deposited with one angle, then it is oxidized and finally a second layer is deposited with the opposite angle.

Two resist layers are used, PMMA-MAA as the bottom layer and PMMA as the top layer. The key point is that the bottom layer is more sensitive to the electrons than the top layer. As shown in Fig. 4.2 (a) when the electrons hit the substrate they are scattered in several directions. This scattering depends on the acceleration voltage used. Higher voltage reduce the scattering significantly<sup>91</sup>. Due to the scattering the electrons affect not only the exposed area but its surroundings. This phenomenon is called *proximity effect*. As illustrated in Fig. 4.2 (b) due to the different sensitivity the bottom resist is more affected than the top one. This creates an *undercut*  $\delta_0$  that is crucial for Josephson junction fabrication. In the Niemeyer-Dolan technique<sup>92,93</sup> a suspended bridge of resist is created (see Fig. 4.2 (b) left). It is used as a mask to fabricate Josephson junctions. This process is illustrated in Fig. 4.3. First a metal deposition is performed at one angle  $\theta$ . Then this metal is oxidized in a pure oxygen atmosphere. Finally a second deposition is performed with the opposite angle minus  $\theta$ . Thanks to the suspended bridge a junction is created in the middle.

Despite its wide use this technique has three major drawbacks. First, due to the suspended bridge, the substrate area where the junction is fabricated cannot be cleaned beforehand. This means that the metal is deposited on a surface with some residual resist<sup>94</sup>. Second, there is always a shadow pattern at both sides of the junction, Fig. 4.3 (c). This metallic islands might create undesired charging effects. This might be a concern when fabricating complex structures as the arrays of SQUIDS used in this work. Finally, for large junctions the bridge of resist becomes quite fragile and might collapse. In order to avoid these issues we use a different technique, the Bridge Free Fabrication (BFF) technique<sup>95</sup>. As the previous one this technique uses two resist layers. However, in this case no bridge is involved.

The idea of the BFF is to make use of an asymmetry in the undercut whenever we want to keep only one of the two metal depositions. This means that a controlled undercut  $\delta$  is needed. As explained before, by using a high acceleration voltage we reduce the proximity effect. This reduces the possibility of undesired undercut  $\delta_0$ . We divide the structure in two layers, one written at high dose and the other written at low dose, see Fig. 4.4 (a). After the development, thanks to

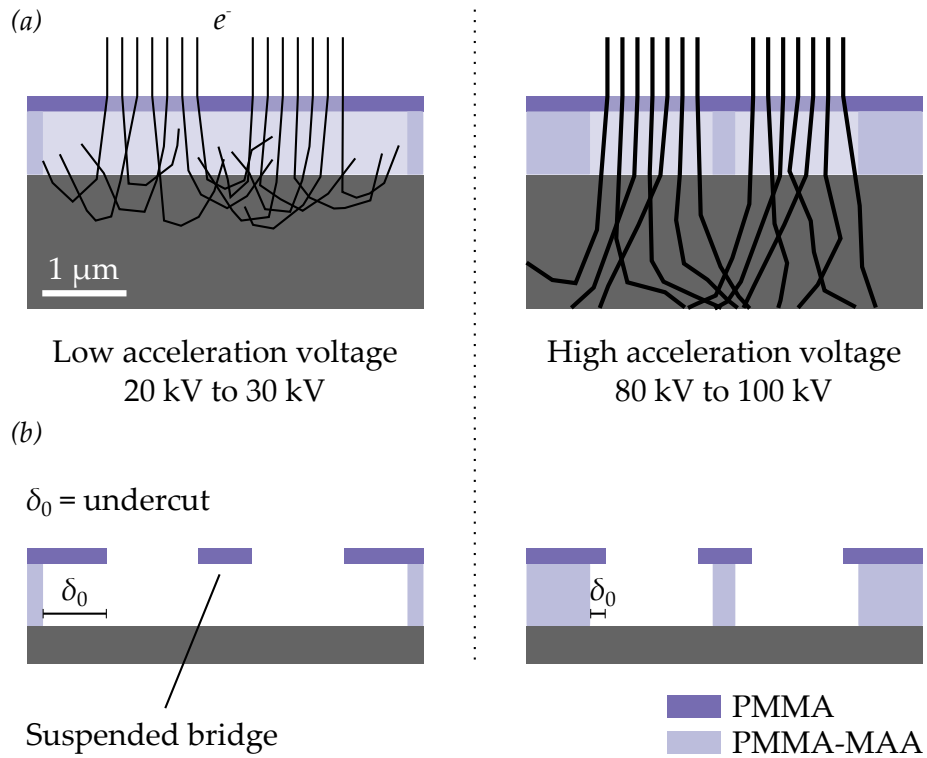


Figure 4.2 – (a) Electrons are scattered by the resist and the substrate over an area wider than the scanned pattern. Due to its higher sensitivity the lower resist is more affected than the upper one. A higher acceleration voltage reduces the affected area. (b) After the development an undercut  $\delta_0$  is created. With the proper design this leads to a suspended bridge of resist that can be used for Josephson junction fabrication. When using a higher acceleration voltage this undercut becomes smaller.

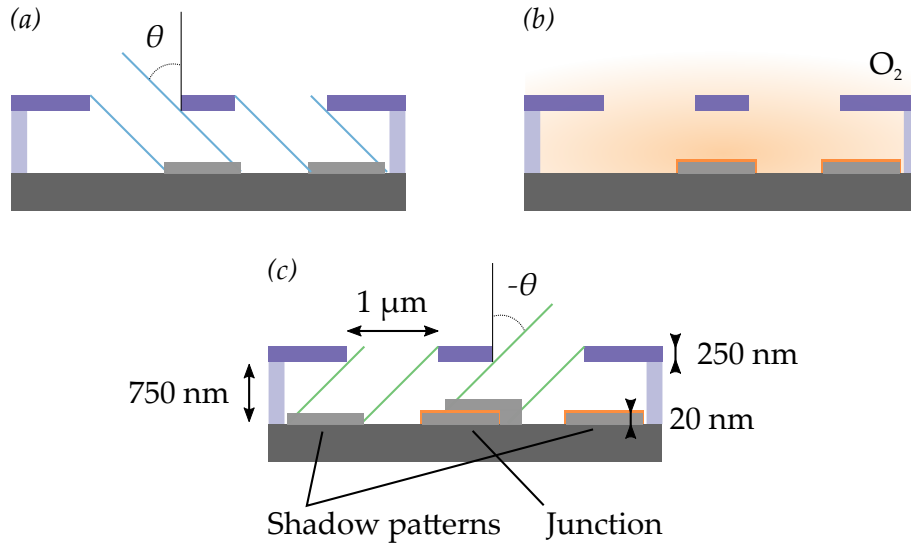


Figure 4.3 – The Niemeyer-Dolan technique. (a) A first metal deposition is performed with an angle  $\theta$ . (b) Then the metal is oxidized in a pure oxygen atmosphere. (c) A second evaporation at angle minus  $\theta$  creates the junction under the suspended bridge. We include usual dimensions in Josephson junction fabrication.

the higher sensitivity of the lower resist layer, we obtain a fully controlled undercut  $\delta$  at the part exposed to low dose, see Fig. 4.4 (b). In this work we used  $\delta = 700\text{ nm}$ . At high dose there is still some small undercut  $\delta_0$  but it can usually be neglected. It is found to be around 40 nm for an acceleration voltage of 100 kV<sup>95</sup>. Using this technique we choose to have parts with no undercut, asymmetric undercut and symmetric undercut depending on the purpose. As shown

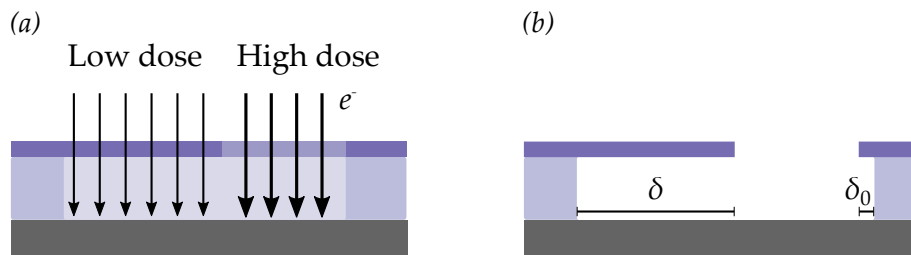


Figure 4.4 – Controlled undercut. (a) Two different layers are used. One is written with low dose (left) and the other with high dose (right). At high doses both resists are exposed, however at low dose only the lower resist is affected. (b) After development the part written at low dose gives the undercut  $\delta$  and the part written at high dose gives the pattern mask. There is always some residual undercut  $\delta_0 \sim 40\text{ nm}$  in the part written at high dose.

in Fig. 4.5 thanks to this asymmetric undercut Josephson junctions can be fabricated with no suspended bridge. Whenever we want to create a wire we use an asymmetric undercut. One of the angles reaches the substrate and the other hits the resist wall (Fig. 4.5 (a) upper and lower panel) and is removed during the lift-

off. Then for creating a junction a symmetric undercut is used overlapping both metal depositions (Fig. 4.5 (a) middle panel). In Fig. 4.5 (b) a Scanning Electron Microscope (SEM) image of a Josephson junction fabricated with this technique is shown.

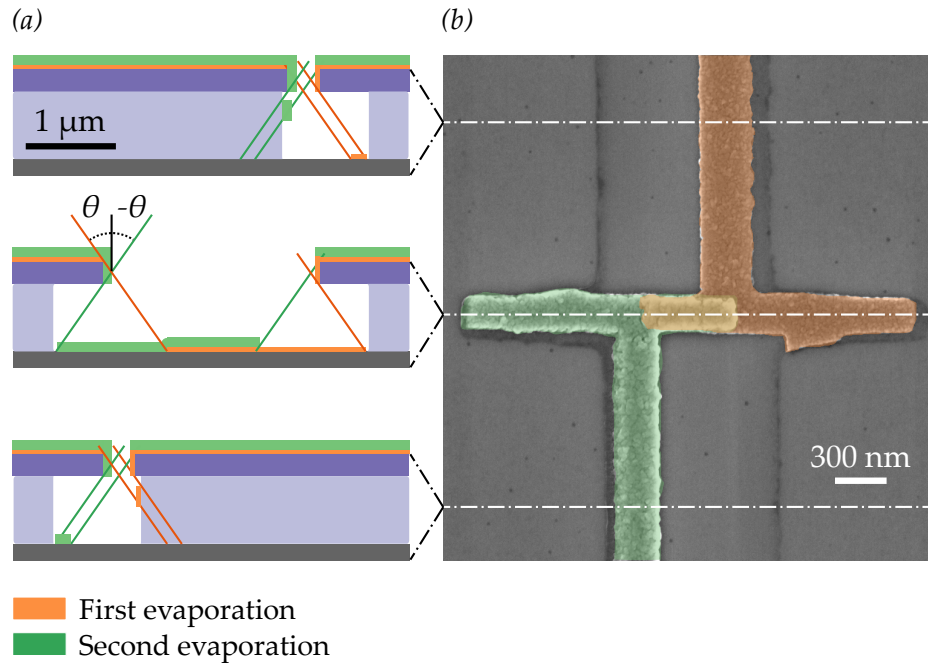


Figure 4.5 – Bridge Free Fabrication technique. (a) The two angles in the metal deposition (the oxidation step is not shown) for three different parts. Top panel and bottom panel are wires and middle panel is the junction. At angle  $\theta$  metal is deposited on the substrate for the upper and middle panel (orange), however for the bottom panel the metal hits the resist wall. A second evaporation at angle minus  $\theta$  deposits metal in the middle and bottom panel (green) but not in the upper panel. After lift-off only the metal on the substrate remains. (b) Josephson junction fabricated with this technique with the different metal depositions in different colors.

Finally, given the fact that there is no suspended bridge involved in this technique, the substrate is easily accessible. This means that we can remove any residual resist on the surface prior to the evaporation using Reactive Ion Etching (RIE). This residual resist is known to affect the quality of the junctions<sup>94</sup>.

#### Detailed explanation of the BFF technique

When using any angle evaporation technique the different geometrical parameters, i.e. the resists thickness, the undercut size, the evaporation angle and the metal thickness should be designed properly so the desired junction is obtained.

First of all, one should choose properly the thickness of the metal deposition. If we denote the thickness of the first metal deposition as  $t_1$  and of the second as  $t_2$ , we need to have  $t_2 > t_1$ . As illustrated in Fig. 4.6, this is needed in order

to obtain a good metallic contact after the second deposition. In our case we use  $t_1 = 20$  nm and  $t_2 = 50$  nm.

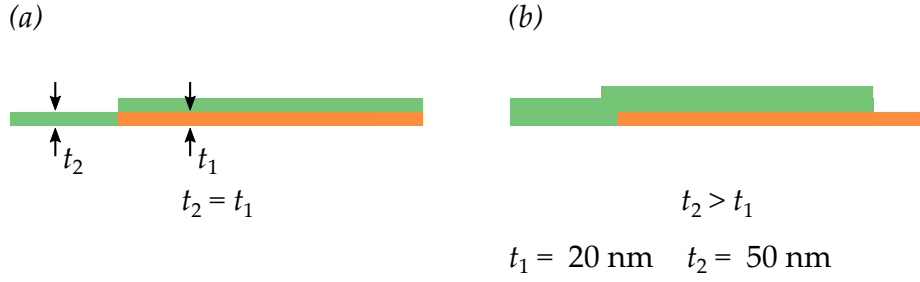


Figure 4.6 – Josephson junction after the two depositions. (a) When both layers have similar thickness there might be a discontinuity at the edges of the junction. (b) The problem can be solved by increasing the thickness of the second metal layer.

Regarding the BFF technique, we show in this section the relation between the different geometrical parameters for the Josephson junction fabrication. To do so we reproduce the middle panel of Fig. 4.5 (a) with greater detail in Fig. 4.7. Here  $d_1$  and  $d_2$  are the resist thickness of the bottom and upper layer respectively.  $\theta$  is the evaporation angle and  $\delta$  the size of the undercut. Finally we call  $L_{\text{mask}}$  the size of the gap in the upper resist layer. This gap is the part that is written at high dose. To make things clearer we define an  $x$  axis whose origin is the beginning of the upper resist gap.

In the first evaporation (orange) metal is deposited from  $x_1$  to  $x_2$ . Doing some trigonometry we see that

$$x_1 = (d_1 + d_2) \tan \theta, \quad (4.1)$$

$$x_2 = L_{\text{mask}} + d_1 \tan \theta. \quad (4.2)$$

Therefore the length of the first evaporation is

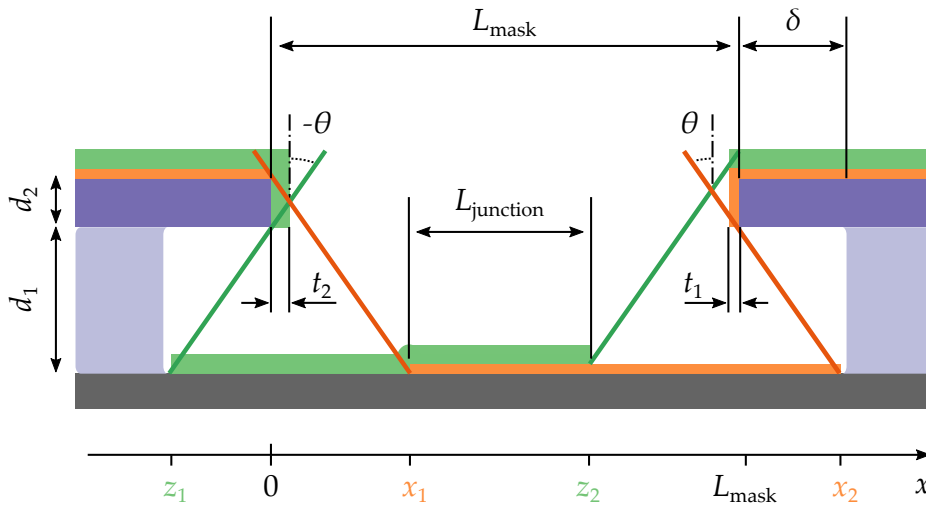


Figure 4.7 – Close-up of the middle panel in Fig. 4.5 (a).

$$L_1 = x_2 - x_1 = L_{\text{mask}} - d_2 \tan \theta. \quad (4.3)$$

We see that it is *shorter* than the designed length  $L_{\text{mask}}$ . Now we follow the same procedure to obtain the length of the second deposition  $L_2 = z_2 - z_1$ . But first we have to notice that after the first deposition a metal layer of thickness  $t_1$  is already on top of the last resist layer. This will affect slightly the second deposition. We have

$$z_1 = -d_1 \tan \theta, \quad (4.4)$$

$$z_2 = L_{\text{mask}} - t_1 - (d_1 + d_2 + t_1) \tan \theta. \quad (4.5)$$

This gives

$$L_2 = z_2 - z_1 = L_{\text{mask}} - d_2 \tan \theta - t_1 (1 + \tan \theta). \quad (4.6)$$

We see that the second deposition is smaller than the first one,  $L_2 < L_1$ . Now we can obtain the junction size  $L_{\text{junction}}$

$$L_{\text{junction}} = z_2 - x_1 = L_{\text{mask}} - t_1 (1 + \tan \theta) - 2 (d_1 + d_2) \tan \theta. \quad (4.7)$$

This means that whenever we are designing a junction, we have to choose  $L_{\text{mask}}$  to obtain the desired  $L_{\text{junction}}$ . From Eq. (4.7) we obtain

$$L_{\text{mask}} = L_{\text{junction}} + t_1 (1 + \tan \theta) + 2 (d_1 + d_2) \tan \theta. \quad (4.8)$$

We have to choose the proper undercut  $\delta$  in order not to have metal deposited on the resist wall. This condition reads  $x_2 - z_1 \leq L_{\text{mask}} + 2\delta$  which gives

$$\delta \geq d_1 \tan \theta. \quad (4.9)$$

This means that the undercut should be wide enough for the deposited metal to fit. On the other hand, when designing a wire, see Fig. 4.5 top and bottom panel, we need to deposit metal only at one of the angles. This puts a constraint on the wire width  $L_{\text{wire}}$ . For the first angle (orange) the constraint reads  $x_1 > L_{\text{wire},\theta}$  which gives

$$L_{\text{wire},\theta} < (d_1 + d_2) \tan \theta - \delta_0. \quad (4.10)$$

For the second angle (green) the constraint is  $z_2 < 0$  which gives

$$L_{\text{wire},-\theta} < (d_1 + d_2) \tan \theta + t_1 (1 + \tan \theta) - \delta_0. \quad (4.11)$$

These constraints guarantees that the wire shadows are fully removed during lift-off.

#### *Wires resistance*

One important consequence of the described process is how the wires size depends on whether they were deposited with angle  $\theta$  or minus  $\theta$ . This means that in this technique the wire resistance depends on whether it was fabricated with angle  $\theta$  or minus  $\theta$ .

First, as explained before, we use a different thickness for the first and the second layer,  $t_2 > t_1$ . Second, as shown in Eqs. (4.3) and (4.6) the width of the



wire depends on the deposition angle,  $L_2 < L_1$ . The resistance per unit length of a wire is given by

$$R_l = \rho \frac{1}{\text{width} \times \text{thickness}}, \quad (4.12)$$

where  $\rho$  is the resistivity of the material. Assuming that both wires are made of the same material, we have for the ratio of resistances  $R_\theta/R_{-\theta} \equiv R_1/R_2$

$$\frac{R_1}{R_2} = \frac{t_2 L_2}{t_1 L_1} = \frac{t_2}{t_1} \left( 1 - t_1 \frac{1 + \tan \theta}{L_{\text{mask}} - d_1 \tan \theta} \right). \quad (4.13)$$

In this work we used  $t_1 = 20 \text{ nm}$ ,  $t_2 = 50 \text{ nm}$ ,  $\theta = 35^\circ$ ,  $d_1 = 250 \mu\text{m}$  and  $L_{\text{mask}} = 350 \text{ nm}$ . These parameters give  $R_1/R_2 \sim 3$  which is consistent with the experimentally found value of  $3.2 \pm 0.8$ . This difference in resistance must be kept in mind when performing room temperature DC measurements as will be explained in Section 4.2.

### Structure design

The design of the structure is done in a CAD program in files with the `.gds` extension. These files contain not only the structure we want to write but the different layers we want to use. Each layer is related to a different dose.

As explained before, for writing Josephson junctions two layers are used, one with high dose for the mask and one with low dose for the undercut. An example of the different junctions used in this work is shown in Fig. 4.8 with their respective pattern files. We use two different designs for the Josephson junctions. For fabricating the array of SQUIDS we need big junctions, several micrometers long and therefore the design shown in Fig. 4.8 (a), (c) and (d) is well suited. It is compact and reliable for these sizes. However when fabricating small junctions, in the nanometer regime, this design is not that reliable. A small error in the evaporation angle gives a strong deviation in the junction area. By using the design in Fig. 4.8 (b) we see that even if the angle is not perfect, the variation in the area is not that big and moreover we are sure that both depositions will overlap. For the array of SQUIDS we connect several of them in series, see Fig. 4.8 (d). It is very important to use an alternating undercut for the wires. This is done to avoid a shunt in the structures.

#### 4.1.2 Focus

The basic idea behind e-beam lithography is that using a beam of electrons we write structures in the nanometer scale on the surface of a given substrate. However, depending on the size of the structure we want to write, it might be necessary to move the stage where the substrate lies.

To do this the structure is divided in squares called *main fields* (in our case  $300 \mu\text{m} \times 300 \mu\text{m}$ ) and *subfields* ( $20 \mu\text{m} \times 20 \mu\text{m}$ ). Between any two of these main fields the stage moves mechanically. Between two subfields the electron beam moves using coarse deflection coils. Therefore it becomes a crucial task to focus properly the electron beam in order to *stitch* all these fields together, see Fig. 4.9 (a).

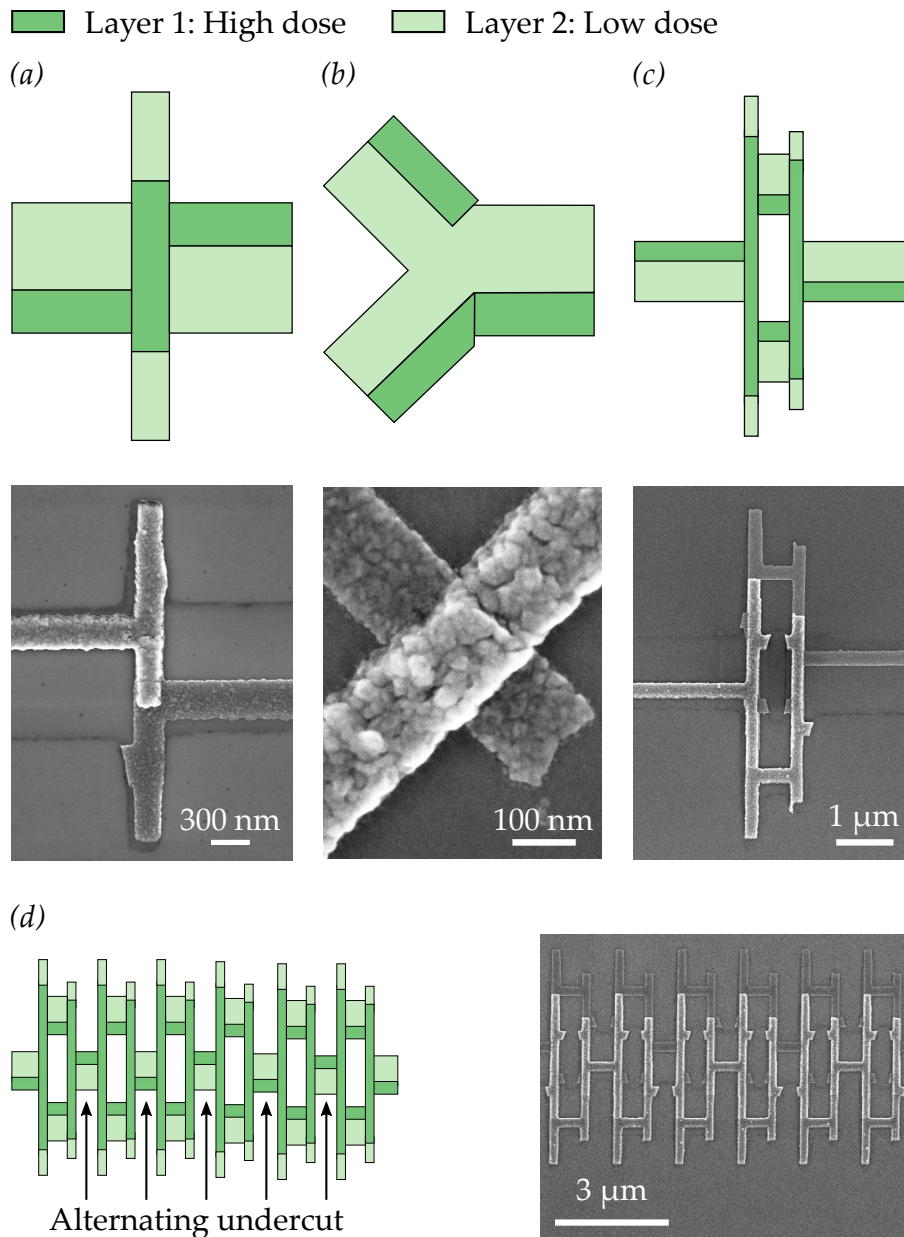


Figure 4.8 – Pattern files (top) with the Scanning Electron Microscope (SEM) image of their corresponding structures (bottom). Two layers are used, one for the structure (layer 1) and one for the undercut (layer 2). (a) Josephson junction design for big junctions. (b) Josephson junction design for small junctions. (c) SQUID formed by two different junctions designed as in (a). (d) Array of SQUIDs. The alternating undercut in the wires avoids shunts in the structures.

With the proper focus the beam goes from one subfield to another without leaving any gap. However, if the beam is not properly focused it leaves a space between subfields that is not written leading to gaps in the structures as shown in Fig. 4.9 (b). This is called a *stitching error*. This error is larger at the edges of the main fields. As it can be seen this error effectively breaks the structure at several

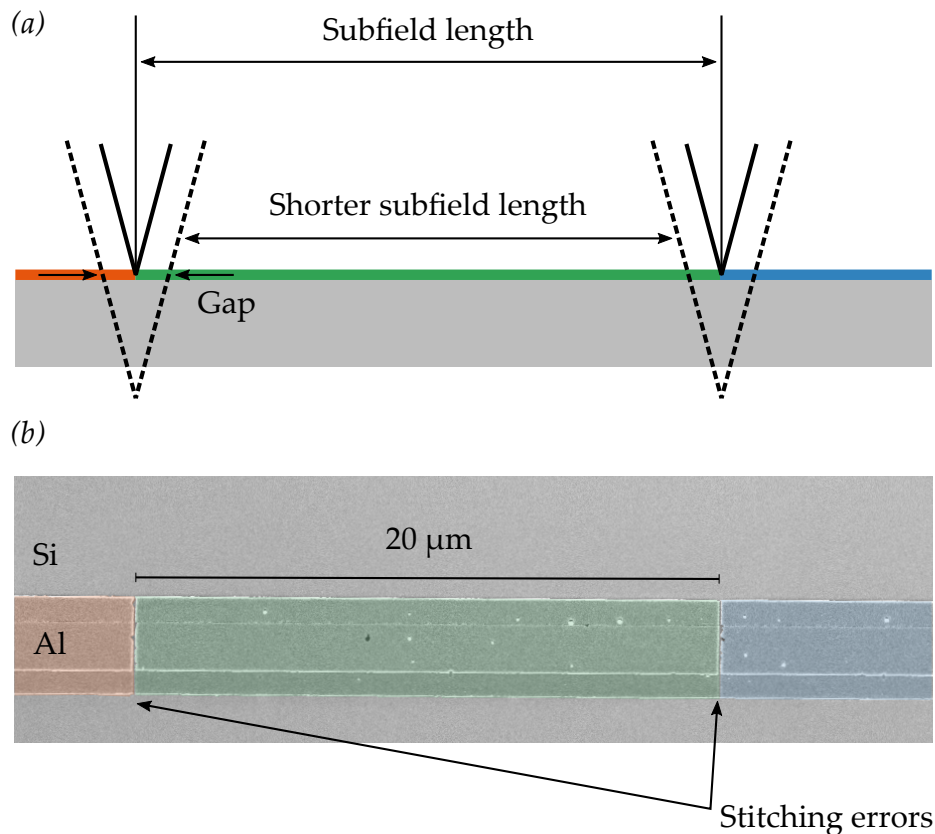


Figure 4.9 – (a) Graphical explanation for the stitching error. When the beam is properly focused (solid black line) there is no gap between the subfields, shown in orange, green and red. When the beam is not properly focused (dashed black line) a gap appears between them. (b) Example of stitching error showing the gap between the subfields.

spots. In order to obtain the best possible focus and avoid the stitching errors we write focus marks on the wafer. These marks are  $8\ \mu\text{m} \times 8\ \mu\text{m}$  squares made of gold, see Fig. 4.10. Once we have these gold marks the e-beam can use them to focus. It measures the contour of the square at different heights until the measured contour fits the known size of the mark ( $8\ \mu\text{m} \times 8\ \mu\text{m}$ ). At this point the focus is good enough for writing.

One important feature of the e-beam writer used in this work is the *focus map*. This allows to readjust the focus dynamically during the writing. The surface of the substrate is fitted with a plane to take into account any tilt in the substrate. This feature becomes crucial when writing over large surfaces as it is done with the arrays of SQUIDS in this work.

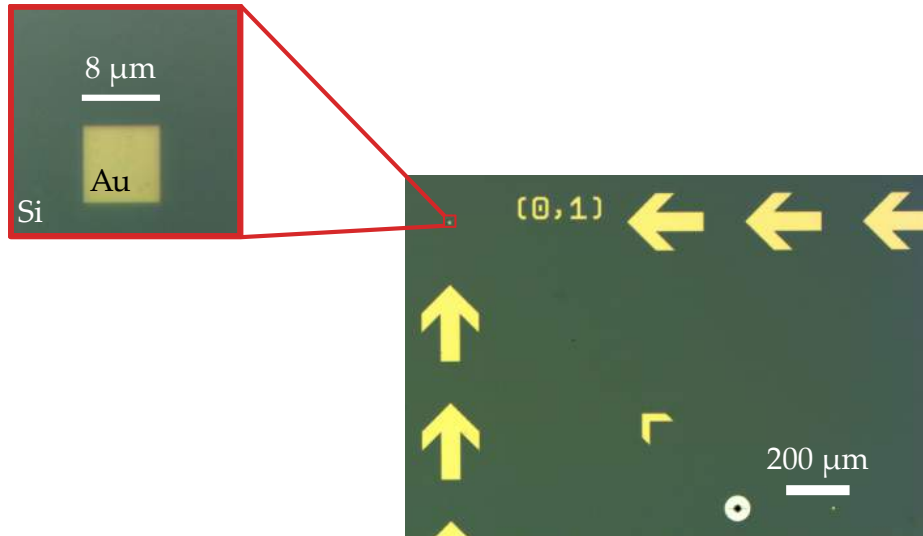


Figure 4.10 – Optical image showing the arrow marks to help the user find the focus marks. In the inset a focus mark is shown, a  $8\ \mu\text{m} \times 8\ \mu\text{m}$  square. Both structures are made of gold.

### 4.1.3 Dose tests

Choosing the correct dose for the different parts of the circuit to be written is very important to obtain an optimum result. Due to the proximity effect the electrons do not only affect the desired area but can propagate several micrometers and affect their surroundings<sup>91</sup>.

The points more sensitive to the proximity effect are those where several structures are packed together. This includes arrays of Josephson junctions, big structures (pads) next to small structures (junctions) and interdigital capacitors. As explained before, in Josephson junction arrays the side of the undercut for the wires is alternated to avoid a shunt in the junctions. However, if too high dose is used an undercut might appear on both sides. This means that during the metal deposition both angles reach the substrate creating a shunt in the array, see Fig. 4.11. This is specially true when writing big junctions ( $L_{\text{junction}} > 5\ \mu\text{m}$ ). To solve this problem we divide each junction in two layers, see Fig. 4.12 (a). The first layer is written at a normal dose and the second layer at a lower dose. A dose test is shown in Fig. 4.13 (a). We vary the dose at layer 3 for an array of SQUIDS. As it can be seen, at too low dose the junctions are not well defined and at too high dose the junctions are shunted. To avoid the proximity effect between junctions and contact pads we include long narrow arms between each pad and each junction, see Fig. 4.12 (b). These arms are between  $50\ \mu\text{m}$  to  $300\ \mu\text{m}$  long. Because these arms are quite narrow, their proximity effect on the surroundings is lower. In this way we protect the Josephson junction from the dose applied to the contact pad. Given the narrowness of these arms a slightly higher dose is used. Finally, for the interdigital capacitors we performed a dose test to obtain the right dose for the fingers, see Fig. 4.13 (b).

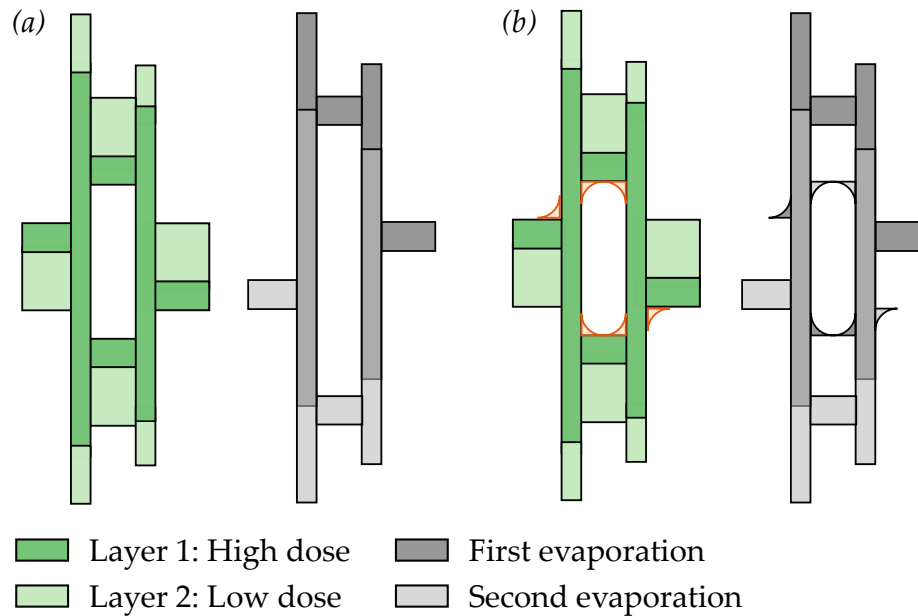


Figure 4.11 – Proximity effect in SQUIDS. (a) With no proximity effect, the desired pattern is obtained. (b) With proximity effect part of the shadow pattern of the wires reaches the substrate.

#### 4.1.4 Detailed fabrication process

In this section the different steps in the fabrication process are described in detail. The exact recipe for the whole process can be found in Appendix C. The first aspect to point out about our fabrication process is both its high success rate ( $\sim 90\%$ , limited mainly by the oxide thickness variation) and its high throughput. All our samples were fabricated on 2 inch intrinsic silicon wafers. In each of these wafers we write several samples (from 9 up to 20 depending on the single chip size). Given the fact that the full fabrication process takes one week this gives as many as 20 samples per week. In addition, thanks to the large size of the wafer, the thickness of the spin coated resist is much more homogeneous than for a single chip.

In Fig. 4.14 (a) a drawing of the front side of the wafer is shown. The dashed line divides the wafer in several chips. The yellow squares represent the focus marks. There are two types of focus marks. The global marks (outside the dashed lines) are used for obtaining the right focus for the whole wafer. They allow to define a global coordinate system as well. Due to the presence of some resist's inhomogeneity, it is important to perform a local focus in each of the samples individually. The local marks (inside each of the chips) are used for this purpose. In Fig. 4.14 (b) the bottom part of the wafer is shown. It is gold plated to be used as the ground of the circuit. A photograph of the wafer after the whole fabrication process is shown in Fig. 4.14 (c). Once the fabrication is finished the wafer is diced in individual chips as the one in Fig. 4.14 (d). The different fabrication steps are described in the following paragraphs.

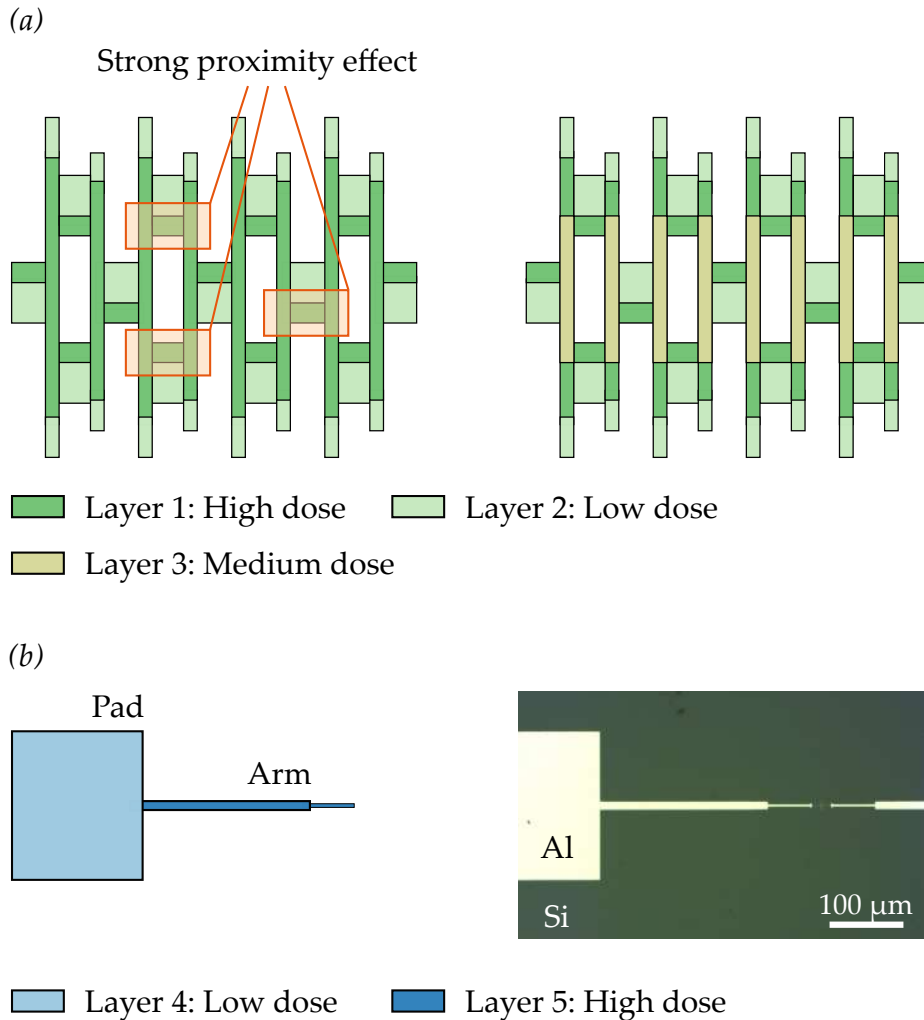


Figure 4.12 – (a) SQUID array pattern. In orange the points where the SQUID might be shunted due to proximity effect are shown. For arrays with big junctions a third layer (layer 3) with intermediate dose is used in order to reduce the proximity effect. (b) Long narrow arms between pads (layer 4) and structures. Due to their narrowness a layer with a slightly higher dose is used (layer 5).

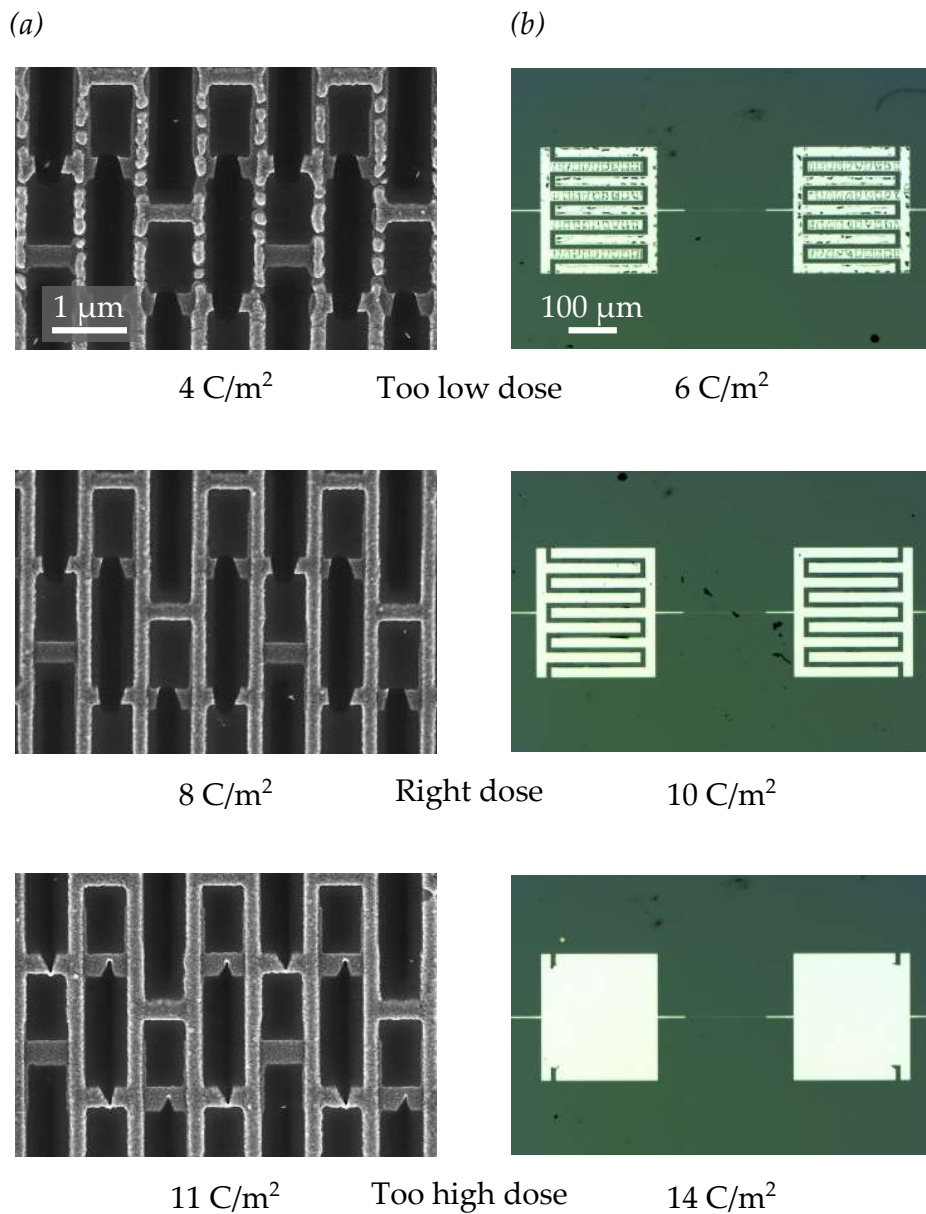


Figure 4.13 – Dose tests for samples fabricated with an acceleration voltage of 80 kV. (a) Close-up of three different arrays of SQUIDS with different doses in layer 3. At low dose the junctions are broken and at high dose the junctions are shunted. (b) Interdigital capacitors for different doses.



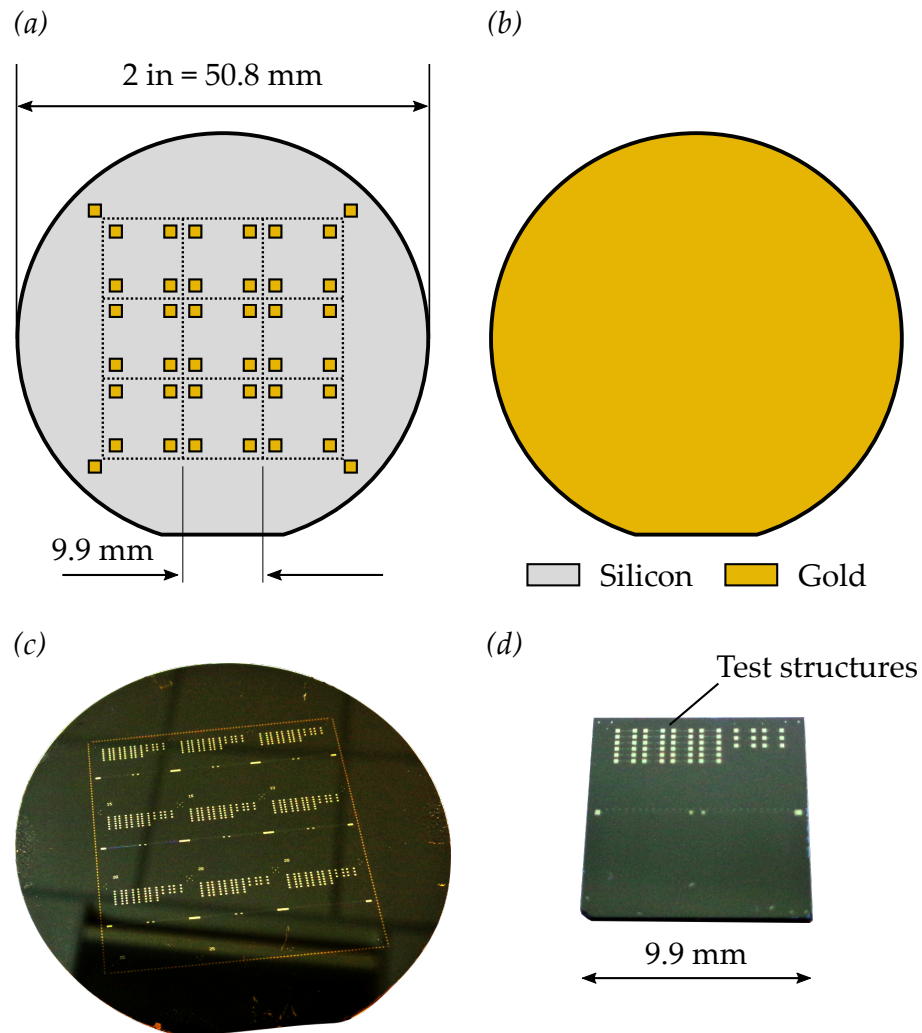


Figure 4.14 – Two inch wafer used in the fabrication process. (a) Front part of the wafer. Several chips can be written in one single wafer. In yellow the focus marks are shown,  $8\ \mu\text{m} \times 8\ \mu\text{m}$  squares (not to scale). (b) Backside of the wafer gold plated to ensure a good ground. (c) Photograph of a wafer with the different chips already written with structures. (d) A single chip after dicing the two inch wafer.



*Gold plating*

As will be explained later in Section 4.3.1, our circuits are designed in the *microstrip* geometry. In this geometry the center conductor is placed over the substrate while the ground is placed below. We have to ensure a good metallic contact between the sample and the sample holder to avoid losses. To do so we gold plate the bottom face of the two inch wafer. First we evaporate a 10 nm thick layer of titanium to allow the gold to stick to the silicon substrate and then a 200 nm thick layer of gold.

*Writing of the focus marks*

Prior to the deposition of the resists we bake the wafer for some minutes. This removes the adsorbed water at the surface. We then spin coat PMMA 3%<sup>a</sup> on the wafer and bake it. We write both the local and the global marks plus the dicing marks. We make sure that the focus marks are centered on the main fields. Then we develop the structure and perform first a titanium evaporation (10 nm) followed by a gold evaporation (50 nm). Finally we do a five hours lift-off in N-Methyl-2-pyrrolidone (NMP).

*Writing the structures*

As explained in Section 4.1.1 we need two layers of resist, PMMA-MAA<sup>b</sup> and PMMA<sup>c</sup>. We first spin coat and bake the PMMA-MAA ( $d_1 = 750$  nm) and then we repeat the process with PMMA ( $d_2 = 250$  nm). We then load the sample in the e-beam writer to write the desired pattern. Once the writing is finished we perform the development. We use as a developer Methyl isobutyl ketone (MIBK-IPA) diluted in isopropanol (IPA) in proportion 1 to 3.

After the development we evaporate the Al on the sample. As a first step we clean the sample using oxygen RIE. This removes the remaining of resist that adhere to the wafer surface even after development<sup>94</sup>. We then load the sample in the PLASSYS<sup>®</sup> evaporator and perform the evaporation at high vacuum ( $5 \times 10^{-8}$  mbar). In order to obtain a reliable vacuum and reduce the presence of water at most the sample is loaded on the evening and evaporated the morning after. Therefore the chamber and load lock are pumped for more than ten hours reaching a pressure of  $\sim 1 \times 10^{-8}$  mbar. Between the two metal depositions an oxidation is performed using pure oxygen at 4 mbar. We then perform a lift-off in NMP at 80 °C during several hours.

*Dicing*

After the whole fabrication process we dice the two inch wafer to obtain the individual chips that are introduced in the cryostat. To protect the samples during the dicing we spin coat optical resist s1818 on top of the wafer without baking.

<sup>a</sup>PMMA 950K AR-P 679.04 diluted in ethyl lactate (3 volumes of AR-P per volume of ethyl lactate)

<sup>b</sup>AR-P 617.14 diluted in AR 600.07 (9/5)

<sup>c</sup>PMMA 950K AR-P 679.04 diluted in ethyl lactate (4 volumes of AR-P per volume of ethyl lactate)

### 4.1.5 Writing process

In this section we introduce in detail the different files created to write the desired pattern at the desired spot in the two inch wafer. First we briefly describe the Python scripts used to create the pattern file and then we give specific details on the files managed by the e-beam system.

#### *Designing the structures with Python*

During this work we had to fabricate several samples with arrays of SQUIDS of different sizes in order to find the best parameters for the experiment. Doing so by hand in a reproducible way is not easy. In order to create the pattern files automatically we wrote several Python scripts, see Appendix B.2. The base library for the scripts is called `gdsCAD`. This library allows to create different basic shapes and then save the design in the `.gds` format. First we defined a class for each of the desired components, i.e. single Josephson junctions, SQUIDS and arrays of SQUIDS (see Fig. 4.8). Then we defined some templates to automatize the creation of the `.gds` files, e.g. a template for creating test structures for the DC measurements.

An example of the flexibility of this approach is the pattern shown in Fig. 4.15. We can modulate the size of each junction following any function, in this case a cosine. By doing this we modulate the inductance, self-capacitance and capacitance to ground of each of the sites in the array. In this way we can engineer the dispersion relation of the modes propagating along this array. For example, when modulated with a cosine function we can open a gap in the dispersion relation.

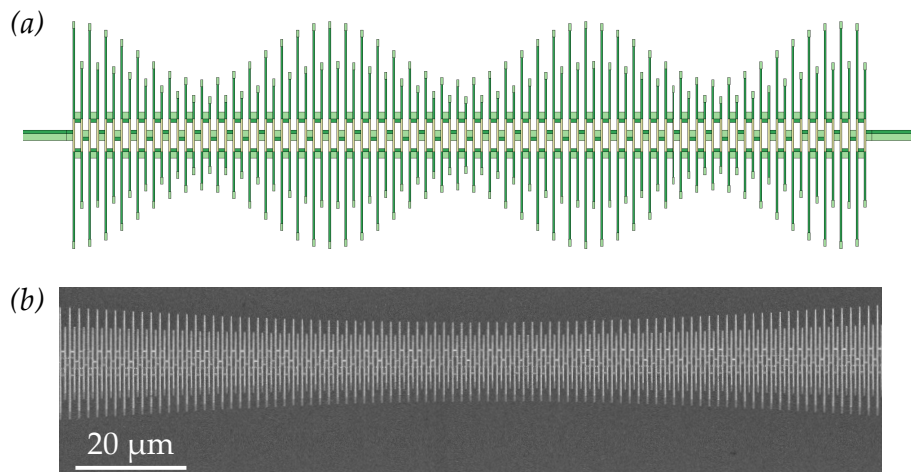


Figure 4.15 – (a) Pattern design for a cosine modulated chain created with Python. (b) SEM picture of a real sample (different design than the one in (a)).

#### *E-beam file system*

After designing the patterns it is necessary to prepare the different files for the e-beam system to write them in the proper place. As mentioned in Section 4.1.4 we write several samples on a 2 inch wafer. This means that we need to arrange properly the different structures over the wafer. The system uses three types of files

- Nanobeam pattern file (`.npf`). This file contains the pattern to be written. It specifies the different layers, the mean fields and the sub fields. Usually patterns are created in a `.gds` file and then converted into `.npf` format using a software called nbPat which is given with the e-beam writer.
- Nanobeam job file (`.njf`). This file contains all the necessary information to write the different `.npf` files over the 2 inch wafer. It gives the position of the focus marks, both global and local, the path to the different `.npf` files and the dose associated to each of their layers. It is convenient to create two `.njf` files. In the first one a low current is used ( $\sim 1$  nA) to write the small structures i.e. Josephson junctions and wires. The second one is written at high current ( $\sim 12$  nA) and contains the big structures, i.e. pads and capacitors.
- Nanobeam batch file (`.nbf`). This file is used to execute several `.njf` files one after the other. The desired writing parameters such as the acceleration voltage and the writing current are specified in this file. They can be specified for each of the `.njf` files independently.

A detailed explanation of each of these files is given in Appendix B.1.

## 4.2 DC measurements

Until now we have focused on the fabrication of the superconducting circuits. In order to evaluate our process we perform room temperature DC measurements of several test structures. This allows to check the reproducibility of the process and the aging of the junctions.

### 4.2.1 Measurement setup

The measurement consists on a DC resistance measurement. With a current source<sup>d</sup> we apply a DC current  $I$ . Using a voltmeter<sup>e</sup> we measure the voltage drop  $V$  across the sample, see Fig. 4.16. We make this for several  $I$  values and obtain an  $IV$  curve. From the slope of this curve we obtain the resistance of the sample.

Contrary to the usual 4-point probes method here we use a 2-point measurement. This reduces the number of pads needed per test structure (two instead of four) which greatly simplifies the structure design and reduces the area needed in the chip. As will be explained later, we remove the overall resistance in the setup by varying the number of junctions in the test structures and performing a linear fit afterward. The measurement of the  $IV$  curve and the estimation of the resistance is automated via a Python script, see Appendix B.3.

### 4.2.2 Reproducibility of the fabrication process

The most sensitive part in the structures is the oxide barrier of the Josephson junctions. As explained before, the critical current  $I_c$  of a junction depends exponen-

<sup>d</sup>Keithley 2400 SourceMeter<sup>®</sup>

<sup>e</sup>Keithley 2000 Multimeter<sup>®</sup>

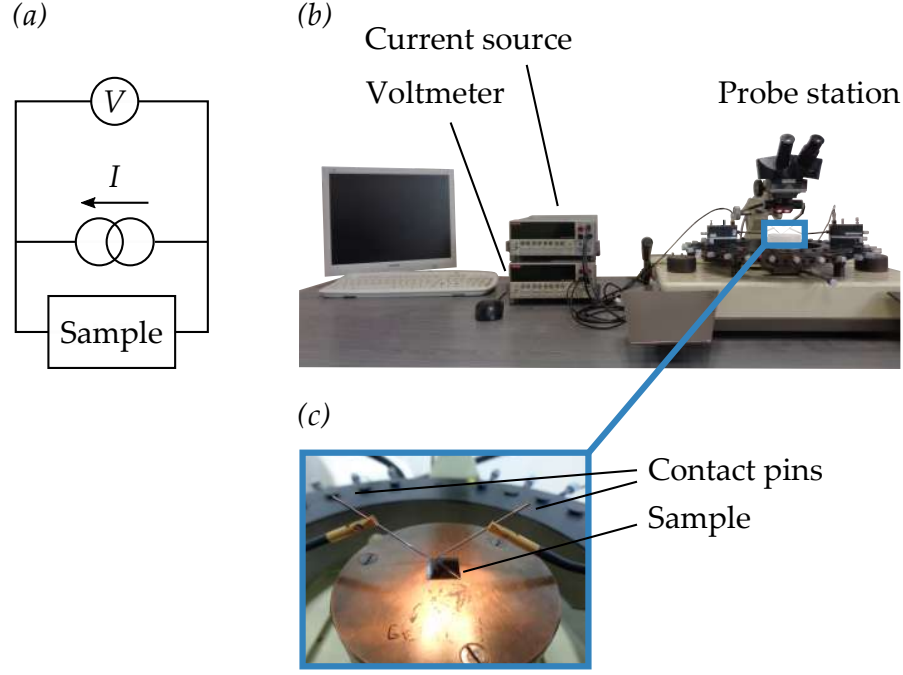


Figure 4.16 – Experimental setup for the DC measurements. (a) Circuit diagram of the measurement. (b) Measurement setup including a current source, a voltmeter, a probe station and a computer to run the measurement scripts. (c) Zoom in showing the sample and the contact pins.

tially on the barrier thickness. Therefore a high reproducibility in the fabrication process depends on a high reproducibility in  $I_c$ .

The value for  $I_c$  can be obtained from the normal state resistance of the Josephson junction  $R_n$ . The relation between both is given by the Ambegaokar-Baratoff formula<sup>96</sup>, Eq. (4.14).

$$I_c(T) = \frac{\pi\Delta_{Al}}{2e} \tanh\left(\frac{\Delta_{Al}}{2k_B T}\right) \frac{1}{R_n} \quad (4.14)$$

Here  $\Delta_{Al} = 210 \mu\text{eV}$  is the superconducting gap of aluminum for thin films and  $k_B$  is the Boltzmann constant. In the experiment we measure at  $T = 20 \text{ mK}$  and therefore  $\Delta_{Al}/2k_B T \sim 6 \times 10^4$ . This means that  $\tanh(\Delta_{Al}/2k_B T)$  is approximated to one leading to the simplified equation:

$$I_c = \frac{\pi\Delta_{Al}}{2e} \frac{1}{R_n}. \quad (4.15)$$

As explained before we obtain the room temperature resistance of the junction  $R_{300\text{K}}$  from the slope of the  $IV$  curve. If we want to obtain a good estimation for  $R_n$ , resistance at  $T \sim 4 \text{ K}$ , we need to correct for the temperature effects. The resistance of a tunnel junction can decrease between 30% to 50% with increasing temperature<sup>97</sup>. This decrease comes from the thermal broadening of the Fermi-Dirac distribution<sup>98</sup> i.e. at high temperatures electrons have more energy available for tunneling through the junction. To take into account this effect we introduce a constant  $\beta_0$  (Eq. (4.16)). This factor is found to be around 1.3 for an oxide thickness

between 1 nm to 2 nm.

$$R_n = \beta_0 R_{300K} \quad (4.16)$$

We perform DC measurements on one hundred test structures. They consists of an asymmetric SQUID connected at the left and the right to two aluminum square pads of  $200\ \mu\text{m} \times 200\ \mu\text{m}$ . The dimensions of the junctions are  $3.2\ \mu\text{m} \times 0.2\ \mu\text{m}$  and  $2.0\ \mu\text{m} \times 0.2\ \mu\text{m}$ . We measure the  $IV$  curve of 100 SQUIDS obtaining  $R_{300K}$  for each of them. The obtained histogram is shown in Fig. 4.17 along with a fit to a Gaussian (solid line). The mean value  $\bar{x}$  and the standard deviation  $s$  for  $R_{300K}$  of

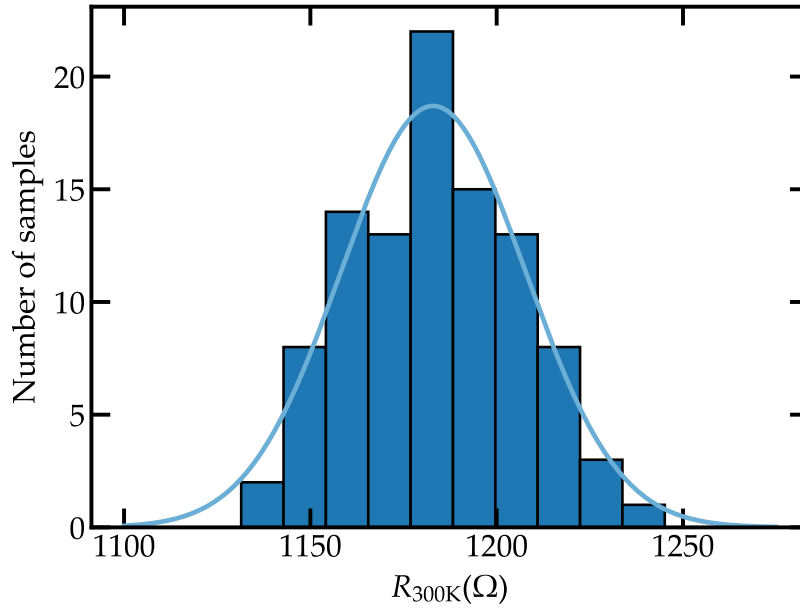


Figure 4.17 – Histogram for the room temperature resistance of the SQUIDS. The junctions dimensions in each of the SQUIDS are  $3.2\ \mu\text{m} \times 0.2\ \mu\text{m}$  and  $2.0\ \mu\text{m} \times 0.2\ \mu\text{m}$ . The solid line is a fit with a Gaussian to the center point of each bin.

this 100 junctions is

$$\bar{x} = 1184\ \Omega \quad s = 35\ \Omega. \quad (4.17)$$

This gives a fabrication error ( $s/\bar{x}$ ) of 3% among samples fabricated in the same evaporation step.

### 4.2.3 Accurate measurement of the critical current

Although useful for obtaining the reproducibility of the fabrication process, the above method is not accurate to obtain the room temperature resistance of the junctions. The reason is that we do not remove the overall resistance of the setup, i.e. cables, on chip wires and contact resistance between the pads and the contact pins.

In order to remove this overall resistance we perform DC measurements of several test structures with an increasing number of Josephson junctions. From

these measurements we obtain a linear dependence of the resistance with the number of junctions. Because in each measurement we keep the setup constant and we only change the number of junctions we remove any additional resistance created by the setup. From the slope of the linear fit to the data we obtain a good estimate for the room temperature resistance per junction. Once we have this resistance we can estimate the  $I_c$  per junction from Eqs. (4.15) and (4.16).

There is however one caveat: as explained in Section 4.1.1, due to the different wire thickness, the wire resistance depends on whether they were evaporated at angle  $\theta$  or minus  $\theta$ . This means that the overall resistance will be different between odd and even number of junctions. To keep the setup resistance constant we use only an odd number of junctions in the test structures, see Fig. 4.18. In Fig. 4.19 we show an example of a linear fit for several test SQUIDS. The dimensions are the same as before, two Josephson junctions of  $3.2\ \mu\text{m} \times 0.2\ \mu\text{m}$  and  $2.0\ \mu\text{m} \times 0.2\ \mu\text{m}$ . We extract a resistance per SQUID of  $R_{300\text{K}} = 453\ \Omega$  and an offset of  $R_{\text{offset}} = 311\ \Omega$ . It is important to point out that although identical, these SQUIDS belong to a different wafer than the ones in Fig. 4.17 and thus were fabricated in different oxidation conditions. This is the explanation for the difference in resistance between the two.

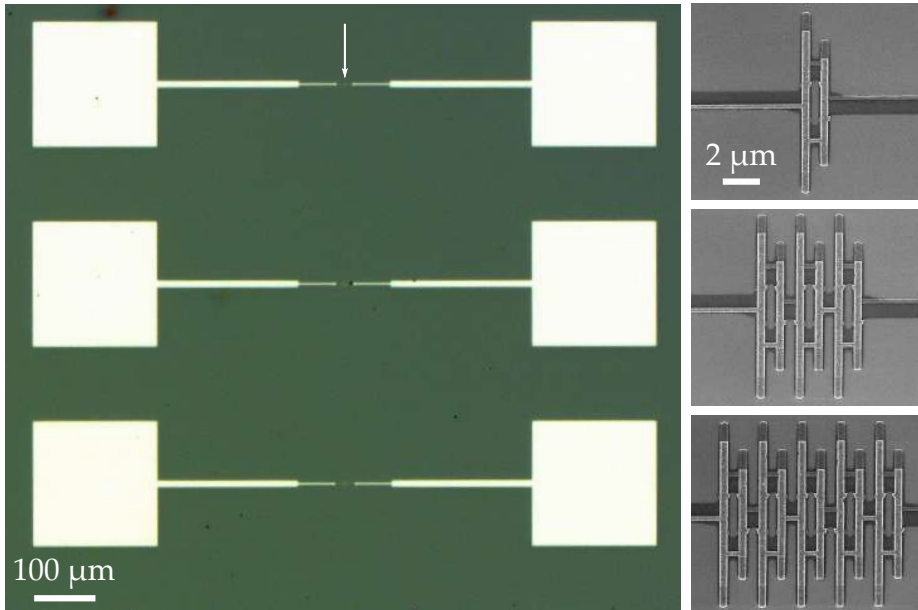


Figure 4.18 – Test structures. From top to bottom the number of junctions increases. We use always an odd number of junctions. The white arrow indicates where the test structure is located.

#### 4.2.4 Josephson junction aging

An important aspect of the fabrication of Josephson junctions is their aging. Due to the diffusion of oxygen into the junctions the thickness of the oxide barrier increases with time<sup>99</sup>. This leads to an increase in  $R_{300\text{K}}$  (decrease in  $I_c$ ) that can suppress the tunneling through the junction.

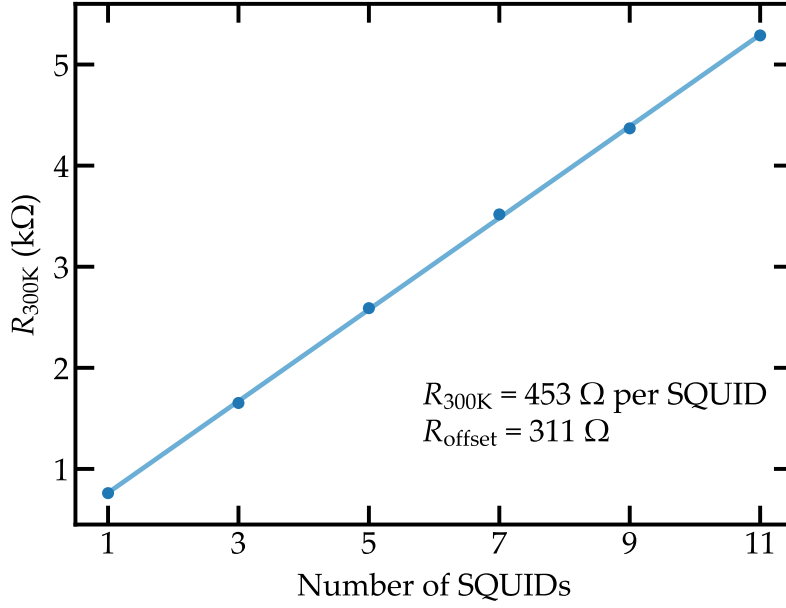


Figure 4.19 – Linear fit of the room temperature resistance for several SQUIDS of dimensions  $3.2\ \mu\text{m} \times 0.2\ \mu\text{m}$  and  $2.0\ \mu\text{m} \times 0.2\ \mu\text{m}$ . From the slope we can obtain the resistance per SQUID while removing the setup offset.

#### The plasma frequency as a fabrication constant

A decrease in  $I_c$  can be related to a decrease in the plasma frequency of the junctions  $\omega_p = 1/\sqrt{L_J C_J}$  and therefore the plasma frequency of the array of SQUIDS, see Sections 2.1.1 and 2.2.1.

This plasma frequency depends only on the thickness of the oxide barrier  $t$ . Given the dimensions of usual Josephson junctions it is safe to assume that they form an infinite parallel plate capacitor. Then we write  $C_J \propto A/t$  where  $A$  denotes the junction area. A well-known experimental relation for  $C_J$  is<sup>39,100</sup>

$$C_J = 45\ \text{fF}/\mu\text{m}^2 A. \quad (4.18)$$

On the other hand, the Josephson inductance can be replaced by the critical current of the junction  $L_J = \varphi_0/I_c$ . The critical current of the junction depends linearly on  $A$  and exponentially on  $t$  for barrier thicknesses in the nm and barrier heights in the eV<sup>101</sup>. We therefore obtain

$$\omega_p = \frac{1}{\sqrt{L_J C_J}} = \sqrt{\varphi_0} \sqrt{\frac{I_c}{C_J}} \propto \frac{\sqrt{A} e^{-t/2}}{\sqrt{A/t}} = \sqrt{t} e^{-t/2}. \quad (4.19)$$

Therefore, the only geometrical parameter left is the thickness of the insulating barrier  $t$ . Moreover, the dependence on the Josephson inductance  $L_J$  is exponential. This means that for an increase in barrier thickness  $\Delta t$  the capacitance  $C_J$  can be taken as constant in relation to the inductance  $L_J$ . For a reproducible fabrication process the plasma frequency of the array of SQUIDS should be constant. It



therefore constitutes a good proxy for the quality of the fabrication process.

### *Experimental results*

We kept track of the aging of the junctions by measuring the room temperature resistance of the test structures over time using the method described before. Two identical evaporators were used, *Evaporator 1* and *Evaporator 2*. While using *Evaporator 1* a severe increase of the junction's room temperature resistance was observed within weeks, see Fig. 4.20 in green. To avoid this problem we switched to *Evaporator 2*. Although nominally identical there are two main differences between both evaporators. Unlike *Evaporator 1*, *Evaporator 2* is fully automatized and therefore enhances sample reproducibility. More importantly *Evaporator 2* counts with a good maintenance which keeps it always working at optimal conditions. This avoids, for example, the pollution of the aluminum crucible with metal from other crucibles. Due to the change in evaporator the Josephson aging was practically eliminated, see Fig. 4.20 in blue.

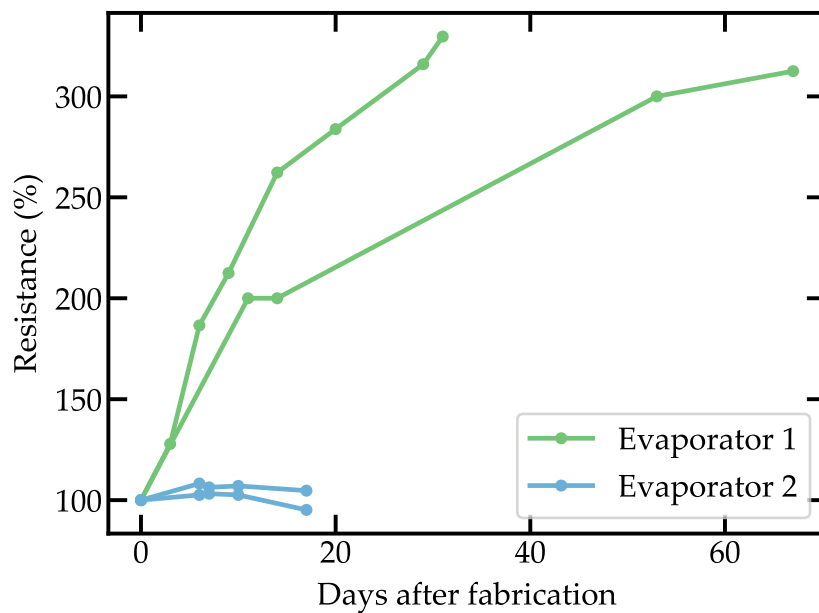


Figure 4.20 – Room temperature resistance for several test structures as a function of time. In green two samples fabricated with *Evaporator 1* and in blue two samples fabricated with *Evaporator 2*. As it can be seen the first ones aged much more than the second ones.

## 4.3 Circuit parameters

Before the fabrication of the devices it is important to make some predictions of the several parameters that play a role in the circuit. One needs to make a link between the real circuit design, i.e. the specific materials used and its geometry,



and the lumped element model that represents that design. In this section we focus on the specific geometry of the circuits. Then we introduce the method used to predict the sample parameters before fabrication.

### 4.3.1 Circuit geometry

As mentioned in Section 2.2.1, a transmission line has two conductors. Depending on how these conductors are placed we will have a different circuit geometry. As a very common example coaxial cables use an inner conductor surrounded by a dielectric. The outer conductor is an outer cylinder around this dielectric. When working with integrated circuits one has to change to more suitable geometries. In this work we chose to use the *microstrip geometry*<sup>102</sup>. This geometry is shown in Fig. 4.21.

It consists of a ground plane at the bottom face of the chip and a metal layer on the top. This metal layer plays the role of the inner conductor in the coaxial cable. The dielectric is the combination of the wafer, in our case silicon, and vacuum. The advantage of this geometry is that we can write our samples in one lithography step. Several analytic expressions have been found for this and other geometries as a function of the geometrical parameters  $W$ ,  $t$  and  $H$ <sup>102</sup>. We use them to get a first estimation of the dimensions of the components. Then we get more quantitative results using a software to simulate our system.

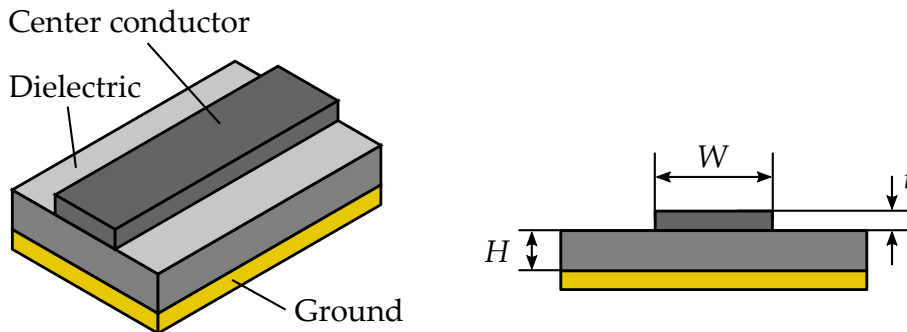


Figure 4.21 – Microstrip geometry. It consists of a center conductor of thickness  $t$  and width  $W$  over a dielectric layer of thickness  $H$ . The ground plane lies at the bottom of the dielectric.

### 4.3.2 Estimation of the capacitances of the system

In order to estimate the capacitances of the system we use an Electromagnetic simulation software (EM software)<sup>f</sup>. This software solves Maxwell equations in three dimensions using the method of moments<sup>103</sup> for a given circuit design and returns the scattering parameters for the circuit, i.e. the transmission ( $S_{21}$ ) and reflection ( $S_{11}$ ) coefficients. It takes into account the substrate material and its thickness as well as the metal used. Lumped elements can be included in the design that are assumed ideal by the EM software. In this case we are going to simulate the coupling capacitors shown in Fig. 4.13 (b) in addition to the stray capacitances given by the transmon qubit SQUID design.

<sup>f</sup>In this work we used a software called Sonnet<sup>®</sup>.

## Coupling capacitors

A drawing of the capacitors we are going to simulate is given in Fig. 4.22 (a). The

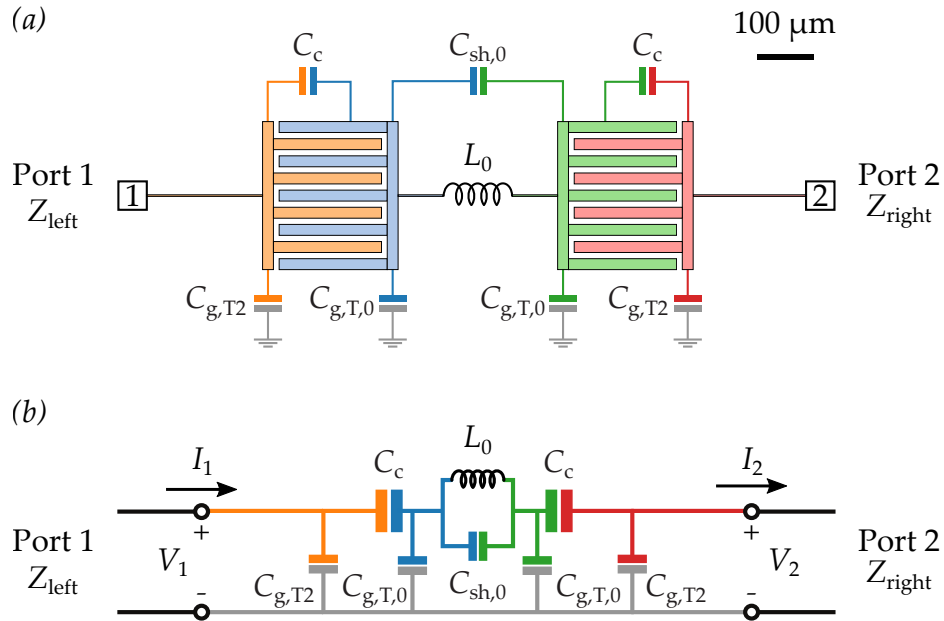


Figure 4.22 – (a) Real capacitor design. It consists of aluminum on a silicon substrate 300  $\mu\text{m}$  thick. (b) Lumped element model used to simulate the capacitances of the system.

circuit consists of aluminum on top of a 300  $\mu\text{m}$  thick silicon substrate. Due to the fact that we work with superconducting circuits we model the aluminum as a lossless metal. The capacitors themselves are connected to the left and to the right to input and output ports of characteristic impedances  $Z_{\text{left}}$  and  $Z_{\text{right}}$  respectively. We add a linear inductor of inductance  $L_0$  between the capacitors. This inductor gives a resonance frequency that will be used later to fit the simulated data.

With the EM software we can obtain the transmission of the circuit as a function of frequency for any values of  $Z_{\text{left}}$ ,  $Z_{\text{right}}$  and  $L_0$ . Because we are only interested in simulating the capacitors, we can choose these values at convenience. We set  $L_0 = 18.1$  nH because it gives a resonance frequency close to the one measured in the experiment.

In Fig. 4.22 (b) the lumped element circuit used to model these capacitors is shown. We include seven capacitors. Assuming the system is symmetric we obtain four capacitances;  $C_c$  is the capacitance between the capacitors plates,  $C_{g,T,0}$  and  $C_{g,T,2}$  are the capacitance to ground of each of the four plates and  $C_{sh,0}$  is the shunting capacitance between the two capacitors. We include the input and output ports of impedances  $Z_{\text{left}}$  and  $Z_{\text{right}}$  and the inductor  $L_0$ .

As explained in Section 3.2.2, for low  $Z_{\text{left}}$  and  $Z_{\text{right}}$  the capacitance  $C_{g,T,2}$  is going to be shunted, i.e. it is not going to affect the transmission of the circuit. We therefore perform a first EM simulation setting  $Z_{\text{left}} = Z_{\text{right}} = 50 \Omega$  plotted in Fig. 4.23 (blue circles). From this simulation we extract the capacitances  $C_c$ ,  $C_{g,T,0}$  and  $C_{sh,0}$  by fitting the transmission for the circuit in Fig. 4.22 (b) using the ABCD matrix method described in Section 2.2.2. The result is plotted as a solid line in Fig. 4.23 (a). The position and width of the peak in transmission depends on

the three capacitances. However, the position of the dip in transmission depends only in the value of  $C_{\text{sh},0}$ . We can therefore obtain  $C_{\text{sh},0}$  and then independently fit  $C_c$  and  $C_{g,T,0}$  from the peak position and width. This gives three out of the four capacitance values in Fig. 4.22 (b). In order to fit the last capacitance,  $C_{g,T2}$ , we perform a second EM simulation setting  $Z_{\text{left}} = 50 \Omega$  and  $Z_{\text{right}} = 3000 \Omega$ , Fig. 4.23 (b) blue circles. Now  $C_{g,T2}$  affects the transmission of the circuit. We obtain the transmission for the lumped element circuit and fit the simulated data varying only  $C_{g,T2}$ , Fig. 4.23 (b) solid line. In this way we obtain the four capacitances independently. The error bar in the capacitances is obtained as the range where the agreement between the EM simulation and the  $ABCD$  matrix data was within 10%. There is however one capacitance in the system that cannot be simulated using EM software, the self-capacitance of the Josephson junction  $C_{J,T}$ . In order to estimate it we use the empirical relation in Eq. (4.18). The error in this capacitance is given by the error in the measurement of the junction area using a Scanning Electron Microscope (SEM). For a junction of dimensions  $250 \text{ nm} \times 250 \text{ nm}$  this error is around  $20 \text{ nm}$  for each length. The obtained capacitances for the system are summarized in Table 4.1.

#### Stray capacitances from the transmon SQUID

As will be shown in Section 7.1, the transmon qubit has a SQUID with a large loop ( $\sim 55 \mu\text{m} \times 1.2 \mu\text{m}$ ). Due to its large size, the capacitances associated to this SQUID are not negligible. In Fig. 4.24 (a) the SQUID design with the different capacitances is given. The lumped element model used for simulating the system is shown in Fig. 4.24 (b)

We follow the same procedure as before. Given the small number of fitting parameters ( $C_{\text{sh},S}$  and  $C_{g,S}$ ) we can perform a single fit with  $Z_{\text{left}} = 50 \Omega$  and  $Z_{\text{right}} = 3000 \Omega$ . The result of the fit is shown in Fig. 4.25 with the obtained capacitance values. The SQUID increases both the shunting capacitance and the ground capacitance of the transmon qubit. All the transmon qubit capacitances, including those from the coupling capacitors and from the SQUID, are given in Table 4.1.

Capacitance	Value (fF)
$C_{g,T2}$	$33 \pm 1$
$C_{g,T} = C_{g,T,0} + C_{g,S}$	$48 \pm 2$
$C_c$	$119 \pm 2$
$C_{\text{sh}} = C_{\text{sh},0} + C_{\text{sh},S}$	$6.9 \pm 0.1$
$C_{J,T}$	$5.2 \pm 0.3$

Table 4.1 – Simulated capacitances for the measured sample. The first capacitances were obtained using EM simulation software. The last one was obtained using the empirical relation in Eq. (4.18).

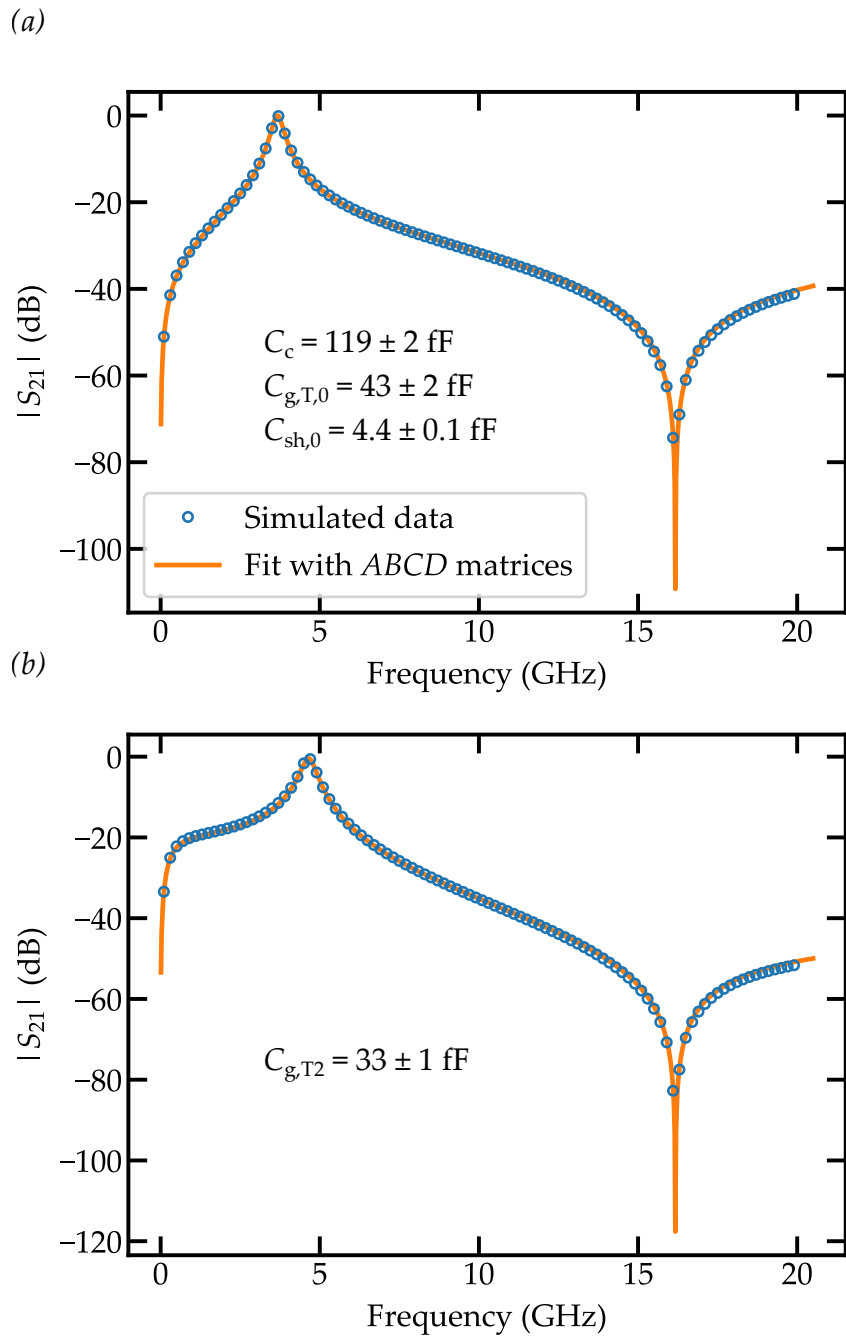


Figure 4.23 – Capacitances estimation. Simulated transmission from the EM software (blue circles) and fit from the lumped element model, orange solid line. (a) First simulation with  $Z_{\text{left}} = Z_{\text{right}} = 50 \Omega$ . (b) Second simulation with  $Z_{\text{left}} = 50 \Omega$  and  $Z_{\text{right}} = 3000 \Omega$ .

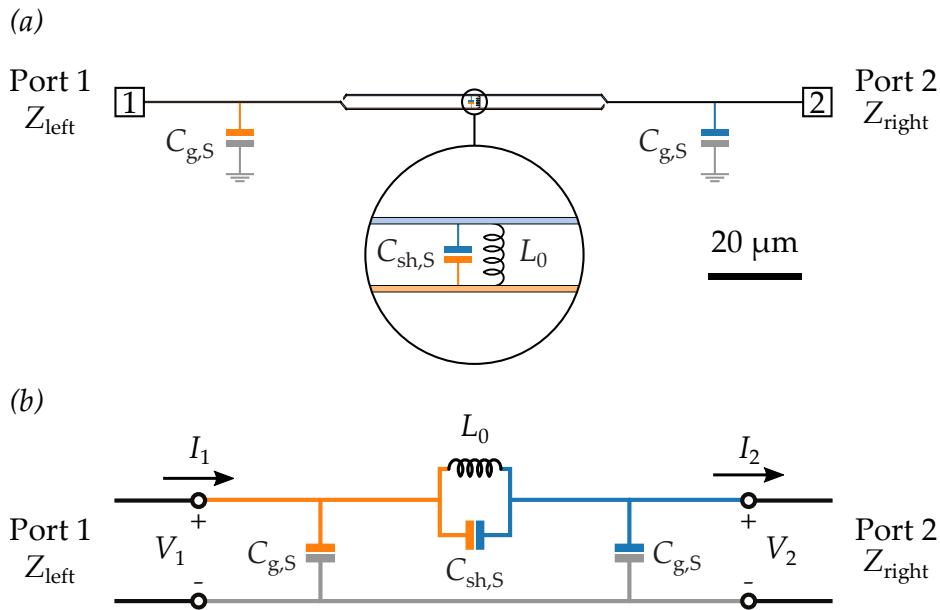


Figure 4.24 – (a) Real design of the SQUID of the transmon qubit. In the inset the shunting capacitance  $C_{sh,S}$  and test inductance  $L_0$  are shown. (b) Lumped element model used to simulate the capacitances of the system.

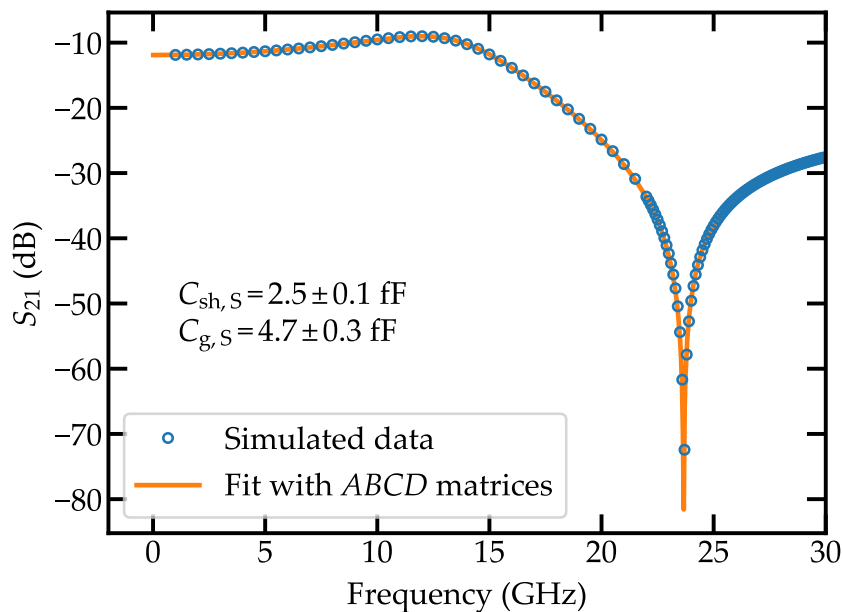


Figure 4.25 – SQUID capacitances estimation. Simulated transmission (blue circles) and fit from the lumped element model, orange solid line. The simulation was performed setting  $Z_{\text{left}} = 50 \Omega$  and  $Z_{\text{right}} = 3000 \Omega$ .

# Experimental setup

# 5

This chapter contains all the information related to how the different samples were measured. First we introduce the cryostat where the experiments were performed. Then we introduce the different upgrades realized during my PhD: thermalization of the microwave components, a hydrogen filter for the mixture, magnetic shielding of the sample and radiation filtering at the input lines. Finally we describe the microwave setup as well as the sample holder.

## 5.1 *The dilution refrigerator*

When measuring superconducting quantum circuits it is important to ensure that there are no thermal excitations in the system. The relevant transition frequencies in these circuits are in the GHz range.

In order to measure these transitions we need to reach a temperature where the thermal excitations in the circuits are negligible. If we denote the mean number of thermal photons as a function of frequency and temperature by  $n(\omega, T)$ , we need to work at a temperature where  $n(\omega, T) \ll 1/2$ , below the quantum vacuum oscillations.  $n(\omega, T)$  is given by the Bose-Einstein distribution,

$$n(\omega, T) = \frac{1}{e^{\frac{\hbar\omega}{k_B T}} - 1}. \quad (5.1)$$

In Fig. 5.1 we show the average number of photons as a function of frequency for four different temperatures. We show frequencies from 0.3 GHz to 20 GHz which is the range of the energy transitions in superconducting quantum circuits. The limit  $n(\omega, T) = 1/2$  is shown as a horizontal dashed line. As it can be seen we need to reach a temperature as low as 20 mK to reduce the thermal excitations in the system below this limit. Even at this temperature there are some thermal excitations for the lowest frequencies, see inset in Fig. 5.1. This means that for long arrays of SQUIDS the lowest frequency modes are going to be affected by thermal photons.

In order to reach temperatures of 20 mK we use a dilution refrigerator. For a detailed description of the working principle of a dilution refrigerator refer to De Waele<sup>104</sup> and Pobell<sup>105</sup>. Here we describe the refrigerator where we performed the measurements pointing out the upgrades introduced during my PhD.

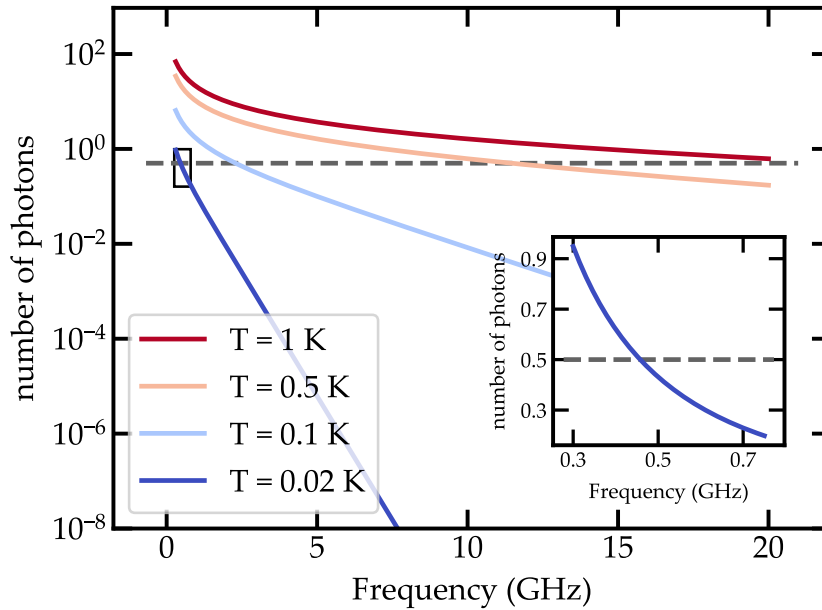


Figure 5.1 – Average number of photons as a function of their frequency for several values of temperature. The dashed line marks the limit  $n(\omega, T) = 1/2$ . The curves are obtained using the Bose-Einstein distribution. A zoom in for frequencies below 1 GHz for  $T = 20$  mK is given in the inset.

### 5.1.1 The Inverse Dilution Refrigerator

The working principle of the Inverse Dilution Refrigerator (IDR) used in this work is the same as the usual one. Its main peculiarity is that it is inverted, the coldest part is at the top of the fridge and the warmest at the bottom. It uses two different flows. The primary one is the usual  $^3\text{He}/^4\text{He}$  flow of dilution refrigerators. The secondary one is a  $^4\text{He}$  flow used for cooling down the cryostat to 4 K. The cryostat lies on top of a 100 L  $^4\text{He}$  dewar from where it takes the  $^4\text{He}$  for this flow, see Fig. 5.2 (a). This dewar is kept slightly over pressured to ensure a continuous flow during operation. When cooling down, a pump is used to increase the helium flow. The  $^4\text{He}$  consumption during operation is around 13 L per day, therefore it needs to be refilled at least once a week.

The fridge is divided in several stages each related to one temperature, see Fig. 5.3. Each of these stages counts with a metal plate to thermalize the different parts of the cryostat and the different microwave components. The first two stages are the 100 K stage and the 20 K stage. The next one is the 4 K stage. The helium from the  $^4\text{He}$  dewar is stored in the 4 K pot at this stage. The primary cooling cycle is thermally connected to the 4 K pot. The next stage is the 800 mK stage and is where the *still* lies. The last two stages are in the same plate. The outer ring of the plate is the 40 mK stage and contains the *cold plate*. This cold plate is the link between the continuous and the discrete heat exchanger. The inner part is at 20 mK and is thermally connected to the *mixing chamber*. Both parts are mechanically connected via a poor heat conductor (stainless steel) to reduce the

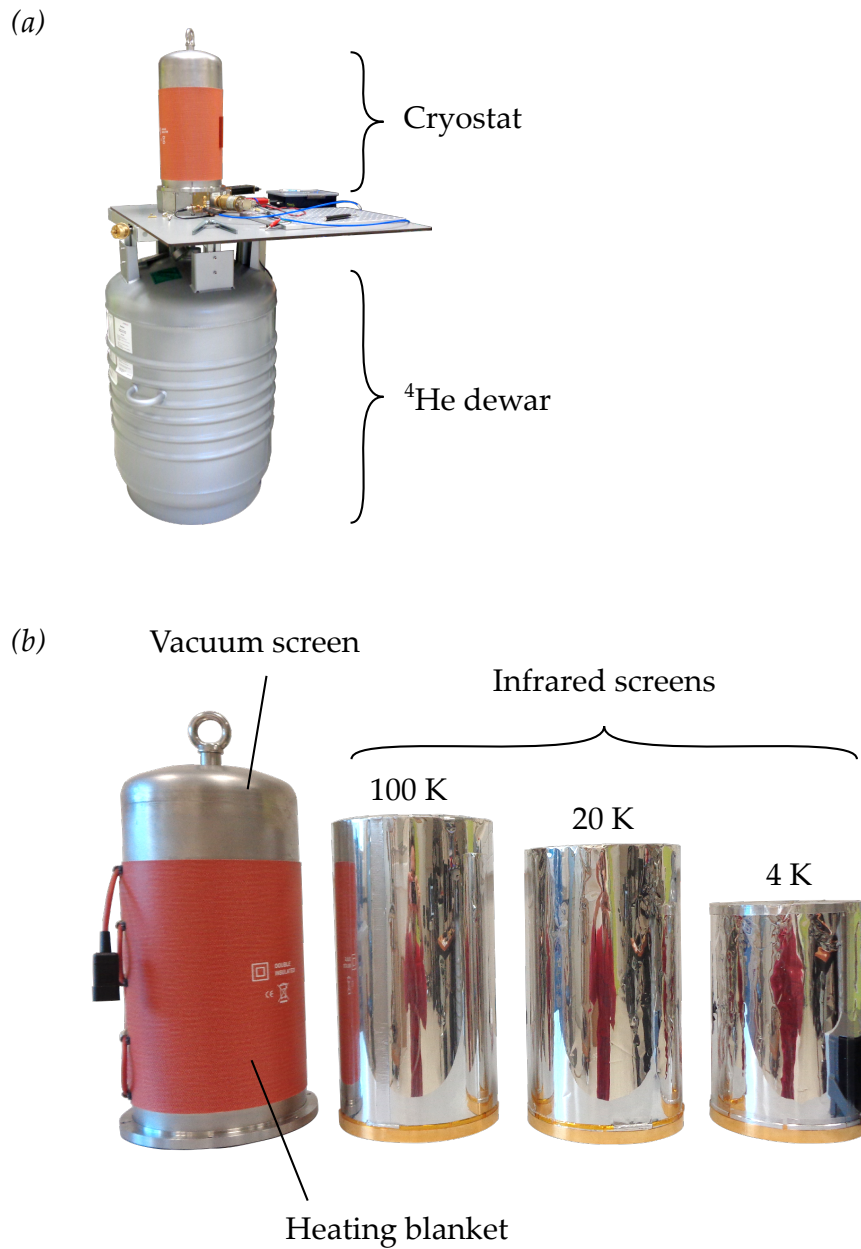


Figure 5.2 – Inverse Dilution Refrigerator. (a) General picture of the IDR. The cryostat lies on top of a helium dewar. (b) Vacuum screen and the three infrared radiation screens anchored at the 100 K, 20 K and 4 K stage respectively. A heating blanket around the vacuum screen speeds up the warm up.



heat flow from the 40 mK stage to the 20 mK stage. We anchor the sample we want to measure at 20 mK.

To avoid infrared radiation from warmer stages heating colder ones highly reflective screens are used, see Fig. 5.2 (b). These are mirror polished aluminum screens that we anchor at each of the stages' plates. Finally the outermost screen covers the whole cryostat and keeps it under vacuum. It is wrapped with a heating blanket to speed up the warming up of the fridge. The fridge operation is fully automated. The IDR cools down from room temperature to base temperature in less than ten hours. Using the heating blanket it can warm up in less than two hours.

### 5.1.2 Nitrogen and hydrogen traps

The closed circulation cycle of  $^3\text{He}$  goes from room temperature to 20 mK. If we would have some impurity in the cycle it would solidify at a given stage in the fridge clogging the  $^3\text{He}$  circulation. To avoid that a *nitrogen trap* is used. It consists of a very porous material (activated charcoal) that at low temperatures traps any liquid that goes through it. To cool it down we sink it in liquid nitrogen (70 K) and circulate the mixture through it, see Fig. 5.4 (a). Everything with a condensation temperature above 70 K is trapped there and does not reach the cryostat. The trap needs to be warmed up and pumped every month to keep it empty.

Any impurity with a boiling point below 70 K still goes through the trap. During my PhD the cryostat clogged frequently after one or two days of operation despite the nitrogen trap. Hydrogen, with a boiling point of 10 K, was getting trapped between the 20 K stage and the 4 K stage. This hydrogen is known to come from the oil of the different pumps and the grease of the various seals in the setup. A hydrogen filter<sup>a</sup>, Fig. 5.4 (b), was installed right after the nitrogen trap. It uses a metal powder to adsorb the Hydrogen. After the installation of this filter the cryostat could operate during weeks without clogging.

### 5.1.3 Thermalization of the microwave components

The components we use for the experiment must be thermally connected to the cryostat. Otherwise they will release heat during the cool down and the cryostat will not reach its base temperature. Most of the components are anchored to their respective stage via copper brackets, see Fig. 5.5 (a). This ensures that the component is at the same temperature as the plate.

In the case of coaxial cables, they link stages at different temperatures. This might create a thermal shortcut between the two stages with heat from the warmer stage reaching the colder one. To avoid this the cables need to be long enough so there is a temperature gradient along them. Following the approach in Dumur<sup>106</sup> we can model a coaxial cable as an homogeneous metal cylinder of length  $L$  and cross section  $S$  with a linear thermal conductivity  $\kappa(T) = \kappa_0 T$ . If the cable links a stage with temperature  $T_2$  with a stage with temperature  $T_1$  ( $T_2 > T_1$ ) the heat load arriving to the colder stage is given by

$$P = \frac{\kappa_0 S}{2L} (T_2^2 - T_1^2). \quad (5.2)$$

<sup>a</sup>[http://www.nupure.com/Pages/PF\\_Series.htm](http://www.nupure.com/Pages/PF_Series.htm)

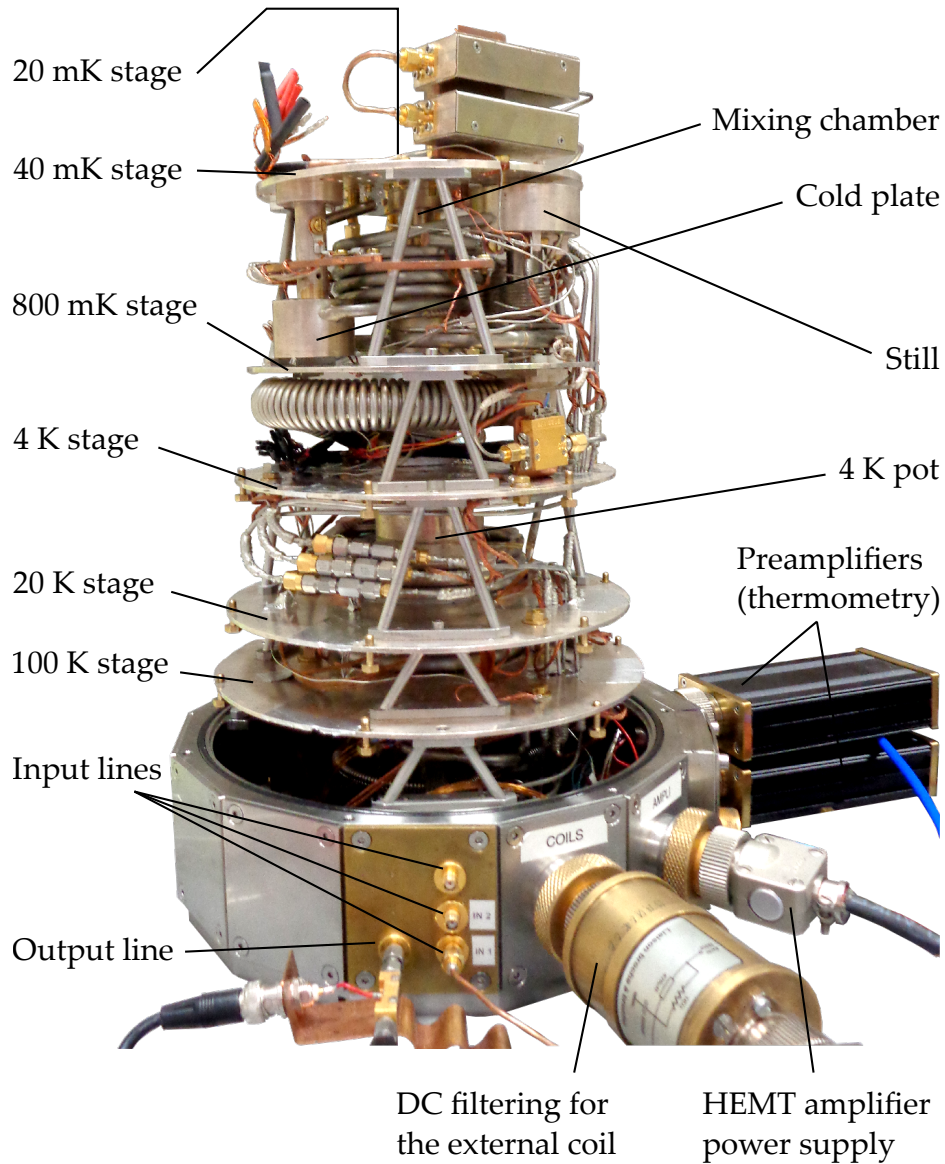


Figure 5.3 – Open cryostat showing the different stages and the different parts of the dilution refrigerator. The temperature decreases from bottom to top. The sample holder is placed at the top of the cryostat anchored to the mixing chamber. At the bottom the input and output lines as well as the power supply for the amplifier and the connection for the external coil are shown. At the right the two preamplifiers used for the thermometers measurement can be seen.

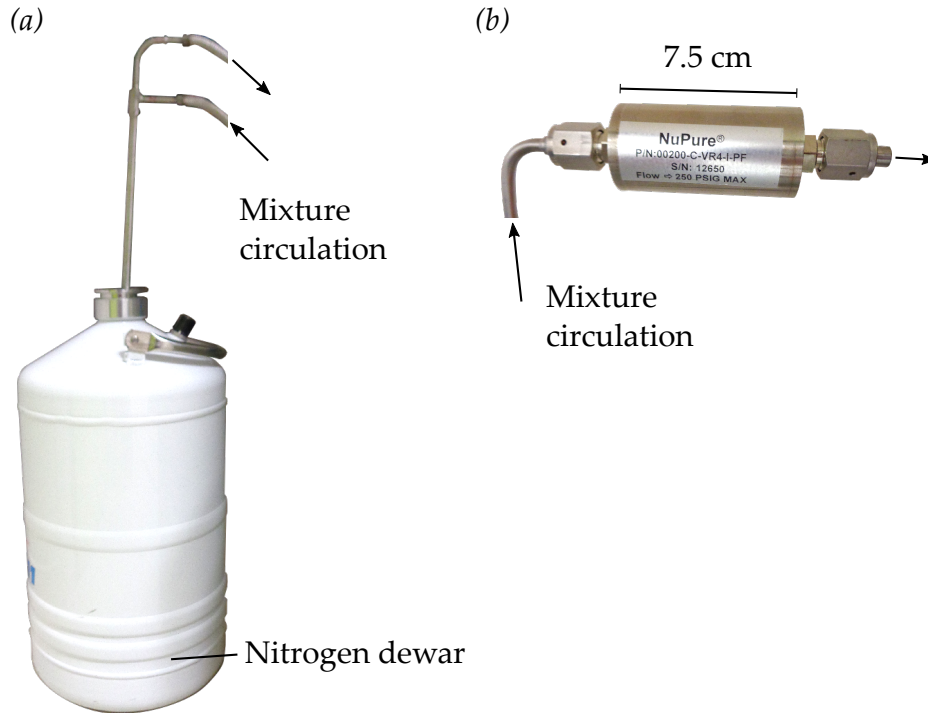


Figure 5.4 – (a) Nitrogen trap inside a nitrogen dewar. The mixture circulates through the trap leaving the impurities trapped inside. (b) Hydrogen trap. It eliminates the hydrogen via adsorption by a metallic powder. It is used at room temperature.

The cooling power for the IDR is around  $P_0 \sim 1 \mu\text{W}$  at the mixing chamber just above base temperature (20 mK). If we use a standard coaxial cable made of copper ( $\kappa_0 = 4200 \text{ W}/(\text{mK}^2)$ ) with a cross section of  $S = 1.8 \text{ mm}^2$  connecting the still ( $T_2 = 800 \text{ mK}$ ) and the mixing chamber ( $T_1 = 20 \text{ mK}$ ) we would need a cable around two kilometers long in order to get a heat load lower than  $P_0$ . We therefore use stainless steel cables<sup>b</sup> with a much lower thermal conductivity,  $\kappa_0 = 4.3 \times 10^{-3} \text{ W}/(\text{mK}^2)$ . In the setup we use three cables of length  $L = 40 \text{ cm}$  which give a heat load  $P = 18 \text{ nW} \ll P_0$ .

The important point now is to make sure that each portion of the cable is thermalized at each of the stages it goes through. This thermalization consists of a copper braid soldered to the external conductor of the cable, see Fig. 5.5 (b). At the other end of the copper braid we put a hook so we can anchor the braid to the stage plate. This is done for several stages. Finally at the cold plate we use a through to both thermalize and make a stable connection, see Fig. 5.5 (c).

Finally, due to the fact that the inner and outer conductors are thermally isolated from each other, we use microwave attenuators at the input line between the cables to thermalize the inner conductor. On top of that, these attenuators thermalize the photons arriving to the sample from room temperature to the cryostat's base temperature<sup>106</sup>. Regarding the output lines, to avoid thermal noise from warmer stages interfering with our outgoing signal we use two isolators in series, Fig. 5.5 (a). All the thermal noise coming from the warmer stages is directed by

<sup>b</sup>Reference for the cables: SC-219/50-SS-SS from COAX CO., LTD.

these isolators to a  $50\ \Omega$  load where it is dissipated.

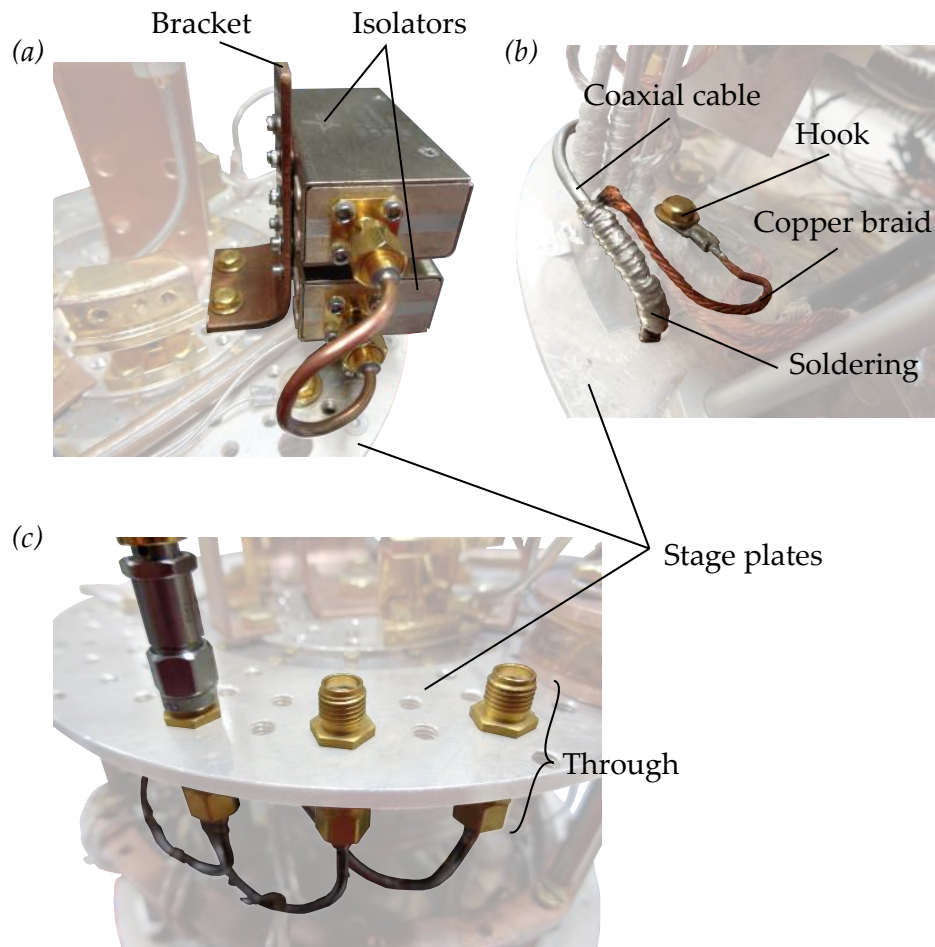


Figure 5.5 – Microwave components thermalization. (a) Most components are thermalized via a copper bracket. In the image two isolators are anchored to the 20 mK stage. (b) Wires are thermalized at each stage using a copper braid. (c) At the 40 mK stage we use a through for thermalization and for mechanical stability.

#### 5.1.4 Magnetic and radiation filtering

To screen the external magnetic field at the sample we place it inside a *mu-metal* screen. The term *mu-metal* refers to a metal with high magnetic permeability  $\mu$ . When an external magnetic field reaches the screen it penetrates its walls but not its interior. In this work we used a copper screen and we wrapped it with Metglas<sup>c</sup>, see Fig. 5.7 (a).

Regarding external radiation, it can enter the cryostat and excite quasi particles in the circuits<sup>107</sup>. It has been shown<sup>108,109,110</sup> that these quasi particles influence the coherence and relaxation of superconducting qubits. This radiation can enter directly into the cryostat through the different screens or through the coaxial cables. To avoid the former we coated the interior of the *mu-metal* screen with black

<sup>c</sup>Metglas 2714A Magnetic Alloy

coating<sup>107</sup>, Fig. 5.7 (a). This coating consists of silicon balls, carbon powder and black STYCAST<sup>®d</sup>.

For the radiation coming from the coaxial cables we use home made dissipative filters, see Fig. 5.7 (b). They consists of a short section of a coaxial cable where the inner conductor is made of silver-plated copper and the outer conductor of copper. The filter is impedance matched to the  $50\ \Omega$  cables to avoid reflections. For the dielectric we use a microwave absorbing material<sup>e</sup> that filters out very high frequency radiation ( $> 20\ \text{GHz}$ ). In Fig. 5.6 we plot the transmission  $S_{21}$  and reflection  $S_{11}$  for the filter shown in Fig. 5.7 (b). Our measurement range stops at  $20\ \text{GHz}$  and therefore we cannot measure the cut-off frequency of the filter. However we see a slope in transmission that is related to the high-frequency filtering.

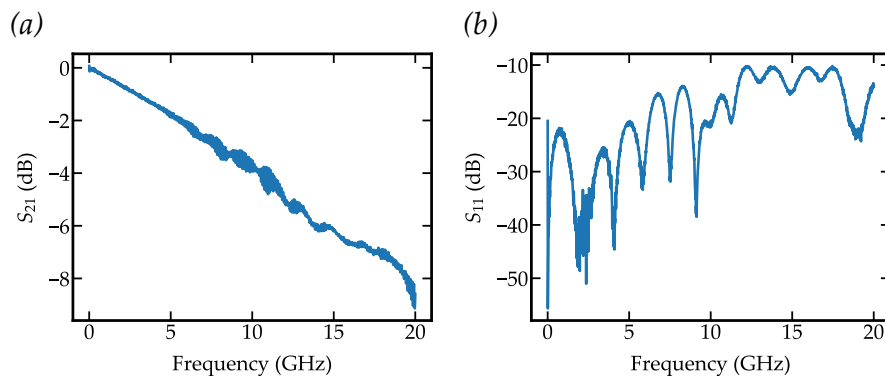


Figure 5.6 – (a)  $S_{21}$  and (b)  $S_{11}$  parameters for the filter in Fig. 5.7 (b).

## 5.2 Microwave setup

In order to probe our system we perform microwave transmission measurements using a Vector Network Analyzer<sup>f</sup> (VNA). The VNA has two ports that can both generate and detect microwave signals. Sweeping the frequency in the GHz range the VNA obtains the amplitude and phase of the desired scattering parameter as a function of frequency. To perform these transmission measurements we need to connect the VNA at room temperature to our sample inside the dilution fridge at  $20\ \text{mK}$ . As mentioned before, we use microwave attenuators to thermalize the inner conductor of the input cables and to attenuate the black body radiation of the higher temperature stages. In addition, these attenuators reduce the electrical power arriving to the sample. This makes it possible to reach power levels corresponding to one microwave photon times unit bandwidth. We need to amplify the outgoing signal from the sample to be able to detect it with the VNA. We use two amplifiers, a HEMT amplifier<sup>g</sup> at  $4\ \text{K}$  and a standard amplifier<sup>h</sup> at room temperature. The former defines the signal to noise ratio and the latter amplifies the signal for the VNA detection. As will be explained later, see Chapter 6, in order

<sup>d</sup>STYCAST<sup>®</sup> 2850 FT. Emerson & Cumming.

<sup>e</sup>RS-4000HT Series Solid Form Microwave Absorber. Resin System Corporation.

<sup>f</sup>R&S<sup>®</sup> ZNB20

<sup>g</sup>LNF-LNC1\_12a

<sup>h</sup>MITEQ JS4



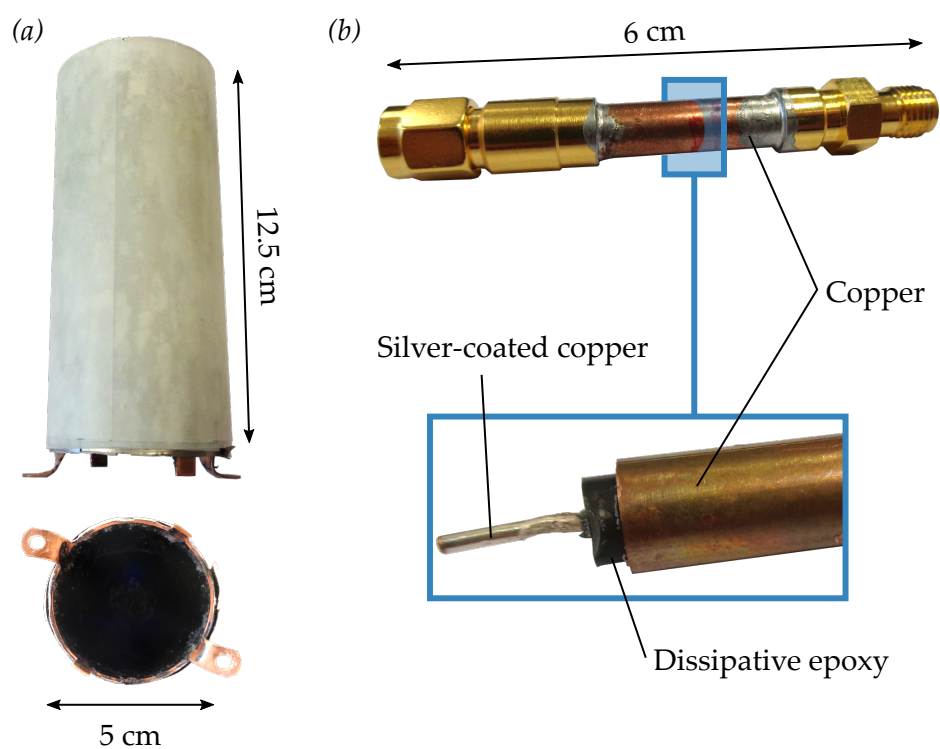


Figure 5.7 – (a) Mu-metal screen used to shield the sample against external magnetic fields. The inner part of the screen was coated with a radiation absorber (bottom). (b) Home made radiation filters. As inner conductor we use silver-coated copper, copper as the outer conductor and a microwave absorbing epoxy (see main text) as the dielectric.

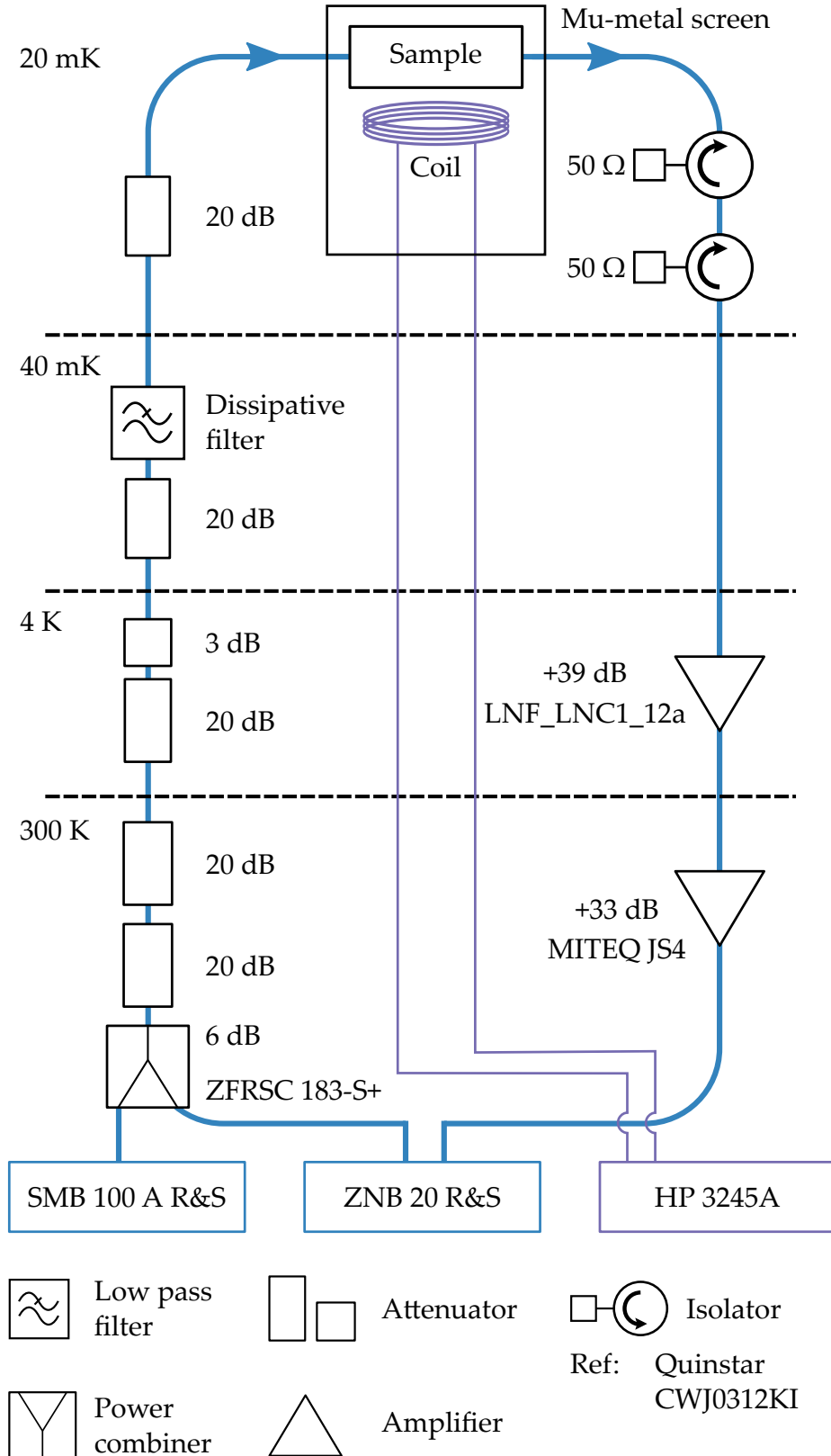


Figure 5.8 – Experimental setup. The measurement consists in microwave transmission measurements through the sample using a VNA. The external magnetic flux is applied via a superconducting coil in purple. For the two tone measurements a microwave source is used.

to measure outside our setup bandwidth we perform a *two tone measurement*. It uses two microwave tones, one for probing the system and the other for driving it. The first tone is applied with the VNA. For the second tone we use a microwave source<sup>i</sup>. They are both connected to the input line via a power combiner<sup>j</sup>.

The external magnetic flux is applied via a superconducting coil anchored to the upper part of the sample holder. We use a current source<sup>k</sup> to apply a DC current to the coil. The sample holder with the sample and the external coil are both inside the mu-metal shield. The whole microwave setup is shown in Fig. 5.8.

### 5.2.1 The sample holder

To perform the transmission measurements we fit the sample in a sample holder. The input and output pads of the sample are connected to the input and output ports of the sample holder. On the other end, these ports can be directly connected to the input and output lines of the microwave setup. In this way the transmission through the sample can be measured. In addition, the sample holder is anchored to the cryostat and therefore thermalizes the sample.

#### *Description*

The sample holder consists of two parts, see Fig. 5.9 (a). The lower part is a foot that is anchored to the mixing chamber. It provides the thermal contact between the cryostat and the sample. The upper part is where the chip is placed, see Fig. 5.9 (a) right picture. It has four coaxial cables which are directly soldered to the sample holder. Inside it the cables were cut in half exposing the inner conductor where the sample can be directly wire bonded. This design ensures a light-tight sample holder, i.e. the unwanted radiation reaching the sample through the input and output ports is reduced at most. However, this comes with a drawback, whenever the inner conductor bends or is damaged the sample holder needs to be refurbished.

The sample is glued to the sample holder using silver conducting adhesive paint<sup>l</sup>. This paste ensures a good electrical contact between the sample and the sample holder. Care needs to be taken so the silver does not reach the connectors shunting them to ground. The superconducting coil is screwed on top of the sample holder as shown in Fig. 5.9 (b). The sample holder together with the superconducting coil is designed to fit inside the mu-metal screen shown in Fig. 5.7 (a). This sample holder was used to perform all the measurements presented in this work.

#### *Characteristics*

To characterize the sample holder we measure its transmission ( $S_{21}$ ) and reflection ( $S_{11}$ ) in the VNA frequency range (100 kHz to 20 GHz). A microstrip through is installed instead of the sample. We perform the measurement for the two pairs of

---

<sup>i</sup>SMB 100A

<sup>j</sup>ZFRSC-183-S+

<sup>k</sup>HP 3245A

<sup>l</sup>RS Pro Bottle of Silver Conductive Adhesive Paint. Stock No: 186-3600



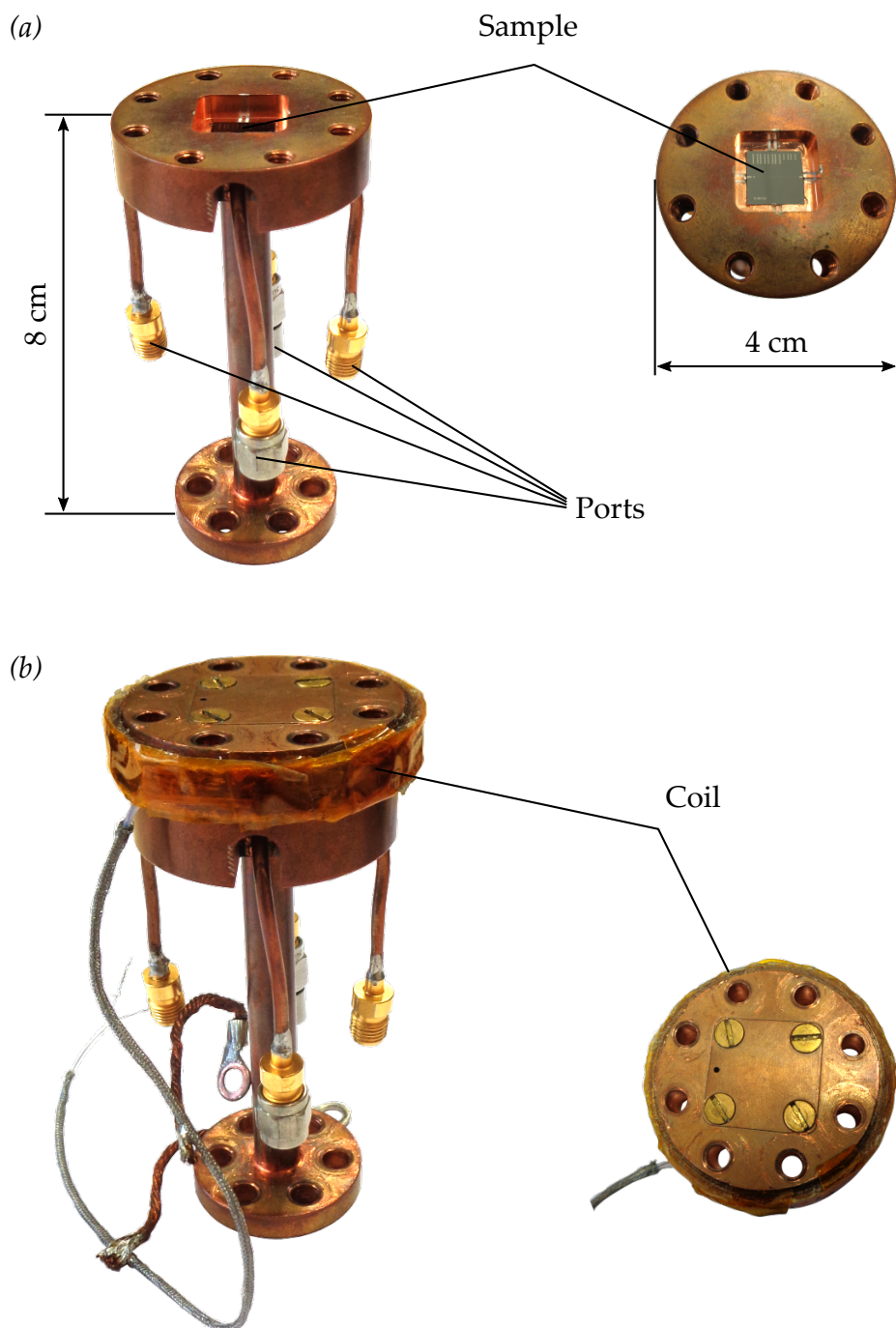
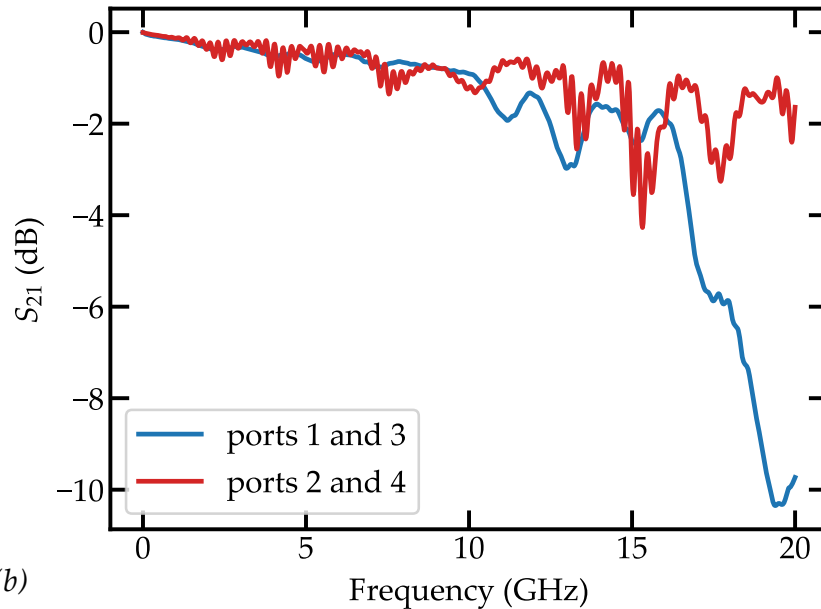


Figure 5.9 – (a) Sample holder used in this work. The sample is placed in the upper part and wire bonded directly to the inner conductor of the coaxial cables, see right picture. The foot connects the sample holder to the mixing chamber of the dilution fridge. (b) The superconducting coil (right) is placed on top of the sample holder (left).

ports. The obtained curves are shown in Fig. 5.10. As it can be seen, the transmission is above  $-4$  dB and reflection is below  $-10$  dB for ports 2 and 4. For ports 1 and 3 there was a finite conductance to ground coming from the silver paint that is responsible for the high reflection at high frequencies.

(a)



(b)

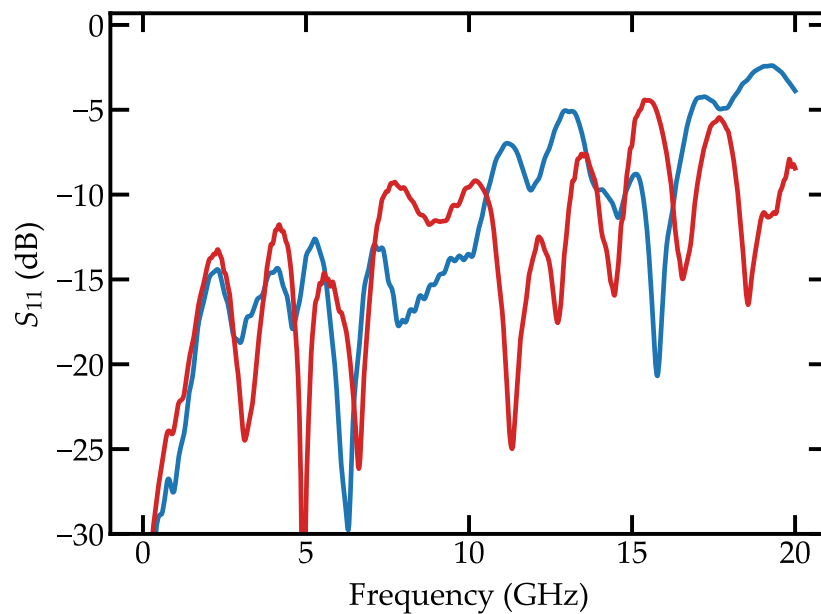


Figure 5.10 – (a)  $S_{21}$  and (b)  $S_{11}$  parameters for the sample holder in Fig. 5.9 for its four ports.



# Characterization of the arrays of SQUIDS

# 6

As a tunable high impedance environment we use an array of SQUIDS. Here we present the transmission measurements of several of these arrays and observe the flux modulation of their modes. Finally we fit the dispersion relation of one of them to obtain its parameters.

## 6.1 Measured samples

During my PhD several arrays of SQUIDS were measured. They are all fabricated on a  $300\ \mu\text{m}$  thick intrinsic silicon substrate. The dimension of the chip is  $1\ \text{cm} \times 1\ \text{cm}$  ( $1\ \text{cm} \times 0.45\ \text{cm}$  for some samples). A photograph of one of these samples is shown in Fig. 6.1. The two  $50\ \Omega$  pads can be seen at both ends of the chip. In the inset an

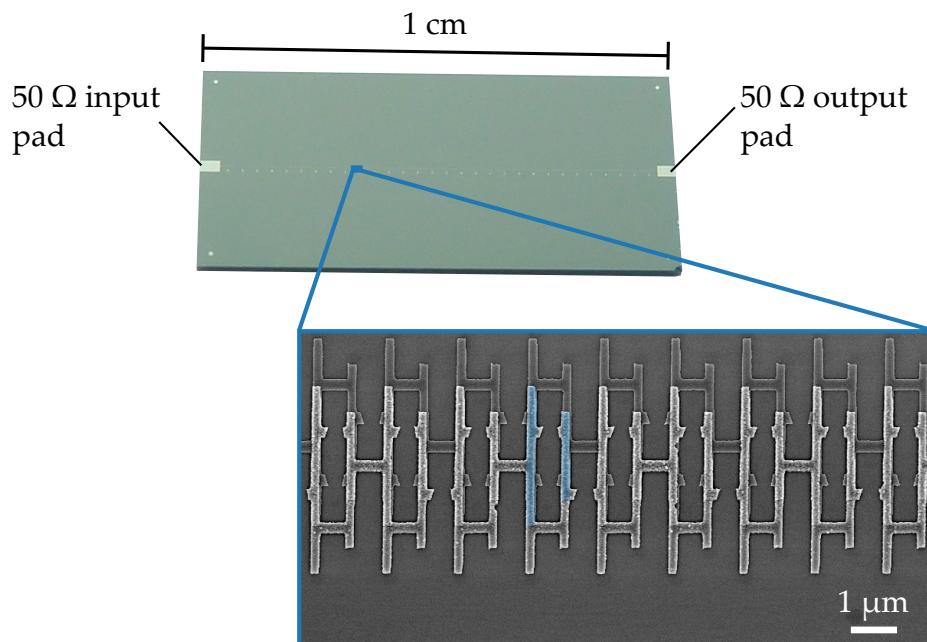


Figure 6.1 – Photograph of a sample containing an array of asymmetric SQUIDS galvanically coupled to two ports. The substrate is silicon and the metal is aluminum. The two  $50\ \Omega$  input and output pads are located at both ends of the chip. The inset contains an SEM picture of the array. In blue the Josephson junctions are shown.

SEM picture of one part of the array is given. It can be seen that for this array the

SQUIDS are asymmetric, i.e. one junction is larger than the other. As will be shown later this has an effect on the flux modulation of the modes of the array.

## 6.2 Transmission measurements

We perform transmission measurements of the sample using a VNA. We obtain  $S_{21}$  as a function of the applied microwave frequency. To perform the measurements the sample is mounted in the sample holder shown in Fig. 5.9 and wire bonded to its input and output ports. We use two different geometries for the arrays. In the first one the array is side coupled to a transmission line while in the second one it is in line coupled.

### 6.2.1 Side coupled array

The array is capacitively coupled at one side of a  $50\ \Omega$  transmission line, see Fig. 6.2. When measuring the transmission line we obtain a dip at each of the resonance frequencies of the array. The advantage of this configuration is that we can obtain the internal and external quality factors from the measured dips. The amplitude and the phase of one of the resonances of an array of length  $N = 500$  is shown in Fig. 6.3. We fit each of the resonances using the expression for the transmission  $S_{21}$  of side coupled resonator<sup>111,112</sup>. The expression is given in Eq. (6.1).

$$S_{21}(\omega) = \frac{1 + 2iQ_{\text{int}}\tilde{\omega}}{1 + \frac{Q_{\text{int}}}{Q_{\text{c}}} + 2iQ_{\text{int}}\tilde{\omega}} \quad (6.1)$$

$$\tilde{\omega} = \frac{\omega - \omega_{\text{r}}}{\omega_{\text{r}}}$$

Here  $Q_{\text{int}}$  and  $Q_{\text{c}}$  are the internal and coupled quality factors of the resonance and  $\omega_{\text{r}}$  is its resonance frequency. A fit of one of these resonances is given in Fig. 6.3 with a red dashed line for both amplitude and phase. As it can be seen we obtain an internal quality factor of around  $Q_{\text{int}} \sim 10^4$ . The fact that  $Q_{\text{int}} > Q_{\text{c}}$  shows that the losses in the array are mainly given by its coupling to the transmission line.

### 6.2.2 In line coupled arrays

In this configuration the arrays are galvanically coupled to two ports at both ends. The impedance of these ports is approximately<sup>a</sup>  $50\ \Omega$ . As discussed in Section 2.2.2 there is an impedance mismatch between the input and output  $50\ \Omega$  pads and the array. Because of this some of the microwave signal is reflected and some is transmitted at the boundary between the array and the  $50\ \Omega$  pads. This gives rise to an interference phenomena similar to the one in a Fabry-Pérot interferometer. For some frequencies  $\omega_k$  standing waves (both for voltage and current) are formed, see Fig. 6.4. These frequencies are the eigenfrequencies of the array and the standing waves are its eigenmodes.

<sup>a</sup>The wire bonds act as small inductors but generally they can be neglected if several of them are used.

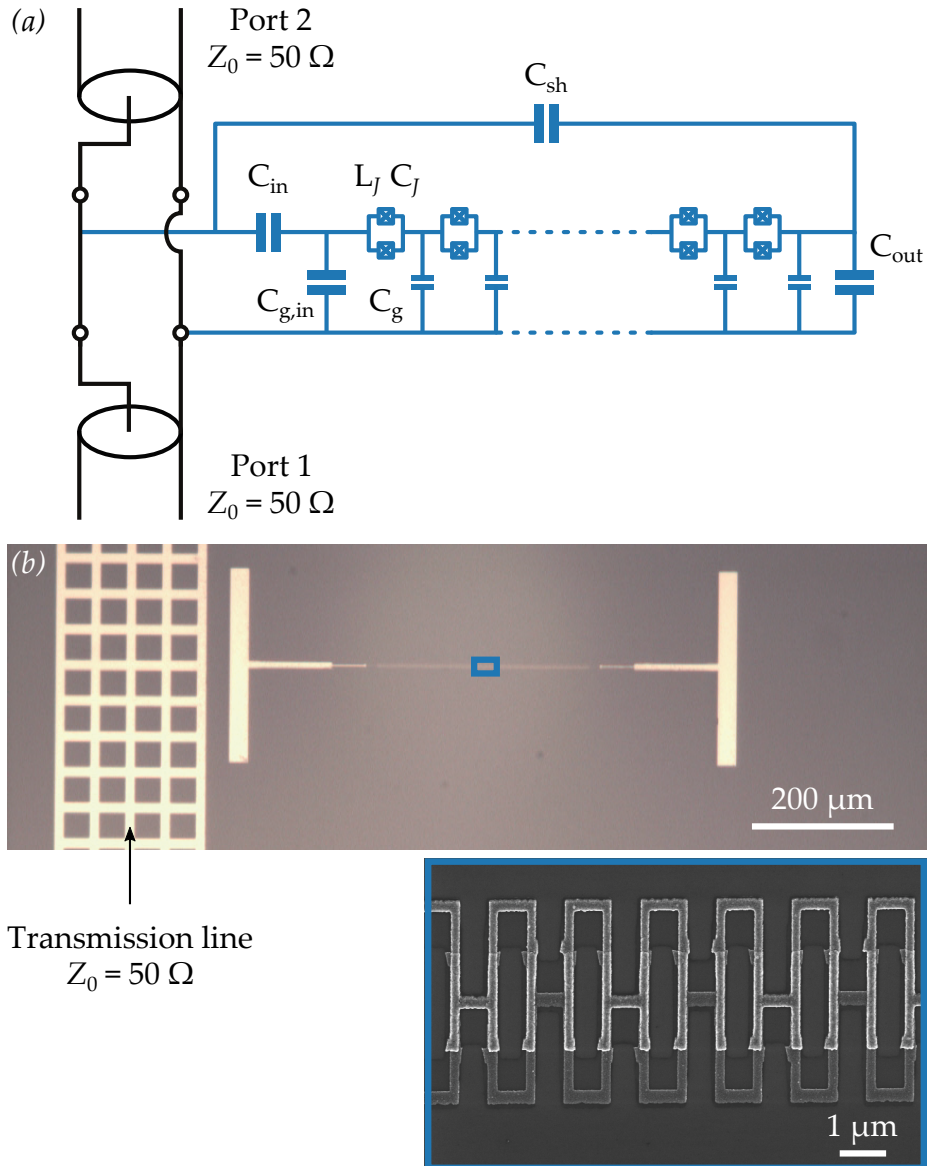
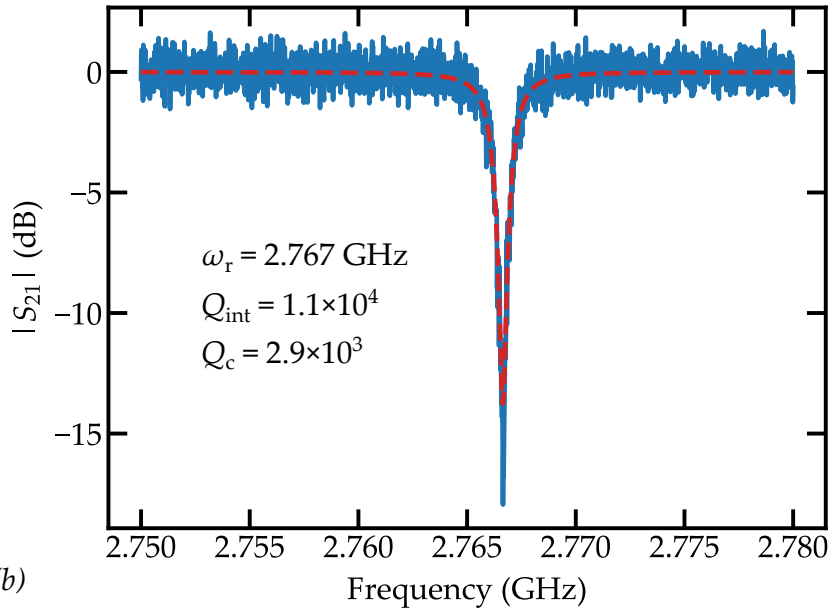


Figure 6.2 – Side coupled array. (a) Circuit diagram of the sample. A capacitance  $C_{in}$  couples the array to the transmission line. The other capacitances of the system are given. (b) Optical image of the sample. The  $50 \Omega$  transmission line is shown at the left. The inset shows an Scanning Electron Microscope (SEM) image of the array (blue square).

(a)



(b)

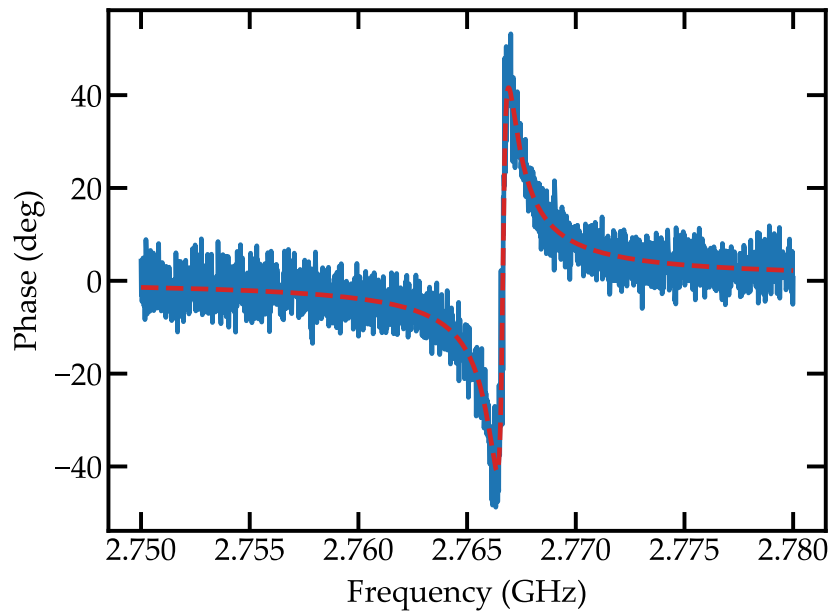


Figure 6.3 – Fit of one of the resonances of the array using Eq. (6.1) for both (a) the amplitude and (b) the phase.

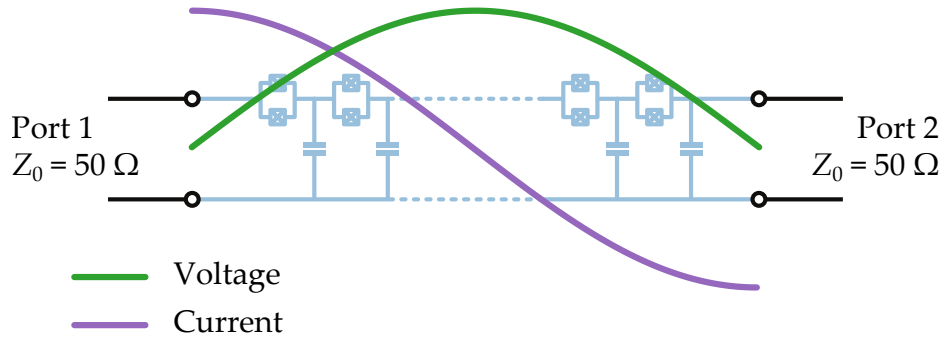


Figure 6.4 – Representation of the voltage (green) and current (purple) corresponding to the first mode of the array.

For each  $\omega_k$  we measure a peak in transmission, see Fig. 6.5. This is similar to the result obtained using  $ABCD$  matrices in Section 2.2.2. The width of these resonances is directly related to the losses in the system. We perform a fit with a Lorentzian of one of the resonances and obtain a width of  $\Gamma_{\text{array}} = (6.18 \pm 0.02)$  MHz. This gives a quality factor of  $Q = (7.20 \pm 0.02) \times 10^2$  for the resonance at 4.45 GHz. This value is comparable to the quality factor obtained using  $ABCD$  matrices for an array with the same parameters and for the same mode frequency,  $Q_{ABCD} = 6.9 \times 10^2$ . Given the fact that all arrays are fabricated following the same fabrication procedure, we can assume that the internal quality factors of the arrays are the same. If we compare the obtained  $Q$  for this array with the internal quality factor obtained previously for the side coupled array  $Q_{\text{int}} \sim 10^4$ , we observe that the width of the resonances is mainly given by the coupling to the  $50 \Omega$  input and output ports.

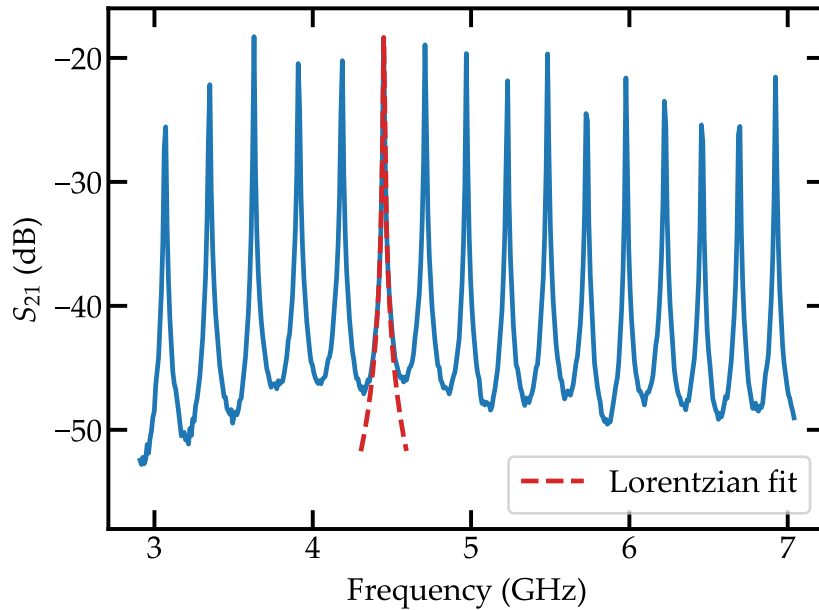


Figure 6.5 – Transmission through the array as a function of the microwave frequency. In red a fit to a Lorentzian of one of the peaks is shown.



### Flux tuning

Each of the sites in the array contains a SQUID. Therefore we can tune the eigenfrequencies of the array via an external magnetic flux  $\Phi_C$ . This flux tunes the critical current of the SQUIDS following Eq. (2.10). This changes the inductance of each of the SQUIDS in the array and hence its dispersion relation according to

$$\omega(k, \Phi_C) = \frac{1}{\sqrt{L_J(\Phi_C) C_J}} \sqrt{\frac{1 - \cos(ka)}{1 - \cos(ka) + \frac{C_g}{2C_J}}}. \quad (6.2)$$

Here  $L_J(\Phi_C)$  is modulated via Eq. (6.3). As already mentioned in Section 2.1.1,  $d$  is the asymmetry between the junctions in the SQUID.

$$L_J(\Phi_C) = \frac{L_J}{\left| \cos\left(\pi \frac{\Phi_C}{\Phi_0}\right) \right| \sqrt{1 + d^2 \tan^2\left(\pi \frac{\Phi_C}{\Phi_0}\right)}}. \quad (6.3)$$

In Fig. 6.6 we show the transmission of two different samples as a function of frequency and the applied magnetic flux  $\Phi_C$ . The first sample, Fig. 6.6 (a), is an array of SQUIDS with 500 symmetric SQUIDS. The second one, Fig. 6.6 (b), is the array of 5394 asymmetric SQUIDS from Fig. 6.1. It is clear that the Free Spectral Range (FSR) becomes smaller the longer the array. For coupling a system to several modes it is important to reduce the FSR so it becomes comparable to the coupling strength. This was the main motivation for increasing the length of the array. The difference in the asymmetry can be also observed in Fig. 6.6. For the symmetric chain all the modes go to zero for  $\Phi_C = \pm\Phi_0/2$ . However for the asymmetric one we see that the modes reach a minimum frequency. At this point the FSR is highly reduced. A zoom in of this region (red square in Fig. 6.6 (b)) is shown in Fig. 6.7. All the modes of the array are tuned without any loss of visibility. This is a direct proof of the low disorder present in the array<sup>86</sup>.

## 6.3 Dispersion relation

From now on the results correspond to the in line coupled array corresponding to Fig. 6.6 (b). From the dispersion relation in Eq. (6.2) we can obtain the parameters of the array. To fit the dispersion relation we need to measure its eigenfrequencies in a wide frequency range, from 0.1 GHz to 20 GHz. We are however limited to the bandwidth of the microwave readout setup, from 2.5 GHz to 13 GHz. To overcome this difficulty we perform what is known as a *two tone measurement*<sup>46,86</sup>. We take advantage of the fact that the array is not completely linear. As a consequence, when applying a microwave tone at a given resonance of the chain, the other resonant frequencies are shifted. This is known as the cross Kerr effect<sup>86,113</sup>. With the VNA we measure the transmission of the system at a constant frequency  $\omega_{\text{VNA}}$ . This frequency is set to an eigenfrequency of the array,  $\omega_{\text{VNA}} = \omega_1$ . With a microwave source we apply a second tone at a variable frequency  $\omega_{\text{MW}}$ . Whenever this second tone matches a resonance of the system, the resonance  $\omega_1$  moves to  $\tilde{\omega}_1$  due to the cross Kerr effect. Because of this,  $\omega_{\text{VNA}}$  is no longer a resonance frequency of the circuit and we measure a dip in transmission. In this way we obtain

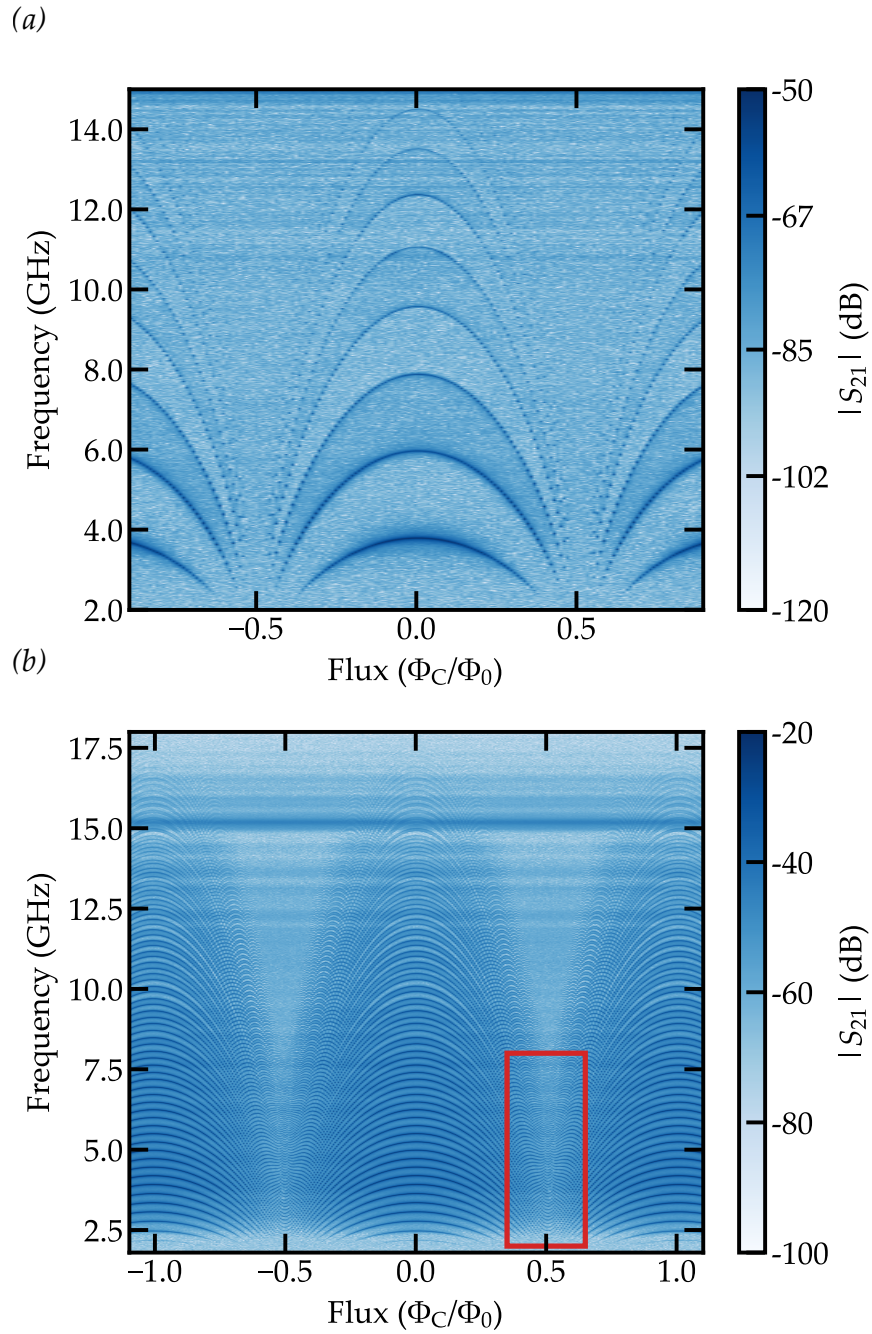


Figure 6.6 – Transmission measurement as a function of the applied magnetic flux  $\Phi_C$  for two different samples, (a) short sample ( $N = 500$ ) and (b) long sample ( $N = 5394$ ).

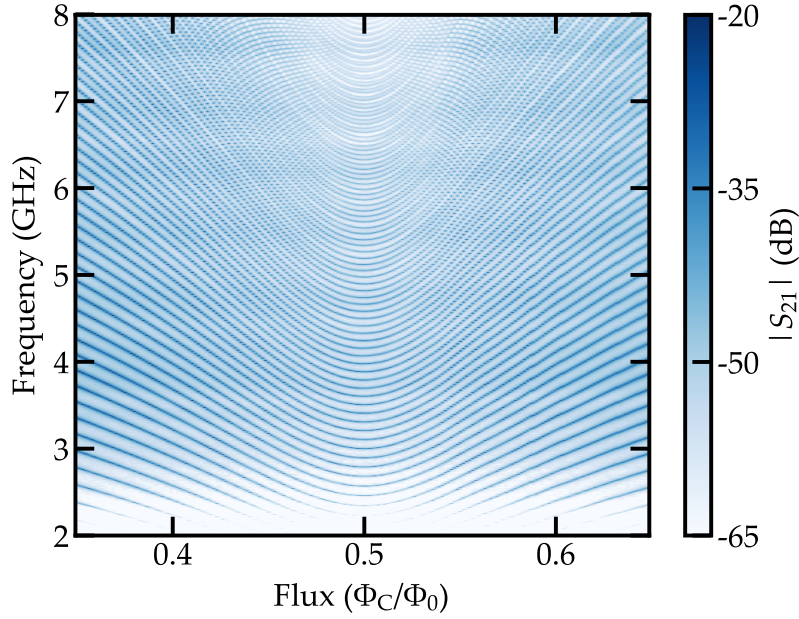


Figure 6.7 – Zoom in for the region around  $\Phi_C = \Phi_0/2$ , red square in Fig. 6.6 (b).

all the resonances of the array. Due to the fact that the VNA is only measuring at one frequency, we are not limited by the bandwidth of the microwave readout setup anymore. We are only limited by the range of the microwave source used, in this case from 100 kHz to 20 GHz, and the input microwave bandwidth. In Fig. 6.8 we show a two tone measurement for the sample with  $N = 5394$ . It can clearly be seen that the dips disappear above 17 GHz. This is the plasma frequency of the array, above it no mode propagates. We fit each of the dips to a Lorentzian line shape in order to obtain the position of each resonance frequency. The fit is not very accurate for the width of the dip. This is because for the two tone measurement we need to use high microwave power. At high power the resonances are not Lorentzians anymore. However this fit gives the resonance frequency with enough accuracy, see Fig. 6.8 inset.

From each of the resonances in Fig. 6.8 we obtain a point in Fig. 6.9 (a). We denote the lowest mode as the first mode,  $n = 1$  and label the following ones successively. We fit the obtained data points in Fig. 6.9 (a) with the expression for the dispersion relation obtained from the lumped element model, Eq. (6.2). As shown in Section 2.2.2, we can approximate the two  $50 \Omega$  pads as connections to ground. We therefore impose closed boundary conditions to the array obtaining the allowed  $k_n$  values for the eigenfrequencies,

$$k_n = \frac{n\pi}{Na}. \quad (6.4)$$

Introducing this expression in Eq. (6.2) we fit the data points in Fig. 6.9 (a) as a function of the mode index  $n$ . We point out that in the fit of the dispersion relation, the effect of  $C_J$  and  $L_J$  cannot be distinguished for  $C_J \gg C_g$ . Therefore we need to fix one of them. As previously done in Section 4.2.4, we can estimate  $C_J$  from the

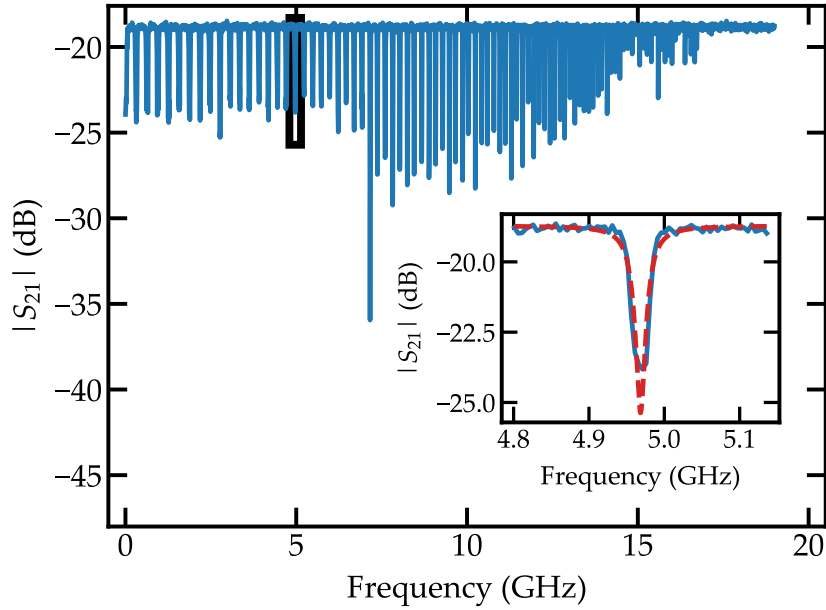


Figure 6.8 – Two tone measurement of the array of SQUIDS. For this measurement we set  $\omega_{\text{VNA}} = 7.168$  GHz. The VNA power at room temperature was set to  $P_{\text{VNA}} = -30$  dbm and the microwave source power to  $P_{\text{MW}} = -30$  dbm. The inset shows a Lorentzian fit (red) of one of the resonances.

junction area  $A$  using Eq. (4.18), reproduced here,

$$C_J = 45 \text{ fF}/\mu\text{m}^2 \times A. \quad (6.5)$$

Therefore we obtain  $C_J$  from the junction area and fit only  $L_J$  and  $C_g$ . The obtained parameters are listed in Table 6.1.

<i>Lumped element model</i>	
$L_J$	$(1.30 \pm 0.06)$ nH
$C_J$	$(46.8 \pm 0.5)$ fF
$C_g$	$(0.07 \pm 0.01)$ fF

Table 6.1 – Parameters for the array of SQUIDS extracted from the fit of the dispersion relation. The errors give a maximum discrepancy between theory and experiment of 10%.

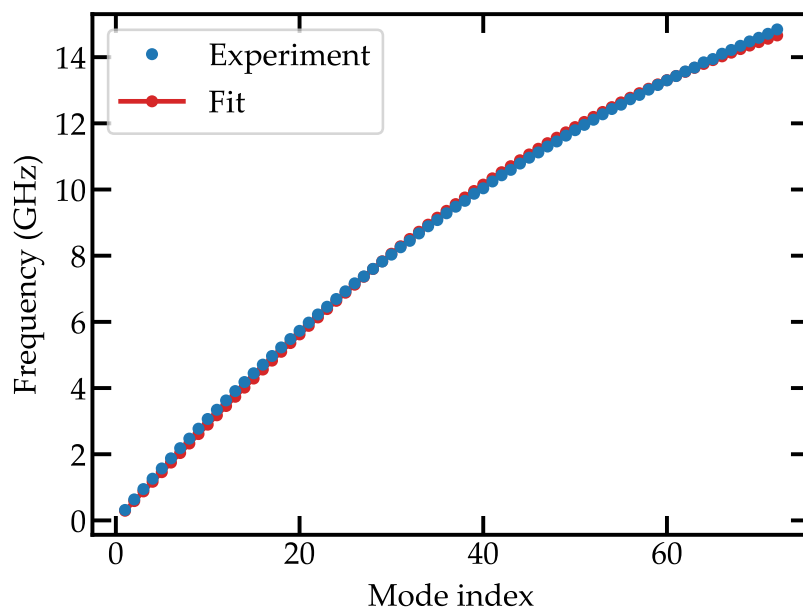


Figure 6.9 – Fit of the dispersion relation of the array.

# Transmon qubit coupled to an array of SQUIDS

# 7

The main experimental results are given in this chapter. We couple a transmon qubit to an array of SQUIDS. First we give a description of the measured sample, then we describe the different measurements performed and finally we use the phase shift introduced in Section 3.4 to obtain the coupling strength, the transmon qubit frequency and the number of modes coupled to the transmon.

## 7.1 *The sample*

The sample consists of a transmon qubit coupled to an array of 4700 SQUIDS. The qubit is placed at one end of the array. It is capacitively coupled to the array at one side and to a  $50\ \Omega$  pad at the other side. The array is galvanically coupled at one end to a  $50\ \Omega$  pad. The circuit is the one discussed in Section 3.4. It is reproduced in Fig. 7.1 (a). As it can be seen, we have a SQUID in the transmon qubit and SQUIDS in the array. The area of the SQUID loop in the transmon qubit is around thirty times larger than the area of the SQUIDS in the array. If we denote as  $\Phi_T$  the flux inside the SQUID for the transmon qubit and  $\Phi_C$  the flux inside the SQUIDS in the array, given the difference in loop area, we expect  $\Phi_T \sim 30 \times \Phi_C$  for the same magnetic field. This gives two totally different periods with respect to the applied magnetic field. As will be explained later, this allows us to study the system at different coupling regimes. An optical picture of the sample is given in Fig. 7.1 (b). As with the arrays, the substrate is silicon and the metal is aluminum. The coupling capacitors are the interdigital capacitors explained in Section 4.3.2. The value for the different capacitances is given in Table 4.1.

## 7.2 *Transmission measurements*

We probe the system by measuring the transmission  $S_{21}$  through it. As explained in Section 6.2, due to the impedance mismatch between the system and the two  $50\ \Omega$  pads we obtain several peaks in transmission, see Fig. 7.2 (a). If we compare this measurement with the one in Fig. 6.5 (b) for a bare array we can clearly see a broadening of the peaks due to the presence of the qubit. The reason for this is that the impedance seen by the array depends on the transmon qubit. At the transmon resonance this impedance is higher than  $50\ \Omega$  (and thus more matched) and therefore the transmission is higher and the width of the resonances of the array increases.



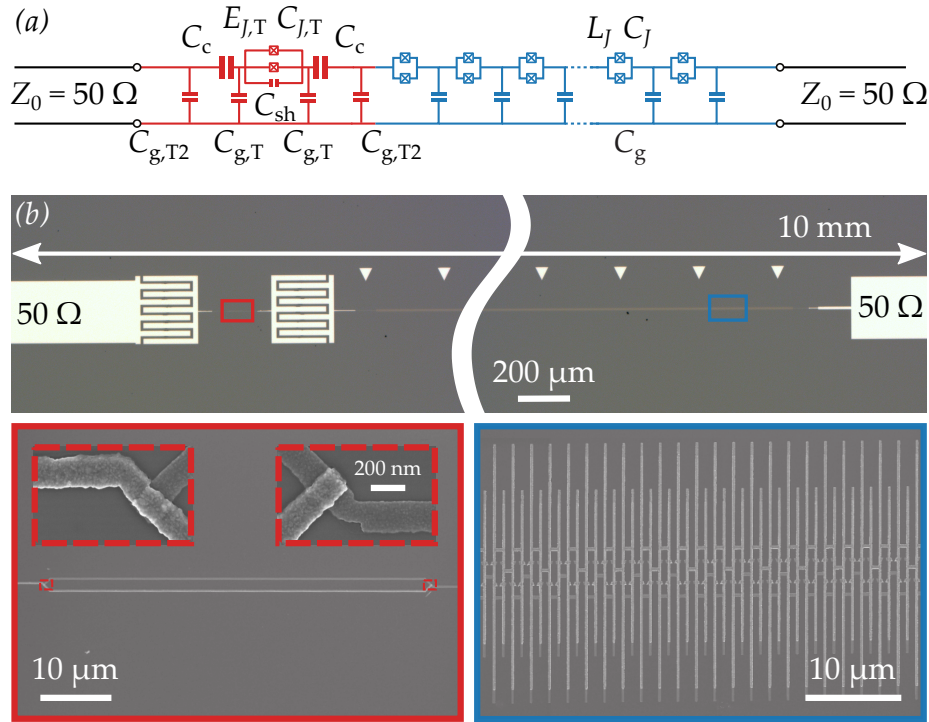


Figure 7.1 – Measured sample, a transmon qubit coupled to an array of SQUIDS. (a) Circuit diagram of the sample. In red the transmon qubit and in blue the array. We include the input and output ports of characteristic impedance  $Z_0 = 50 \Omega$ . (b) Optical image of the sample. Only a portion of the array of SQUIDS is shown. The insets show the SQUID in the transmon (red) and the SQUIDS in the array (blue). The Josephson junctions for the transmon are given as insets in the former (red dashed squares).

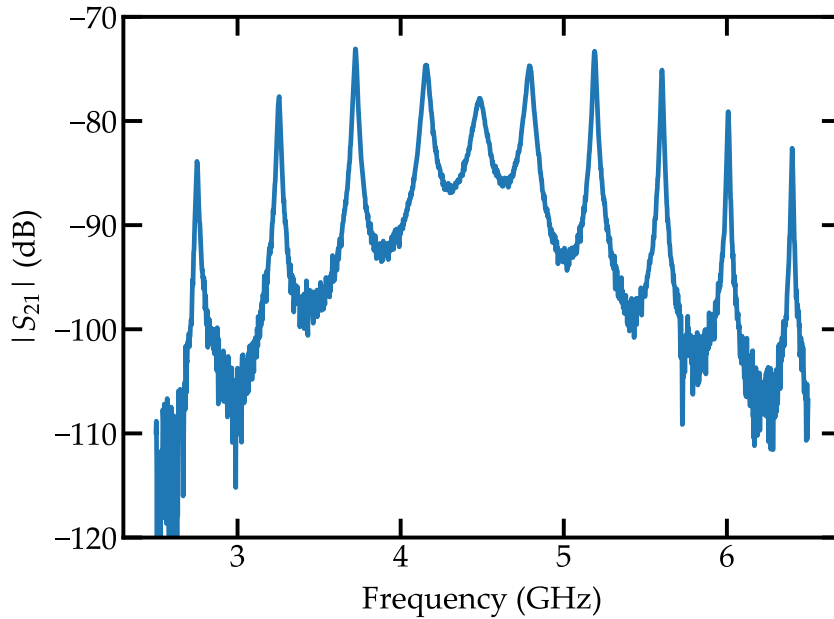


Figure 7.2 – Transmission of the circuit as a function of frequency for  $\Phi_T = 0$  and  $\Phi_C = 0$ .

### 7.2.1 Flux tuning

In the same way as with the bare arrays, we can apply a magnetic field via the external coil. Given the fact that we have SQUIDS in the transmon and in the array we tune both at the same time. The transmission of the circuit as a function of frequency and magnetic flux in the array  $\Phi_C$  is shown in Fig. 7.3 (a). Two periods with flux are clearly distinguishable. The long one is related to the SQUIDS in the array and is similar to the one for a bare array in Fig. 6.6 (b). The short one is related to the SQUID in the transmon qubit. The ratio between these periods is given by the ratio of the areas of the SQUIDS loops in the transmon and in the array. A zoom in of the measurement in Fig. 7.3 (a) is given in Fig. 7.3 (b). The period related to the transmon qubit can clearly be seen as well as the avoided crossings between the modes of the array and the transmon mode.

If we take a closer look to one of the qubit arcs, Fig. 7.4, we clearly see how the transmon mode hybridizes with each of the modes in the array. The horizontal lines are the array modes. They are almost constant in flux due to the difference in area between the SQUIDS. The square root cosine shape is the transmon like mode. It can be seen in this measurement that the size of the avoided crossings is comparable to the FSR, given by the frequency difference between two consecutive modes in the array. This means that at any point in flux the qubit is interacting not only to the resonant mode but with modes above and below its frequency. In other words, the qubit is never in the dispersive regime<sup>66</sup> with respect to the modes of the array.



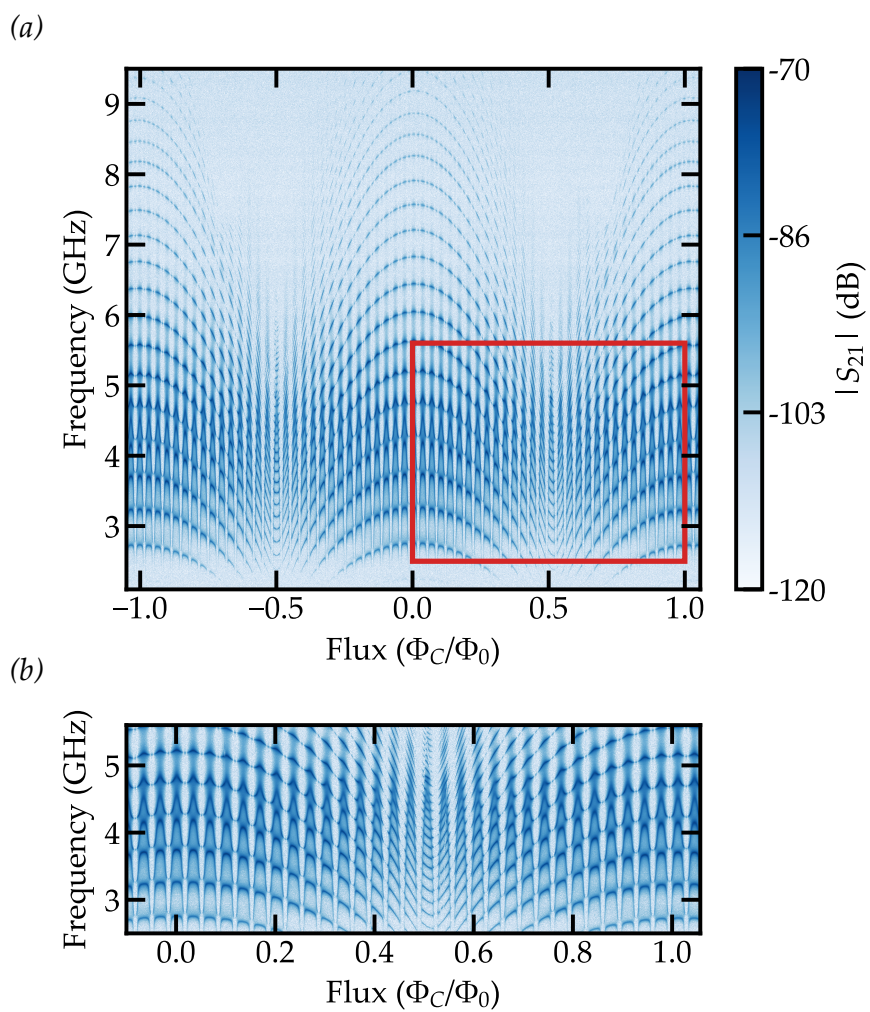


Figure 7.3 – Transmission of the circuit as a function of the magnetic flux in the array  $\Phi_C$  and the microwave frequency. A zoom in of the area in the red rectangle is shown in the bottom plot.

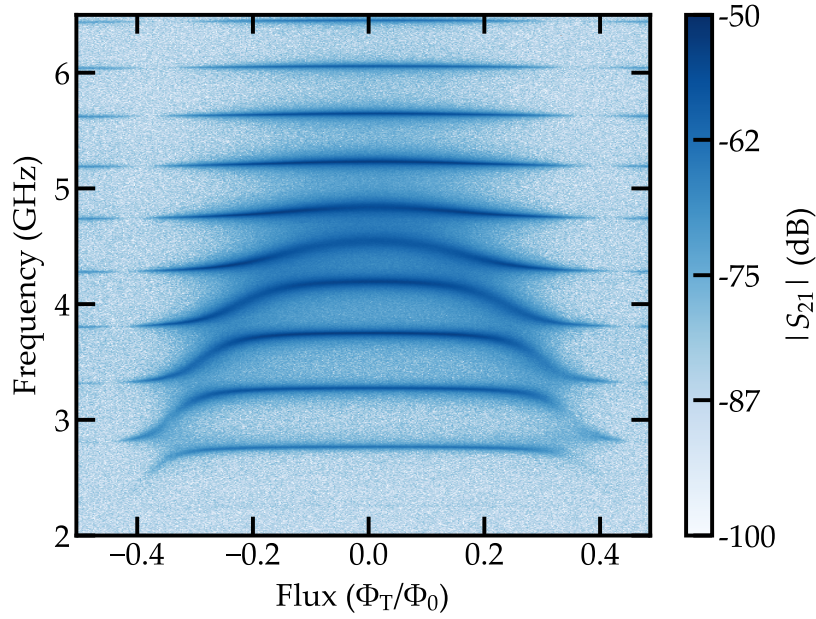


Figure 7.4 – Transmission spectrum as a function of the applied flux  $\Phi_T$  and microwave frequency for  $\Phi_C = 0$ . The horizontal lines are the modes of the array. The transmon frequency is tuned with  $\Phi_T$ . This tuning can be seen as a series of avoided crossings with the modes of the array.

### 7.2.2 Dispersion relation

In a similar way as with the sample in Chapter 6, we can perform a two tone measurement to obtain the resonances of the array. However, in this case the transmon qubit affects the dispersion relation of the circuit. To avoid this we set  $\Phi_T = \Phi_0/2$ . At this point the Josephson energy of the transmon qubit is zero (its inductance is infinite) and therefore it does not interact with the modes in the array. Therefore the modes obtained from the two tone measurement are only due to the array. The two tone measurement is given in Fig. 7.5. The result is similar to the one obtained for the bare array.

We fit each of the resonances with a Lorentzian to get their center frequency and then fit the dispersion relation. Contrary to what we did with the bare array, we choose open/closed boundary conditions. The reason is that for  $\Phi_T = \Phi_0/2$  the transmon qubit can be seen as an open. This gives a different condition for the  $k_n$ ,

$$k_n = \frac{\left(n - \frac{1}{2}\right) \pi}{Na}. \quad (7.1)$$

Using this condition we fit the obtained peaks with the dispersion relation for a bare array in Eq. (6.2). The result of the fit is given in Fig. 7.6 (a). The obtained parameters are given in Table 7.1. In Fig. 7.6 (b) we plot the obtained FSR as a function of the mode frequency  $\omega_k$  in blue. In red we obtain the theoretical one obtained from the lumped element model. As we see, for the measurement range

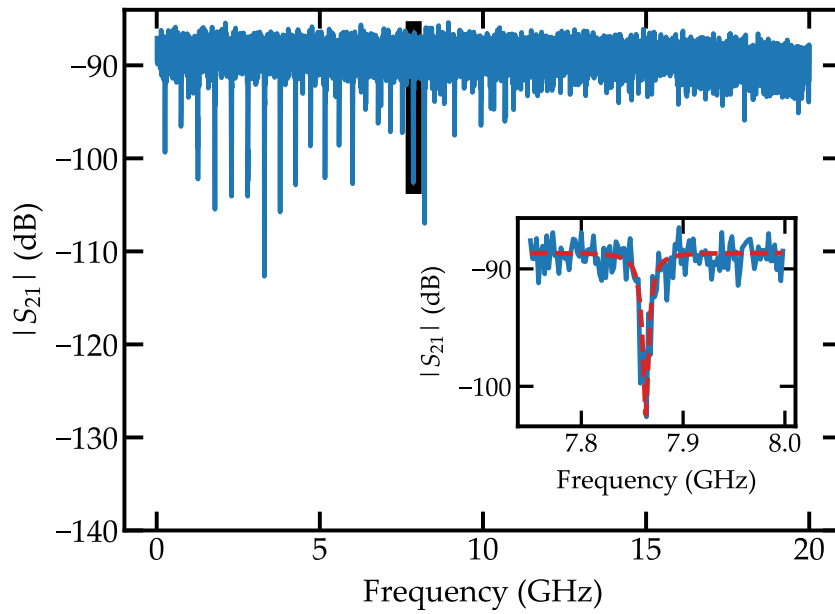


Figure 7.5 – Two tone measurement of the modes of the array. The frequency trace is taken for  $\Phi_T = \Phi_0/2$  and  $\Phi_C = 0$ . The inset shows a lorentzian fit of one of the dips in red. The power is set to  $P_{\text{VNA}} = -10$  dbm and  $P_{\text{MW}} = 10$  dbm at room temperature. The frequency of the VNA is set to  $\omega_{\text{VNA}} = 5.1692$  GHz.

where the qubit is interacting with the array, we obtain  $\text{FSR} \sim 0.4 \text{ GHz}$ , comparable to the  $2g_k$  obtained in Section 3.3.

<i>Lumped element model</i>	
$L_J$	$(0.33 \pm 0.02) \text{ nH}$
$C_J$	$(259 \pm 14) \text{ fF}$
$C_g$	$(0.13 \pm 0.01) \text{ fF}$

Table 7.1 – Parameters for the array of SQUIDS extracted from the fit of the dispersion relation. The errors give a maximum discrepancy between theory and experiment of 5%.

### 7.2.3 Power dependence

Up to this point we did not measure any non linear behavior in the circuit. A way of probing this behavior is to measure the transmission of the circuit as a function of the applied microwave power. For a non linear circuit, the resonance frequency associated to the qubit should saturate with increasing power<sup>19,25,34,57</sup> i.e. the peak in transmission should disappear. For this measurement we set  $\Phi_C = 0$  and  $\Phi_T = 0$ . Then we measure  $S_{21}$  with the vna and sweep the vna power,  $P_{\text{VNA}}$ . In Fig. 7.7 we show three traces for three different values of power at room temperature,  $P_{\text{VNA}} = -20 \text{ dbm}$ ,  $-10 \text{ dbm}$  and  $12 \text{ dbm}$ . At low power we measure five resonances, same result as in Fig. 7.2 (a). Four of these resonances are more array-like and the one in the center is more qubit-like. As expected, with increasing power we observe that the height of the qubit-like resonance is reduced. At very high power the qubit-like resonance disappears completely and only the four array-like resonances remain. In addition these four resonances shift in frequency. This can be better seen in Fig. 7.8 where we show a color plot of the same type of measurement. We include dashed lines at the low power position of the peaks. It can clearly be seen that one resonance disappears and the four other peaks shift inwards. At high power, the transmon qubit is saturated and does not couple to the array anymore. Therefore the modes that were coupled to the qubit shift to their bare position. This is a qualitative signature of multi-mode coupling in this system.

## 7.3 System-environment interaction

Contrary to other works coupling a qubit to open waveguides<sup>19,22</sup>, in our system each mode of the environment is spectrally resolved. As already shown, this allows us to obtain the dispersion relation of our environment including its cut-off frequency. In addition we can use the frequency shift to measure the number of modes coupled to the qubit, the strength of this coupling and the qubit frequency. Moreover our environment is tunable and we can study different regimes in qubit-array coupling.

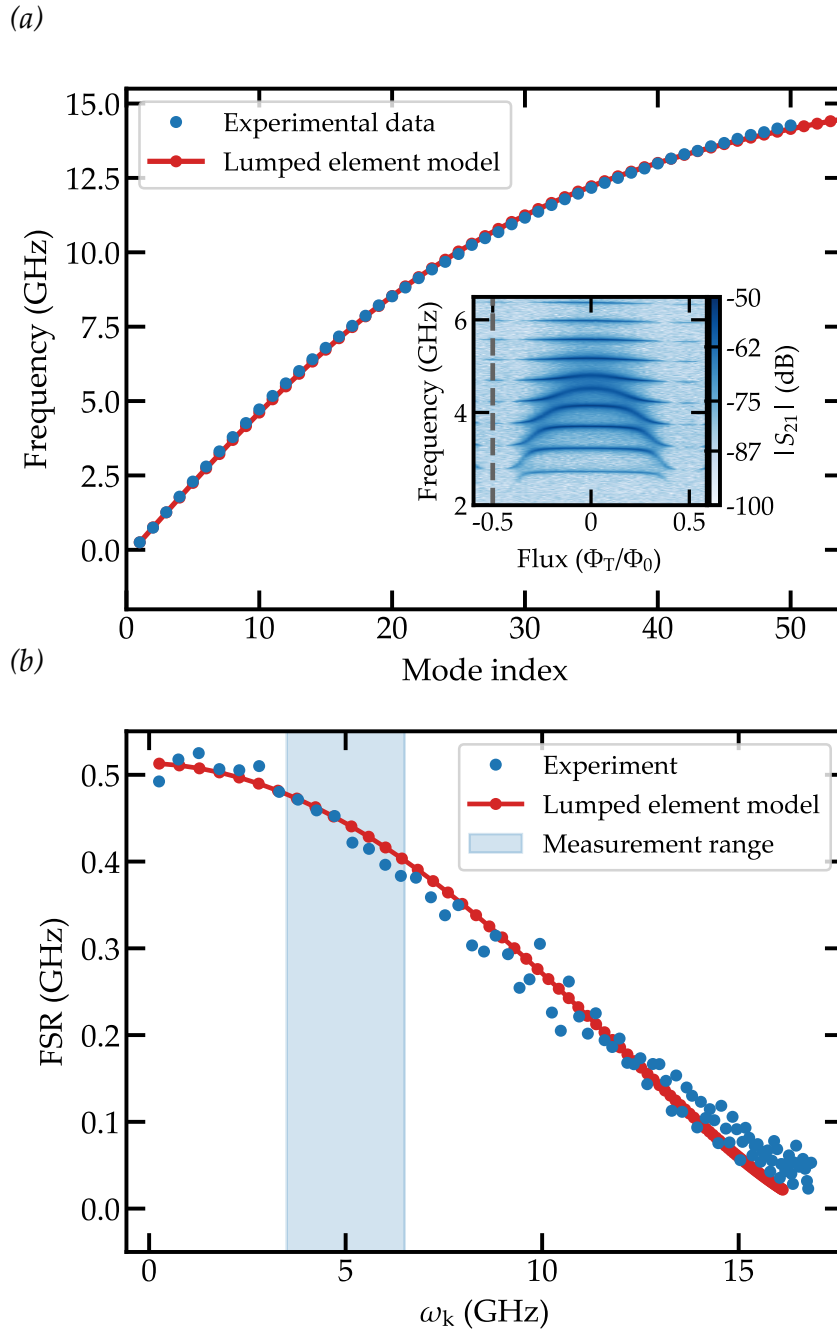


Figure 7.6 – (a) Dispersion relation of the array. The inset shows a color-scale plot of the transmission amplitude as function of  $\Phi_T$  and frequency, with a gray dashed line indicating the fixed flux value employed to determine the dispersion relation of the uncoupled array. (b) Free Spectral Range of the array as a function of the mode frequency  $\omega_k$ , blue dots. In red the obtained FSR from the lumped element model is shown. The blue area gives the frequency range where we measure the qubit-array interaction.

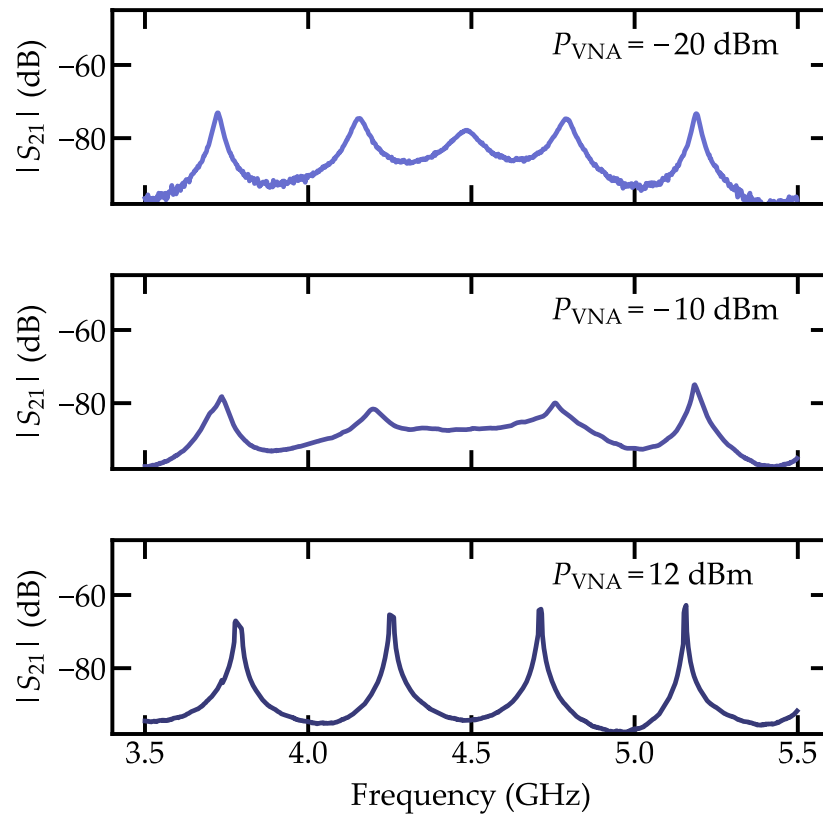


Figure 7.7 – Transmission for several values of  $P_{VNA}$ , –20 dbm top, –10 dbm middle and 12 dbm bottom.

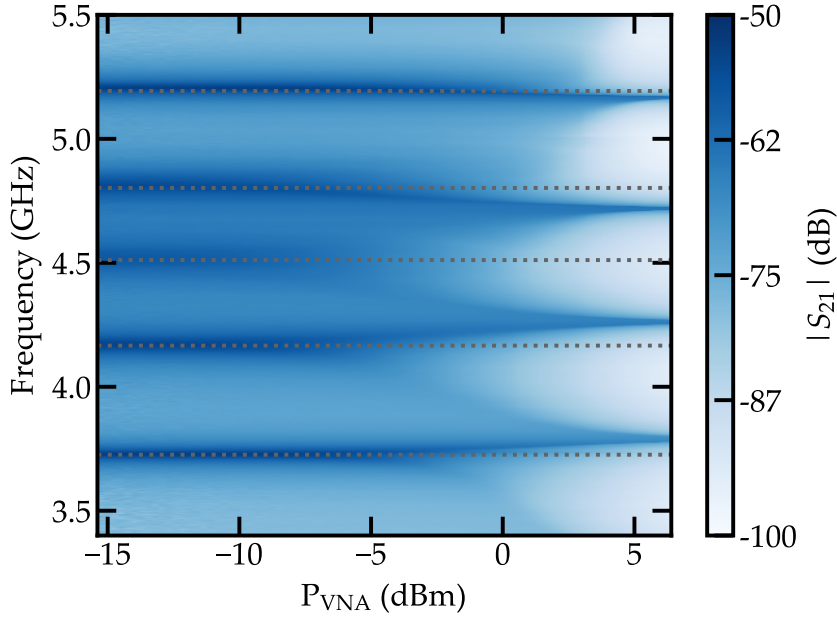


Figure 7.8 – Transmission spectrum as a function of the applied power  $P_{\text{VNA}}$  and microwave frequency for fixed  $\Phi_C = 0$  and  $\Phi_T = 0$ . The dashed gray lines indicate the eigenfrequencies at low power.

### 7.3.1 Monitoring the environment

A common approach when dealing with Circuit QED systems is to map the circuit Hamiltonian to a quantum optics Hamiltonian and diagonalize it to obtain the eigenenergies of the system. Then compare these eigenenergies with the measured energy spectrum.

It has been shown<sup>30,34,85</sup> that our system, a transmon qubit coupled to an array of Josephson junctions, can be mapped into the spin-boson model or its multi-level version. We could then in principle obtain this Hamiltonian and diagonalize it. The size of the Hilbert space would be given by  $q \times (n + 1)^m$ . Here  $q$  is the number of transmon qubit levels involved in the calculation,  $m$  is the number of modes and  $n$  is the number of photons allowed per mode. This already is in the order of  $10^3$  for  $q = 2$ ,  $n = 1$ , and  $m = 10$ . To capture all the effects of the ultrastrong coupling regime and the associated counter-rotating terms, we would need  $n$  to be much larger than one, which would give a matrix size greater than  $10^4$ . Performing a fitting algorithm with this matrix is not optimal.

We therefore follow a different approach. As explained in Section 3.4 we can obtain all the information we need from our transmon qubit via the phase shift that it creates in the modes in the array. We first need to linearize the system. In the case of the array it is straightforward due to the large  $E_J/E_C$  of its junctions. As explained in Section 2.2.1 we define a linear Josephson inductance as  $L_J = \varphi_0^2/E_J$  and treat the Josephson junctions as linear inductors. For the transmon qubit however this is not that easy due to the fact that the ratio  $E_{J,T}/E_{C,T}$  is not that large. However, we can use the SCHA described in Section 2.3 to obtain an harmonic



approximation of the transmon qubit which still accounts for the vacuum phase fluctuations. We can then solve the system as in Section 3.4 and use the transmon phase shift  $\delta\phi$  to obtain the coupling strength  $\Gamma_T$ , the transmon frequency  $\omega_T$  and the number of coupled modes. Experimentally we measure the frequency shift induced by the transmon qubit in the modes of the array. This frequency shift is given in Eq. (3.54) and reproduced here,

$$\delta\phi_n(\Phi_C, \Phi_T) = \pi \frac{\omega_n(\Phi_C, \Phi_0/2) - \omega_n(\Phi_C, \Phi_T)}{\omega_n(\Phi_C, \Phi_0/2) - \omega_{n-1}(\Phi_C, \Phi_0/2)}. \quad (7.2)$$

In order to obtain  $\delta\phi_n$  we fit each resonance of the system with a Lorentzian to obtain its center frequency. We can do this at several values of  $\Phi_C$  and  $\Phi_T$ . In this way we obtain the center frequency of each of the modes as a function of  $\Phi_C$  and  $\Phi_T$ . Then from Eq. (7.2) we obtain  $\delta\phi_n(\Phi_C, \Phi_T)$ . There is however one caveat. When working close to  $\Phi_C \sim 0$  the array modes are flat and therefore we can easily compare modes for  $\Phi_T = \Phi_0/2$  and modes with  $\Phi_T \neq \Phi_0/2$ , see Fig. 7.9 (a). However for  $\Phi_C \neq 0$  there is a slope as a function of flux. To overcome this difficulty we proceed as follows. We take two traces as reference, one at  $\Phi_T = -0.5\Phi_0$  and the other at  $\Phi_T = 0.5\Phi_0$ , orange squares in Fig. 7.9 (b). Then for each of the modes we obtain the straight line joining them. Now whenever we want to obtain  $\delta\phi$  we choose as bare modes, i.e.  $\omega_n(\Phi_0/2, \Phi_C)$  the correspondent point in this straight line, green squares. We therefore remove the slope with flux in the  $\delta\phi_n$ , Fig. 7.9 (b) right plot. We obtain similar curves as the ones in Fig. 3.16. The number of modes coupled to the transmon can be directly obtained from the plots. We obtain  $\sim 8$  for the upper plot and  $\sim 11$  for the lower one. This is related to the reduction in the Free Spectral Range at high impedances.

Before comparing the experimentally obtained  $\delta\phi_n$  and the theoretical one  $\delta\phi$  we need to determine the only unknown parameter in the system, the Josephson energy of the transmon  $E_{J,T}$ . We can determine it from the transmon frequency  $\omega_T$  directly using Eq. (2.88) as

$$\omega_T = \sqrt{E_{J,T}E_{C,T} - \frac{E_{C,T}}{8}}. \quad (7.3)$$

The charging energy is directly given by the system capacitances in Eq. (3.34). The transmon maximum frequency,  $\omega_{T,\max}$ , is obtained as follows. For each value of  $\Phi_C$  and  $\Phi_T$  we obtain  $\delta\phi_n$  as shown in Fig. 7.9. We can fit these curves with an arc-tangent and obtain their width  $\Gamma_{\delta\phi}$  and their center frequency  $\omega_{\delta\phi}$ . As explained in Section 3.4.4, this width  $\Gamma_{\delta\phi}$  and frequency  $\omega_{\delta\phi}$  give the width and frequency associated to the transmon qubit. Therefore from now on we refer to them as  $\Gamma_T$  and  $\omega_T$ . For each transmon period, usually with  $\Phi_T \in [-0.3\Phi_0, 0.3\Phi_0]$ , we obtain  $\omega_T(\Phi_T)$ .

The flux dependence of the transmon frequency can be obtained from the  $I_c$  modulation in a SQUID, see Section 2.1.1. This modulation gives a flux dependent



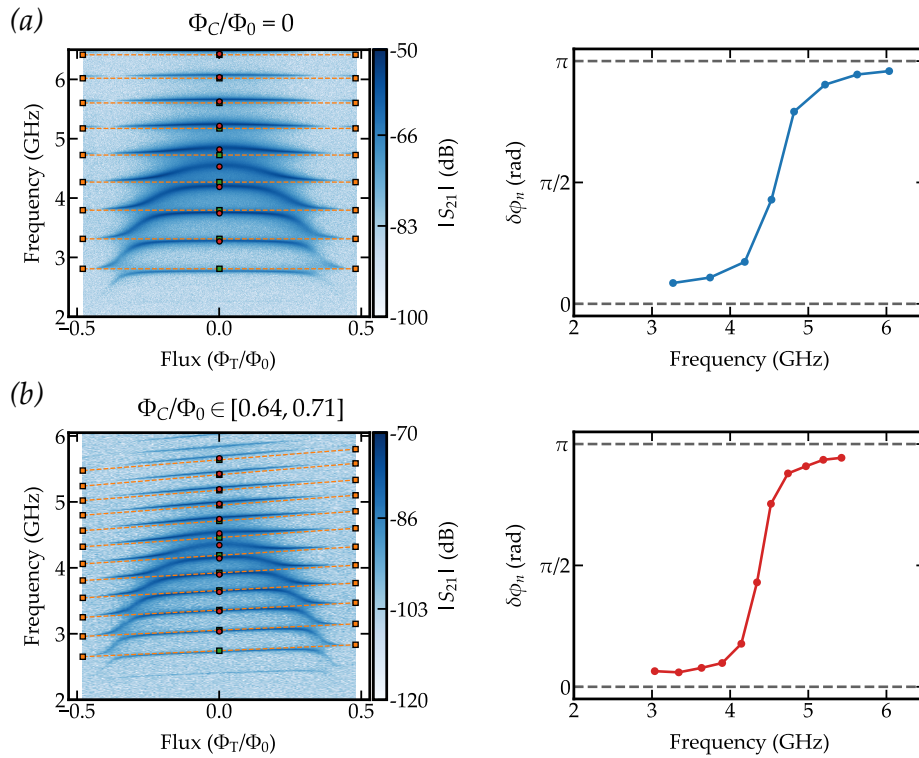


Figure 7.9 – Frequency shift explanation. From the measurements on the left we can get the frequency shift  $\delta\phi_n$  and obtain the curves on the right. The gray dashed lines in the plots on the right represent the limit values of  $\delta\phi$ , 0 and  $\pi$ . (a) For  $\Phi_C \sim 0$  we can directly obtain the frequency shift. (b) For  $\Phi_C \neq 0$  we need to correct for the slope of the array modes with respect to flux.

qubit frequency given by

$$\omega_T(\Phi_T) = \omega_{T,\max} \sqrt{\left| \cos\left(\pi \frac{\Phi_T}{\Phi_0}\right) \right| - \frac{E_{C,T}}{8}}, \quad (7.4)$$

$$\omega_{T,\max} = \sqrt{E_{J,T,\max} E_{C,T}}.$$

Using Eq. (7.4) we perform a fit of  $\omega_T(\Phi_T)$  to obtain  $\omega_{T,\max}$ . From the value of  $\omega_{T,\max}$  and the obtained  $E_{C,T}$  from the system capacitances we obtain  $E_{J,T,\max}$ . All the transmon related energies are given in Table 7.2.

	Energy (GHz)
$\omega_{T,\max}/2\pi$	$4.65 \pm 0.01$
$E_{J,T,\max}/h$	$10.2 \pm 0.4$
$E_{C,T}/h$	$2.4 \pm 0.1$

Table 7.2 – Energies for the transmon qubit.

Now we have all the parameters that define the system. We can obtain the phase shift  $\delta\phi$  using the analytical expression in Eq. (3.52) and compare the result with the obtained experimental data. This is done for one arc in Fig. 7.10. As it can be seen, there is a good agreement between theory and experiment with no fitting parameter. A similarly good agreement is present in all arcs, see Appendix D.

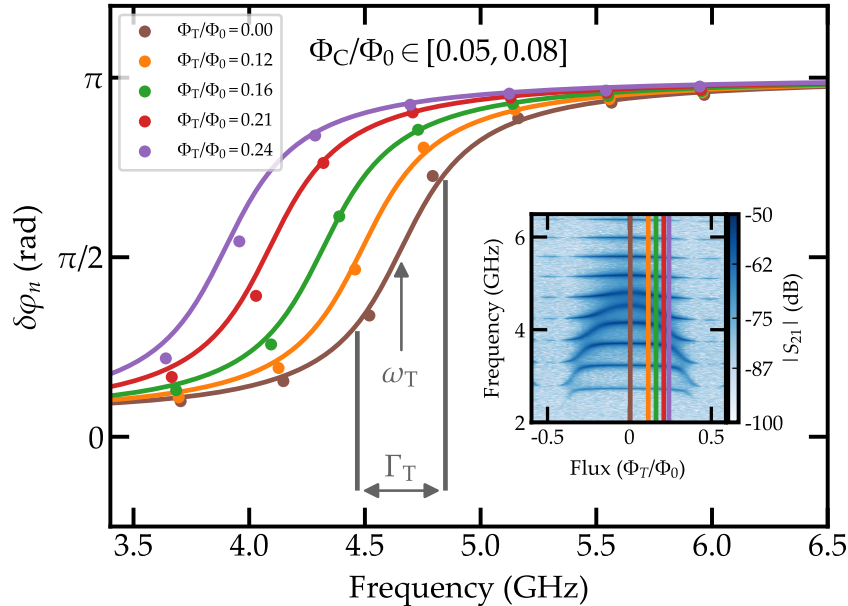


Figure 7.10 – Comparison between the experimental phase shift  $\delta\phi_n$  and the theoretical one  $\delta\phi$  with no fitting parameter. The curves are taken for several values of  $\Phi_C$ . In the inset the transmon period from where the data is taken is shown.

### 7.3.2 Tuning the system-environment coupling

As we pointed out earlier, one of the advantages of the system presented in this work is that we can easily tune the environment. By using SQUIDS in the array we can tune it using an external magnetic flux. In Fig. 7.11 we plot several transmon periods for different fluxes in the array  $\Phi_C$ . This gives a different impedance  $Z_{\text{array}}$  in the array. From these figures we see that with increasing impedance the FSR is

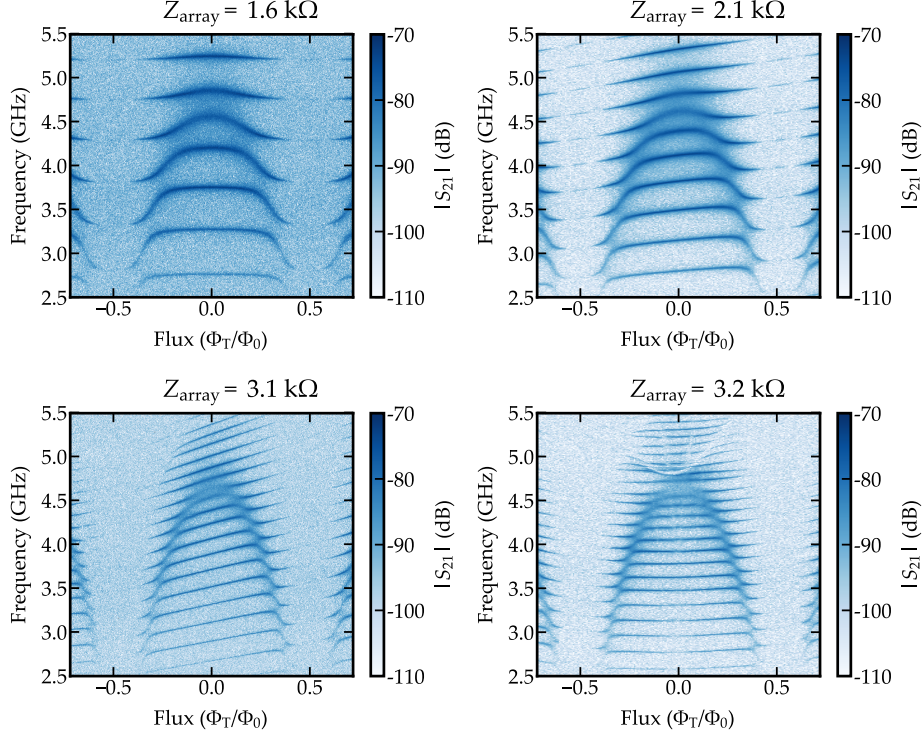


Figure 7.11 – Several transmon qubit periods for different array impedances  $Z_{\text{array}}$ .

reduced. This increases the number of modes the transmon couples to. However, as will be shown later, the coupling decreases. At too high impedance the coupling is reduced due to capacitances  $C_{g,T}$  and  $C_{g,T2}$ . One could think that the decrease in the coupling strength could be directly seen in the size of the avoided crossings. However we have to keep in mind that whenever the coupling strength is in the order of the FSR, the avoided crossing is not a good measure of the coupling strength anymore. For the same array and transmon parameters the size of the avoided crossings would depend on the length of the array.

Following the method described in the previous section, we can obtain the width of the transmon  $\Gamma_T(\Phi_C, 0) = \Gamma_{T,\text{max}}(\Phi_C)$  for different values of  $\Phi_C$ . We obtain for each  $\Phi_C$  and  $\Phi_T$  a phase shift curve that we fit with an arctangent to obtain  $\omega_T(\Phi_C, \Phi_T)$  and  $\Gamma_T(\Phi_C, \Phi_T)$ . We take as  $\Gamma_{T,\text{max}}$  the  $\Gamma_T$  closest to  $\Phi_T = 0$ . The obtained  $\Gamma_{T,\text{max}}$  are given in Fig. 7.12 as blue dots. The error bar comes from the error in the different fits. We follow the same procedure with the theoretical phase shift given in Eq. (3.52), we fit each curve with an arctangent to obtain a theoretical transmon width. The result is shown in Fig. 7.12 as a blue shaded area. The area represents the interval in the theoretical transmon width given by the errors in the estimation of the system parameters. The agreement between

theory and experiment is quite good keeping in mind we did not use any fitting parameter. It can clearly be seen how the environment system coupling depends on the impedance of the former. For the parameters in this system we are more impedance matched at  $\Phi_C = 0$  than at  $\Phi_C = \pm 0.5 \Phi_0$  and therefore the coupling is reduced with increasing impedance.

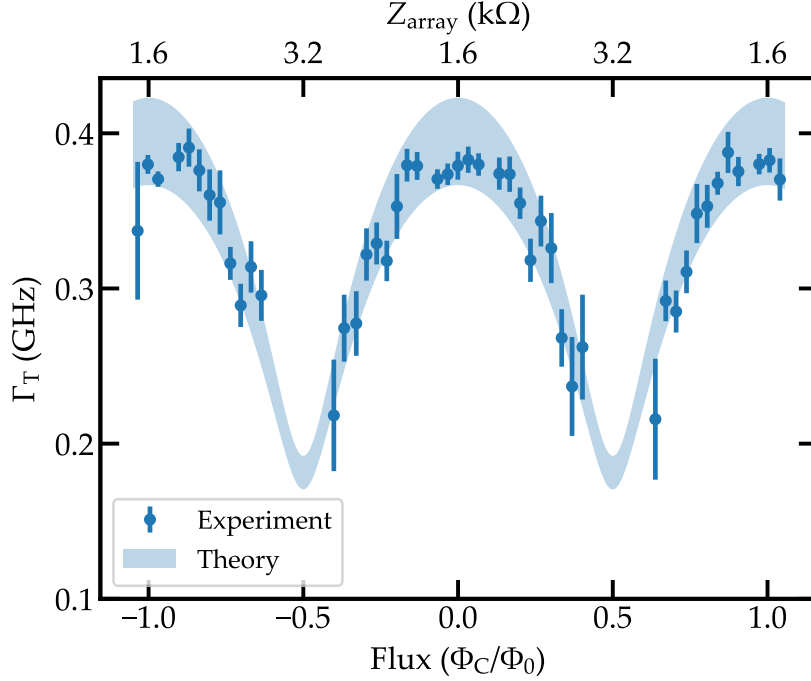


Figure 7.12 – Transmon qubit maximum width as a function of the flux in the array  $\Phi_T$ . The blue dots are experimental data. The error bars come from the error in the fitting procedure. The blue shaded area is the theoretical curve. The area represents the error in the estimation of the system parameters.

If we compare the obtained transmon qubit width  $\Gamma_T(\Phi_C = 0, \Phi_T = 0)$  with its maximum frequency  $\omega_{T,\max}$  in Table 7.2 we obtain a ratio  $\Gamma_T/\omega_{T,\max} \sim 8\%$  close to the ultra strong coupling regime. However, due to the fact that the qubit frequency is tunable, we can tune it to lower values to increase the coupling. In this way, if we take the minimum qubit frequency  $\omega_T(\Phi_C = 0.2 \Phi_0, \Phi_T = 0.3 \Phi_0) = 3.6$  GHz for which we have a value for the width we obtain a ratio of 10% thus reaching the ultra strong coupling regime<sup>14,15</sup>.



# Conclusion and perspectives

## *Conclusion*

In this work we have obtained a deep understanding of a complex circuit containing a transmon qubit capacitively coupled to a mesoscopic environment consisting of an array of 4700 SQUIDS.

On the theoretical side, we have reviewed some results regarding capacitive coupling between a circuit and its environment. We have presented a new model for an array of SQUIDS that takes into account the effect of long range interactions when the ground plane is far away from the SQUIDS in the array. Regarding the transmon-array circuit, we have shown a new technique to obtain the transmon properties as well as the number of modes coupled to it via the phase shift it induces in the modes of the array. This was particularly challenging since all the ingredients of many-body physics are at play in such circuit: high density of modes, ultra-strong coupling and non-linearity comparable to the relevant energy scales.

The fabrication process for the array of SQUIDS was fully developed during this project in a new e-beam writer. It involved solving usual lithography problems such as stitching errors and proximity effect over large substrates, two inch wafers. In addition, a serious aging problem forced us to move from one evaporator to another once the fabrication process was stabilized. However, as we have shown, we obtained a high reproducibility in Josephson junction fabrication, via room temperature DC measurements.

The transmission measurements performed on the sample show the simultaneous coupling of the transmon qubit to several modes in the array. Thanks to the phase shift induced by the transmon in the modes of the array we have shown that up to 10 modes are effectively coupled to the transmon. Moreover, we could obtain from this phase shift its frequency  $\omega_T$  and its width  $\Gamma_T$  related to the coupling strength between the transmon and the array. We get a ratio  $\Gamma_T/\omega_T \sim 10\%$  thus entering in the ultra strong coupling regime. In addition our experiment sits in the very interesting and new regime where the nonlinearity and the coupling of the transmon qubit are similar to the free spectral range of its environment. Finally we obtained a good data theory agreement with no fitting parameter showing that the finite array of SQUIDS behaves as an infinite dissipative environment.

## *Perspectives*

In this section we include some new lines of investigation that can directly be followed from the results presented in this manuscript.

### Different environments

During my PhD thesis we considered an array of SQUIDS to fabricate a high impedance environment. However, different implementations as using other materials or shaping the junctions in the array can be studied. In this section we develop these ideas.

### Disordered superconductors

The main topic of my work is the coupling of a system to a high impedance environment. It has been shown that disordered superconductors such as InOx<sup>114</sup>, granular aluminum<sup>115</sup>, NbN<sup>116</sup> and MoRe<sup>28,117</sup> show a very high kinetic inductance and therefore can be used to fabricate high impedance transmission lines. As a preliminary result we measured a microwave resonator made of InOx. It consists of a thin wire of length  $7010 \mu\text{m}$  and width  $1 \mu\text{m}$  capacitively coupled via two identical capacitors of capacitance  $C_c$  to input and output  $50 \Omega$  pads, see Fig. 5 (a). The thickness of the deposited InOx layer is  $40 \text{ nm}$ . It was fabricated on a silicon substrate. The pads are made of gold. In Fig. 5 (b) an optical picture of the sample is shown. In Fig. 5 (c) an SEM of the area in the blue rectangle in Fig. 5 (b) is given. We performed transmission measurements of the InOx resonator similar to

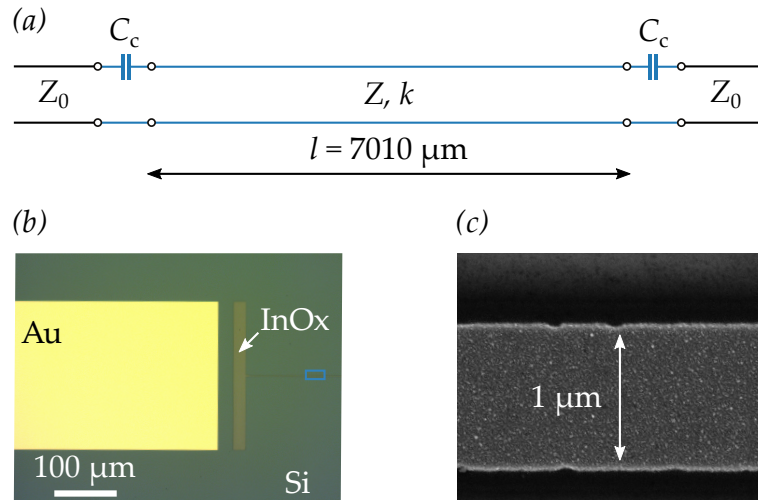


Figure 5 – Measured InOx resonator. (a) Circuit diagram of the sample. It consists of a transmission line of impedance  $Z$  and propagation constant  $k$  coupled via capacitances  $C_c$  to input and output  $50 \Omega$  ports. (b) Optical image of the sample showing one of the coupling capacitors and one  $50 \Omega$  pad. The pads are made of gold. The substrate is silicon. (c) SEM image of the InOx wire. It corresponds to the blue square in (b).

the ones presented in the manuscript. In a similar way as with the chain, there is an impedance mismatch between the resonator and the  $50 \Omega$  pads. This creates a Fabry-Pérot interferometer that gives several resonances in transmission, Fig. 6 (a). In addition, the coupling capacitors  $C_c$  modify the width of this resonances. For fitting the dispersion relation we performed two tone measurements and fitted each resonance with a Lorentzian to obtain its frequency. The obtained frequencies are shown in Fig. 6 (b). As it can be seen the dispersion relation does not follow

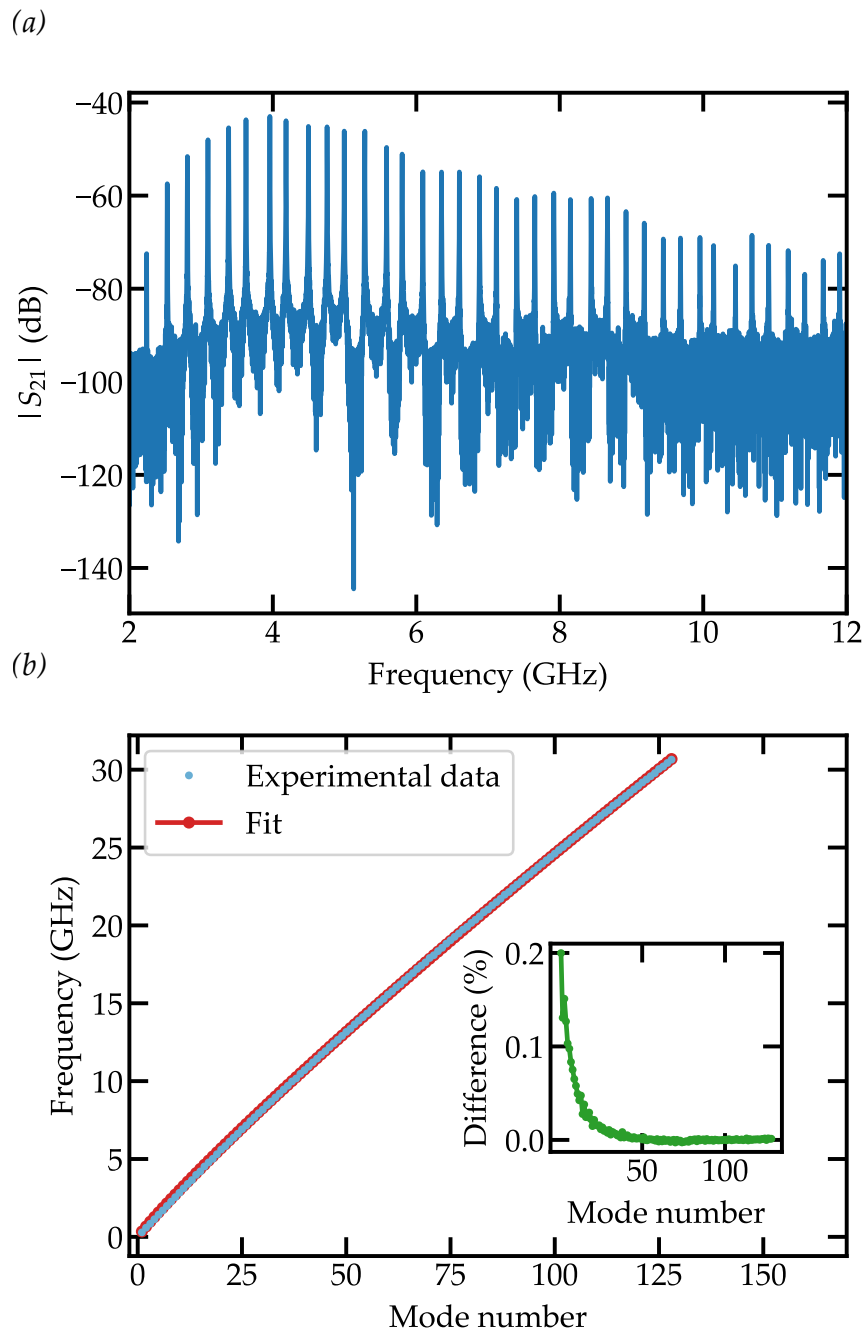


Figure 6 – (a) Transmission of the InOx resonator as a function of frequency. (b) Measured dispersion relation (blue circles) with fit (red circles). In the inset the difference between the fit and the experimental data is given as a percentage of the experimental value.



a linear law. This deviation from the linear behavior has been predicted theoretically<sup>118,119</sup> for modes propagating along a superconducting wire but has never been measured. We perform a fit using the first equation in Camarota et al.<sup>119</sup> that models the plasma modes propagating along a transmission line as a wire of radius  $r_0$  using London equations,

$$\omega_k^2 = \frac{r_0^2}{\epsilon_0 \mu_0 \epsilon \lambda_L^2(T)} k^2 \ln \left( \frac{1}{kr_0} \right). \quad (7.5)$$

Here,  $\lambda_L$  is the London penetration depth of InOx. The fit is shown as red dots in Fig. 6 (b) and describes perfectly the experimental data with a deviation of less than 0.2%, see inset in Fig. 6 (b). The deviation from the linear behavior is given by the logarithmic term in Eq. (7.5) which comes from long range Coulomb interactions<sup>119</sup>. The obtained parameters are  $r_0 = 0.2 \mu\text{m}$  and  $\lambda_L = 14 \mu\text{m}$ . From these values a kinetic inductance per square can be calculated<sup>120</sup> giving  $L_K \sim 6 \text{ nH/sq}$ .

Using the value for the capacitance per unit length for the microstrip geometry<sup>102</sup> we can estimate the characteristic impedance of the line to be around  $Z_0 \sim 8 \text{ k}\Omega$  which is comparable to the one obtained with the arrays of SQUIDS. The lack of knowledge about the exact value of  $\lambda_L$  for InOx did not allow us to check the consistency of the obtained parameters. However, if a new experiment is performed including DC lines and a Hall bar a proper characterization of the material could be done.

A final feature of the InOx resonator is that its plasma frequency seems to be at very high frequencies. Therefore the coupling strength between a qubit and an InOx transmission line will not be affected by it anymore.

### *Engineered dispersion relations*

As already mentioned in Chapter 4 we can fabricate arrays of SQUIDS with some modulation in the junctions' areas. This gives a modulation in the inductance of the array. As already shown in optical systems<sup>121</sup> and Circuit QED architectures<sup>54</sup> this modulation opens several gaps in the dispersion of the medium.

We measured the transmission of one array of SQUIDS with a cosine modulation, see Fig. 7. As it can be seen it shows a gap in transmission. This gap is given by the period of the cosine modulation. This gap in the dispersion relation can be used as a Purcell filter<sup>122</sup> to reduce the qubit's relaxation rate into the environment. It might be also useful in the optimization of Traveling Wave Parametric Amplifiers (TWPA)<sup>123</sup> or to study the formation of bound states when a qubit is placed on the edge of such gaps<sup>54</sup>.

### *Different system*

Given how versatile superconducting circuits are, we can think of replacing the transmon qubit by some other impurity and study how this impurity interacts with the environment. New experiments are being carried out in the group where a single junction is galvanically coupled to the array of SQUIDS. In this case no coupling capacitors are needed and therefore we remove the parasitic capacitances to

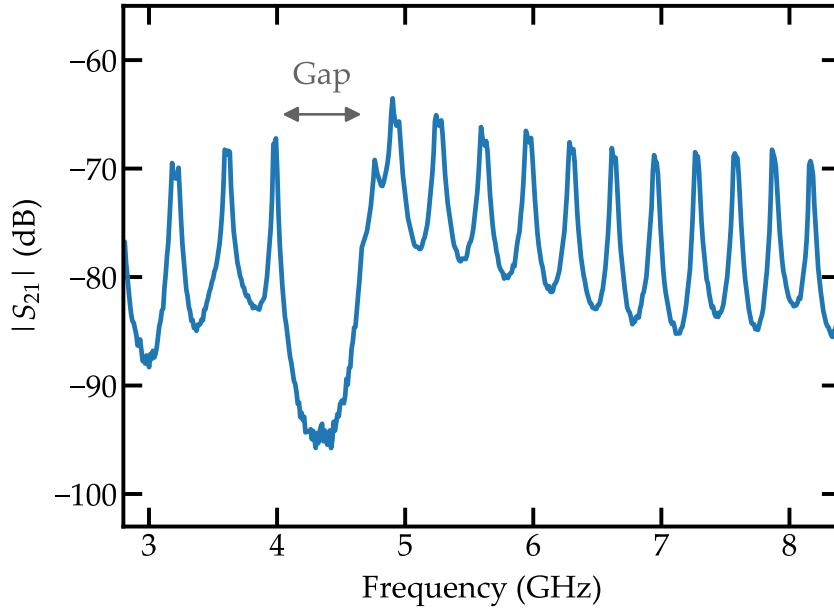


Figure 7 – Transmission measurement of a chain of SQUIDs with a cosine modulation. The gap in the dispersion relation is shown in gray.

ground that reduced the coupling in the transmon-array circuit. The circuit diagram of this new design is shown in Fig. 8. The Hamiltonian of this circuit can be mapped to the sine-Gordon Hamiltonian<sup>124</sup>. From the lumped element diagram in

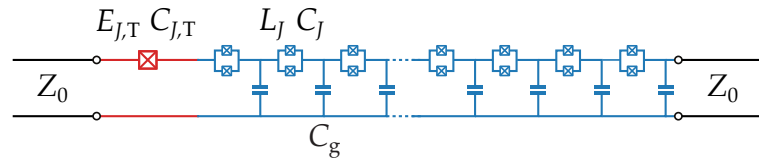


Figure 8 – Circuit diagram of a single Josephson junction (red) galvanically coupled to an array of SQUIDs (blue).

Fig. 8 we can get an intuition of the resulting transmission spectrum. For very low or very high frequencies the single junction does not play any role and we measure a bare array. However, at  $\omega = 1/\sqrt{L_{J,T}C_{J,T}}$ , we measure a dip in transmission coming from the single junction. This is the antiresonance described in Section 3.2.2. As discussed there, classically it should not depend on the impedance of the environment. However, due to many-body quantum effects<sup>24,34,52</sup>, the Josephson energy of the junction  $E_{J,T} = \varphi_0^2/L_{J,T}$  should be renormalized due to the coupling to the high impedance environment. Therefore if we measure a shift in this frequency it will be a direct and quantitative proof of a quantum many-body effect.



# Appendices



# Calculations



## A.1 Characteristic impedance of a periodic transmission line

Lets assume an array whose unit cell of length  $a$  is given by a series impedance  $Z_s$  and an impedance to ground  $Z_g$ , see Fig. A.1. From Fig. A.1 we see that the

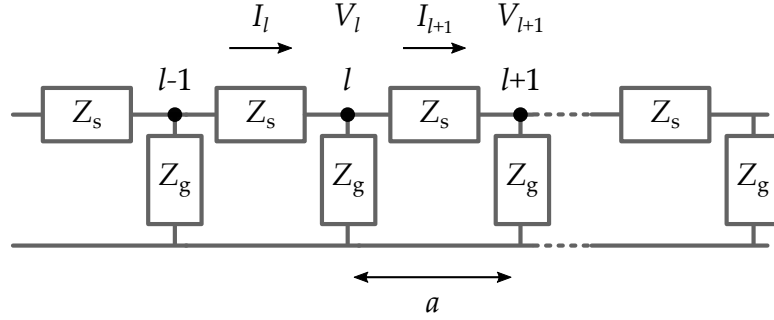


Figure A.1 – Circuit diagram showing an infinite array of impedances in series  $Z_s$  and impedances to ground  $Z_g$ . The length of the unit cell is  $a$ .

voltages and the currents need to fulfill the following equations,

$$V_{l+1} = V_l - Z_s I_{l+1}, \quad (\text{A.1})$$

$$I_{l+1} = I_l - \frac{V_l}{Z_g}. \quad (\text{A.2})$$

We can decouple these equations in the following way. We take Eq. (A.1) and evaluate it at  $l$  giving

$$V_l = V_{l-1} - Z_s I_l. \quad (\text{A.3})$$

Then using Eqs. (A.1) and (A.2) we obtain another expression for  $V_l$ ,

$$V_l = V_{l+1} + Z_s \left( I_l - \frac{V_l}{Z_g} \right). \quad (\text{A.4})$$

Equating these two expressions we remove the dependence in  $I_l$ . Doing this for both voltage and current we obtain

$$\frac{Z_s}{Z_g} V_l = V_{l+1} + V_{l-1} - 2V_l, \quad (\text{A.5})$$

$$\frac{Z_s}{Z_g} I_l = I_{l+1} + I_{l-1} - 2I_l. \quad (\text{A.6})$$

This is the discrete form of the wave equations in Eq. (2.19). In principle, an exact expression for the impedance of the line can be obtained for the discrete array. However, the result is the same as the one for a continuous array as long as  $Z_g \ll Z_s$  which is the case of the arrays in this work. We therefore go to the continuous limit in Eqs. (A.1) and (A.5) and obtain

$$\frac{\partial V}{\partial x} = -Z_s I, \quad (\text{A.7})$$

$$\frac{\partial^2 V}{\partial x^2} = \gamma^2 V. \quad (\text{A.8})$$

Here we defined the propagation constant as

$$\gamma = \sqrt{\frac{Z_s}{Z_g}}. \quad (\text{A.9})$$

Now we use as ansatz the plane wave defined in Eq. (2.21) for the voltage and introduce it in Eqs. (A.7) and (A.8). This gives

$$\frac{V_0^+}{I_0^+} = \frac{-V_0^-}{I_0^-} = Z_0 = \sqrt{Z_s Z_g}. \quad (\text{A.10})$$

For the linearized array of SQUIDS we therefore obtain

$$Z_0(\omega) = \sqrt{\frac{L_J}{C_g(1 - L_J C_J \omega^2)}}. \quad (\text{A.11})$$

## A.2 Linear Hamiltonian in eigenmodes

We start with the definition of the charge and flux operators,

$$\hat{Q}_n = \sqrt{\frac{\hbar}{2}} \sum_{k=1}^N \zeta_{n,k} (a_k + a_k^\dagger) \quad \hat{\Phi}_n = i\sqrt{\frac{\hbar}{2}} \sum_{k=1}^N \pi_{n,k} (a_k - a_k^\dagger). \quad (\text{A.12})$$

We impose the commutation relations for the creation and annihilation operators and for the charge and flux operators,

$$[a_n, a_m^\dagger] = \delta_{n,m} \quad [a_n, a_m] = 0 \quad [a_n^\dagger, a_m^\dagger] = 0, \quad (\text{A.13})$$

$$[\widehat{\Phi}_n, \widehat{Q}_m] = i\hbar\delta_{n,m} \quad [\widehat{\Phi}_n, \widehat{\Phi}_m] = 0 \quad [\widehat{Q}_n, \widehat{Q}_m] = 0. \quad (\text{A.14})$$

The flux charge commutator is given by

$$\begin{aligned} [\widehat{\Phi}_n, \widehat{Q}_m] = & i\frac{\hbar}{2} \left\{ \sum_{k=1}^N \pi_{n,k} (a_k - a_k^\dagger) \sum_{k'=1}^N \zeta_{m,k'} (a_{k'} + a_{k'}^\dagger) \right\} \\ & - i\frac{\hbar}{2} \left\{ \sum_{k'=1}^N \zeta_{m,k'} (a_{k'} + a_{k'}^\dagger) \sum_{k=1}^N \pi_{n,k} (a_k - a_k^\dagger) \right\} \end{aligned} \quad (\text{A.15})$$

Given the commutation relations, all the terms in this expression are zero except for  $k = k'$ . This gives

$$\begin{aligned} [\widehat{\Phi}_n, \widehat{Q}_m] = & i\frac{\hbar}{2} \sum_k \pi_{m,k} \left\{ (a_k - a_k^\dagger) (a_k + a_k^\dagger) - (a_k + a_k^\dagger) (a_k - a_k^\dagger) \right\} \zeta_{n,k} \\ = & i\frac{\hbar}{2} \sum_k \pi_{m,k} \left\{ 2 [a_k, a_k^\dagger] \right\} \zeta_{n,k} = i\hbar\delta_{n,m}. \end{aligned} \quad (\text{A.16})$$

Taking into account that  $[a_k, a_k^\dagger] = 1$  we obtain

$$\sum_k \pi_{m,k} \zeta_{n,k} = \delta_{n,m}, \quad (\text{A.17})$$

which means

$$\pi \zeta^T = I. \quad (\text{A.18})$$

### A.3 SCHA derivation for the full system

Here we give a detailed derivation of the SCHA equation in Eq. (2.93) of the main text. We start with the full Hamiltonian of the system,

$$\mathcal{H} = \frac{(2e)^2}{2} \sum_{l,s} \widehat{C}_{l,s}^{-1} \widehat{n}_l \widehat{n}_s + \sum_l \frac{E_J}{2} (\widehat{\varphi}_l - \widehat{\varphi}_{l+1})^2 - E_{J,T} \cos \widehat{\varphi}_T. \quad (\text{A.19})$$

We rewrite it as

$$\mathcal{H} = \mathcal{H}_0 - E_{J,T} \cos \widehat{\varphi}_T. \quad (\text{A.20})$$

We use as trial state the ground state  $|\Psi\rangle$  of the harmonic Hamiltonian

$$\mathcal{H}_{\text{trial}} = \mathcal{H}_0 + \frac{E_S}{2} \widehat{\varphi}_T^2. \quad (\text{A.21})$$



Now we impose the variational principle in the full Hamiltonian,

$$\frac{\partial}{\partial E_S} \langle \Psi | \mathcal{H} | \Psi \rangle = 0. \quad (\text{A.22})$$

We express the full Hamiltonian  $\mathcal{H}$  with respect to the trial one  $\mathcal{H}_{\text{trial}}$ ,

$$\frac{\partial}{\partial E_S} \langle \Psi | \mathcal{H}_{\text{trial}} - E_{J,T} \cos \hat{\varphi}_T - \frac{E_S}{2} \hat{\varphi}_T^2 | \Psi \rangle = 0. \quad (\text{A.23})$$

The first term gives

$$\begin{aligned} \frac{\partial \langle \Psi | \mathcal{H}_{\text{trial}} | \Psi \rangle}{\partial E_S} &= E_\Psi \left( \frac{\partial \langle \Psi |}{\partial E_S} | \Psi \rangle + \langle \Psi | \frac{\partial | \Psi \rangle}{\partial E_S} \right) + \frac{1}{2} \langle \Psi | \hat{\varphi}_T^2 | \Psi \rangle \\ &= E_\Psi \underbrace{\frac{\partial \langle \Psi | \Psi \rangle}{\partial E_S}}_{=0} + \frac{1}{2} \langle \Psi | \hat{\varphi}_T^2 | \Psi \rangle \end{aligned} \quad (\text{A.24})$$

Introducing this in Eq. (A.23) and simplifying we obtain

$$E_S = -2E_{J,T} \frac{\frac{\partial}{\partial E_S} \langle \Psi | \cos \hat{\varphi}_T | \Psi \rangle}{\frac{\partial}{\partial E_S} \langle \Psi | \hat{\varphi}_T^2 | \Psi \rangle}. \quad (\text{A.25})$$

Now we express  $\hat{\varphi}_T$  in terms of the normal modes of  $\mathcal{H}_{\text{trial}}$ ,

$$\hat{\varphi}_T = \sum_k \varphi_k (a_k + a_k^\dagger). \quad (\text{A.26})$$

Therefore the cosine term is given by

$$\begin{aligned} \cos \hat{\varphi}_T &= \frac{1}{2} \left( e^{i\hat{\varphi}_T} + e^{-i\hat{\varphi}_T} \right) \\ &= \frac{1}{2} e^{i\sum_k \varphi_k (a_k + a_k^\dagger)} + \text{h.c.} \\ &= \frac{1}{2} \left( e^{i\sum_k \varphi_k a_k^\dagger} \right) \left( e^{i\sum_k \varphi_k a_k} \right) \left( e^{-\frac{1}{2}\sum_k \varphi_k^2} \right) + \text{h.c.} \end{aligned} \quad (\text{A.27})$$

In the last step we used the Baker-Campbell-Hausdorff formula. We are evaluating the expected value for the ground state, then

$$a_k | \Psi \rangle = 0. \quad (\text{A.28})$$

We therefore obtain

$$\begin{aligned} \langle \Psi | \cos \hat{\varphi}_T | \Psi \rangle &= \frac{1}{2} \underbrace{\langle \Psi | e^{i\sum_k \varphi_k a_k^\dagger}}_{\langle \Psi |} \underbrace{e^{i\sum_k \varphi_k a_k} | \Psi \rangle}_{| \Psi \rangle} e^{-\frac{1}{2}\sum_k \varphi_k^2} + \text{h.c.} = \\ &= e^{-\frac{1}{2}\sum_k \varphi_k^2}. \end{aligned} \quad (\text{A.29})$$

We can relate this expression to the expected value  $\langle \Psi | \hat{\varphi}_T^2 | \Psi \rangle$  by noting that

$$\langle \Psi | \hat{\varphi}_T^2 | \Psi \rangle = \sum_{k,k'} \varphi_k \varphi_{k'} \langle \Psi | (a_k + a_k^\dagger) (a_{k'} + a_{k'}^\dagger) | \Psi \rangle = \sum_k \varphi_k^2. \quad (\text{A.30})$$

Now substituting Eq. (A.30) in Eq. (A.29) we obtain

$$\langle \Psi | \cos \hat{\varphi}_T | \Psi \rangle = e^{-\frac{1}{2} \langle \Psi | \hat{\varphi}_T^2 | \Psi \rangle}. \quad (\text{A.31})$$

Now we can obtain the elements in the expression for  $E_S$  in Eq. (A.25),

$$\frac{\partial}{\partial E_S} \langle \Psi | \cos \hat{\varphi}_T | \Psi \rangle = -\frac{1}{2} \left[ \frac{\partial}{\partial E_S} \langle \Psi | \hat{\varphi}_T^2 | \Psi \rangle \right] e^{-\frac{1}{2} \langle \Psi | \hat{\varphi}_T^2 | \Psi \rangle}. \quad (\text{A.32})$$

Introducing this in Eq. (A.25) we obtain the sCHA equation in Eq. (2.93) in the main text.

## A.4 TPS calculations

### A.4.1 Dispersion relation

We want to obtain the expression in Eq. (3.43) in the main text. We start with the dispersion relation of the array,

$$\omega_k^2 = \frac{1}{L_J C_J} \frac{1 - \cos(ka)}{1 - \cos(ka) + \frac{C_g}{2C_J}}. \quad (\text{A.33})$$

Using the plasma frequency  $\omega_p = 1/\sqrt{L_J (C_J + C_g/4)}$  and the trigonometric relation  $1 - \cos x = 2 \sin^2 x/2$  we obtain

$$\omega_k^2 = \omega_p^2 \left( 1 + \frac{C_g}{4C_J} \right) \left( \frac{2 \sin^2 \left( \frac{ka}{2} \right)}{2 \sin^2 \left( \frac{ka}{2} \right) + \frac{C_g}{2C_J}} \right). \quad (\text{A.34})$$

To get to the desired expression we need to obtain the cotangent as a function of the sine. They are related via

$$\cot^2 x = \frac{1}{\sin^2 x} - 1. \quad (\text{A.35})$$

From Eq. (A.34) we obtain

$$\cot^2 \left( \frac{ka}{2} \right) = \frac{1}{\sin^2 \left( \frac{ka}{2} \right)} - 1 = \left( \frac{4C_J}{C_g} + 1 \right) \left( \left( \frac{\omega_p}{\omega_k} \right)^2 - 1 \right). \quad (\text{A.36})$$

This already gives Eq. (3.43).

### A.4.2 Solving the system of equations

We want to solve the system of equations given by Eqs. (3.44) to (3.46) in the main text. We reproduce it here;

$$\frac{1}{L_{J,T,S}} (\Phi_L - \Phi_R) = \omega^2 (C_1 \Phi_L - C_{sh} \Phi_R), \quad (\text{A.37})$$

$$\frac{1}{L_{J,T,S}} (\Phi_R - \Phi_L) = \omega^2 (-C_{sh} \Phi_L + C_1 \Phi_R - C_c \Phi_1), \quad (\text{A.38})$$

$$\frac{1}{L_J} (\Phi_1 - \Phi_2) = \omega^2 (-C_c \Phi_R + C_2 \Phi_1 - C_J \Phi_2). \quad (\text{A.39})$$

Combining Eqs. (A.37) and (A.38) we obtain

$$\Phi_R = \frac{C_c [\omega^2 C_1 - 1/L_{J,T,S}]}{(C_1 - C_{sh}) [(C_1 + C_{sh}) \omega^2 - 2/L_{J,T,S}]} \Phi_1 = M(\omega) \Phi_1 \quad (\text{A.40})$$

Now use Eqs. (A.39) and (A.40) to obtain an expression relating  $\Phi_2$  and  $\Phi_1$ . We rewrite Eq. (A.39) as

$$\frac{1}{L_J \omega^2} (\Phi_1 - \Phi_2) = (-C_c \Phi_R + C_2 \Phi_1 - C_J \Phi_2). \quad (\text{A.41})$$

We can substitute  $\omega$  in this expression using the dispersion relation for the chain, Eq. (A.33). As an intermediate step we obtain

$$\frac{1}{L_J \omega^2} = C_J + \frac{C_g}{2(1 - \cos k)}. \quad (\text{A.42})$$

Inserting this into Eq. (A.39) and simplifying we get

$$\frac{C_g}{2[1 - \cos(ka)]} (\Phi_1 - \Phi_2) = (C_2 - C_J - C_c M(\omega)) \Phi_1 \equiv C_{\text{eff}} \Phi_1. \quad (\text{A.43})$$

Here we introduced the capacitance  $C_{\text{eff}}$  that is given in Eq. (3.49) in the main text.

The final step is to substitute both  $\Phi_1$  and  $\Phi_2$  with their mode definition,

$$\Phi_l = \varphi_0 N(\omega) \cos[ka(l-1) - \phi] \quad \text{with } l = 1, 2, 3, \dots \quad (\text{A.44})$$

$$\Phi_1 = \varphi_0 N(\omega) \cos \phi, \quad (\text{A.45})$$

$$\Phi_2 = \varphi_0 N(\omega) \cos(ka - \phi). \quad (\text{A.46})$$

We can take out the phase  $\phi$  for  $\Phi_2$  by using the following trigonometric relation

$$\cos(x - y) = \cos x \cos y + \sin x \sin y. \quad (\text{A.47})$$

This gives

$$\Phi_2 = \varphi_0 N(\omega) [\cos(ka) \cos \phi + \sin(ka) \sin \phi]. \quad (\text{A.48})$$

We can now substitute the expressions for  $\Phi_1$  and  $\Phi_2$  in Eq. (A.43). This gives

$$\frac{C_g}{2[1 - \cos(ka)]} (\cos \phi - \cos(ka) \cos \phi - \sin(ka) \sin \phi) = C_{\text{eff}} \cos \phi. \quad (\text{A.49})$$

We divide at both sides of the expression by  $\cos \phi$  obtaining

$$\frac{C_g}{2[1 - \cos(ka)]} (1 - \cos(ka) - \sin(ka) \tan \phi) = C_{\text{eff}}. \quad (\text{A.50})$$

Now we finally obtain

$$\tan \phi = \left(1 - \frac{2C_{\text{eff}}}{C_g}\right) \left(\frac{1 - \cos(ka)}{\sin(ka)}\right) = \left(1 - \frac{2C_{\text{eff}}}{C_g}\right) \tan\left(\frac{ka}{2}\right). \quad (\text{A.51})$$

### A.4.3 Correlation function of an harmonic system

We want to obtain the correlation function given by

$$\langle [\hat{\varphi}_l(t), \hat{\varphi}_l(0)] \rangle = \langle \hat{\varphi}_l(t) \hat{\varphi}_l(0) \rangle - \langle \hat{\varphi}_l(0) \hat{\varphi}_l(t) \rangle. \quad (\text{A.52})$$

The discrete definition of  $\hat{\varphi}_l$  is given by

$$\hat{\varphi}_l = i \sqrt{\frac{\hbar}{2}} \frac{1}{\varphi_0} \sum_k \pi_{l,k} (a_k - a_k^\dagger), \quad (\text{A.53})$$

where  $\varphi_0 = \hbar/2e$  is the reduced magnetic flux quantum. For the infinite array we define a continuous function for  $\hat{\varphi}_l$  given by

$$\hat{\varphi}_l = i \frac{1}{\sqrt{2}} \int_0^{\omega_p} d\omega \varphi_l(\omega) (b_\omega - b_\omega^\dagger). \quad (\text{A.54})$$

Here we defined the bosonic operators  $b_\omega$  and  $b_\omega^\dagger$  for mode frequency  $\omega$ . They satisfy the commutation relation

$$[b_\omega, b_{\omega'}^\dagger] = \delta(\omega - \omega'). \quad (\text{A.55})$$

We introduced also the mode profile  $\varphi_l(\omega)$ . It is given by Eq. (3.42), reproduced here for the superconducting phase

$$\varphi_l(\omega) = N(\omega) \cos[ka(l-1) - \phi] \quad \text{with } l = 1, 2, 3, \dots \quad (\text{A.56})$$

From the definition in Eq. (A.54) we can get the correlation function in Eq. (A.52). First we calculate

$$\begin{aligned} \langle \hat{\varphi}_l(t) \hat{\varphi}_l(0) \rangle &= \langle e^{i\mathcal{H}t} \hat{\varphi}_l(0) e^{-i\mathcal{H}t} \hat{\varphi}_l(0) \rangle = \\ &= \int d\omega \int d\omega' \varphi_l(\omega) \varphi_l(\omega') \langle 0 | e^{i\mathcal{H}t} (b_\omega - b_\omega^\dagger) e^{-i\mathcal{H}t} (b_{\omega'} - b_{\omega'}^\dagger) | 0 \rangle. \end{aligned} \quad (\text{A.57})$$

We introduce the completeness relation in the eigenstates of  $\mathcal{H}$

$$\int d\Omega |\Omega\rangle \langle \Omega| = I \quad (\text{A.58})$$

and obtain

$$\begin{aligned} \langle \hat{\varphi}_l(t) \hat{\varphi}_l(0) \rangle &= \\ &= \int d\omega \int d\omega' \varphi_l(\omega) \varphi_l(\omega') \langle 0 | e^{i\mathcal{H}t} (\mathbf{b}_\omega - \mathbf{b}_\omega^\dagger) e^{-i\mathcal{H}t} (\mathbf{b}_{\omega'} - \mathbf{b}_{\omega'}^\dagger) | 0 \rangle = \\ &= \int d\omega \int d\omega' \varphi_l(\omega) \varphi_l(\omega') \int d\Omega \langle 0 | (\mathbf{b}_\omega - \mathbf{b}_\omega^\dagger) |\Omega\rangle e^{-i\Omega t} \langle \Omega | (\mathbf{b}_{\omega'} - \mathbf{b}_{\omega'}^\dagger) | 0 \rangle = \\ &= \int d\omega \int d\omega' \varphi_l(\omega) \varphi_l(\omega') \int d\Omega \delta(\omega - \Omega) e^{-i\Omega t} \delta(\omega' - \Omega) = \\ &= \int d\Omega |\varphi_l(\Omega)|^2 e^{-i\Omega t}. \end{aligned} \quad (\text{A.59})$$

Finally we obtain for the commutator

$$\langle [\hat{\varphi}_l(t), \hat{\varphi}_l(0)] \rangle = \int d\Omega |\varphi_l(\Omega)|^2 (e^{-i\Omega t} - e^{i\Omega t}) \quad (\text{A.60})$$

*The spectral density*

We define the spectral density as

$$\tilde{C}_{[\varphi, \varphi]} = \frac{2E_S}{\omega_T} \text{Re} \int_0^\infty \frac{dt}{2\pi} e^{i\omega t} \langle [\hat{\varphi}_T(t), \hat{\varphi}_T(0)] \rangle. \quad (\text{A.61})$$

Introducing Eq. (A.60) we obtain

$$\begin{aligned} \tilde{C}_{[\varphi, \varphi]} &= \frac{2E_S}{\omega_T} \text{Re} \int_0^\infty \frac{dt}{2\pi} e^{i\omega t} \int_0^\infty d\Omega |\varphi_l(\Omega)|^2 (e^{-i\Omega t} - e^{i\Omega t}) = \\ &= \frac{2E_S}{\omega_T} \int_0^\infty d\Omega |\varphi_l(\Omega)|^2 \frac{1}{2\pi} [\pi \delta(\omega - \Omega)] = \\ &= \frac{E_S}{\omega_T} \varphi_l(\omega)^2 \end{aligned} \quad (\text{A.62})$$

Therefore, for the transmon phase  $\hat{\varphi}_T = \hat{\varphi}_R - \hat{\varphi}_L$  we obtain

$$\tilde{C}_{[\varphi, \varphi]} = \frac{E_S}{\omega_T} (\varphi_R(\omega) - \varphi_L(\omega))^2 \quad (\text{A.63})$$

Now we need to obtain the normalization constant  $N$  in Eq. (A.56) to compute the correlation function analytically. As it is shown in Eq. (2.57) in the main text,

the amplitudes  $\varphi_l(\omega)$  must fulfill

$$\sum_{l,s=L,R,1,2,\dots} \varphi_0^2 \varphi_l(\omega) \widehat{L}_0^{-1}[l,s] \varphi_s(\omega') = \hbar \omega \delta(\omega - \omega'). \quad (\text{A.64})$$

From the mode definition in Eq. (A.56) we can write

$$\varphi_0 \sum_{l>1} \widehat{L}_0^{-1}[l,s] \varphi_s(\omega') = 2E_J [1 - \cos(k'a)] N(\omega') \cos(lk'a - \phi'). \quad (\text{A.65})$$

As explained in Snyman and Florens<sup>30</sup>, we only need to take into account the prefactor to  $\delta(\omega - \omega')$  in Eq. (A.64). We now obtain

$$\begin{aligned} & \sum_{l,s>1} \varphi_0^2 \varphi_l(\omega) \widehat{L}_0^{-1}[l,s] \varphi_s(\omega') = \\ & = 2E_J [1 - \cos(k'a)] N(\omega) N(\omega') \sum_{l=1}^{\infty} \cos(lka - \phi) \cos(lk'a - \phi') + \\ & + \text{finite terms when } \omega = \omega'. \end{aligned} \quad (\text{A.66})$$

The last sum can be simplified using the following relations,

$$\begin{aligned} \cos(a-b) \cos(c-d) &= \frac{1}{2} [\cos((a-c) - (b-d)) + \\ & + \cos((a+c) - (b+d))] \end{aligned} \quad (\text{A.67})$$

and

$$\sum_{l=1}^{\infty} \cos(lx+y) = \pi \cos y \delta(x \bmod(2\pi)) - \frac{1}{2}. \quad (\text{A.68})$$

Again, dropping finite terms we arrive to

$$\begin{aligned} & \sum_{l=1}^{\infty} \cos(lka - \phi) \cos(lk'a - \phi') = \frac{\pi}{2} \cos(\phi - \phi') \delta(a(k - k')) = \\ & = \frac{\pi}{2} \frac{1}{\partial(ka)/\partial\omega} + \text{finite terms when } k = k'. \end{aligned} \quad (\text{A.69})$$

We therefore obtain

$$\hbar \omega \delta(\omega - \omega') = \frac{\pi E_J [1 - \cos(ka)]}{\partial(ka)/\partial\omega} \delta(\omega - \omega') N(\omega) N(\omega') + \text{finite terms}. \quad (\text{A.70})$$

It can be shown<sup>30</sup> that this finite terms are zero. Finally we arrive to

$$N = \sqrt{\frac{\hbar \omega}{\pi E_J [1 - \cos(ka)]} \frac{\partial ka}{\partial \omega}}. \quad (\text{A.71})$$



# Scripts

# B

## B.1 *NanoBeam files*

First all pattern files need to be converted from `.gds` to `.npf`. This is easily done using a specific software provided by the manufacturer. Then we have to prepare the `.njf` files. The basic structure of a `.njf` file is given in the following lines.

```
1 .global
2 registration      (x_g1,y_g1)    (x_g2, y_g1)
3 marktype          mark_type
4 focus             focus_type
5 .end
```

First we find two global marks to guaranty horizontal alignment and a proper definition of the distances. Then we need to tell the e-beam to register these marks. This is done in the first part of the `.njf` file. With the keywords `.global` and `.end` we define the environment to register these two global marks. First we give the  $x, y$  coordinates for the lower left  $(x_{g1}, y_{g1})$  and lower right  $(x_{g2}, y_{g1})$  marks. They are horizontally aligned, that is why we use the same  $y$  coordinate in both. They are registered using the keyword `registration`. Then we need to specify the shape of the mark. This is done via the command `marktype`. For a  $8\mu\text{m} \times 8\mu\text{m}$  square we set `mark_type` to `sqr8`. Finally with the keyword `focus` we set the type of focus.

```
6 .block
7 origin           (x_0,y_0)
8 registration      (x_u_left, y_u_left) (x_u_right,y_u_right)
9 registration      (x_l_left, y_l_left) (x_l_right,y_l_right)
10 marktype         mark_type
11 focus            focus_type
12 stepsize         (x_step, y_step)
13 grid             (x_grid, y_grid)
14 base_dose        base_dose_value
15
16 pattern          pattern_id_1    (x_p1_0, y_p1_0)
17 pattern          pattern_id_2    (x_p2_0, y_p2_0)
18 .end
```

Now we include the structures we want to write. With the keywords `.block` and `.end` we define a block environment with local focus marks. In practice a



block environment is just a single chip in the two inch wafer. The first thing to do is to give the  $x, y$  coordinates of the lower left corner of the block in the *global* coordinate system, i.e. referenced to the origin  $x_{g1}, y_{g1}$  defined in the global environment. To do so we write `origin` and the coordinates  $(x_0, y_0)$ . Next we give to the e-beam the coordinates of the local focus marks in the *local* coordinate system. It is *mandatory* to give them as shown in the example.  $(x_{u\_left}, y_{u\_left})$  is the upper left corner,  $(x_{u\_right}, y_{u\_right})$  is the upper right corner,  $(x_{l\_left}, y_{l\_left})$  is the lower left corner and  $(x_{l\_right}, y_{l\_right})$  is the lower right corner. We again define the type of focus mark and the type of focus with the commands `marktype` and `focus`. Now we can create copies of this block and distribute them in a grid. With `stepsize` we define the step of the grid  $(x\_step, y\_step)$ . With `grid` we give the size  $(x\_grid, y\_grid)$ , e.g.  $(3, 2)$  for a  $3 \times 2$  matrix. With `base_dose` we give a factor that multiplies all the doses in the block. Finally we include all the patterns we want to write in this block using `pattern` followed by a pattern id that will be defined afterward (`pattern_id_1` and `pattern_id_2` in the example) and the coordinates of the lower left corner of the pattern in the *local* coordinate system,  $(x_{p1\_0}, y_{p1\_0})$  and  $(x_{p2\_0}, y_{p2\_0})$  in the example.

```

19 .pattern
20   id      pattern_id_1
21   filename file_path/_pattern_name_1.npf
22   dose    layer_number_1      layer_dose_1
23   dose    layer_number_2      layer_dose_2
24 .end
25
26 .pattern
27   id      pattern_id_2
28   filename file_path/_pattern_name_2.npf
29   dose    layer_number_1      layer_dose_1
30   dose    layer_number_2      layer_dose_2
31 .end

```

It is necessary now to relate the desired pattern `.npf` files to the given pattern ids. This is done in the pattern environment between `.pattern` and `.end`. First the `id` of the structure is given. This has to be the same as the one given previously with the `pattern` keyword. The path to the `.npf` file is given with the command `filename`. Then the doses are specified using `dose` followed by the layer number and the dose in  $C/m^2$ . The total dose in a layer is given by the base dose multiplied by the local dose.

```

32 .write
33   current current_type
34 .end

```

Finally we tell the e-beam to write the given structures. For doing so we use `.write` and `.end`. In between we set the `current` to a `current_type`.

We are going to use two `.njf` files. The first one (`njf_jj`) is for writing the small structures, Josephson junctions and wires (layers 1, 2 and 3). This layers are written at low current which ensures a high precision. In the second one

(njf\_PADs) we include the rest of the structures, mainly the big pads and the arms (layers 4, 5, ...). Due to their big size it would take too long to write them at the same current as the first ones and therefore we use a much higher current. In order to run both files one after the other we use a .nbf file.

```

1 loadchuck chuck_number
2
3 run auto_conjugate
4 run nbwrite path/njf_jj -1=mark_1:nr1 -2=mark_2:nr2
5
6 find_db bc=36 datum=8 L=1
7 run auto_conjugate
8 sleeps 3600
9 run auto_conjugate
10 run nbwrite path/njf_PADs -1=mark_1:nr1 -2=mark_2:nr2
11
12 find_db bc=0.9 datum=8
13 unloadchuck
14 run check_gun

```

First we specify the chuck that should be loaded using `loadchuck`. With the command `run` we run the different files needed for writing. Then we run the command `auto_conjugate` which aligns and sets up the column, i.e. sets the focus, corrects for the astigmatism etc. Then using `nbwrite` we run the desired .njf file specifying two global focus marks horizontally aligned, `mark_1` and `mark_2`. As it can be seen we use two .njf files, one for the junctions and one for the pads. Between these two files the writing current is increased. This is done with the `find_db` command that loads a state from a database with the desired writing parameters. Finally we unload the chuck and run `check_gun`. This procedure allows to check the emission current while the machine is not being used.

## B.2 Python GDS

In this section we include a short example of how to obtain the pattern shown in Fig. 4.15 (a) using Python. As a first step it is important to be familiar with some of the classes defined in the [gdsCAD documentation](#). We use mainly

- `gdsCAD.core.Cell`
- `gdsCAD.core.Layout`
- `gdsCAD.shapes.Rectangle`

First we import the needed libraries. From the basic shapes provided by the library `gdsCAD` we created our own library called `gds_classes` which contains classes for Josephson junctions, SQUIDS and wires.

```

1 import numpy as np
2 import gdsCAD
3 import gds_classes #Structures library

```

Now we define the parameters of the SQUID array.

```

4 filename = 'cosine_chain'
5
6 #SQUID_parameters
7 junction_width = 0.2
8 width_squid = 0.6
9 height_squid = 4
10 asymmetry = 0.25
11 wire_width = 0.35
12 inner_height = 3.3 #y dimension of layer 3
13
14 number_of_elements = 50 #Number of SQUIDS
15                          #in the array

```

Using the `gds_classes` we define a single SQUID. This SQUID will be later used to create the array. It is an instance of the `SQUID_multi` class. This class is used to define SQUIDS with an inner layer, layer 3 in Fig. 4.12.

```

16 squid = gds_classes.SQUID_multi(x_real=junction_width,
17                                y_inner=inner_height,
18                                x_squid=width_squid,
19                                y_squid=height_squid,
20                                asymmetry=asymmetry,
21                                wire_y_real=wire_width)

```

Now we create a chain of these SQUIDS. We use the method `wired_chain` from the `Component` class. We specify the element present in the chain (`squid`) and the number of elements we want to have (`number_of_elements`). With the argument `length_vec` we can specify the height of the junctions in each of the SQUIDS. If we put a single value the chain will be homogeneous. Because we want to create a cosine chain we obtain `y_height_big_junction_vec` accordingly (not shown). Finally we obtain the pattern with the method `get_polygon`. This method return a list of `gdsCAD.shapes.Rectangle` that we can add to a cell.

```

22 squid_chain = gds_classes.Component.wired_chain(
23             squid,
24             N=number_of_elements,
25             length_vec=y_height_big_junction_vec)
26
27 squid_chain_polygon = squid_chain.get_polygon()

```

We create a cell to add `squid_chain_polygon` using `gds.core.Cell`. Finally we create an instance of the class `gds.core.Layout` and add the created cell. We can show the layout and save it as a GDS file.

```

28 cell_squid_chain = gdsCAD.core.Cell('SQUID_chain')
29 cell_squid_chain.add(squid_chain_polygon)
30
31 layout = gdsCAD.core.Layout('Sample')
32 layout.add(cell_total)
33 layout.show()

```

```
34 layout.save(filename + '.gds')
```

### B.3 Python DC measurements

Here we include the Python script used to perform the DC measurements. We put all the needed functions into a class named `measurement`. For simplicity we include each of the functions separately. The script performs the following tasks

- Importation of the devices, current source and voltmeter.
- Measurement of the *IV* curve.
- Linear fit of the *IV* curve.
- Saving the results.

For importing the devices we use the Python library [PyVISA](#). First we import the needed libraries.

```
1 import numpy as np
2 import visa #PyVISA library
3 from scipy.optimize import leastsq #for the linear fit
```

Then we import the devices

```
4 current_source = visa.instrument(address_1)
5 voltage_meter = visa.instrument(address_2)
```

We obtain the *IV* curve. We use a function `reach_target_current` to set the current in the current source. This function depends on the specific current source used.

```
6 current_values = np.linspace(c_start,
7                               c_end,
8                               c_step)
9
10 voltage_values = np.zeroslike(current_values)
11
12 for current_value in current_values:
13     # Set the current
14     reach_target_current(current_source,
15                           current_value)
16
17     # Get the voltage
18     v = float(voltage_meter.ask(':SENSE:DATA?'))
19     voltage_values = np.append(voltage_values, v)
```

We perform the linear fit using `polyfit` from `numpy`.

```
20 resistance, offset = np.polyfit(current_values,
21                                 voltage_values, 1)
```

Finally we save the result in the desired file.

```
22 filename = 'dc_measurement.dat'  
23  
24 file = open(filename, 'a')  
25 file.write(str(resistance)+'\n')  
26 file.close()
```

# Fabrication recipe



## 1. Gold evaporation.

Metal	Angle	Thickness (nm)
Ti	0°	10
Au	0°	200

## 2. Focus marks.

### (a) Spin Coating

- i. Bake the wafer at 200 °C during 2 min
- ii. Spin coat the resist

Resist	rpm	rpm <sup>2</sup>	$T_{\text{baking}}$ (°C)	$t_{\text{baking}}$ (min)	$d$ (nm)	$t$ (s)
PMMA 3% <sup>a</sup>	4000	4000	180	5	150	30

(b) Development: 60 s in MIBK-IPA and 30 s in IPA.

### (c) Evaporation

Metal	Angle	Thickness (nm)
Ti	0°	10
Au	0°	50

(d) Lift off: At least 5 h in NMP at 80 °C

## 3. Writing the structures

(a) RIE cleaning: 60 s, O<sub>2</sub>, 50 W, Pressure:  $2 \times 10^{-1}$  mbar

### (b) Spin Coating

- i. Bake the wafer at 200 °C during 2 min
- ii. Spin coat the resist

Resist	rpm	rpm <sup>2</sup>	$T_{\text{baking}}$ (°C)	$t_{\text{baking}}$ (min)	$d$ (nm)	$t$ (s)
PMMA-MAA 9% <sup>b</sup>	4000	4000	200	10	750	30
PMMA 4% <sup>c</sup>	5000	5000	180	5	250	30

(c) Writing. The doses are

Part	Dose (C/m <sup>2</sup> )
Wire	11
Junction	11
Inner junction	variable
Undercut	3
Pad	10
Pad arm	12

(d) Development: 60 s in MIBK-IPA:IPA 1:3 and 30 s in IPA.

(e) RIE cleaning: 15 s, O<sub>2</sub>, 10 W, Pressure:  $7 \times 10^{-2}$  mbar

(f) Evaporation

Evaporation		
Metal	Angle	Thickness (nm)
Al 1	+ 35	20
Al 2	- 35	50

Oxidation	
$t_{\text{ox}}$ (min)	Pressure (mbar)
5	4

(g) Lift off: At least 5 h in NMP at 80 °C. Then 1 min ultrasonics at 60 % power.

4. Dicing. Spin coat the sample with resist to protect the structures. Do not bake the resist.

Resist	rpm	rpm <sup>2</sup>	$t$ s
s1818	4000	4000	30

<sup>a</sup>PMMA 950K AR-P 679.04 diluted in ethyl lactate (3 volumes of AR-P per volume of ethyl lactate)

<sup>b</sup>AR-P 617.14 diluted in AR 600.07 (9/5)

<sup>c</sup>PMMA 950K AR-P 679.04 diluted in ethyl lactate (4 volumes of AR-P per volume of ethyl lactate)

# Additional transmon phase shift data D

Here we give several figures showing the good agreement between the experimentally obtained frequency shift  $\delta\phi_n$  and the theoretical one  $\delta\phi$ . The details of the process followed for obtaining the experimental points are given in Section 7.3.1. The theoretical curves are given by Eqs. (3.51) and (3.52), reproduced here

$$\delta\phi = \phi(\Phi_T \neq \Phi_0/2) - \phi(\Phi_T = \Phi_0/2),$$
$$\tan \phi = \left[ 1 - \frac{2C_{\text{eff}}(\omega, \Phi_T)}{C_g} \right] \sqrt{\frac{C_g}{C_g + 4C_J} \frac{1}{\sqrt{\left(\frac{\omega_p(\Phi_C)}{\omega}\right)^2 - 1}}}. \quad (\text{D.1})$$

In Fig. D.1 we show the obtained experimental data with the theoretical curves obtained from Eq. (D.1). As we see, the data theory agreement is good at several  $\Phi_C$  and  $\Phi_T$  values with no fitting parameter.



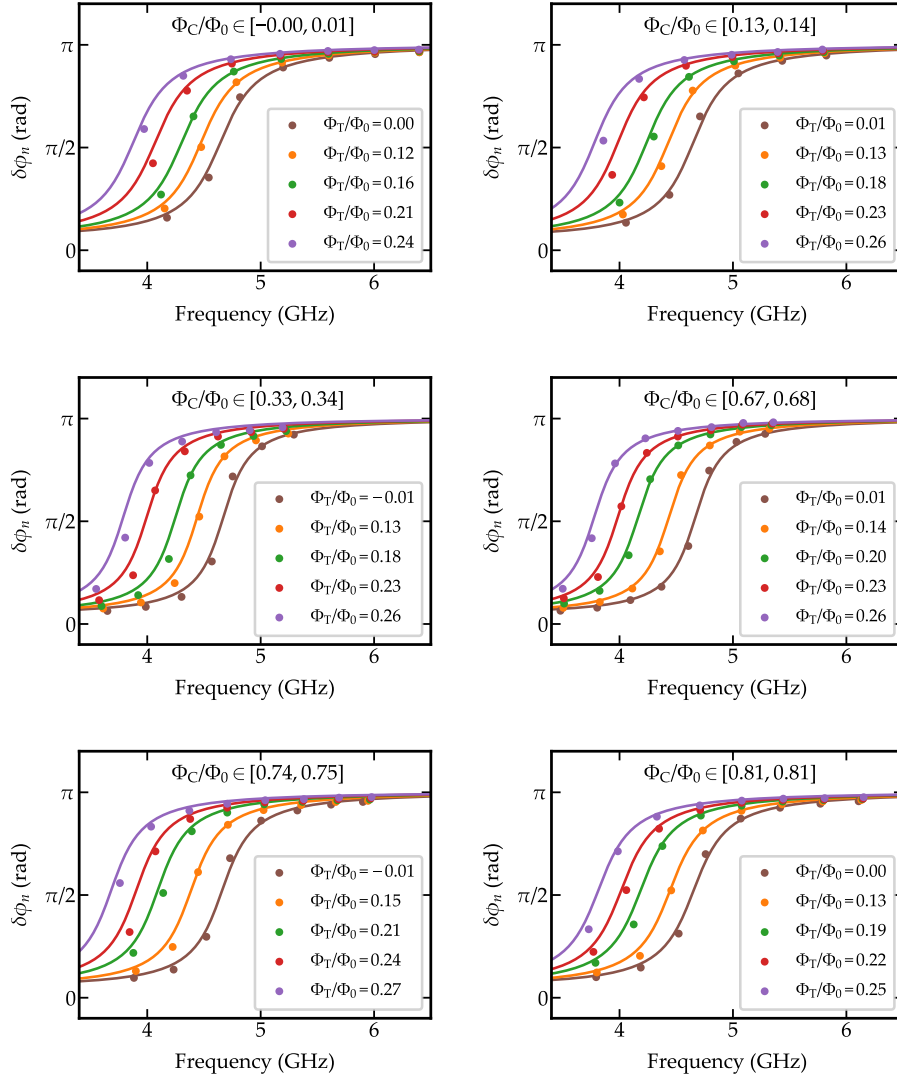


Figure D.1 – Comparison between the experimentally obtained  $\delta\phi_n$  and the theoretical one  $\delta\phi$  for several values of flux in the array  $\Phi_C$  and flux in the transmon  $\Phi_T$ .

# Bibliography

- [1] G. J. M. D.F. Walls, *Quantum Optics* (Springer, 2010), ISBN 9783540285731.  
(Cited on pages 1, 13, and 14.)
- [2] J. Q. You and F. Nori, “Atomic physics and quantum optics using superconducting circuits”, *Nature* 474, 589 (2011).  
(Cited on page 1.)
- [3] T. D. Ladd, F. Jelezko, R. Laflamme, Y. Nakamura, C. Monroe, and J. L. O’Brien, “Quantum computers”, *Nature* 464, 45 (2010).  
(Cited on page 1.)
- [4] G. Wendin, “Quantum information processing with superconducting circuits: a review”, *Reports on Progress in Physics* 80, 106001 (2017).  
(Cited on page 1.)
- [5] M.-J. Hwang, R. Puebla, and M. B. Plenio, “Quantum Phase Transition and Universal Dynamics in the Rabi Model”, *Physical Review Letters* 115, 180404 (2015).  
(Cited on page 1.)
- [6] Z.-J. Ying, M. Liu, H.-G. Luo, H.-Q. Lin, and J. Q. You, “Ground-state phase diagram of the quantum Rabi model”, *Physical Review A* 92, 053823 (2015).  
(Cited on pages 2 and 18.)
- [7] M. Devoret, S. Girvin, and R. Schoelkopf, “Circuit-QED: How strong can the coupling between a Josephson junction atom and a transmission line resonator be?”, *Ann. Phys. (Leipzig)* 16, 767 (2007).  
(Cited on pages 2, 15, 18, and 51.)
- [8] V. E. Manucharyan, A. Baksic, and C. Ciuti, “Resilience of the quantum Rabi model in circuit QED”, *Journal of Physics A* 50, 294001 (2017).  
(Cited on pages 2, 18, 51, and 52.)
- [9] A. Wallraff, D. I. Schuster, A. Blais, L. Frunzio, R.-S. Huang, J. Majer, S. Kumar, S. M. Girvin, and R. J. Schoelkopf, “Strong coupling of a single photon to a superconducting qubit using circuit quantum electrodynamics”, *Nature* 431, 162 (2004).  
(Cited on pages 2 and 18.)
- [10] I. Chiorescu, P. Bertet, K. Semba, Y. Nakamura, C. J. P. M. Harmans, and J. E. Mooij, “Coherent dynamics of a flux qubit coupled to a harmonic oscillator”,

- Nature* **431**, 159 (2004).  
(Cited on pages **2** and **18**.)
- [11] A. Wallraff, D. I. Schuster, A. Blais, L. Frunzio, J. Majer, M. H. Devoret, S. M. Girvin, and R. J. Schoelkopf, "Approaching Unit Visibility for Control of a Superconducting Qubit with Dispersive Readout", *Physical Review Letters* **95**, 060501 (2005).  
(Cited on pages **2** and **18**.)
- [12] D. I. Schuster, A. Wallraff, A. Blais, L. Frunzio, R.-S. Huang, J. Majer, S. M. Girvin, and R. J. Schoelkopf, "ac Stark Shift and Dephasing of a Superconducting Qubit Strongly Coupled to a Cavity Field", *Physical Review Letters* **94**, 123602 (2005).  
(Cited on pages **2**, **18**, and **71**.)
- [13] J. A. Schreier, A. A. Houck, J. Koch, D. I. Schuster, B. R. Johnson, J. M. Chow, J. M. Gambetta, J. Majer, L. Frunzio, M. H. Devoret, S. M. Girvin, and R. J. Schoelkopf, "Suppressing charge noise decoherence in superconducting charge qubits", *Physical Review B* **77**, 180502 (2008).  
(Cited on pages **2** and **28**.)
- [14] T. Niemczyk, F. Deppe, H. Huebl, E. P. Menzel, F. Hocke, M. J. Schwarz, J. J. Garcia-Ripoll, D. Zueco, T. Hümmer, E. Solano, A. Marx, and R. Gross, "Circuit quantum electrodynamics in the ultrastrong-coupling regime", *Nature Physics* **6**, 772 (2010).  
(Cited on pages **2**, **10**, **19**, and **141**.)
- [15] P. Forn-Díaz, J. Lisenfeld, D. Marcos, J. J. García-Ripoll, E. Solano, C. J. P. M. Harmans, and J. E. Mooij, "Observation of the Bloch-Siegert Shift in a Qubit-Oscillator System in the Ultrastrong Coupling Regime", *Physical Review Letters* **105**, 237001 (2010).  
(Cited on pages **2**, **10**, **19**, and **141**.)
- [16] F. Yoshihara, T. Fuse, S. Ashhab, K. Kakuyanagi, S. Saito, and K. Semba, "Superconducting qubit-oscillator circuit beyond the ultrastrong-coupling regime", *Nature Physics* **13**, 44 (2016).  
(Cited on page **2**.)
- [17] N. K. Langford, R. Sagastizabal, M. Kounalakis, C. Dickel, A. Bruno, F. Luthi, D. J. Thoen, A. Endo, and L. DiCarlo, "Experimentally simulating the dynamics of quantum light and matter at deep-strong coupling", *Nature Communications* **8**, 1715 (2017).  
(Cited on pages **2** and **19**.)
- [18] J. Braumüller, M. Marthaler, A. Schneider, A. Stehli, H. Rotzinger, M. Weides, and A. V. Ustinov, "Analog quantum simulation of the Rabi model in the ultra-strong coupling regime", *Nature Communications* **8**, 779 (2017).  
(Cited on pages **2** and **19**.)
- [19] O. Astafiev, A. M. Zagoskin, A. A. Abdumalikov, Y. A. Pashkin, T. Yamamoto, K. Inomata, Y. Nakamura, and J. S. Tsai, "Resonance fluorescence

- of a single artificial atom.”, *Science* **327**, 840 (2010).  
(Cited on pages [3](#) and [133](#).)
- [20] A. A. Abdumalikov, O. Astafiev, A. M. Zagoskin, Y. A. Pashkin, Y. Nakamura, and J. S. Tsai, “Electromagnetically Induced Transparency on a Single Artificial Atom”, *Physical Review Letters* **104**, 193601 (2010).  
(Cited on page [3](#).)
- [21] B. Peropadre, D. Zueco, D. Porras, and J. J. García-Ripoll, “Nonequilibrium and Nonperturbative Dynamics of Ultrastrong Coupling in Open Lines”, *Physical Review Letters* **111** (2013).  
(Cited on page [3](#).)
- [22] P. Forn-Díaz, J. J. García-Ripoll, B. Peropadre, M. A. Yurtalan, J. L. Orgiazzi, R. Belyansky, C. M. Wilson, and A. Lupascu, “Ultrastrong coupling of a single artificial atom to an electromagnetic continuum”, *Nature Physics* **13**, 39 (2016).  
(Cited on pages [3](#), [8](#), [22](#), [53](#), and [133](#).)
- [23] L. Magazzù, P. Forn-Díaz, R. Belyansky, J. L. Orgiazzi, M. A. Yurtalan, M. R. Otto, A. Lupascu, C. M. Wilson, and M. Grifoni, “Probing the strongly driven spin-boson model in a superconducting quantum circuit”, [arXiv:1709.01157](#) (2017).  
(Cited on page [3](#).)
- [24] A. J. Leggett, S. Chakravarty, A. T. Dorsey, M. P. A. Fisher, A. Garg, and W. Zwerger, “Dynamics of the dissipative two-state system”, *Reviews of Modern Physics* **59**, 1 (1987).  
(Cited on pages [3](#), [19](#), [20](#), and [147](#).)
- [25] I.-C. Hoi, C. M. Wilson, G. Johansson, T. Palomaki, B. Peropadre, and P. Delsing, “Demonstration of a Single-Photon Router in the Microwave Regime”, *Physical Review Letters* **107**, 073601 (2011).  
(Cited on pages [3](#) and [133](#).)
- [26] I.-C. Hoi, C. M. Wilson, G. Johansson, J. Lindkvist, B. Peropadre, T. Palomaki, and P. Delsing, “Microwave quantum optics with an artificial atom in one-dimensional open space”, *New Journal of Physics* **15**, 025011 (2013).  
(Cited on page [3](#).)
- [27] N. M. Sundaresan, Y. Liu, D. Sadri, L. J. Szöcs, D. L. Underwood, M. Malekakhlagh, H. E. Türeci, and A. A. Houck, “Beyond Strong Coupling in a Multimode Cavity”, *Physical Review X* **5**, 021035 (2015).  
(Cited on pages [3](#) and [22](#).)
- [28] S. J. Bosman, M. F. Gely, V. Singh, A. Bruno, D. Bothner, and G. A. Steele, “Multi-mode ultra-strong coupling in circuit quantum electrodynamics”, *npj Quantum Information* **3**, 46 (2017).  
(Cited on pages [3](#) and [144](#).)

- [29] M. Goldstein, M. H. Devoret, M. Houzet, and L. I. Glazman, “Inelastic microwave photon scattering off a quantum impurity in a Josephson-junction array”, *Physical Review Letters* **110**, 017002 (2013).  
(Cited on pages 4 and 20.)
- [30] I. Snyman and S. Florens, “Robust Josephson-Kondo screening cloud in circuit quantum electrodynamics”, *Physical Review B* **92**, 085131 (2015).  
(Cited on pages 4, 37, 51, 63, 64, 136, and 159.)
- [31] N. Gheeraert, S. Bera, and S. Florens, “Spontaneous emission of Schrödinger cats in a waveguide at ultrastrong coupling”, *New Journal of Physics* **19**, 023036 (2017).  
(Cited on pages 4 and 20.)
- [32] N. Gheeraert, X. H. H. Zhang, S. Bera, N. Roch, H. U. Baranger, and S. Florens, “Particle Production in Ultra-Strong Coupling Waveguide QED”, *arXiv:1802.01665* (2018).  
(Cited on pages 4 and 20.)
- [33] S. J. Bosman, M. F. Gely, V. Singh, D. Bothner, A. Castellanos-Gomez, and G. A. Steele, “Approaching ultrastrong coupling in transmon circuit QED using a high-impedance resonator”, *Physical Review B* **95**, 224515 (2017).  
(Cited on page 4.)
- [34] K. Le Hur, “Kondo resonance of a microwave photon”, *Physical Review B* **85**, 140506 (2012).  
(Cited on pages 4, 20, 133, 136, and 147.)
- [35] C. Lobb, “Phase transitions in arrays of Josephson junctions”, *Physica B+C* **126**, 319 (1984).  
(Cited on page 4.)
- [36] B. J. van Wees, H. S. J. van der Zant, and J. E. Mooij, “Phase transitions of Josephson-tunnel-junction arrays at zero and full frustration”, *Physical Review B* **35**, 7291 (1987).  
(Cited on page 4.)
- [37] C. D. Chen, P. Delsing, D. B. Haviland, and T. Claeson, “Experimental investigation of two-dimensional arrays of ultrasmall Josephson junctions”, *Physica Scripta* **1992**, 182 (1992).  
(Cited on page 4.)
- [38] P. Delsing, C. D. Chen, D. B. Haviland, Y. Harada, and T. Claeson, “Charge solitons and quantum fluctuations in two-dimensional arrays of small Josephson junctions”, *Physical Review B* **50**, 3959 (1994).  
(Cited on page 4.)
- [39] S. Corlevi, W. Guichard, F. W. J. Hekking, and D. B. Haviland, “Phase-Charge Duality of a Josephson Junction in a Fluctuating Electromagnetic Environment”, *Physical Review Letters* **97**, 096802 (2006).  
(Cited on pages 4, 32, and 96.)

- [40] T. Weißl, G. Rastelli, I. Matei, I. M. Pop, O. Buisson, F. W. J. Hekking, and W. Guichard, “Bloch band dynamics of a Josephson junction in an inductive environment”, *Physical Review B* **91**, 014507 (2015).  
(Cited on page 4.)
- [41] I. M. Pop, I. Protopopov, F. Lecocq, Z. Peng, B. Pannetier, O. Buisson, and W. Guichard, “Measurement of the effect of quantum phase slips in a Josephson junction chain”, *Nature Physics* **6**, 589 (2010).  
(Cited on page 4.)
- [42] V. E. Manucharyan, N. A. Masluk, A. Kamal, J. Koch, L. I. Glazman, and M. H. Devoret, “Evidence for coherent quantum phase slips across a Josephson junction array”, *Physical Review B* **85**, 024521 (2012).  
(Cited on page 4.)
- [43] A. Ergül, T. Weißl, J. Johansson, J. Lidmar, and D. B. Haviland, “Spatial and temporal distribution of phase slips in Josephson junction chains”, *Scientific Reports* **7**, 11447 (2017).  
(Cited on page 4.)
- [44] C. Altimiras, O. Parlavecchio, P. Joyez, D. Vion, P. Roche, D. Esteve, and F. Portier, “Tunable microwave impedance matching to a high impedance source using a Josephson metamaterial”, *Applied Physics Letters* **103**, 212601 (2013).  
(Cited on page 4.)
- [45] T. Weißl, B. Küng, E. Dumur, A. K. Feofanov, I. Matei, C. Naud, O. Buisson, F. W. J. Hekking, and W. Guichard, “Kerr coefficients of plasma resonances in Josephson junction chains”, *Physical Review B* **92**, 104508 (2015).  
(Cited on page 4.)
- [46] N. A. Masluk, I. M. Pop, A. Kamal, Z. K. Mineev, and M. H. Devoret, “Microwave Characterization of Josephson Junction Arrays: Implementing a Low Loss Superinductance”, *Physical Review Letters* **109**, 137002 (2012).  
(Cited on pages 4, 32, and 122.)
- [47] M. T. Bell, I. A. Sadovskyy, L. B. Ioffe, A. Y. Kitaev, and M. E. Gershenson, “Quantum Superinductor with Tunable Nonlinearity”, *Physical Review Letters* **109**, 137003 (2012).  
(Cited on pages 4 and 32.)
- [48] V. E. Manucharyan, J. Koch, L. I. Glazman, and M. H. Devoret, “Fluxonium: single cooper-pair circuit free of charge offsets.”, *Science* **326**, 113 (2009).  
(Cited on page 4.)
- [49] B. Yurke, M. L. Roukes, R. Movshovich, and A. N. Pargellis, “A low-noise series-array Josephson junction parametric amplifier”, *Applied Physics Letters* **69**, 3078 (1996).  
(Cited on page 4.)

- [50] M. A. Castellanos-Beltran, K. D. Irwin, G. C. Hilton, L. R. Vale, and K. W. Lehnert, "Amplification and squeezing of quantum noise with a tunable Josephson metamaterial", *Nature Physics* **4**, 929 (2008).  
(Cited on page 4.)
- [51] X. Zhou, V. Schmitt, P. Bertet, D. Vion, W. Wustmann, V. Shumeiko, and D. Esteve, "High-gain weakly nonlinear flux-modulated Josephson parametric amplifier using a SQUID array", *Physical Review B* **89**, 214517 (2014).  
(Cited on page 4.)
- [52] U. Weiss, *Quantum dissipative systems* (World Scientific., 2008), 3rd ed., ISBN 13 978-981-279-162-7.  
(Cited on pages 4, 19, 20, and 147.)
- [53] T. Shi, Y. Chang, and J. J. Garcia-Ripoll, "Ultrastrong coupling few-photon scattering theory", *arXiv:1701.04709* (2017).  
(Cited on page 4.)
- [54] Y. Liu and A. A. Houck, "Quantum electrodynamics near a photonic bandgap", *Nature Physics* **13**, 48 (2016).  
(Cited on pages 4 and 146.)
- [55] D. J. Egger and F. K. Wilhelm, "Multimode Circuit Quantum Electrodynamics with Hybrid Metamaterial Transmission Lines", *Physical Review Letters* **111**, 163601 (2013).  
(Cited on page 4.)
- [56] B. L. T. Plourde, H. Wang, F. Rouxinol, and M. D. LaHaye, in *Quantum Information and Computation XIII*, edited by E. Donkor, A. R. Pirich, and M. Hayduk (SPIE, 2015), vol. 9500, p. 95000M.  
(Cited on page 4.)
- [57] B. Peropadre, J. Lindkvist, I.-C. Hoi, C. M. Wilson, J. J. Garcia-Ripoll, P. Delsing, and G. Johansson, "Scattering of coherent states on a single artificial atom", *New Journal of Physics* **15**, 035009 (2013).  
(Cited on pages 8, 28, and 133.)
- [58] D. Pozar, *Microwave Engineering* (John Wiley and Sons, 2005), 4th ed., ISBN 9780470631553.  
(Cited on pages 10, 30, 31, and 39.)
- [59] P. Meystre and M. Sargent, *Elements of quantum optics* (Springer, 2007), ISBN 9783540742098.  
(Cited on page 14.)
- [60] I. I. Rabi, "On the Process of Space Quantization", *Physical Review* **49**, 324 (1936).  
(Cited on page 15.)
- [61] D. Braak, "Integrability of the Rabi model", *Physical Review Letters* **107**, 100401 (2011).  
(Cited on pages 15 and 18.)



- [62] E. Jaynes and F. Cummings, “Comparison of quantum and semiclassical radiation theories with application to the beam maser”, *Proceedings of the IEEE* **51**, 89 (1963).  
(Cited on page 15.)
- [63] S. Haroche and J.-M. Raimond, *Exploring the Quantum* (Oxford University Press, 2006), ISBN 9780198509141.  
(Cited on page 17.)
- [64] R. J. Thompson, G. Rempe, and H. J. Kimble, “Observation of normal-mode splitting for an atom in an optical cavity”, *Physical Review Letters* **68**, 1132 (1992).  
(Cited on page 17.)
- [65] O. Buisson and F. W. J. Hekking, in *Macroscopic Quantum Coherence and Quantum Computing*, edited by D. V. Averin, B. Ruggiero, and P. Silvestrini (Springer, 2001), pp. 137–147, ISBN 978-1-4613-5459-8, 0008275v1, URL <https://arxiv.org/pdf/cond-mat/0008275.pdf>.  
(Cited on page 17.)
- [66] A. Blais, R.-S. Huang, A. Wallraff, S. M. Girvin, and R. J. Schoelkopf, “Cavity quantum electrodynamics for superconducting electrical circuits: An architecture for quantum computation”, *Physical Review A* **69**, 062320 (2004).  
(Cited on pages 17 and 129.)
- [67] J. M. Fink, M. Göppl, M. Baur, R. Bianchetti, P. J. Leek, A. Blais, and A. Wallraff, “Climbing the Jaynes–Cummings ladder and observing its nonlinearity in a cavity QED system”, *Nature* **454**, 315 (2008).  
(Cited on page 18.)
- [68] L. S. Bishop, J. M. Chow, J. Koch, A. A. Houck, M. H. Devoret, E. Thuneberg, S. M. Girvin, and R. J. Schoelkopf, “Nonlinear response of the vacuum Rabi resonance”, *Nature Phys.* **5**, 105 (2008).  
(Cited on page 18.)
- [69] S. Bera, S. Florens, H. U. Baranger, N. Roch, A. Nazir, and A. W. Chin, “Stabilizing spin coherence through environmental entanglement in strongly dissipative quantum systems”, *Physical Review B* **89**, 121108 (2014).  
(Cited on pages 18, 20, and 22.)
- [70] Q. Xie, H. Zhong, M. T. Batchelor, and C. Lee, “The quantum Rabi model: solution and dynamics”, *Journal of Physics A* **50**, 113001 (2017).  
(Cited on page 19.)
- [71] Y. Nazarov and Y. M. Blanter, *Quantum Transport* (Cambridge University Press, 2009), ISBN 9788578110796.  
(Cited on pages 19 and 20.)
- [72] M. Malekakhlagh, A. Petrescu, and H. E. Türeci, “Cutoff-Free Circuit Quantum Electrodynamics”, *Physical Review Letters* **119**, 073601 (2017).  
(Cited on pages 20 and 56.)



- [73] A. O. Caldeira and A. J. Leggett, “Influence of Dissipation on Quantum Tunneling in Macroscopic Systems”, *Physical Review Letters* **46**, 211 (1981).  
(Cited on page 20.)
- [74] A. Caldeira and A. Leggett, “Quantum tunnelling in a dissipative system”, *Annals of Physics* **149**, 374 (1983).  
(Cited on page 20.)
- [75] M. Haeblerlein, F. Deppe, A. Kurcz, J. Goetz, A. Baust, P. Eder, K. Fedorov, M. Fischer, E. P. Menzel, M. J. Schwarz, F. Wulschner, E. Xie, L. Zhong, E. Solano, A. Marx, J.-J. García-Ripoll, and R. Gross, “Spin-boson model with an engineered reservoir in circuit quantum electrodynamics”, *arXiv:1506.09114* (2015).  
(Cited on page 22.)
- [76] B. Josephson, “Possible new effects in superconductive tunnelling”, *Physics Letters* **1**, 251 (1962).  
(Cited on page 23.)
- [77] K. A. Matveev, A. I. Larkin, and L. I. Glazman, “Persistent Current in Superconducting Nanorings”, *Physical Review Letters* **89**, 096802 (2002).  
(Cited on page 24.)
- [78] R. C. Jaklevic, J. Lambe, A. H. Silver, and J. E. Mercereau, “Quantum interference effects in Josephson tunneling”, *Physical Review Letters* **12**, 159 (1964).  
(Cited on page 24.)
- [79] M. Tinkham, *Introduction to superconductivity* (Dover, 2004), 2nd ed., ISBN 0486435032.  
(Cited on pages 24 and 25.)
- [80] J. Koch, T. M. Yu, J. Gambetta, A. A. Houck, D. I. Schuster, J. Majer, A. Blais, M. H. Devoret, S. M. Girvin, and R. J. Schoelkopf, “Charge-insensitive qubit design derived from the Cooper pair box”, *Physical Review A* **76**, 042319 (2007).  
(Cited on pages 25, 27, 28, 46, and 52.)
- [81] M. Devoret, *Quantum Fluctuations in Electrical Circuits* (Les Houches, 1995).  
(Cited on pages 26, 27, and 36.)
- [82] Y. Nakamura, Y. A. Pashkin, and J. S. Tsai, “Coherent control of macroscopic quantum states in a single-Cooper-pair box”, *Nature* **398**, 786 (1999).  
(Cited on page 27.)
- [83] A. Cottet, “Implementation of a quantum bit in a superconducting circuit”, Ph.D. thesis, Université Paris VI (2002).  
(Cited on page 27.)
- [84] V. E. Manucharyan, N. A. Masluk, A. Kamal, J. Koch, L. I. Glazman, and M. H. Devoret, “Evidence for coherent quantum phase slips across a Josephson junction array”, *Physical Review B* **85** (2012).  
(Cited on page 32.)

- [85] C. K. Andersen and A. Blais, "Ultrastrong coupling dynamics with a transmon qubit", *New Journal of Physics* **19**, 023022 (2017).  
(Cited on pages 36, 51, and 136.)
- [86] T. Weißl, "Quantum phase and charge dynamics in Josephson junction chains", Ph.D. thesis, Université Joseph Fourier (2014).  
(Cited on pages 36 and 122.)
- [87] D. A. Frickey, "Conversions between S, Z, Y, h, ABCD, and T parameters which are valid for complex source and load impedances", *IEEE Transactions on microwave theory and techniques* **42**, 205 (1994).  
(Cited on page 39.)
- [88] S. E. Nigg, H. Paik, B. Vlastakis, G. Kirchmair, S. Shankar, L. Frunzio, M. H. Devoret, R. J. Schoelkopf, and S. M. Girvin, "Black-Box Superconducting Circuit Quantization", *Physical Review Letters* **108**, 240502 (2012).  
(Cited on page 54.)
- [89] M. Malekakhlagh and H. E. Türeci, "Origin and implications of an A<sub>2</sub>-like contribution in the quantization of circuit-QED systems", *Physical Review A* **93**, 012120 (2016).  
(Cited on page 56.)
- [90] M. F. Gely, A. Parra-Rodriguez, D. Bothner, Y. M. Blanter, S. J. Bosman, E. Solano, and G. A. Steele, "Convergence of the multimode quantum Rabi model of circuit quantum electrodynamics", *Physical Review B* **95**, 245115 (2017).  
(Cited on page 56.)
- [91] H. J. Levinson, *Principles of Lithography* (SPIE PR, 2005), ISBN 0819456608.  
(Cited on pages 75, 76, and 85.)
- [92] J. Niemeyer and V. Kose, "Observation of large dc supercurrents at nonzero voltages in Josephson tunnel junctions", *Applied Physics Letters* **29** (1976).  
(Cited on page 76.)
- [93] G. J. Dolan, "Offset masks for lift-off photoprocessing", *Applied Physics Letters* **31** (1977).  
(Cited on page 76.)
- [94] I. M. Pop, T. Fournier, T. Crozes, F. Lecocq, I. Matei, B. Pannetier, O. Buisson, and W. Guichard, "Fabrication of stable and reproducible submicron tunnel junctions", *Journal of Vacuum Science & Technology B* **30**, 010607 (2012).  
(Cited on pages 76, 79, and 90.)
- [95] F. Lecocq, I. M. Pop, Z. Peng, I. Matei, T. Crozes, T. Fournier, C. Naud, W. Guichard, and O. Buisson, "Junction fabrication by shadow evaporation without a suspended bridge", *Nanotechnology* **22**, 315302 (2011).  
(Cited on pages 76 and 78.)
- [96] V. Ambegaokar and A. Baratoff, "Tunneling Between Superconductors", *Physical Review Letters* **10**, 486 (1963).  
(Cited on page 93.)

- [97] J. Claudon, “Oscillations cohérentes dans un circuit quantique supraconducteur : le SQUID dc”, Ph.D. thesis, Université Joseph Fourier (2006), URL <https://tel.archives-ouvertes.fr/tel-00011407>.  
(Cited on page 93.)
- [98] K. Gloos, R. S. Poikolainen, and J. P. Pekola, “Wide-range thermometer based on the temperature-dependent conductance of planar tunnel junctions”, *Applied Physics Letters* **77**, 2915 (2000).  
(Cited on page 93.)
- [99] P. J. Koppinen, L. M. Väistö, and I. J. Maasilta, “Complete stabilization and improvement of the characteristics of tunnel junctions by thermal annealing”, *Applied Physics Letters* **90**, 053503 (2007).  
(Cited on page 95.)
- [100] A. Fay, “Couplage variable entre un qubit de charge et un qubit de phase”, Ph.D. thesis, Université Joseph Fourier (2008), URL <https://tel.archives-ouvertes.fr/tel-00310131/document>.  
(Cited on page 96.)
- [101] R. Gross and A. Marx, *Applied Superconductivity* (2004), URL <https://www.wmi.badw.de/teaching/Lecturenotes/AS/AS{ }Chapter1.pdf>.  
(Cited on page 96.)
- [102] I. B. K.C. Gupta, Ramesh Garg, *Microstrip lines and slotlines* (ARTECH, 1979).  
(Cited on pages 98 and 146.)
- [103] R. F. Harrington, *Field Computation by Moment Methods* (Wiley-IEEE Press, 1993), ISBN 978-0-7803-1014-8.  
(Cited on page 98.)
- [104] A. T. A. M. De Waele, “Basic Operation of Cryocoolers and Related Thermal Machines”, *J Low Temp Phys* **164**, 179 (2011).  
(Cited on page 103.)
- [105] F. Pobell, *Matter and methods at low temperatures* (Springer, 2007), ISBN 3540463569.  
(Cited on page 103.)
- [106] E. Dumur, “A V-shape superconducting artificial atom for circuit quantum electrodynamics”, Ph.D. thesis, Université Grenoble Alpes (2015), URL <https://tel.archives-ouvertes.fr/tel-01147222/document>.  
(Cited on pages 106 and 108.)
- [107] R. Barends, J. Wenner, M. Lenander, Y. Chen, R. C. Bialczak, J. Kelly, E. Lucero, P. O ’malley, M. Mariani, D. Sank, H. Wang, T. C. White, Y. Yin, J. Zhao, A. N. Cleland, J. M. Martinis, and J. J. A. Baselmans, “Minimizing quasiparticle generation from stray infrared light in superconducting quantum circuits”, *Appl. Phys. Lett* **99**, 113507 (2011).  
(Cited on pages 109 and 110.)

- [108] J. Aumentado, M. W. Keller, J. M. Martinis, and M. H. Devoret, "Nonequilibrium Quasiparticles and  $2e$  Periodicity in Single-Cooper-Pair Transistors", *Physical Review Letters* **92**, 066802 (2004).  
(Cited on page 109.)
- [109] M. D. Shaw, R. M. Lutchyn, P. Delsing, and P. M. Echternach, "Kinetics of nonequilibrium quasiparticle tunneling in superconducting charge qubits", *Physical Review B* **78**, 024503 (2008).  
(Cited on page 109.)
- [110] J. M. Martinis, M. Ansmann, and J. Aumentado, "Energy Decay in Superconducting Josephson-Junction Qubits from Nonequilibrium Quasiparticle Excitations", *Physical Review Letters* **103**, 097002 (2009).  
(Cited on page 109.)
- [111] E. Dumur, B. Delsol, T. Weißl, B. Kung, W. Guichard, C. Hoarau, C. Naud, K. Hasselbach, O. Buisson, K. Ratter, and B. Gilles, "Epitaxial Rhenium Microwave Resonators", *IEEE Transactions on Applied Superconductivity* **26** (2016).  
(Cited on page 118.)
- [112] Y. Krupko, "Kerr-effect in a non-linear superconducting Josephson metamaterial", In preparation (2018).  
(Cited on page 118.)
- [113] J. Bourassa, F. Beaudoin, J. M. Gambetta, and A. Blais, "Josephson-junction-embedded transmission-line resonators: From Kerr medium to in-line transmission", *Physical Review A* **86**, 013814 (2012).  
(Cited on page 122.)
- [114] O. V. Astafiev, L. B. Ioffe, S. Kafanov, Y. A. Pashkin, K. Y. Arutyunov, D. Shahar, O. Cohen, and J. S. Tsai, "Coherent quantum phase slip", *Nature* **484**, 355 (2012).  
(Cited on page 144.)
- [115] L. Grünhaupt, N. Maleeva, S. T. Skacel, M. Calvo, F. Levy-Bertrand, A. V. Ustinov, H. Rotzinger, A. Monfardini, G. Catelani, and I. M. Pop, "Quasiparticle dynamics in granular aluminum close to the superconductor to insulator transition", *arXiv:1802.01858* (2018).  
(Cited on page 144.)
- [116] D. Niepce, J. Burnett, and J. Bylander, "High Kinetic Inductance NbN Nanowire Superinductors", *arXiv:1802.01723* (2018).  
(Cited on page 144.)
- [117] V. Singh, B. H. Schneider, S. J. Bosman, E. P. J. Merkx, and G. A. Steele, "Molybdenum-rhenium alloy based high-Q superconducting microwave resonators", *Applied Physics Letters* **105**, 222601 (2014).  
(Cited on page 144.)

- [118] J. E. Mooij and G. Schön, “Propagating plasma mode in thin superconducting filaments”, *Physical Review Letters* **55**, 114 (1985).  
(Cited on page 146.)
- [119] B. Camarota, F. Parage, I. Wooldridge, P. Delsing, and O. Buisson, “Plasma Modes in Superconducting Wires: Optimized Experimental Configuration”, *Journal of Low Temperature Physics* **118**, 589 (2000).  
(Cited on page 146.)
- [120] A. J. Annunziata, D. F. Santavicca, L. Frunzio, G. Catelani, M. J. Rooks, A. Frydman, and D. E. Prober, “Tunable superconducting nanoinductors”, *Nanotechnology* **21**, 445202 (2010).  
(Cited on page 146.)
- [121] D. Tanese, E. Gurevich, F. Baboux, T. Jacqmin, A. Lemaître, E. Galopin, I. Sagnes, A. Amo, J. Bloch, and E. Akkermans, “Fractal Energy Spectrum of a Polariton Gas in a Fibonacci Quasiperiodic Potential”, *Physical Review Letters* **112**, 146404 (2014).  
(Cited on page 146.)
- [122] N. T. Bronn, Y. Liu, J. B. Hertzberg, A. D. Córcoles, A. A. Houck, J. M. Gambetta, and J. M. Chow, “Broadband filters for abatement of spontaneous emission in circuit quantum electrodynamics”, *Applied Physics Letters* **107**, 172601 (2015).  
(Cited on page 146.)
- [123] R. P. Erickson and D. P. Pappas, “Theory of multiwave mixing within the superconducting kinetic-inductance traveling-wave amplifier”, *Physical Review B* **95**, 104506 (2017).  
(Cited on page 146.)
- [124] J. Cuevas Maraver, P. G. Kevrekidis, and F. Williams, *The sine-Gordon Model and its Applications* (Springer, 2014), ISBN 978-3-319-06721-6.  
(Cited on page 147.)